Investigating the Molecular Origins of Biocompatibility: Intermolecular Interactions between Human Serum Albumin and Various Chemically Modified Surfaces via High Resolution Force Spectroscopy

by

Monica Anne Rixman

B.S. Chemistry
University of Massachusetts Lowell, 1999

SUBMITTED TO THE DEPARTMENT OF MATERIALS SCIENCE AND ENGINEERING
IN PARTIAL FULFILLMENT OF THE REQUIREMENTS FOR THE DEGREE OF

DOCTOR OF PHILOSOPHY IN POLYMER SCIENCE AND TECHNOLOGY
AT THE
MASSACHUSETTS INSTITUTE OF TECHNOLOGY
FEBRUARY 2004

Signature of Author: ______________________
Department of Materials Science and Engineering
December 15, 2003

Certified by: ______________________
Christine Ortiz
Professor of Materials Science and Engineering
Thesis Supervisor

Accepted by: ______________________
Professor Harold Tuller
Professor of Materials Science and Engineering
Chairman, Committee on Graduate Students

Investigating the Molecular Origins of Biocompatibility: Intermolecular Interactions between Human Serum Albumin and Various Chemically Modified Surfaces via High Resolution Force Spectroscopy

by

Monica Rixman

Submitted to the Department of Materials Science and Engineering
on December 15, 2003 in Partial Fulfillment of the
Requirements for the Degree of Doctor of Philosophy in
Polymer Science and Technology

ABSTRACT

The first step in two of the most troublesome biological responses to the implantation of blood-contacting biomaterials, i.e. thrombosis and inflammation, is the adhesion of blood plasma proteins to the biomaterial surface, which may then initiate platelet adhesion and activation, and thereby set in motion a cascade of adverse host responses. If devices could be developed that prevent that first step from occurring altogether, a new generation of "stealth" biomaterials would be born. Such was the motivation of this project, which sought to investigate the constituent intermolecular interaction forces governing protein adhesion to biomaterials, using the technique of high resolution force spectroscopy. The model protein chosen for our study was human serum albumin (HSA), the smallest and most abundant blood protein in the human body, and typically the first to adsorb to a blood-contacting, implanted device. In the first stage of our investigation, HSA was covalently grafted to a nanosized probe tip at the end of a soft, microfabricated cantilever force transducer. The intermolecular interaction potential, U(D), was recorded between the HSA-modified probe tip and four different model surfaces, including: 1) gold, 2) a hydrophobic, CH_3-terminated alkanethiol self-assembling monolayer (SAM), 3) a hydrophilic, COO^--terminated alkanethiol SAM, and 4) individual, covalently end-grafted molecules of poly(ethylene oxide), in aqueous sodium phosphate buffer solution (PBS, ionic strength IS = 0.01M, pH = 7.4). Both theoretical and numerical modeling were employed to evaluate the experimental results on each of the different surfaces, and to characterize the nature of the protein-bound probe tip. In the second part of this study, we aimed to elucidate the various constituent intermolecular interaction forces contributing to U(D) by strategically manipulating experimental conditions such that we were able to isolate, and in some cases quantify, the electrostatic, steric, and hydrophobic components. It was found theoretically that electrostatic and steric forces accounted for approximately 8% and 4% of the total intermolecular interaction force; experimentally, these forces are observed to be completely dominated by a repulsive force which increases in magnitude as the ionic strength of the solution is increased. It is believed that this additional force is imparted by the PEO, and may be due to a change in the conformation of the PEO coil, or the structure of the network of water molecules in the space between the PEO coil and the approaching probe tip. The hydrophobic component was experimentally quantified to be approximately 20% of the total intermolecular interaction force at D ~ 1 nm. In the third part of this investigation, we sought to study the interactions between HSA and a series of oligosaccharide-functionalized surfaces inspired by the glycocalyx, which coats all living cells and is naturally and necessarily hemocompatible. The results of this study were then compared to experiments conducted in parallel on poly- and oligo(ethylene oxide) modified surfaces. Our results suggest that higher oligosaccharides may indeed be effective candidates for novel biomaterial surface coatings with enhanced hemocompatibility, and in fact have the potential to outperform both poly- and oligo(ethylene oxide), which are well-known to be the most protein-resistant biocompatible materials currently in use. Finally, we demonstrate the versatility of our technique in probing a variety of intermolecular interactions, by extending it to the investigation of the binding forces and affinities between the HIV therapeutic drug Cyanovirin-N and oligosaccharides mimicked from the specific glycoprotein on the HIV viral envelope which is responsible for the binding of the virus to host cells.

Thesis Supervisor: Christine Ortiz

Title: Assistant Professor of Materials Science and Engineering

BIOGRAPHICAL NOTE

Monica Anne Rixman was born on November 15, 1977, in Oklahoma City, Oklahoma, USA to Terie A. M. Rixman and Dwight E. A. Rixman. She grew up in Plano, Texas, and graduated from Plano East Senior High School in 1995. She then attended the University of Texas at Dallas from 1995-1997, whereupon she relocated with her mother and her brother, Jonathan K. Rixman, to Burlington, Massachusetts, and continued her studies in chemistry at the University of Massachusetts Lowell. During her final two years of undergraduate studies, she worked as a research assistant conducting polymer synthesis and characterization by novel "green chemistry" routes, under the supervision of Daniel J. Sandman, Professor of Chemistry. Her undergraduate research culminated in three first-author publications in such peer-reviewed journals as *Macromolecules* and *The Nucleus*, as well as an undergraduate thesis. She graduated magna cumlaude with a Bachelor of Science from the University of Massachusetts Lowell in June of 1999, whereupon she undertook a summer internship at the Max Planck Institute for Polymer Research in Mainz, Germany, under the supervision of Professor Dr. Gerhard Wegner. During this time she worked closely with Dr. Andreas Taubert on the effects of polymeric substrates on the crystallization of zinc oxide. In the fall of 1999, she began her doctoral studies in the Program in Polymer Science and Technology, in the Department of Materials Science and Engineering at the Massachusetts Institute of Technology. She has since worked to complete the research reported herein, which has been published multiple times in *Langmuir*. She has also presented her work at scientific conferences both nationally and internationally, including at several meetings of the American Chemical Society, the American Physical Society, and the Gordon Research Conferences, as well as the Euregionale Chemistry Conference. She has won several academic awards, including a full academic scholarship to the University of Texas at Dallas, multiple undergraduate research scholarships from the American Chemical Society, and a National Science Foundation Graduate Fellowship, as well as awards for "Best Speaker" and "Best Poster Presentation" at conferences both domestic and international. The motivation to transition from chemistry to polymer science was initially fueled by Monica's desire to conduct science that demonstrated the tangible capability of helping to better the lives of mankind. Upon graduation, she continues in this mission, as she join Mitek Worldwide, a subsidiary of Johnson & Johnson, as a Senior Engineer. Her projects in the near future will focus on polymeric devices and components for reattachment of soft tissue to bone.

ACKNOWLEDGEMENTS

There are so many who have helped me along the path to where I am now, that I hardly know where to begin to thank them all. In many ways, we shape our own futures, and determine our own possibilities by our own passions and efforts. But somehow we always seem to go so much further than we ever dreamed imaginable, and that is undoubtedly due to the selfless contributions of our friends and loved ones. In this all-too-human section of my thesis, I hope to pay some tribute to those who have carried me, pushed me, and cried with me. I only regret that I should be so brief.

I can't imagine a more important person in my life than my mother. From the first day we stepped foot on the MIT campus, headed straight for the chemistry department to demand to know just how one gets admitted to a place like MIT, to the day we cried in the airport when I told her that I had been accepted; the day *we* first visited as a prospective student, and the day I passed my qualifying exams and we met and celebrated in our special place; the day I finished writing my thesis, and, finally, the day I *defended* my thesis – she has been my foundation and voice of encouragement from Day One. Her confidence through the years, the sacrifices she has made, the laughs we shared and the tears we dried, and our unending faith in each other, have formed a friendship deeper than many have the privilege to ever know. To me, she is the epitome of what it means to be a strong woman, and I only hope to be more and more like her through the years. Thank God for you, Momma.

I wish that I could give everyone an entire paragraph, and also that I didn't have to choose an order; I would like to assure the reader that the following order of gratitude does not reflect the relative importance of these people in my life. First, to my father, I would like to say thank you for believing in me, and for being a constant voice of pride and encouragement, despite the miles between us. Your confidence in me has meant so very much. To my brother, Jonathan, who is undoubtedly the best person I have ever known, thank you for always supporting me, in spite of our by-the-book sibling rivalry. I'll never forget the day you were late to work just so that I would have someone to hug when I got the phone call that I had been accepted to MIT. To my grandmother, Shari, who, along with my mother, lovingly took care of me during those long weeks of writing in Burlington, and who has ever been eager to lend an understanding ear or an insight into the bright side of things. You are truly an amazing woman, and one of my fondest role models. To my grandfather, Papa, who has been my scientific inspiration and the ever-present gentle but strong hand on my back, guiding me along the way. I only wish he had lived long enough to see me graduate. Surely he is watching. To my grandmother, Momar, who, like her daughter (or vice versa), has taught me the merits of being a strong and independent woman, and at the same time the comforts of not having to be strong *all the time.* And finally, to my Great Aunt Eunice, the first Dr. Rixman, for being a source of inspiration and support since I first began this whole process.

To Karl Ruping, whose objectivity and wisdom so often brought logic to chaos, and whose love and friendship carried me through so many ups and downs. I can't imagine the past three years without you. To my girlfriends Kristina Muskiewicz, Kristine Friesen, Malinda Tupper, and Celia Macias, for the comfort of a confidant, and the warmth of laughter. To John Lock, Bill Schmitt, Sophie Louvel, Cody Friesen, and Mazen Ferzly, whose valued friendship are of a vintage truly to be savored. Lord knows how long the Ph.D. path may have seemed without the good times we shared! To Joost Bonsen, who has been an invaluable source of direction, as well as a genuine and close friend. To Timothy Doyle, whose group therapy, generosity, and laughter has made it all worthwhile.

To LaShanda James-Korley, Shashi Murthy, Greg Pollock, and Tseh-Hwan Yong, without whom I may never have made it through the first year in engineering, and especially to LaShanda, who has pain-stakingly kept me gripped in reality, and who I am very lucky to call a true friend. To Kip Hauch, a fellow adventurer who I am fortunate to have met just in time, and who has helped to pull me through the thick of it. To Kelly Cassidy, a loyal and wonderful friend who has not missed a single big moment in my life since I moved to Massachusetts; to Robin Danzini, whose serious humor has kept it real; and to Susan Angel, who is one of the loveliest people I have ever known. And finally, to Geoff Owens, who I was privileged to meet again when I was old enough to appreciate his friendship.

To the cast at the Muddy Charles – my coworkers Michaela Wiegel, Solar Olugebefola, Holly Michael, Keith Santarelli, John Mills, Paige Hopewell, Troy Simpson, and Janice Lansita, my boss, Joe Contrada, and my beloved customers Michael Cook, Barbara Skinner, Jimmy Carter, Tom Callahan, Tony Puttick, Paul Bethge, Paul Campbell, and Teddy and Jack, of course… I don't know that I could ever articulate what having you all in my life has meant to me. It's kept me sane, and light-hearted, and absolutely made my time at MIT a whole lot of fun!

To the gals in the Association of MIT Alumnae; Gwelle Boissiere, Sarah Simon, and Joan Coyne, who have given me not only beautiful friendships, but also a unique view of what it really means to me a female graduate of MIT.

To the members of the Ortiz group, whose insights and discussions have been absolutely invaluable. And in particular to Christine Ortiz, Delphine Dean, Celia Macias, and Jae Hyeock Choi, who have each had a significant hand in the development of this thesis. Delphine, the mistress of numerical modeling and electrostatic interactions, Celia, my lovely assistant with whom it has been a true pleasure to work, and who shares the credit for all results presented in Chapters 5-7, and Jae, my successor in this adventure. And, of course, Christine, my mentor. When I joined her research group in the fall of 1999, it was in no small part because I felt I could learn quite a bit from this young, successful, brilliant, and *vivid* female Professor. Four years later, I have indeed learned quite a bit about science, technique, and professionalism, and yet I have not even begun to catch up to her. Thank you, Christine, for having faith in me, and for teaching me so very much.

I would also like to thank the members of my thesis committee, Professors Daniel Blankschtein, Anne Mayes, and Peter So, who, along with Christine, have provided the insight and guidance that has made this thesis something to be proud of.

Finally, I would like to thank Professor Daniel Sandman, without whom I would not be writing this today. He provided me with opportunity and possibility, and effectively handed me my future. *Thank you.*

And last, but by no means least special thanks to the National Science Foundation, which awarded me the graduate fellowship that made all of the work reported herein possible.

Monica Anne Rixman

TABLE OF CONTENTS

CHAPTER 3

Nanoscale Intermolecular Interactions Between Human Serum Albumin and Alkanethiol Self-Assembled Monolayers

LIST OF FIGURES

LIST OF TABLES

Chapter 1

GENERAL INTRODUCTION

1.1 Biomaterials: Materials and Design

1.1.1 Definitions.

A **biomaterial** may be defined as: "a synthetic material used to replace part of a living system or to function in intimate contact with living tissue." A **bio-based** material, while sometimes referred to as a "biomaterial", is perhaps more accurately defined as: "an egineering material made of substances derived from living tissues". [1] This project is primarily involved with devices fitting within the former definition of biomaterials, and specifically with those materials that are used as surface coatings on implantable biomaterials in order to elicit a desired response from the biological system. A biomaterial may be further be identified as belonging to one of three classes: "Class 1" refers to devices intended for percutaneous, temporary use, such as Band-Aids™; "Class 2" refers to devices used for temporary internal applications, such as drug delivery systems; "Class 3" includes devices that are permanently implanted in a body and intended to integrate and fuction with the living body, such as vascular grafts. [2] Here we focus primarily on the interactions of Class 3 devices with the biological system in which they have been implanted.

1.1.2 Design Criteria.

A combination of factors govern the design of Class 3 devices. Not only must they be able to perform the intended biological function, but they must also be capable of illiciting an appropriate response from the host organism; this latter requirement is increasingly the accepted definition of "biocompatibility". The "desired host response" is most often evasion of attack by the host's immune system, but may also include intentional signaling of various biochemical pathways, e.g. initiation of tissue integration with the implanted device. Another factor governing material design is that the device must be capable of withstanding the wide variety of forces it will be subjected to in the host organism. For example, a vascular graft must be strong enough both not to break under high systolic blood pressures and also not to collapse under low blood pressures; at the same time, the graft must also be flexible enough to weave around bones, tissues, and organs, and to bend when the body bends – but without collapsing. The graft must also be structurally and chemically sound so as not to degrade or erode prematurely in the organism, as loosened debris may trigger an unfavorable response from the host's immune system. Finally, it may be important in some cases to match the compliance of the surrounding tissues, so as to prevent degradation of the existing tissues. For example, in the design of joint prosthetics such as total hip replacement devices, if the modulus of the prosthetic is much greater than that of the surrounding bone, the prosthetic will preferentially absorb the majority of applied forces as the host walks or runs, e.g., and the surrounding bone will begin to atrophy, ultimately resulting in loosening of the prosthetic in the joint, great pain to the patient, and the need for replacement of the device.

There are two great caveats to the above material requirements: first, those materials which are strong enough not to break or degrade under the various loads applied by the normal activities of the host, most often have much migher moduli than the surrounding tissue, and therefore compliance matching becomes extremely challenging; second, those materials that may fit the majority of mechanical requirements, are often not compatible with the human body. The first of these is a rather difficult problem that remains to be solved, and which will not be addressed in this document. The second caveat may be addressed by the introduction of a protective coating around the implanted device to shield it from attack by the host immune system, and/or to initiate a specific biochemical response. Common examples of materials used to impart biocompatibility to implantable devices include the coating of total hip replacements with porous hydroxy apatite to encourage bone in-growth, [3]and the coating of vascular grafts with heparin to reduce thrombosis. [4]Materials may be coated by either chemical attachment (i.e. "chemisorption", by covalent grafting) of the coating material onto the outer surface of the device, or by "physisorption", i.e. by the adhesion of the coating material to the device by nonspecific intermolecular interactions such as hydrophobic interactions, van der Waals forces, etc. Clearly the latter method is not as robust of a design as the former, and erosion can be a significant problem in physisorbed systems.

1.1.3 Materials.

Coatings and core materials may be made from a number of different materials, depending on the necessary processing and desired application. Some of the most common materials include titanium alloys and stainless steel (total joint prosthetics and coronary stents), and calcium phosphate derivatives (bone substitutes); a variety of polymers are also used in biomaterials, including poly(tetrafluoro ethylene) (Teflon™, vascular grafts), poly(hydroxyethyl methacrylate) (contact lenses), polyethylene (total joint prosthetics), polylactide, polyglycolide, and copolymers thereof, as well as polycaprolactone (drug delivery systems) and poly(ethylene oxide) (surface coatings). The introduction of polymers into the field of biomaterials has launched a new era in the fabrication of prosthetics, [5]regenerative guides, [6,7] chromatographic supports, contact lenses, and drug delivery systems. [8-10] The advantages of polymeric devices over those manufactured from other materials include ease of processing, the ability to microscopically tailor texture, shape and mechanical properties, and profoundly lesser cost. Polymeric coatings in the form of physisorbed or end-grafted "brushes" (i.e. polymers which are packed so closely on the surface that they stand up on end to accommodate their neighbors and to retain their own excluded volume in a more crowded environment) are frequently employed to improve the biocompatibility of a wide array of biomaterials.

1.1.4 The Challenge of Evading Protein Adsorption.

One of the greatest challenges to biomaterials scientists is preventing the nonspecific, noncovalent surface adsorption of proteins, the well-known first step in many undesirable processes such as triggering inflammation around artificial organs, fouling of contact lenses, and accelerated clearing of bare liposomes by the reticuloendothelial system. [11] Thrombosis, the process of blood clot formation and build-up on or within a blood vessel or blood-contacting surface, is a common problem in blood-contacting devices, and is a cascade of multiple biochemical reactions which is first initiated by the adsorption of blood plasma proteins, and followed by platelet adhesion and activation, initiation of the coagulation cascade, and finally, thrombus formation. [12,13] As shown schematically in Figure 1.1, protein adsorption, the first step in the coagulation cascade, can take place by myriad mechanisms depending on a number of factors such as the protein "radius," R_P, the height of the polymer brush, L_0, and the mean distance between polymer end-grafting sites, s.

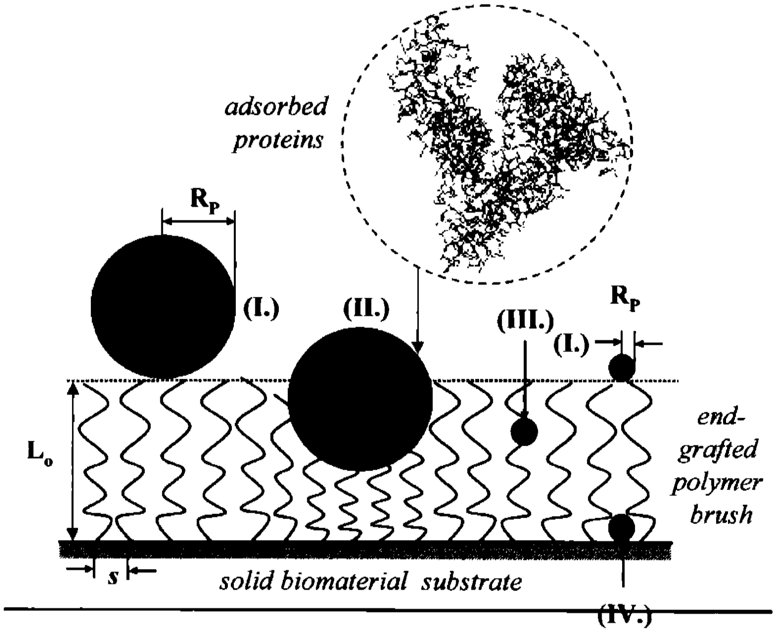

Figure 1.1 Schematic showing the interaction of proteins with a polymer brush end-grafted to a biomaterial substrate *(adapted from Halperin, 1999[14])*

These include: (I.) adsorption of proteins to the top boundary of the polymer brush, (II.) local compression of the polymer brush by a strongly adsorbed protein, (III.) protein interpenetration into the brush followed by the noncovalent complexation of the protein and polymer chain, and (IV.) adsorption of proteins to the underlying biomaterial surface via interpenetration with little disturbance of the polymer brush. [14] The adsorption process is determined by the total effective interaction free energy between the protein and the surface, U(D) (where D is the protein-surface separation distance), which is a sum of the protein-brush and protein-substrate interactions. U(D) is a superposition of various repulsive and attractive contributions that lead to complicated intermolecular potentials whose shape varies with the strength and range of the constituent interactions. [14,15]

To produce protein-resistant biomaterial surfaces, it is clear that one must design systems in which repulsive interactions are maximized and attractive ones are minimized. For polymeric surfaces, "steric" or "overlap" interactions, which are enhanced by long chains (i.e. high molecular weight) and high surface grafting densities, are of prime importance.

Other repulsive forces may include hydrophilic hydration forces, orientational entropy penalties for rod-like polymers, enthalpic penalties for disruption of polymeric supramolecular structure, and electrostatic repulsion due to overlap of the surface diffuse counterion electrical double layers (for charged systems). Attractive protein-brush and protein-substrate forces may include hydrophobic interactions, hydrogen bonding, and/or van der Waals (VDW) forces. In order to predict the mathematical form of many of these interactions, a number of theories[16-18] have taken the approach of modeling proteins as dense, rigid, structureless, colloidal particles with nonadsorbing surfaces and the polymer brush as simple, flexible chains.

Subsequent stages of protein adsorption become increasingly complex and depend on the conformation, orientation, and mobility of the adsorbed proteins, the time-scale of conformational changes, protein exchange and desorption, and interactions of adsorbed proteins with each other. [19] The kinetics of the adsorption process and the time-dependent nature of the adsorbed biofilm (e.g. thickness, chemical structure, morphology, etc.) can be probed by a variety of experimental techniques such a radiolabeling, total internal refelection fluorescence, surface plasmon resonance, ellipsometry, optical waveguide lightmode spectroscopy, attenuated total reflectance fourier transform infrared spectroscopy, neutron and X-ray reflectivity, quartz crystal microbalance, electrical techniques, atomic force microscopy (AFM) imaging, and contact angle measurements. A variety of standards[20-23] also exist for *in vitro* hemocompatibility testing using biochemical and immunological assays to test for thrombosis, coagulation, platelet count, etc., which are quicker and less costly than *in vivo* clinical trials. Although widely investigated and discussed in the literature, hemocompatibility, which varies greatly from material to material, is still poorly understood. Hence, attempts to prepare thromboresistant blood-contacting devices such as hemodialysis membranes, intra-arterial chemical sensors and catheters, vascular grafts, and blood pressure monitors have been met with limited success.

1.2 Specific Aims

The main objective of this project was to develop a fundamental understanding the molecular origins of the biocompatibility of blood-contacting, implantable biomaterial devices, and to use this knowledge in the design of novel "smart" biomaterial surface coatings with enhanced protein resistant properties. We began our investigation by targeting the most commonly encountered scenario: we chose as our model biomaterial "surface" poly(ethylene oxide), perhaps the most extensively used polymer for biomaterial surface coatings; as our model protein, we chose human serum albumin, the most abundant blood protein in the human body, and typically the first to adsorb to an implanted, blood-contacting device. [24]

1.2.1 Poly(ethylene oxide)

The model polymer chosen was the neutral, flexible, water-soluble, synthetic polymer, *poly(ethylene oxide)* (PEO), $-[CH_2\text{-}CH_2\text{-}O]_n-$, poly(oxyethylene) (POE), or poly(ethylene glycol) (PEG), $-[CH_2\text{-}CH_2\text{-}O]_n-$, which is a synthetic polymer that is typically thought of as biologically inert and is used extensively to provide a protective coating to improve the protein resistance of biomaterial surfaces. However, a variety of different experimental techniques have shown that proteins do indeed adsorb to PEO given enough time and certain disadvantageous conditions (e.g. high forces, dilute polymer solutions, long incubation times, etc.) [11,25-36] Despite extensive efforts and debates in the literature, the detailed molecular mechanisms of the interaction of PEO with proteins is still largely unknown. Following is a brief summary of the numerous suggested nonspecific attractive and repulsive constituent contributions to the net protein-PEO intermolecular interaction potential as a function of separation distance, U(D).

PEO : Repulsive Interactions. PEO has a number of unique properties that are thought to be directly related to the presence of repulsive interactions which give it a distinctive capability for protein resistance. PEO is hydrophilic (advancing contact angle, $\theta_{W(A)} = 60 \pm 1$) and water soluble at room temperature, with a relatively low Flory-Huggins interaction parameter (χ = 0.41-0.45. at ~25°C [37] and high values of the second virial coefficient (A_2 = 30–60x10^4 cm^{3}mol/g^2 at ~ 25°C [37] due to its strong tendency to form hydrogen bonds with water via the -O- groups. The unique structure of PEO has been predicted by molecular dynamics simulations[38] and studied experimentally by infrared spectroscopy, [39,40] Raman spectroscopy, [41] nuclear magnetic resonance. [40,42] and single molecule force spectroscopy measurements. [43] (all in aqueous solution), as well as calorimetry, [44] and X-ray diffraction (in the crystalline form). [45] It has been postulated that the majority of chain segments exist in a trans-trans-gauche (ttg) conformation that is stabilized by water binding, leading to an (11/2) helical supramolecular structure[44] that is similar to, but more expanded than, that found in the crystalline form (Figure 1.2 (A)-(C)). As shown in Figure 1.2(D), in the more extended planar trans-trans-trans (ttt) configuration the distance between -O- atoms is large enough that a water molecule may only form one hydrogen bond with the PEO backbone.

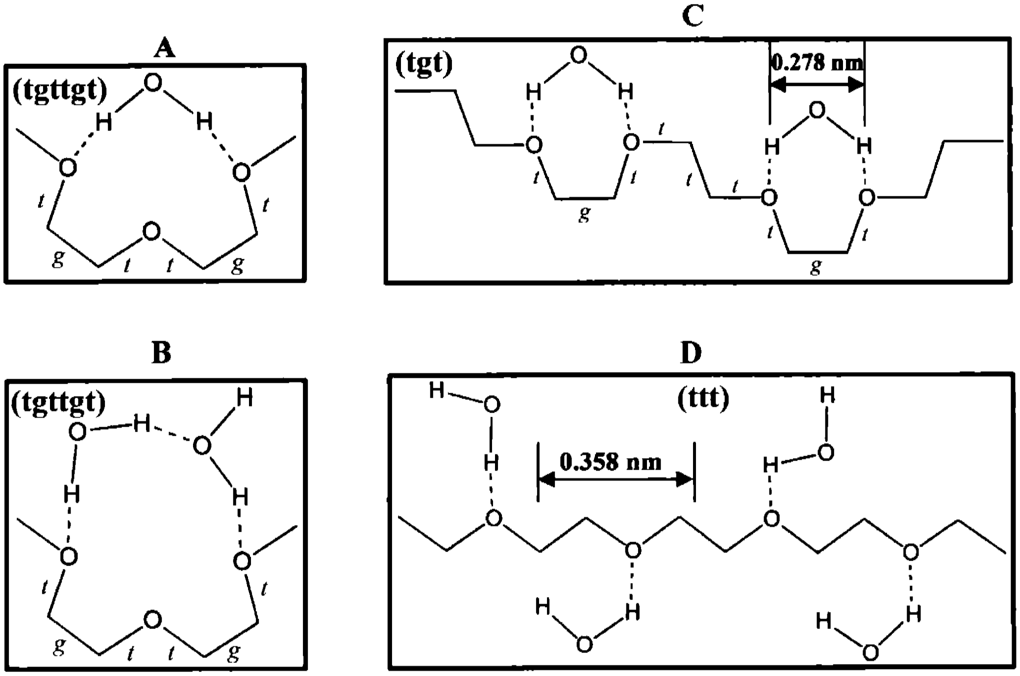

Figure 1.2 Possible conformations of PEO in aqueous solution : In water, PEO may take on a "folded" trans-gauche-trans (tgt) configuration in which the ether oxygen atoms undergo hydrogen bonding in a variety of different ways (**A-C**). The all-trans (ttt) planar zig-zag conformation (**D**) is also shown.

While it is known that the -O- atoms of PEO in the melt may chelate a variety of metal cations including Na^+ and Li^+ (the former of which has a binding energy approximately ten times smaller than that of the latter), thus rendering a fixed positive charge along the chain, in aqueous salt solution PEO has been found to be incapable of chelating certain larger cations, including Na^+, K^+, NH_4^+, and CS^+. [46-49] The buffered solutions employed in the majority of the experiments presented in this report have Na^+ and K^+ cations, and hence, the PEO is assumed here to be effectively neutral; however, since mostly all proteins are typically charged under physiological conditions, there is also the possibility of a repulsive electrostatic double layer force due to the local ionic osmotic pressure and Maxwell electric stress. [50] Correspondingly, attractive electrostatic interactions with proteins of net opposite charge or surface regions of a protein with opposite charge will be minimized. Since PEO does not have any bulky side groups or fixed charge groups, steric and electrostatic hindrances are expected to be minimal (the steric parameter at 20°C, σ = 1.38-2,) [37] and the chain's flexibility and mobility can help accomodate the shortened ttg conformation and continuous structural rearrangements with water. The strong affinity and binding with water thus creates repulsive enthalpic penalties for disruption of these bonds and the helical supramolecular structure. Another repulsive force, which is not unique to PEO, arises from polymeric "steric" or "overlap" interactions, which are enhanced by long chains (i.e. high molecular weight) and high surface grafting densities. For end-grafted polymer brushes in a good solvent, there are two main components to the steric force that are determined: an attractive elastic restoring force due to configurational entropy, and a repulsive osmotic pressure due to an increase in polymer chain segment concentration. The osmotic pressure originates from solvent translational entropy and intrachain excluded volume due to short-range monomer-solvent affinity and/or monomer-monomer repulsion. PEO has a large excluded volume due to its high affinity for water, as reflected by its low value of χ and high value of A_2. For compression of low density surfaces of isolated, end-grafted polymer "mushrooms," the steric force arises from a free energy penalty for chain segment-surface confinement, as well as an entropic elastic penalty for chain stretching in the plane perpendicular to the compression axis. [51-54] Lastly, the compression of a polymer layer (for example by incoming proteins) will also be opposed by a hydrodynamic lubrication force due to lateral expulsion of the solvent residing between the protein and the surface. [15] To summarize, the possible repulsive forces present for PEO include steric, enthalpic penalties for disruption of hydrogen bonds with water, electrostatic counterion double layer forces, and hydrodynamic lubrication forces.

PEO: Attractive Interactions with Proteins. Attractive protein-polymer interactions may include hydrogen bonding, electrostatic, and van der Waals (VDW) forces (including so-called "hydrophobic" interactions).

Hydrogen bonding is a type of secondary bonding originating in dipole-dipole interactions. As is depicted in Figure 1.3, Particularly nucleophilic atoms such as oxygen, nitrogen, and fluorine, form a strong dipole within their covalent bonds to hydrogen atoms, resulting in a partial positive charge on the hydrogen atom. The electrophilic hydrogen atom then becomes available for partial bonding with other nucleophilic atoms in its near vicinity. The hydrogen bond is relatively strong as a secondary bond, but is much weaker than a covalent bond (the strength to break a hydrogen bond is approximately 20 kJ/mol, as compared to 400 kJ/mol for a covalent C-H, O-H, or N-H bond). [55] Water is one of the most polar molecules known, and its hydrogen atoms readily form hydrogen bonds with the ether oxygen atoms in PEO, resulting in the high solubility of PEO in water. The PEO-water system exhibits a lower critical solution temperature (LCST) behavior, i.e. as the temperature of a solution of PEO and water is raised, the PEO solubility decreases. This effect is due to an increased instability of the hydrogen bonds in at the higher energy state. PEO may also hydrogen bond with hydrogen donors on proteins in much the same way that it does with water.

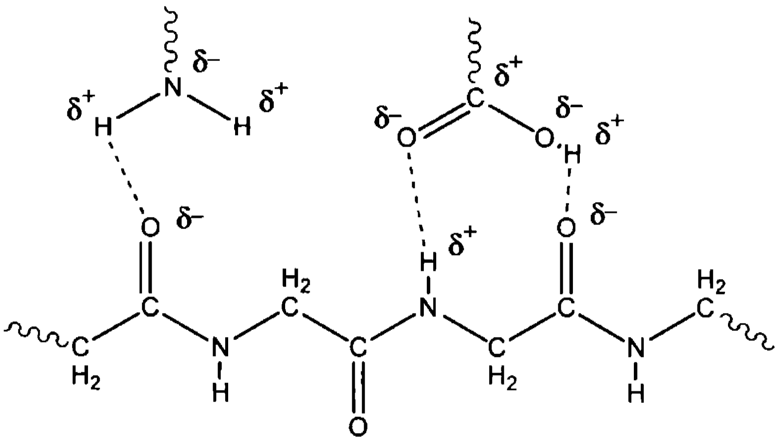

Figure 1.3 Depiction of the mechanism of hydrogen bonding.

The δ^+molecular origin of the hydrophobic interaction is controversial and largely unknown, but generally thought to be entropy-driven. [56] Water molecules near a hydrophobic surface cannot form hydrogen bonds with the surface since there are no donor hydrogen atoms or hydrogen bond acceptors, and hence the original water structure is disturbed. Rather than having interfacial molecules with partially charged dangling bonds, it is thought that water molecules reorient themselves into a more ordered structure so as to preserve as many hydrogen bonds as possible. Although this process is not entropically favorable, the associated entropic penalty is less than the corresponding enthalpic penalty for disruption of hydrogen bonds. The strong attraction felt between two hydrophobic surfaces in water is then not only due to the drive to avoid disruption of the surrounding hydrogen bonded network, but also due to the favorability of minimizing the exposed hydrophobic surface area, and thereby minimizing the entropic penalty for rearrangement of the water molecules.The hydrophobic character of PEO is supported by its known solubility in both aqueous and organic solvents, [32]adsorption to hydrophobic surfaces and the air-water interface, [57-59]and its use as a surfactant in a number of applications. [60-63]

1.2.2 Human Serum Albumin.

55 wt% of blood is plasma or serum (pH = 7.4, ionic strength = 0.15M) which contains 6-8% proteins (over 3,000 different types) including 58% albumins, 38% globulins, and 4% fibrinogens, most of which possess a net negative charge. [64] The model protein chosen for these studies is the highly water-soluble plasma protein, human serum albumin (HSA), which is the smallest and most abundant plasma protein in the human body, and typically the first to adsorb[24] to a blood-contacting implanted biomaterial. Accounting for 55% of the total protein in blood plasma, HSA is a single-stranded polypeptide whose amino acid sequence is known. [65] Its ionizable groups include 116 total acidic groups (98 carboxyl and 18 phenolic -OH) and 100 total basic groups (60 amino, 16 imidazolyl, 24 guanidyl). The absolute molecular weight of HSA, as calculated from the numbers and molar masses of the 565 constituent amino acid residues, is 66,436 g/mol. Assuming a polypeptide repeat unit contour length of 0.38 nm (Figure 1.4), the total contour length of the denatured protein is $L_{contour}$(HSA) = 216 nm.

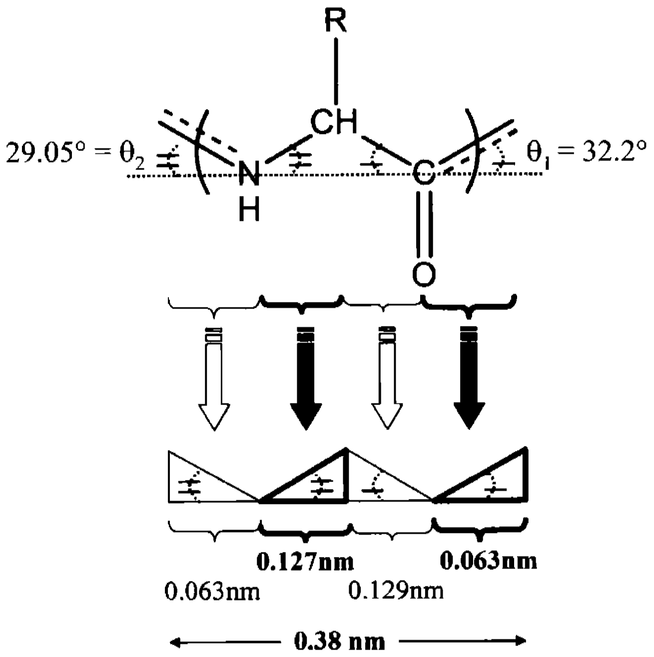

Figure 1.4 Schematic of the contour length of a single polypeptide repeat unit, as calculated from reported peptide bond angles. [66]

HSA contains 17 disulphide bridges, one free thiol (Cys 34), and a single tryptophan (Trp 214). HSA typically binds 1-2 lipids per protein, [67] which effectively reduces the isoelectric point (pI, i.e. the pH at which the total charge including bound ions is zero); in 0.15M NaCl the pI for lipid-bound HSA is 4.7, [68] while pI = 5.7 for lipid-free HSA. [69] As is shown in Figure 1.5(A), at pH = 7.4, the shape of native HSA in solution is thought to be a prolate ellipsoid of revolution with major and minor axes of 12.0 and 2.7 nm, respectively, [70] or 14.1 and 4.1 nm, [56,71] linking three homologous, globular domains in series each carrying net charges of -9*e*(domain I, N-terminal), -8*e*(domain II), and+2*e*(domain III, C-terminal) giving a total net charge for the protein of -15*e* (calculated from the amino acid composition) [67]or -19*e* measured experimentally (due to additional bound ions) at pH = 7.4 (the pH of blood). [72]X-ray determinations of the structure of HSA in a crystal have suggested a “heart-shaped” structure, also with three homologous domains, which can be represented by an equilateral triangle with sides of approximately 8 nm each and an average thickness of 3 nm (Figure 1.5 (B)-(C)). [73-75]

HSA is a dynamic, rapidly moving, "breathing" molecule having a rotational diffusion coefficient of approximately 20 nsec, [67] and is known to have some degree of flexibility, expansion, and contraction, which enables significant conformational transitions. Due to the exceptionally dynamic nature of this protein, the average shape that HSA takes on in aqueous solution remains unclear. [76,77] It is believed that there are six helical subdomains that form hydrophobic channels with basic and hydrophobic amino acid residues placed at the ends, while the overall surface remains extremely hydrophilic. As determined from X-ray diffraction, HSA is 67% α-helical, with the remainder in β-turns and extended polypeptide chains, and contains no β-sheet structure. [67] HSA is known to have a 0.55 nm thick monolayer of closely associated water molecules on its surface, with most (98%) oriented with their H atoms pointed towards the protein surface. The next layer of water is about 30% oriented, creating a "fuzzy" hydrated interphase in aqueous solution. [67]

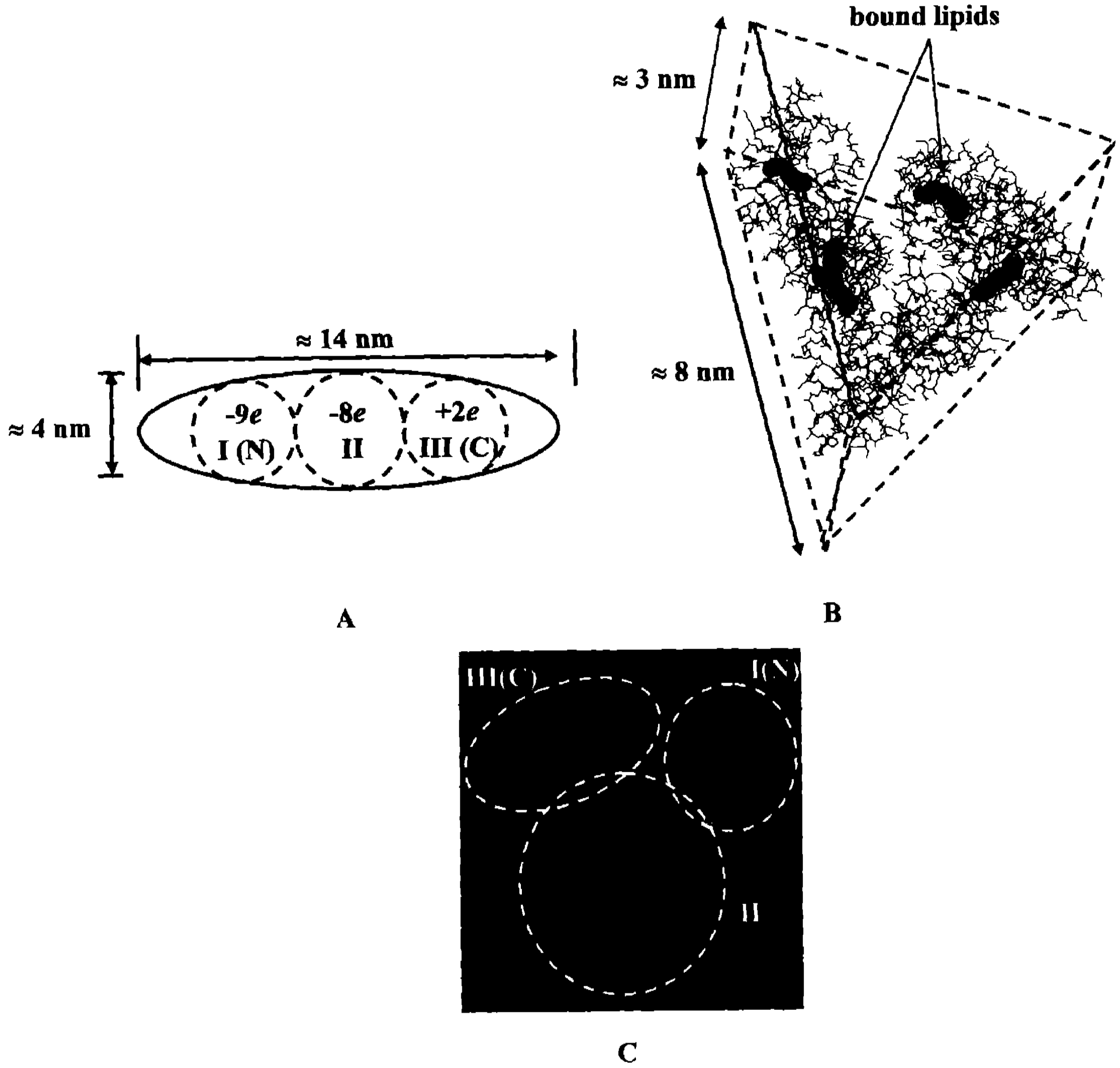

Figure 1.5 (**A**) Schematic of proposed HSA ellipsoidal shape in solution, showing the dimensions and net charges of its three domains (adapted from reference[78]). (**B**) Wireframe display showing the dimensions of HSA in the crystalline form, complexed with myristic acid (downloaded from reference[74], also see reference[73]). (**C**) Ribbon model of the display shown in B.; the three domains I, II, and III are labeled and shown in red, green, and blue, respectively.

The noncovalent complexation between PEO and HSA in dilute aqueous solution has been studied extensively via quasi-elastic light scattering, static light scattering, electrophoretic light scattering, dialysis, and fluorescence spectroscopy under a variety of conditions and for a series of different PEO molecular weights. [26] Complexation is observed to occur at low pH, presumably due to hydrophobic interactions supported by hydrogen bonding between the ether groups of the PEO with the carboxyl and phenolic -OH groups in the protein. Complexation also occurs at high pH since most of the basic groups in the HSA are deprotonated and can also form hydrogen bonds with the ether groups of the PEO.

1.2.3 Instrumentation.

In order to directly quantify the molecular-level interactions between HSA and PEO, we employed the technique of high-resolution force spectroscopy (HRFS), a relatively new method that employs an extremely soft force transducer (e.g. microfabricated cantilever with a fine probe tip) to measure pN-level forces as a function of nm-scale separation distances.

HRFS experiments were conducted using a new cantilever-based instrument, the Molecular Force Probe® (MFP) (Asylum Research, Santa Barbara, CA) to measure force, F (nN), versus tip-sample separation distance, D (nm) (henceforth referred to and labeled on graphs as "Distance"). Similar to the atomic force microscope (AFM), a focused laser beam is reflected off the backside of a microfabricated cantilever force transducer with a fine probe tip into a position sensitive photodetector (PSPD). Data is collected on "approach" (i.e. as the probe tip moves towards surface) and "retract" (i.e. as the probe tip moves away from surface). The vertical sensor output difference of the top minus bottom quadrants of the PSPD, s (nA), is used to measure the cantilever deflection, δ (nm), which is then converted into force, F (nN). Atomic-scale vertical movement of the cantilever is made possible by the use of a piezoelectric crystal, which responds to an applied voltage by expanding and contracting on the unit cell level. A typical HRFS experiment on a hard substrate is depicted in Figure 1.6. Data acquisition is initiated and s (nA) is recorded as a function of z-piezo deflection, z (nm), where z is the axis normal to the sample surface that is converted into tip-surface separation distance, D (nm). A full description of this instrument, its limits of force and displacement detection in fluids, procedures for spring constant calibration and conversion of raw data, details of measurement errors, and description of typical force versus distance curves including the mechanical instabilities of the cantilever, are given in Appendix A.1. It should be noted that in all HRFS experiments, the spring constant of the cantilever, k_c, is much less than the stiffness of the underlying (Au) substrate. Hence, little or no deformation of the substrate occurs, leading to the D = 0 vertical region of apparent infinite slope in the high-force, constant compliance regime and all forces measured are surface forces rather than contact mechanical forces due to substrate elastic and/or plastic deformation. In nanoindentation, the setup is quite the opposite; a very stiff cantilever is pressed into a (relatively) softer surface, which deforms to varying degrees depending on the mechanical properties of the substrate. Force (nN) versus Distance (nm) curves were measured at room temperature using a Thermomicroscopes™ microfabricated V-shaped Si_3N_4 cantilever ($k_c \sim 0.01$ N/m, length, l = 320 μm, resonance frequency, ω_c = 850Hz) with unsharpened ($R_{tip,unmodified} \sim$ 30-100 nm) square pyramidal probe tips at the end that had been modified with HSA as described in the following chapter. The HRFS experimental parameters for all experiments reported here included: z-piezo range = 1 μm, rate of data acquisition = 5000 points/s, constant z-piezo displacement rate = 1 μm/s (slow enough to minimize hydrodynamic effects), and the piezo reversed immediately between approach and retract cycles (i.e. there was no dwell time on the surface)

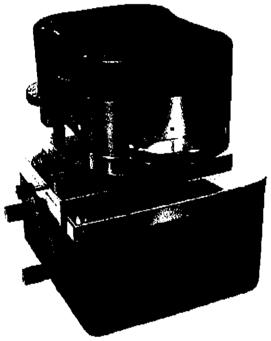

Left: The Molecular Force Probe (MFP).[111] Resolution in fluids: Force ~5pN, Distance ~3 Å

Right: V-shaped cantilever probe tip. The spring constant used in our experiments is 0.01 N/m. The tip radius is ~40-100 nm

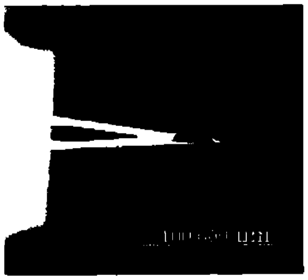

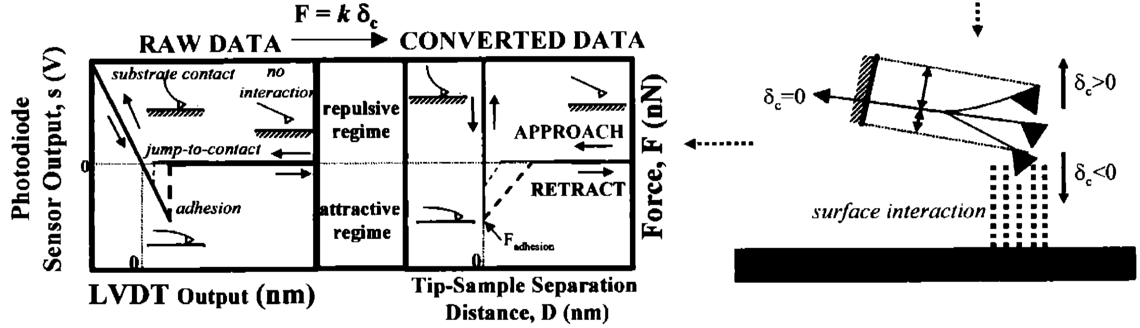

Figure 1.6 Top left: photograph of the 1-D Molecular Force Probe; **top right**: image of a single cantilever force transducer; **bottom right**: deflection of a cantilever in response to intermolecular interactions with the surface; **bottom left**: a typical HRFS force versus distance curve on a hard substrate.

1.2.4 HRFS of Polymers.

Typical polymers in a "good" solvent take on a "freely jointed chain" [79] or "worm-like chain" [80,81] conformation, in which the polymer segments are randomly distributed in a Gaussian manner, about their center of gravity. For surface-bound polymers, the center of gravity is the grafting point of the polymer chain to the surface. The segments are in constant motion, gyrating about their center, and their root-mean-squared average dimension is known as the "radius of gyration", R_g. Flory developed an expression for the R_g of an isolated, end-grafted, polymer chain (similar to the conditions frequently employed in this study); this expression, shown below, is referred to heretofore as the "Flory Radius", R_F: [82]

$$R_F = \alpha l \sqrt{\frac{C_\infty N}{3}} \qquad \textbf{Equation 1.1}$$

where $\alpha^5 - \alpha^3 = 2C_M \left[0.5 - \chi\right]\sqrt{M_n}$; [82] α is the Flory expansion parameter and measures the degree of swelling in solvent, C_M is a constant, χ is the polymer-solvent interaction parameter, M_n is the number average molecular weight of the polymer, l is the mean backbone bond length, C_∞ is the characteristic ratio, and N is the number average number of repeat units in the polymer chain. [83]

The extension of individual polymer chains by HRFS is quite often marked by a continuous, nonlinear peak in the force-versus-distance graph, the force magnitude of which increases with increasing distance of the tethering probe tip from the grafting surface (Figure 1.7, solid line). This behavior is observed for many randomly oriented polymers in a good solvent, and is predicted well by the extensible freely-jointed chain model: [84]

$$D(F) = L_T \coth\left(\frac{Fa}{k_B T} - \frac{k_B T}{Fa}\right)$$ **Equation 1.2**

where $L_T = L_{contour} + nF/k_s$ is the total contour length of the bridging chain which takes into account extensibility of the statistical segments, k_s is the statistical segment elasticity, n is the number of statistical segments, a is the statistical segment length, T is the absolute temperature, and k_B is Boltzmann's constant. This model reflects the entropic elasticity of the polymer as it is being stretched from a randomly oriented state displaying a Gaussian distribution of conformations, to a fully extended conformation in which the bond angles are predominantly in an all-trans configuration and the polymer possesses very little configurational entropy. PEO has been observed[43] to follow this behavior quite well in nonpolar solvents.

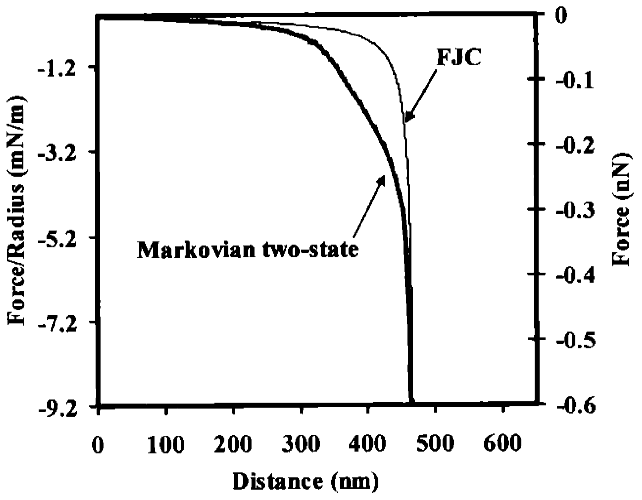

Figure 1.7 Thermodynamic models for extension of individual polymer chains in solution: the extensible freely jointed chain model (thin line), and the Markovian two-state model (thick line).

As mentioned previously, however, in aqueous solution PEO has been predicted[38] to take on a more ordered conformation fortified by intramolecular hydrogen bonding with water molecules (Figure 1.2). Disruption of this structure on extension during a force spectroscopy experiment leads to a fully reversible, strain-induced conformational transition from the water-bound, contracted, trans-trans-gauche (ttg) state to the more extended trans-trans-trans (ttt) state, and involves an additional enthalpic penalty for dehydration of the polymer and breakage of the intramolecular hydrogen bonds. The enthalpic barrier, coupled with the loss in entropy as the polymer is confined to fewer and fewer possible conformations, results in the appearance of an intermediate linear regime in the force-versus-distance curve, as shown in Figure 1.7 (thick line). Such extensional behavior has been observed[43] to closely follow a Markovian two-state thermodynamic model employing an extended Langevin function:

$$D(F) = n \cdot \left(\frac{l_u}{e^{-\Delta G/k_B T} + 1} + \frac{l_f}{e^{+\Delta G/k_B T} + 1} \right) \cdot \left[\coth\left(\frac{F \cdot a}{k_B \cdot T} \right) - \frac{k_B \cdot T}{F \cdot a} \right] + n \cdot \frac{F}{k_S} \qquad \textbf{Equation 1.3}$$

where l_f is the length of the contracted polymer subunit (for PEO ttg, $l_f = 0.278$ nm), l_u is the length of the extended polymer subunit (for PEO ttt, $l_u = 0.358$ nm), n is the number of extended segments (ttt), $\Delta G = 3 \pm 0.3\ k_B T$ is the Gibbs free energy difference between the ttg and ttt conformations, a is the statistical segment length ($a = 0.7$ nm for PEO), [43] and k_S is the segment elasticity ($k_S = 150$ N/m for PEO). [43]

1.2.5 HRFS of Proteins.

High resolution force spectroscopy has been employed in the study of protein binding and unfolding by a number of researchers. [85-89] Perhaps one of the most well-known examples is that of the unfolding of the giant muscle protein, Titin, [85,86,89] a multi-domain modular protein which unfolds one domain at a time, much like the stretching of springs in series. A typical force curve of such a protein is depicted in Figure 1.8; each of the peaks on “retract” is attributed to one of the protein domains being extended by the probe tip, and presumably the domain with the weakest intramolecular nonspecific binding is unraveled first, followed by the second weakest, etc.

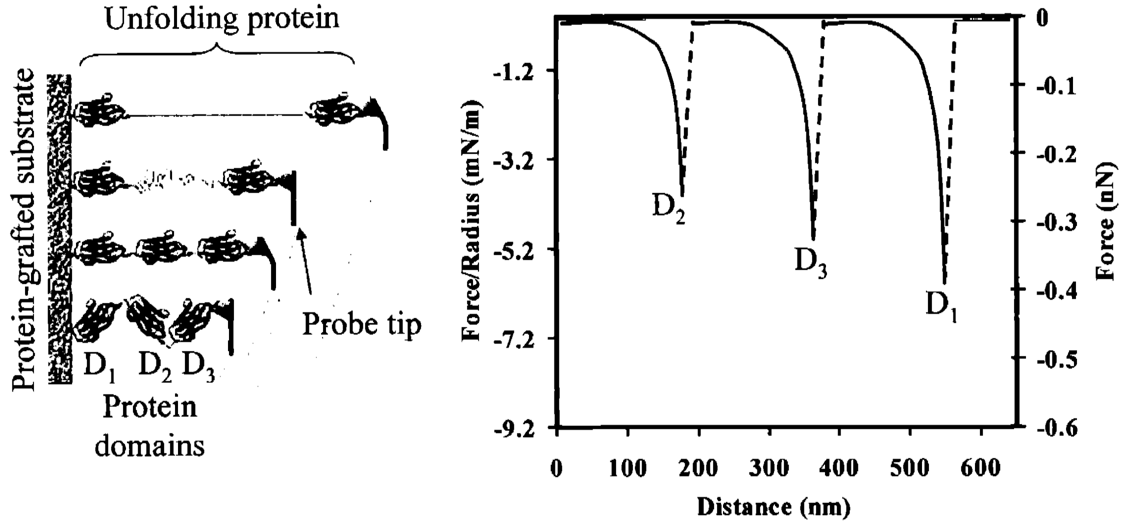

Figure 1.8 Depiction of the extension of an individual modular protein (in the native conformation) by HRFS. **Left**: the domains of a three-domained protein (adapted from reference [90]). **Right**: the force curves of unfolding of each of the domains.

The force curves of a native protein on extension follow the worm-like chain model: [80,81,90]

$$F(D) = \frac{k_B T}{p}\left[\frac{1}{4}\left(1 - \frac{D}{L_{contour}}\right)^{-2} - \frac{1}{4} + \frac{D}{L_{contour}}\right] \qquad \textbf{Equation 1.4}$$

Where k_B is Boltzmann's constant, T is absolute temperature, p is the persistence length of the protein, D is the distance between the probe tip and the surface, and $L_{contour}$ is the total contour length of the protein. At very high stretches, the second and third terms become negligible. It is common that only part of the protein will be unraveled during a given extension, and this is a direct result of the randomness of where the probe tip binds to the protein, and the numbers and strengths of nonspecific bonds tethering the protein to the probe tip. If the protein does fully extend on retract, then the distances of maximum adhesion for each of the retraction peaks should correspond to the individual contour lengths of each of the three domains. If the protein has been denatured, its force versus distance curves will take on a shape resembling that depicted in Figure 1.9, and the peaks will behave similar to the freely jointed chain model (FJC, Equation 1.2). Although HSA is not a modular protein, it does consist of three homologous domains, as was illustrated in Figure 1.5.

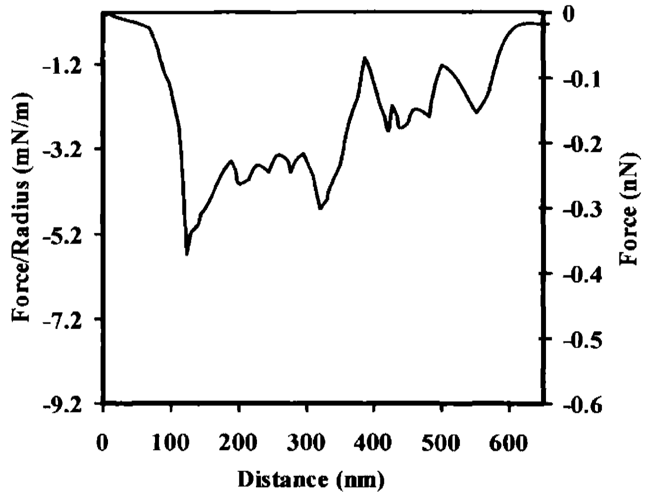

Figure 1.9 Depiction of an HRFS extension curve pulling a denatured protein.

1.3 Summary of the Experimental Approach

The main objective of this project was to develop a fundamental understanding of the molecular origins of hemocompatibility, by targeting the constituent intermolecular interactions between human serum albumin (the most abundant blood protein in the human body) and various chemically modified surfaces, including polygranular Au, a CH_3-terminated self-assembled monolayer (SAM), a COO^--terminated SAM, and an Au substrate sparsely bound with end-grafted PEO. Deconvolution of the total intermolecular interaction potential was carried out by a strategic series of experiments in which solvent conditions were manipulated to selectively probe (and thereby quantify) individual constituent forces. In seeking novel surfaces with enhanced hemocompatibility, we then drew inspiration from high carbohydrate content of the glycocalyx, which coats all living cells and is necessarily hemocompatible. We selected a series of oligosaccharide derivatives on which to perform HRFS, and compared our results with parallel experiments conducted on polymers and oligomers of ethylene oxide, which is perhaps the most protein-resistant material currently in use. Finally, the technique of using HRFS to probe fundamental molecular-level interactions was extended to a novel application, namely the study of the binding of a human immunodeficiency virus (HIV) therapeutic drug to oligosaccharides found on the viral envelope of HIV.

Chapter 2

SINGLE MOLECULE FORCE SPECTROSCOPY OF POLY(ETHYLENE OXIDE) WITH AN UNMODIFIED SI_3N_4 CANTILEVER

2.1 Introduction

Having selected the model polymer for study, we felt it important to first develop a thorough understanding of the intricate details of the nanomechanical behavior of PEO alone, before embarking on an investigation of the nanomechanics and intermolecular interactions of PEO with HSA. Many variables needed to be addressed, such as what substrate we would use as the grafting material, what chemistry we would use to attach the polymers to the substrate, and which polymer molecular weight range to focus on. It was of prime importance for us to choose a system that would allow us to study individual polymer molecules, so that our molecular mechanical analyses would not be complicated by intermolecular interactions or the extensional behavior of multiple, entangled polymers. It is quite easy to detect if the surface has multiple adsorbed layers or entangled polymers, as opposed to single chains: this first indication of multiple chain extension is the observation of force curves extending to distances greater than the theoretical $L_{contour}$ of the polymer chain; a second indication is the shape of the force curve - single PEO chains in an aqueous PBS solution exhibit force curves which follow the shape and magnitude predicted by the Markovian two-state model shown in Figure 1.6, whereas multiple chains tend to exhibit purely nonlinear extensions at forces intermediate between the FJC and Markovian models (Figure 1.6). We also sought a covalent attachment method which would ensure that the polymers would not detach from the surface during our HRFS experiments. Once these preliminary factors had been decided upon, we then verified the efficacy of our attachment protocol by ensuring reproducibility of previous experiments performed on PEO in both aqueous and organic environments. [43] Finally, in order to probe the dependence of the nanomechanical behavior on various experimental conditions, we studied our system using cantilevers of various spring constants, under a range of scan rates, under a broad range of ionic strengths, and in solutions of a variety of types of salts.

2.2 Optimization of Experimental Protocol

2.2.1 High Resolution Force Spectroscopy (HRFS) Measurements.

HRFS experiments were conducted using a new cantilever-based instrument, the Molecular Force Probe® (MFP) (Asylum Research, Santa Barbara, CA) to measure force, F (nN), versus tip-sample separation distance, D (nm) (henceforth referred to and labeled on graphs as "Distance") on approach and retract. A full description of this instrument, its limit of force and displacement detection in fluids, procedures for spring constant calibration and conversion of raw data, details of measurement errors, and description of typical force versus distance curves including the mechanical instabilities of the cantilever, are given in **Appendix A.1**. It should be noted that in all HRFS experiments, the spring constant of the cantilever, k_c is much less than the stiffness of the underlying (Au) substrate. Hence, little or no deformation of the substrate occurs, leading to the $D = 0$ vertical region of apparent infinite slope in the high-force, constant compliance regime and all forces measured are surface forces rather than contact mechanical forces due to substrate elastic and/or plastic deformation. Force (nN) versus Distance (nm) curves were measured at room temperature using a Thermomicroscopes™ microfabricated V-shaped Si_3N_4 cantilever ($k_c \sim 0.01$ N/m, length, $l = 320$ μm, resonance frequency, $\omega = 850$Hz) with unsharpened ($R_{TIP,\, unmodified} \sim$ 30-100 nm) square pyramidal probe tips at the end that had been modified with HSA as described in the following section. The HRFS experimental parameters for all experiments reported here included; z-piezo range = 1 μm, rate of data acquisition = 5000 points/s, constant z-piezo displacement rate = 1 μm/s (slow enough to minimize hydrodynamic effects), with the piezo reversing immediately between approach and retract cycles (no dwell time on the surface), and all experiments were conducted in phosphate buffer saline (PBS) solution (pH = 7.4, IS = 0.01M). PBS solutions were made using sodium phosphate buffer tablets (*Sigma* lot #59H03371) which contain 8 g/L NaCl, 0.2 g/L $K^+H_2PO_4^-$, 1.15 g/L $2Na^+ \cdot HPO_4^{2-}$, and 0.2 g/L KCl. PBS stock solutions (pH = 7.4) were diluted to obtain solutions with an ionic strength of 0.01M. Dilution did not have any effect on the efficacy of the buffer (i.e. the pH of the diluted buffer solutions remained stable). All water used for solutions, rinsing, and storage was first deionized (18 MΩ·cm resistivity, Purelab Plus UV/UF, US Filter, Lowell, MA), then filtered through Millipore® syringe filters (pore size = 0.22μm) prior to use. The force versus distance curves on approach from at least three different sites on the sample surface were averaged (minimum of 50 curves per site) and the standard deviations were calculated and reported. Upon retraction, the full force versus distance curves were not averaged because of the large adhesion force and distance distributions inherent in the nonspecific adhesion events, which would smooth out many characteristic features of the curve. Rather, statistical analysis of the maximum forces and distances of adhesion under each of the experimental conditions was performed. The normalized Force/Radius (mN/m) values are reported along with the unnormalized Force (nN) on a double y-axis for all experimental data for which the probe tip radius was determined. Tethering and extension of individual molecules was evidenced by extension profiles consistently occurring at distances less than or equal to the theoretical contour lengths of the polymers.

In the data that follows, $F_{adhesion}$ is the maximum attractive force observed on retraction for each distinct adhesion event (which may occur more than once for a single force curve if multiple molecules of varying lengths are tethered between the tip and the substrate), and $\langle F_{adhesion} \rangle$ represents the mean value of $F_{adhesion}$ for one dataset, i.e. corresponding to numerous force versus distance curves for one particular probe tip-sample combination (this notation is used consistently throughout the rest of this document). $\langle D_{adhesion} \rangle$ is the mean distance corresponding to $\langle F_{adhesion} \rangle$. $\langle F_{adhesion}/\text{Radius} \rangle$ is the mean adhesive force normalized by the probe tip radius giving an effective adhesive energy of interaction that can be employed universally for all HRFS data employing a hemispherical probe tip. For data conducted with different probe tips, only $\langle F_{adhesion}/\text{Radius} \rangle$ should be compared, not $F_{adhesion}$, and even then differences may arise due to local variations in probe tip geometry.

2.2.2 Choice of Cantilever.

A wide variety of cantilevers are available for HRFS – they may be rectangular or V-shaped, long or short, thick or thin, they may have pyramidal probe tips on the ends, colloidal particles, chemically attached molecules, or no tip or functionalization at all. In choosing the appropriate cantilever, one must consider first which system they intend to study, and what the desired experimental output is. A colloidal particle is useful when wants to study microscopic interactions, e.g., while a sharpened pyramidal probe tip may be more appropriate for nanoscopic applications. The compliance of the cantilever is also of great importance: if the cantilever is much stiffer than the underlying substrate and stronger than the molecular forces it is intended to study, it will indent the substrate in contact and will not be able to reflect the intermolecular interactions it is experiencing; if the cantilever is much, much softer than both the substrate and the molecular forces it is intended to study, it will bend excessively in response to interactions or compression on contact – again, it will not be capable of relaying molecular-level interactions. For these reasons, it is optimal to choose a cantilever that has the same compliance as the forces one is intending to study. Selecting such a cantilever is not always an easy task, and often requires trial and error. Due to the sensitivity of the forces that are the focus of our study, that is, hydrogen bonds and other nonspecific interactions, we chose to begin our studies with the softest cantilever commercially available at the time, the Thermomicroscopes™ standard Si_3N_4 V-shaped cantilever of length ~320 μm, and spring constant $k_c \sim 0.01$ N/m. For all of the data presented in this chapter, the unsharpened model (product #MLCT-AUHM, with a probe tip radius of curvature $R_{TIP} > 20$ nm) was employed; in all subsequent chapters, we found that sharpened model (product #MLST-AUNM, $R_{TIP} < 20$ nm) were more successful when chemically modifying the tip. A study investigating the effect on experimental data by using tips with higher spring contacts was conducted, and is reported later in this chapter.

2.2.3 Choosing the Appropriate Substrate

Many researchers, most notably Gaub, Rief, Li, and Fernandez, have pioneered the technique of single molecule force spectroscopy (SMFS). Their studies on PEO, [43] polysaccharides, [91-93] proteins, [89,94-96] and DNA[97] verified that AFM could be used to successfully study the mechanical behavior of individual synthetic or biological molecules. Various methods have been used among them to attach the molecules to a substrate for study, with gold, mica, and glass being the most popular substrate choices due to their hydrophobicity (enabling adhesion via hydrophobic interactions), relatively negligible interactions with the probe tips, and, in the case of gold and mica, their abilities to form atomically flat surfaces. After a thorough review of the literature, we chose to conduct our experiments on gold, as we felt it offered a wider variety of chemical attachment possibilities than mica. Also, mica substrates are more commonly used in the study of proteins rather than synthetic polymers, which are the focus of our investigations. Although atomically flat gold is commercially available, our access to vapor deposition facilities at MIT provided an easier, and far less expensive, source for materials. The gold used in all of the studies reported in this document was deposited on either silicon wafers or glass slides. The gold is in a rough, polygranular form, with "mounds" on the surface approximately 5nm in height and 50-100nm in diameter, as determined by atomic force microscopy in air. Prior to modification with PEO, all substrates were cleaned using piranha solution (3:1 12M H_2SO_4 : 30% H_2O_2) for ten minutes just before further chemical modification and testing by MFP experiments. [**WARNING!** Piranha solution is extremely oxidizing, reacts violently with organics, and should only be stored in loosely tightened containers to avoid buildup of pressure.]

2.2.4 Attachment of Poly(ethylene oxide) to Polygranular Gold: Chemisorption versus Physisorption, and the Issue of Molecular Weight

A variety of methods have been used to attach molecules to gold substrates for SMFS experimentation. Some researchers allow the molecules to physisorb (i.e. to stick onto the substrate via nonspecific interactions only, such as hydrophobic forces, e.g.) onto the gold substrates from solution, [87,96,97] while other have chosen to allow a solution of the molecule of interest to dry onto the gold substrate, after which it is rinsed off, leaving behind a film on the surface. [98,99] Still others chose to chemically modify the gold with an epoxy- or amine-terminated alkanethiol, which readily chemisorbs (i.e. covalently binds) to the gold via the terminal sulfhydryl group, before attaching the specific molecules of interest to the epoxy groups or amine termini. [100,101] Perhaps one of the simplest and most popular, and most chemically robust, methods of attachment of molecules to gold involves the functionalization of the molecules of interest with thiol groups, which then enable direct chemisorption of the molecules to gold. [89,100,102,103]

We attempted each of the four methods described above, with a broad range of PEO molecular weights. To briefly summarize our experimental results:

- **Drying of the polymer solution onto the substrate, followed by rinsing.**

  Experimental Protocol. Methoxy-PEG-thiol (Shearwater Polymers, Inc., lot #PT-089-12, mw ~ 5,000 g/mol) and methoxy-PEG-succinimidyl propionate (Shearwater Polymers, Inc, lot #PT-119-10, mw ~ 20,000 g/mol) were prepared as 1mM solutions in DI H_2O, and placed dropwise onto 1 cm^2 polygranular gold substrates. The substrate was then placed in an oven and heated at 55°C until the surface had dried. The samples were then rinsed thoroughly with DI H_2O and tested by HRFS immediately. When not under the microscope, the samples were stored in sealed glass vials of DI H_2O.

Results. The attachment of polymers to the surface was immediately apparent by the increased wettability of the substrates. HRFS experiments in DI H_2O, however, revealed the presence of a dense, aggregated layer of polymer chains on the surface. SMFS was not possible under these conditions.

- **Physisorption from solution.**

Experimental Protocol. Polymer solutions (~1 μM) of molecular weights ~ 29,000 and 50,000 (Polymer Source, Inc., product #P1440-EG2OH and #P1621-EG2OH, respectively), as well as ~ 100,000, 200,000, and 300,000 (Acros Chemical, product #17858-0050, 17859-0050, and 17860-0050, respectively), all of which were not end-functionalized with a chemically reactive group, were placed in a vial with a 1 cm^2 gold substrate that had been previously reacted for 12 hours in a solution of 2mM 2-amino ethanethiol (Aldrich, product #12,292-0) to form an amine-terminated self-assembled monolayer (SAM). The polymers were allowed to physisorb to the SAMs for various amounts of times to determine the optimal reaction time to enable SMFS. After incubation in solution, each substrate was rinsed thoroughly with DI H_2O before being tested by HRFS in DI H_2O. This procedure was also repeated on freshly cleaved mica.

Results. For polymers of mw $< 100{,}000$, approximately 12 hours in solution appeared to yield the best results (SMFS was possible), while for polymers of mw $\geq 100{,}000$, incubation times of $>$ 1hour yielded highly aggregated surfaces. Results, however, were not always consistent from sample to sample. No physisorbed polymers were detected on the mica substrate by HRFS.

- **Chemisorption to an amine-terminated self-assembled monolayer**

Experimental Protocol. A 0.2μM solution of methoxy-PEG-succinimidyl propionate (Shearwater Polymers, Inc, product #PT-119-10, mw ~ 20,000 g/mol) in DI H_2O was reacted with a 2-amino ethanethiol SAM (prepared as described above), to form a covalent amide bond between the polymer and the SAM. Incubation times of 1, 6, 8, 10, 12, 18, and 24 hours were attempted. The concentration of the solution was set to present a ten-fold molar excess of PEG to SAM molecules. Vigorous rinsing with DI H_2O was done for each substrate after incubation, before HRFS testing.

Results. A 12-hour incubation time gave the most consistent results, and enabled SMFS. Incubation times of less than 12 hours were insufficient to enable consistent single molecule extension, and longer times resulted in densely aggregated surfaces.

- **Chemisorption to directly gold via thiolate bonding**

Experimental Protocol. Two types of procedures were tried: attachment of thiol-terminated polymers alone to gold, and attachment of thiol-terminated polymers and hydroxyl-terminated alkanethiols to gold simultaneously to aid in the separation of the polymers from one another. In the case of the mixed solutions, a ~50 μM solution of methoxy-PEG_{2K}-thiol (Polymer Source, Inc., lot #P1608-EOSH, mw ~ 2,000 g/mol) and a ~ 20 μM solution of methoxy-PEG_{5K}-thiol (Shearwater Polymers, Inc., lot #PT-089-12, mw ~ 5,000 g/mol) were prepared in DI H_2O, and 11-mercapto undecanol (Aldrich #45,056-1) was added to each solution in a 5.7:1 PEG:undecanol ratio. The solutions were then added to gold substrates and allowed to incubate for 1 hour before being rinsed thoroughly and tested via HRFS. For the homogenous solutions, a 2μM solution of methoxy-PEG$_{5K}$-thiol and a 10μM solution of PEO$_{50K}$-thiol (Polymer Source, Inc. #P2415-EOSH) were prepared and added in 2mL aliquots to gold substrates for 45 minutes before being removed, rinsed thoroughly with DI H_2O, and stored in DI H_2O before testing by HRFS.

Results. HRFS results showed no indication of improved experimental results by backfilling with undecanol as compared to the homogenous grafting procedures. Furthermore, the strain-induced conformational transition reported[43] for PEO was most often observed on the higher molecular weight PEO$_{50K}$ than on the PEG$_{5K}$, which tended to exhibit short-ranged, featureless, worm-like chain force curve profiles.

The above experiments culminated in a scientific decision to employ only direct-grafting of polymers via thiolate bonding, and to only use higher molecular weight polymers which exhibit the most reproducible and interesting force curve profiles. From this point forward, our investigations of polymer-protein interactions focused solely on the thiol-terminated PEO$_{50K}$, which was consistently prepared as described above.

2.2.5 Characterization of the PEO-grafted Surface

The Flory radius, or radius of gyration, in aqueous solution Linear PEO$_{50K}$-SH, M_n = 48,320 g/mol, M_w = 51,700 g/mol, PDI = 1.07 (as determined by GPC in tetrahydrofuran using monodisperse poly(ethylene glycol) standards) was calculated to be R_F = 8.7 nm from Flory statistical mechanics using Equation 1.1: [82]

$$R_F = \alpha l_{c-o}\sqrt{\frac{C_\infty N}{3}} \text{, where } \alpha^5 - \alpha^3 = 2C_M\left[0.5-\chi\right]\sqrt{M_n} \text{ ,}$$

l_{c-o} is the carbon-oxygen bond length (= 0.143 nm), $C_\infty \sim 4$ is the characteristic ratio, [37] C_M = 0.175 is a constant, [37] χ = 0.42. at ~25°C, [37] α = 1.59 is the Flory expansion parameter and measures the degree of swelling in solvent, and N = 1098 is the number average number of repeat units in the polymer chain. The extended contour length, $L_{contour}$, was calculated to be 393 nm from the polymer number average molecular weight using the all-*trans* segment length of 0.358 nm, assuming a C-O bond length of 0.143 nm, a C-C bond length of 0.158 nm, and bond angles of 109.5°. The polymer concentration of the 10 μM stock solution was well below the critical overlap concentration, c* = 0.6 mM, or 0.0291 g/mL, calculated from the equation:

$$c^* = \frac{3M_n}{4N_A \pi R_F^3}$$ **Equation 2.1**

where N_A is Avogadro's number. Contact mode fluid atomic force microscope images of bare Au substrates (Figure 2.1 (A)) compared to PEO grafted surfaces (Figure 2.1 (B)) have allowed the identification of isolated single PEO chains and verified that the distance between grafting sites, $s = 62 \pm 26$ nm, is much greater than twice the Flory radius. Under these conditions the polymers are in the "mushroom" state. [83] The dimensions of the individual polymer chain mushrooms were found to be; $L_\perp$ (length perpendicular to the scan direction) = 7.9 ± 2.2 nm, $L_{\|}$ (length parallel to the scan direction) = 18.5 ± 3.8 nm), and height, $h < 5$ nm. As the polymer chains are unavoidably compressed and dragged by the probe tip in contact mode even under low force imaging, there was a consistent elongation in the scan direction, as well as a reduced height (i.e. $h < R_F$).

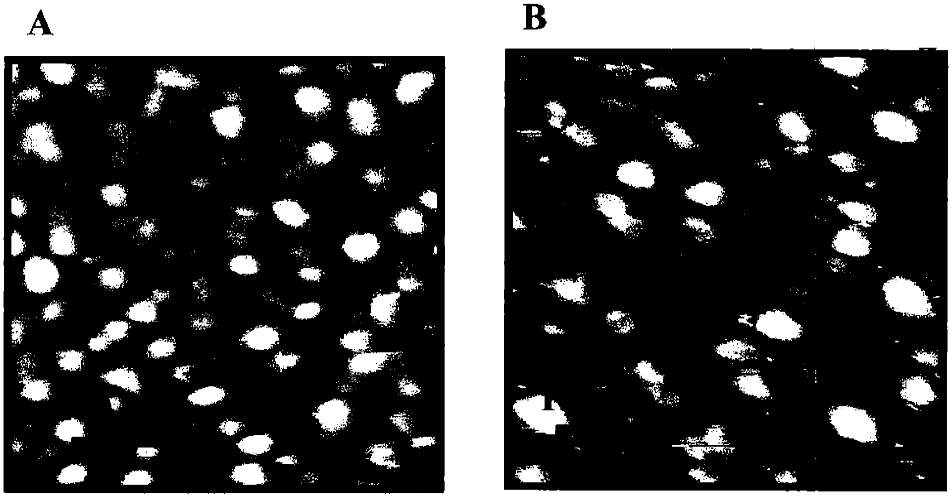

Figure 2.1 Contact mode AFM images in PBS solution of (**A**) a bare polygranular gold substrate, and (**B**) a polygranular gold substrate modified by covalent attachment of PEO_{50K}.

2.2.6 Data Treatment, Analysis, and Presentation

The intermolecular forces exerted on a polymer by a Si_3N_4 probe tip vary in type and magnitude as a function of the distance of the probe tip from the polymer-grafted surface, and in cases in which the probe tip is already *in contact* with the surface, such forces may also vary as a function of the time that the probe tip *remains* in contact if energy dissipating mechanisms are active, as well as the number of polymers present in the interaction area, which is function of the tip radius. In terms of HRFS experiments, this means that the approach and retraction curves may not necessarily correlate, and results from experiment to experiment may vary slightly in range and magnitude if the radii are not similar. For these reasons, we examine the approach and retract portions of our data separately, and then consider the total accumulation of our observations in formulating our final conclusions. For the data on retract, the points of maximum adhesion from at least twenty force curves on each of three different sample sites on each substrate, under each experimental condition, were tabulated and analyzed in a systematic statistical manner. First, each of the data sets was subjected individually to a "Q test" using a 95% confidence level[104] in order to remove statistical "outliers" from the data pool: [66]

$$Q = \frac{\text{gap}}{\text{range}}$$

where the "range" is the total spread of the data, and the "gap" is the difference between the data point in question and the next nearest value. For a certain confidence levels, e.g. for 95% as used in our experiments, Rorabacher, et al. [104] have tabulated corresponding Q values, and the convention holds that if the calculated Q is greater than the tabulated Q, the data point may be rejected from the data set with 95% percent confidence. The tabulated values of Q for a 95% confidence interval were found to fit the following double exponential function quite well, which enabled extrapolation of Rorabacher's table to larger N values:

$$Q = x_1 + x_2 \exp[-x_3 \cdot N] + x_4 \exp[-x_5 \cdot N], \text{ where } \begin{cases} x_1 = 0.257012 \\ x_2 = 0.369178 \\ x_3 = 0.073258 \\ x_4 = 1.30302 \\ x_5 = 0.377264 \end{cases}$$

and N is the number of observations, or the number of data points in the data set containing i points, assuming that the data set has been arranged in order from least to greatest values, and the fifth smallest value represents $i = 5$. To perform a valid Q test, N must be greater than five. [66]

Next, each of the data sets was compared to each of the others within a given set of experiments with the same probe tip using the "*Student's t*", in order to determine if the data sets were statistically different from one another: [66]

$$t = \frac{\langle x_1 \rangle - \langle x_2 \rangle}{s_{pooled}} \sqrt{\frac{n_1 n_2}{n_1 + n_2}}, \text{ where } s_{pooled} = \sqrt{\frac{s_1^2(n_1 - 1) + s_2^2(n_2 - 1)}{n_1 + n_2 - 2}}$$

and $\langle x_i \rangle$ is the average of all of the values in data set i, n_i is the number of data points in data set i, and s_{pooled} is the standard deviation for both of the data sets combined. Again, a 95% confidence level (also often referred to as $p = 0.05$) was set as our minimum criterion for "statistically different". Like the Q test, when $t_{\text{calculated}} > t_{\text{tabulated}}$, the two data points are considered to be statistically different. Student's t values at different confidence intervals are given in Table 5.1. [66]When comparing two data sets, the number of "degrees of freedom" = $n_{\text{total}} - 1$, where n_{total} = the total number of data points in both of the data sets being compared, combined. All "trends" claimed in this chapter and subsequent chapters in this document are > 95% statistically significant according to the tests described above.

Degrees of freedom	**90%**	**95%**	**98%**	**99%**	**99.9%**
1	6.314	12.706	31.821	63.657	636.619
2	2.920	4.303	6.965	9.925	31.598
3	2.353	3.182	4.541	5.841	12.924
4	2.132	2.776	3.747	4.604	8.610
5	2.015	2.571	3.365	4.032	6.869
6	1.943	2.447	3.143	3.707	5.959
7	1.895	2.365	2.998	3.500	5.408
8	1.860	2.306	2.896	3.355	5.041
9	1.833	2.262	2.821	3.250	4.781
10	1.812	2.228	2.764	3.169	4.587
15	1.753	2.131	2.602	2.947	4.073
20	1.725	2.086	2.528	2.845	3.850
25	1.708	2.068	2.485	2.787	3.725
30	1.697	2.042	2.457	2.750	3.646
40	1.684	2.021	2.423	2.704	3.551
60	1.671	2.000	2.390	2.660	3.460
120	1.658	1.980	2.358	2.617	3.373
∞	1.645	1.960	2.326	2.576	3.291

Table 2.1 Values of the "Student's *t*" (adapted from reference [66]).

Finally, the standard deviations for the adhesion frequency data were calculated by comparing average frequencies at different sample sites for each of the experimental conditions.

2.3 Investigating the Dependence of the Single Molecule Force Curve Behavior of Poly(ethylene oxide) on Experimental Conditions.

Having optimized the experimental protocol for SMFS of PEO, we then began to probe the question of how the various experimental parameters in our HRFS protocols affected the experimental results. In order to eliminate the variable of pH, we began immediately to perform our experiments in phosphate buffer saline solution (PBS) (IS = 0.15, pH = 7.4 i.e. physiological conditions). The variables we then individually manipulated included the cantilever spring constant, the scan rate, and the ionic strength of the PBS solution. We also explored the effect of different salts in the solution, as well as the effects of organic solvents on the force curve behavior.

2.3.1 Dependence on Tip Compliance

Force spectroscopy experiments were conducted in PBS on the same substrate using probe tips of spring constants $k_c \sim 0.01$ N/m, 0.03 N/m, 0.06 N/m, and 0.1 N/m. Other fixed experimental parameters included: scan rate = 1.0 μm/s, and tip displacement distance = 1.0 μm. No difference was observed in the results on approach or retract among the various data sets, suggesting that deviation of tip compliance within a reasonable range surrounding our nominal $k_c = 0.01$ N/m does not markedly affect our experimental results. We suspect this would not be the case if the spring constant was increased more than one order of magnitude.

2.3.2 Dependence on Piezo Velocity

Force spectroscopy experiments were conducted in PBS on the same substrate, sequentially, using the same probe tip (spring constant $k_c \sim 0.01$ N/m) with a tip displacement distance of 1.0 μm, at piezo velocities (scan rates) of 0.5, 1.0, 2.0, 5.0, 10.0, and 20.0 N/m. Rates faster than 20.0 N/m are beyond the capabilities of the piezo. No difference was observed in the results on approach or retract among the various data sets, suggesting that deviation of scan rate within a reasonable range surrounding our nominal rate of 1.0 μm/s do not markedly affect our experimental results.

2.3.3 Dependence on Ionic Strength

Force spectroscopy experiments were conducted in PBS on the same substrate, on the same day, using the same probe tip (spring constant $k_c \sim 0.01$ N/m) with a tip displacement distance of 1.0 μm, over three orders of magnitude of ionic strength in the following sequential order: 0.0001M, 0.001M, and 0.01M. Upon changing the solution to each higher ionic strength, both tip and substrate were first rinsed with the new solution, then allowed at least twenty minutes to equilibrate in the new solution before experimentation was begun.

On approach, a long range repulsion was observed, beginning at $D \sim 40$nm, and reaching a maximum force at $D = 0$ of 0.6 nN. The curves at each ionic strength overlap until $D < R_F$, at which point the repulsion between the Si_3N_4 probe tip and the PEO substrate begins to increase with increasing ionic strength (Figure 2.2).

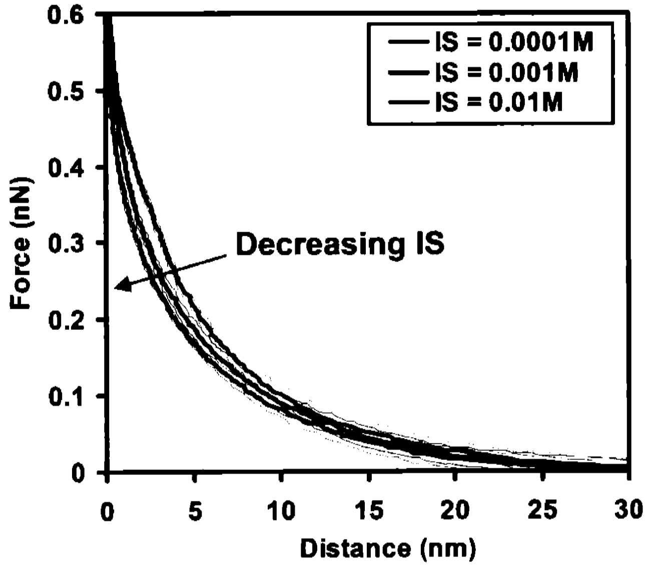

Figure 2.2 Averaged approach curves of a Si_3N_4 probe tip vs a PEO-grafted Au substrate, along with standard deviations, as a function of ionic strength.

These results, which were reproduced several times in various ionic strength ranges from 0.0001M to 3.0M, are somewhat surprising, as they are counter to two hypotheses we may have had about the data: 1) typically, in systems involving electrostatic repulsion, one would expect the repulsion to **decrease** on approach as the charges on the opposing surfaces become "shielded" by an increase in the concentration of counterions available to adsorb to each surface; 2) as was mentioned in Section 1.2.1, PEO is incapable of chelating Na^+ cations in solution, [46-49] and in fact the cation has a desolvating effect on the PEO as it competes for water molecule binding; under these conditions we would expect the repulsion from configurational entropy to decrease, as polymer segment-segment interactions become more favorable than segment-solvent interactions and the chain begins to collapse. Clearly the results at $D < R_F$ do not agree with either of these hypotheses, and by further comparison to parallel experiments on unmodified Au, which follows the expected trend for electrostatic repulsion in that as the ionic strength is increased, the repulsion on approach of Si_3N_4 to Au decreases, we may conclude first that this effect is due to the PEO, rather than the Au substrate, and second that neither steric (configurational entropy) nor electrostatic interactions are of great importance in the PEO system. Rather, another force that is greater in magnitude than either (or perhaps both combined if both are present) is dominating the response to ionic strength.

On retract, increases in ionic strength result in a reduction of the frequency of adhesion, as shown in Figure 2.3. It appears that NaCl concentration has a significant effect on HSA-PEO binding affinity, although the origin is not well understood. No significant effects were observed on any other adhesion statistical parameter ($<D_{adhesion}>$, $<F_{adhesion}>$).

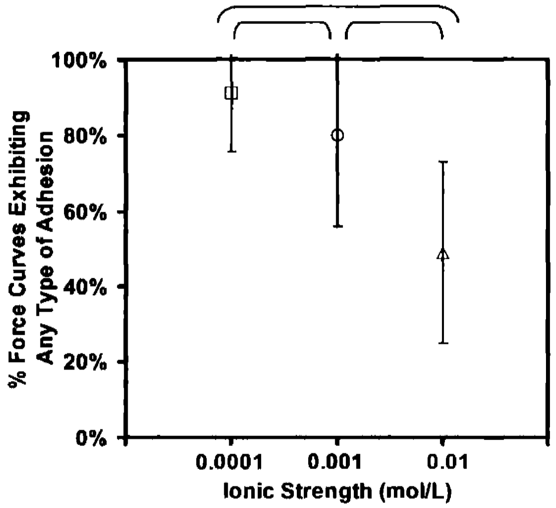

Figure 2.3 Frequencies of adhesion of a Si_3N_4 probe tip from a PEO-grafted substrate on retract, as a function of ionic strength. Statistically different data points (as determined by the "Student's t") are connected by brackets.

2.3.4 Dependence on Salt Type: HRFS in K_2SO_4

Like NaCl, K_2SO_4 has been found to be a poor solvent for PEO. [48] The mechanism of this phenomenon, often referred to as a "salting out" effect, may perhaps best be interpreted in the sense that the water molecules preferentially solvate the particular salts over PEO, thus leaving PEO deficient of solvent molecules. The relative affinity for polymer segment-

segment interactions consequently increases, and R_F decreases. Here we sought to compare our system to previous work reported by Irvine, et al, [48] which studied the effect of K_2SO_4 concentration on the dimensions of PEO star polymers.

Force spectroscopy experiments were conducted in PBS on the same substrate, on the same day, using the same probe tip (spring constant $k_c \sim 0.01$ N/m) with a tip displacement distance of 1.0 μm, over three orders of magnitude of ionic strength in the following sequential order of K_2SO_4 concentration in PBS (IS = 0.15M): 0.1M, 0.3M, and 0.4M. Upon changing the solution to each higher K_2SO_4 concentration, both tip and substrate were first rinsed with the new solution, then allowed at least twenty minutes to equilibrate in the new solution before experimentation was begun. As predicted, the results on approach, shown in Figure 2.4, show a clear decrease in the repulsion with increasing concentration of K_2SO_4. The data on retract, however, did not show any effect from the addition of K_2SO_4.

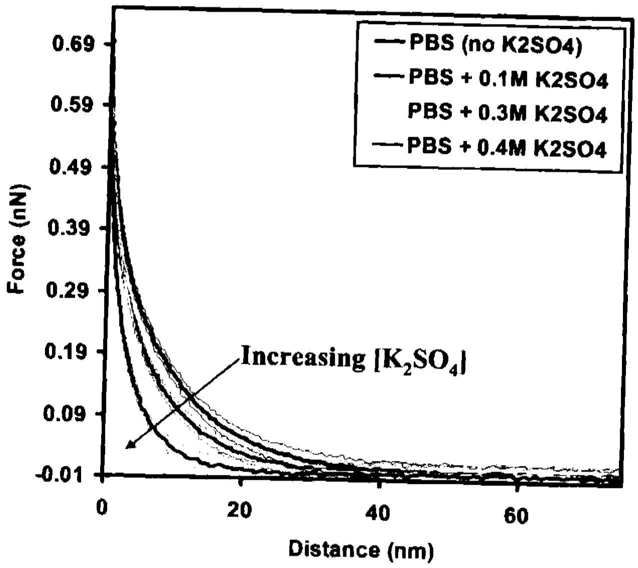

Figure 2.4 Averaged approach curves of a Si_3N_4 probe tip vs a PEO-grafted Au substrate, as a function of K_2SO_4 concentration in PBS (IS = 0.15M).

2.3.5 Dependence on Solvent Affinity: HRFS in Organic Solvents

Force spectroscopy experiments were conducted on PEO using a Si_3N_4 probe tip in hexadecane, a poor solvent for PEO. On approach, a long ranged attraction was observed, beginning at D < 750nm. On retract, a strong surface adhesion was observed, followed by PEO extension. The force did not completely return to zero until D ~ 600nm. The average adhesion values were: $\langle F_{adhesion} \rangle = 0.66 \pm 0.40$ nN, and $\langle D_{adhesion} \rangle = 209 \pm 91.8$ nm, which are at least twice that typically observed in PBS. An example force curve from the experimental data set is shown in Figure 2.5. From the shape of the extension curve on retract, it is clear that the Markovian shape typically observed in aqueous solution has been replaced by a curve which more closely resembles the freely jointed chain model, which is predicted for a polymer chain in a poor solvent.

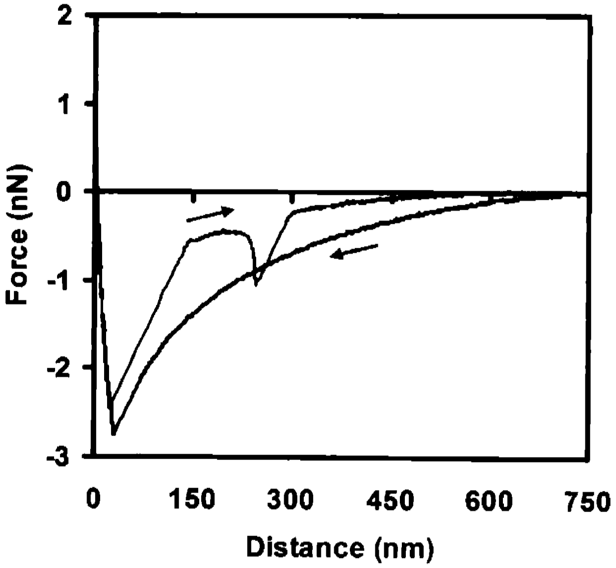

Figure 2.5 Example HRFS force curve between an Si_3N_4 probe tip and a PEO-grafted surface.

Such long-ranged attractive forces have been reported between two hydrophobic surfaces in water, and are often attributed to a "hydrophobic" or "solvophobic" force. These terms are usually interpreted in terms of an indirect interaction force between surface molecules through a solvent with strong intermolecular associations. [105] Attractive forces between silanized surfaces in a salt solution at distances up to 300nm have been reported, [106-108] and are increasingly thought to be due to the bridging of submicroscopic gas bubbles (or solvent "cavities") adsorbed to the respective surfaces. The phenomenon has been observed directly[106] using atomic force and optical microscopy, and is perhaps one of the best explanations to date for such odd, long-ranged attractive forces between surfaces in poor solvents.

This experiment was repeated on both a freshly cleaved mica surface and an unmodified polygranular gold substrate. On mica, the long-ranged attractive force was again observed, at distances spanning the limits of the piezo. On gold, the attractive force was reduced to a maximum range of 300nm, beyond which the force was negligible. Figure 2.6 shows an averaged approach curve of a Si_3N_4 probe tip to Au in hexadecane. It is interesting that this phenomenon is strongest between two hydrophilic surfaces (PEO and mica) in hexadecane, rather than on Au. It may be that the "solvophobic" force is not as pronounced on the relatively hydrophobic Au surface, or, if the "bubble theory" is valid, that the larger bubbles are more stable on the hydrophilic substrates than on Au. Certainly PEO has been observed to be quite stable at an air-water interface due to its amphiphilic nature and capabilities as an effective surfactant.

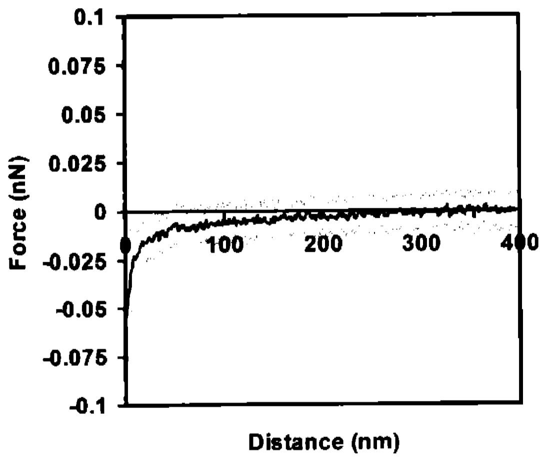

Figure 2.6 Average approach curve (with standard deviations) of a Si_3N_4 probe tip to an unmodified polygranular gold surface in hexadecane.

2.4 Conclusions.

In the experiments reported in this chapter between an unmodified Si_3N_4 probe tip and a PEO-grafted Au substrate, we successfully optimized our experimental protocol for attachment of single molecules of PEO to Au, and found that incubation of a piranha solution-cleaned Au substrate in 2mL of a 1mM solution of PEO_{50K} for 45 minutes, followed by thorough rinsing with DI H_2O, was sufficient to end-graft PEO chains such that the distance between grafting sites, s, is $> 2R_F$ (so the polymers are in the isolated, "mushroom" conformation on the surface), and yet close enough together that HRFS may be done with ease. To test the efficacy of our system, we successfully repeated previously reported results by Oesterhelt, et al, [43]demonstrating the strain-induced conformational transition when a water-solvated PEO molecule is extended in an HRFS experiment, and the freely jointed chain force curve extension profile of PEO in the poor solvent hexadecane. On exploring the sensitivity of our system to ionic strength, we observed an unusual increase in the repulsion on approach, and a decrease in the frequencies and forces of adhesion on retract, as the concentration of NaCl was increased in a standard PBS solution. The origin of this effect is not yet fully understood, but does discourage the hypothesis that the long-range repulsion between Si_3N_4 and PEO is due to electrostatic parameters. Steric effects, on the other hand, were observed to play an important role in the repulsion on approach to PEO; we were able to demonstrate this by investigating the "salting out" effect of PEO in the presence of K_2SO_4, from which we observed a marked reduction in the repulsive force on approach as the concentration of K_2SO_4 in PBS was increased. Finally, we were able to demonstrate that the piezo velocity (scan rate) and tip compliance have negligible effects on both the shape of force curves and the forces and distances of repulsive forces on approach and adhesive forces on retract. Although scan rate can play an important role in larger scale systems in which hydrodynamic effects are nontrivial, our nanosized cantilever probe tips would require a scan rate many times greater than the upper limits achievable by the MFP, in order to exhibit significant sensitivity to the scan rate. Overall, the important achievements reported in this chapter were an optimization of experimental protocol, and the development of a sound understanding of the HRFS behavior of PEO_{50K}, under a variety of experimental conditions.

Chapter 3

NANOSCALE INTERMOLECULAR INTERACTIONS BETWEEN HUMAN SERUM ALBUMIN AND ALKANETHIOL SELF-ASSEMBLED MONOLAYERS

3.1 Introduction

The interaction between the surface of an implanted artificial medical device and blood typically results in the nonspecific, noncovalent surface adsorption of blood plasma proteins followed by platelet adhesion and activation, initiation of the coagulation cascade, and thrombus formation. [12,13] In the absence of transport limitations, the interaction potential between the protein and the surface as a function of separation distance, U(D), will determine whether or not a protein will adsorb and at what rate. U(D) is typically a superposition of numerous nonspecific repulsive (e.g. electrostatic counterion double layer, steric, hydration, etc.) and attractive (e.g. van der Waals, hydrophobic, H-bonding, ionic, etc.) components that can lead to complicated functional forms that vary with the strength and range of the constituent interactions. [11,109] Generally, improved protein resistance can be achieved by maximizing repulsive interactions and minimizing attractive ones.

A variety of standards[20-23] also exist for *in vitro* hemocompatibility testing using biochemical and immunological assays to test for thrombosis, coagulation, platelet count, etc. which are quicker and less costly than *in vivo* clinical trials. Although widely investigated and discussed in the literature, hemocompatibility, which varies greatly from material to material, is still poorly understood. Hence, attempts to prepare thromboresistant blood-contacting devices such as hemodialysis membranes, intra-arterial chemical sensors and catheters, vascular grafts, and blood pressure monitors, have met with limited success.

To attack this problem, we chose to focus on that first step in the thrombosis an inflammatory cascades, i.e. the adhesion of blood proteins to the biomaterial surface. Employing the powerful method of high resolution force spectroscopy (HRFS) to directly measure the net nanoscale intermolecular force between a probe tip covalently bound with blood plasma proteins and a variety of model planar surfaces as a function of protein-surface separation distance, F(D), where $U(D)=-\int F(D)dD$. A more complete understanding of the molecular origins of the protein adsorption process can be achieved through deconvolution of the contributions of each of the individual constituent interactions. This goal can be realized through rigorous experimental and theoretical methodologies, by varying the environmental (solution) conditions and sample characteristics in conjunction with various theoretical model predictions using independently measured parameters. Although HRFS experiments yield an approximation of the actual potential experienced during the initial *in vivo* adsorption process (e.g. since the proteins are constrained in mobility on the probe tip, brought near the surface at a near-constant rate, and isolated from other blood components), experiments on synthetic polyelectrolytes have successfully correlated molecular level forces with adsorbed layer thicknesses measured via ellipsometry. [110] Given this fact, HRFS has great potential to be a useful tool for predicting adsorption kinetics, [111-114] evaluating and prescreening candidate biomaterials for which only extremely small quantities of material are available, and assisting in the chemical design of new hemocompatible biomaterials.

Before moving on to study polymeric surfaces, we chose to study the interaction of our model protein on monolayers of a variety of chemical functionalities, in order to better understand the HRFS behavior of human serum albumin (HSA). In the research presented in this chapter, HSA, the most abundant human blood plasma protein and that which is typically the first to adsorb to a blood-contacting biomaterial, [24] was covalently grafted to a nanosized silicon nitride (Si_3N_4) probe tip at the end of a soft, microfabricated cantilever force transducer. F(D) was recorded between the HSA-modified probe tip and three different surfaces including: 1) gold; 2) a hydrophobic, CH_3-terminated alkanethiol self-assembling monolayer (SAM); and 3) a hydrophilic, COO^--terminated alkanethiol SAM; both on "approach" (i.e. as the probe tip moves towards surface) and "retract" (i.e. as the probe tip moves away from surface), in aqueous sodium phosphate buffer solution (PBS, ionic strength IS = 0.01M, pH = 7.4). SAMs are widely regarded as excellent model surfaces to study protein interactions due their highly uniform, crystalline-like structure, ease of varying chemical head group functionality, ease of deposition, and robustness. [115] A new nanomechanical instrument, the Molecular Force Probe®, [116] which has a limit of force detection $\geq \pm 5$ pN and a limit of displacement detection $\geq \pm 3$ Å (using the cantilevers employed in this study), was used to carry out the HRFS measurements. The approach data was analyzed through a comparison with molecular level theoretical models for the individual constituent components of the total net force (e.g. van der Waals, [117] electrostatic counterion double layer[118]), and the retract data was analyzed statistically using adhesive contact mechanical theories. [119-121] This study was critical to the interpretation and understanding of a series of parallel experiments conducted on more complex surfaces containing chemically end-grafted polymer chains (Chapter 4), a situation more commonly found in clinical applications.

3.2 Experimental Procedures

3.2.1 Surface Preparation and Characterization

Silicon (100) wafers (Recticon Enterprises, Inc., Pottstown, PA; test grade) were cleaned with ethanol and immediately coated with 2 nm of chromium to promote adhesion, followed by 100 nm of Au deposited using a thermal evaporator at 1.5 Å/s at room temperature at a pressure of $2 \bullet 10^{-6}$ Torr. These polycrystalline Au surfaces have a typical root-mean-square (rms) surface roughness of 2 nm and an Au island size range of 25-76 nm, as measured by contact mode atomic force microscopy (AFM) in air (taken with a Digital Instruments™ Multimode®). The Au-coated Si wafers were cleaned using piranha solution (3:1 12M H_2SO_4 : 30% H_2O_2) for ten minutes just before further chemical modification and testing by MFP experiments. [**WARNING!** Piranha solution is extremely oxidizing, reacts violently with organics, and should only be stored in loosely tightened containers to avoid buildup of pressure.] Hydrophobic CH_3-terminated SAMs were prepared by incubating piranha-cleaned 1 cm^2 gold substrates in dodecanethiol, $CH_3(CH_2)_{11}SH$ (Aldrich #47,136-4), (5 mM solution in ethanol), for 48 hours, which was followed by rinsing with hexanes and subsequently PBS before experimentation. Hydrophilic COOH-terminated SAMs were prepared by incubating a piranha-cleaned 1 cm^2 gold wafers in 2 mM solution of 11-mercaptoundecanoic acid ($HS(CH_2)_{10}CO_2H$, Aldrich #45,056-1) in 100% ethanol for 48 hours, followed immediately by rinsing with deionized water and then PBS before experimentation. [110]Receding and advancing contact angle measurements were performed with in DI H_2O, the results of which are summarized in Table 3.1. Alkanethiol SAMs on Au(111) are known to have a $(\sqrt{3}X\sqrt{3})$ R30° structure relative to the underlying substrate, corresponding to a molecule-molecule spacing of ~5Å and an area per molecule of 21.6 $Å^2$ with an all-trans, planar zig-zag hydrocarbon chain tilted by ~34° from the surface normal, ~1.5 nm in height. [115]

SUBSTRATES→	CH_3 SAM	COO^- SAM	Au
$\theta_{W(Advancing)}$	111° ± 1°	44° ± 1°	97° ± 2°
$\theta_{W(Receding)}$	108° ± 2°	13° ± 1°	70° ± 6°
$\Delta\theta_W$	3°	31°	27°

Table 3.1 Contact angle measurements of DI H_2O on Au and alkanethiol SAMs.

3.2.2 Covalent Attachment of Human Serum Albumin on Si_3N_4 Cantilever Probe Tips

HSA was covalently attached to a Si_3N_4 cantilever probe tips using the chemical reaction scheme shown in Figure 3.1. [122,123] Aminobutyldimethylmethoxysilane (ABDMS, #S565350), glutaraldehyde (#G-8552, lot #31K5306), and HSA (#A9511, lot #126H9322, containing bound lipids) were purchased from Sigma. These Si_3N_4 probe tips were prepared by chemical vapor deposition using a 4:1 mixture of dichlorosilane and ammonia gases respectively, resulting in approximately a 4:1 ratio of SiOH:$SiNH_3$ surface groups. [124] Si_3N_4 probe tips were cleaned and oxidized in an oxygen plasma for 10s at 30Pa and 10 W power immediately prior to modification. They were then immersed in a 4% (v/v) toluene solution of ABDMS for 2 hrs. The silanized probes were rinsed in methanol followed by 0.01M PBS before being immersed in a 2.5% (v/v) aqueous solution of glutaraldehyde for 30 min and then rinsed with an excess of DI water. The cantilevers and probe tips were then immersed in a 0.01 % (w/v) HSA solution (in 0.01M PBS) for 1 minute. Finally, the HSA modified probe tips were rinsed copiously with PBS and stored in the same concentration buffer until tested. The ABDMS and glutaraldehyde molecules provide a short linker for the HSA off the probe tip which may allow for some flexibility and retention of the native movements of the protein. Multiple covalent linkages are possible and it should be noted that the orientation and conformation (e.g. elliptical or triangular) of the HSA on the probe tip is not known.

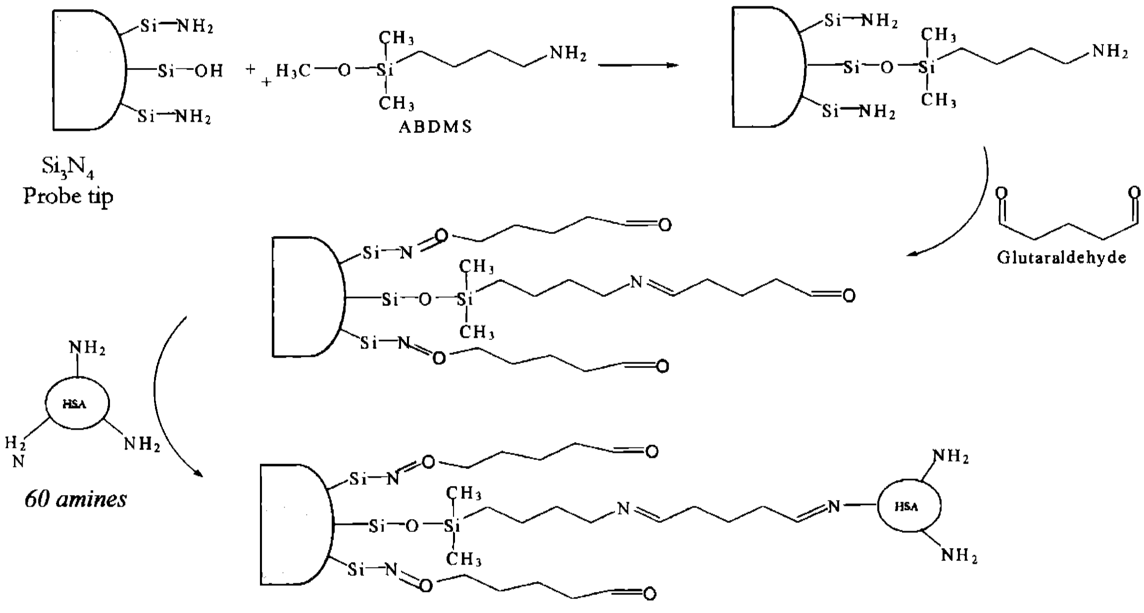

Figure 3.1 Reaction scheme for the covalent attachment of HSA to a Si_3N_4 probe tip. HSA may form multiple tethers to the probe tip via any of its 60 available amino groups.

The success and optimization of the HSA chemical grafting reaction to form a monolayer on the probe tip, and the ability of the HSA to maintain its native conformation, was a critically important component of this work and was verified by three different methodologies. Data obtained by all approaches was compared to control samples which involved the same chemical procedure as was used in the probe tip modification, in which the final reaction step in the chemical procedure was carried out in HSA-free buffer rather than 0.01% (w/v) HSA (henceforth referred to as "glutaraldehyde control").

i. Contact Angle Measurements and AFM Imaging. Characterization of HSA grafted to planar Si_3N_4 wafers (prepared by chemical vapor deposition at 780°C and 0.25 Torr of a 10:1 mixture of dichlorosilane and ammonia gases respectively, thus resulting in approximately a 10:1 ratio of SiOH:$SiNH_3$ surface groups) was carried out by contact angle measurements and contact mode AFM imaging in PBS (Digital Instruments™ Multimode®). Planar Si_3N_4 wafers needed to be employed for these standard techniques since they are not able to obtain measurements on the small surface area of the probe tips. Advancing contact angles were 44 ± 1° for the HSA surface and 63 ± 6° for the glutaraldehyde control. AFM imaging of the HSA-grafted surface suggested complete coverage of the surface with the HSA and showed rounded features 10 nm in relative height that were not observed on the glutaraldehyde control, which showed jagged features approximately 5 nm in relative height (Figure 3.2). Imaging was conducted with a Digital Instruments™ Multimode 3a® atomic force microscope, using the fluid cell setup with PBS (IS = 0.01M, pH=7.4) in contact mode, employing a Thermomicroscopes™ Si_3N_4 v-shaped cantilever (length ~ 320μm, k ~ 0.01 N/m) with an unmodified probe tip of radius ~ 20-50nm.

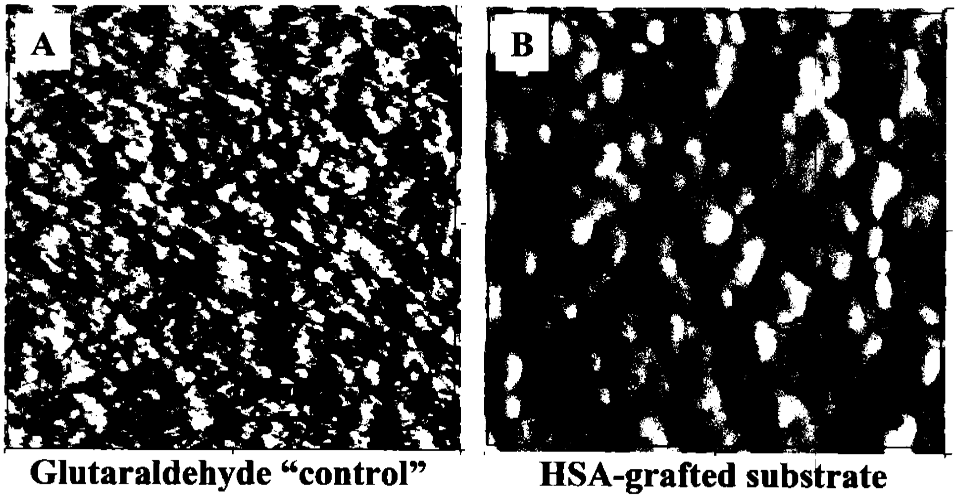

Figure 3.2 Contact-mode atomic force microscopy images taken in PBS (IS=0.01M, pH=7.4) of (**A**) a glutaraldehyde-functionalized flat Si_3N_4 substrate, and (**B**) an HSA-functionalized flat Si_3N_4 substrate.

ii. Flourescence Microscopy. Secondly, glutaraldehyde and HSA-functionalized cantilevers and probe tips were tagged with a flourescent compound by immersing for 48 hrs in a solution of 1.0 mL of 0.01 M PBS and 0.25 mL of a 6.67×10^{-4} M solution of Oregon Green Dye (Molecular Probes, Inc., product # O-6147) in dimethylsulfoxide (DMSO). In this procedure, an active ester on the fluorescent dye readily covalently reacts with free amine groups on the protein, but not with aldehyde groups on the glutaraldehyde “control."

The cantilevers were then rinsed thoroughly first with DMSO and then 0.01 M PBS, and finally stored in PBS until viewing with the fluorescence microscope (*Zeiss* Axiovert 200 fluorescence microscope equipped with a Xe lamp using a 40X objective lens). Excitation was set at a wavelength of 488 nm and emission was detected in the range 510-520 nm, and the two chips were imaged in the same sample well so that background fluorescence could be subtracted from the final images. Total exposure time was 10ms, and data collection was done by z-sampling every 1μm for a total depth of 60μm. The images were taken using a 40x oil-immersion objective collecting on a cool-snap HQ OCD camera. After the images were collected, the background fluorescence was subtracted and the relative brightness was scaled identically for both images, so that the two could be directly compared. Although some nonspecific adsorption of the Oregon Green inevitably occurred on both substrates due to poor solubility of the compound in water, fluorescence on the HSA-grafted cantilever (Figure 3.3(B)) was found to be 8.2X more intense than the glutaraldehyde control (Figure 3.3(A)). It should be noted that the probe tip, located at the end of the cantilever, is not visible under such low magnification.

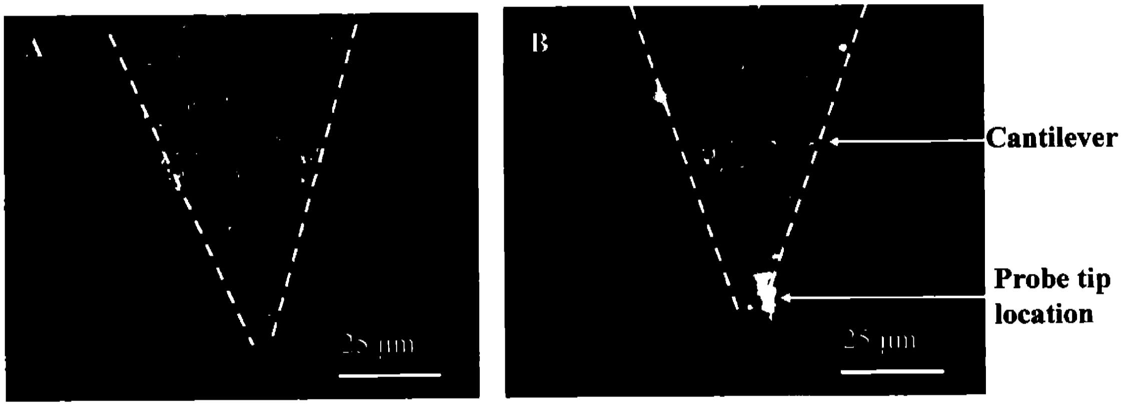

Figure 3.3 Flourescence microscope image of: (**A**) an Oregon green 488-exposed gluteraldehyde control cantilever and (**B**) an Oergon green 488-labeled HSA-modified cantilever.

iii. HRFS in PBS. Lastly, HRFS experiments in PBS were employed to optimize the grafting reaction conditions to produce a well-packed HSA monolayer (as opposed to adsorbed multilayers). The HSA-modified probe tip versus a hydrophobic control surface

(CH_3-terminated SAM) showed the presence of long range, nonlinear attractive forces due to the stretching (unfolding) of protein chains between the probe tip and adsorbed segments which tether the protein to the hydrophobic surface For the probe tip reaction conditions employed, the distance ranges of these long-range protein unfolding events were almost always less than the calculated contour length of an individual HSA molecule, suggesting a monolayer on the probe tip surface. For longer reaction times in step III (of Figure 3.1), the unfolding lengths were observed at distances up to many times greater than the contour length, suggesting multiple adsorbed layers. In addition, the glutaraldehdye control probe tip tested via HRFS showed distinctly different force spectroscopy behavior in magnitude, range, and shape compared to the HSA probe tip on a variety of surfaces tested. Figure 3.4 compares HRFS data between the two tips and a PEO-grafted surface on approach and retract.

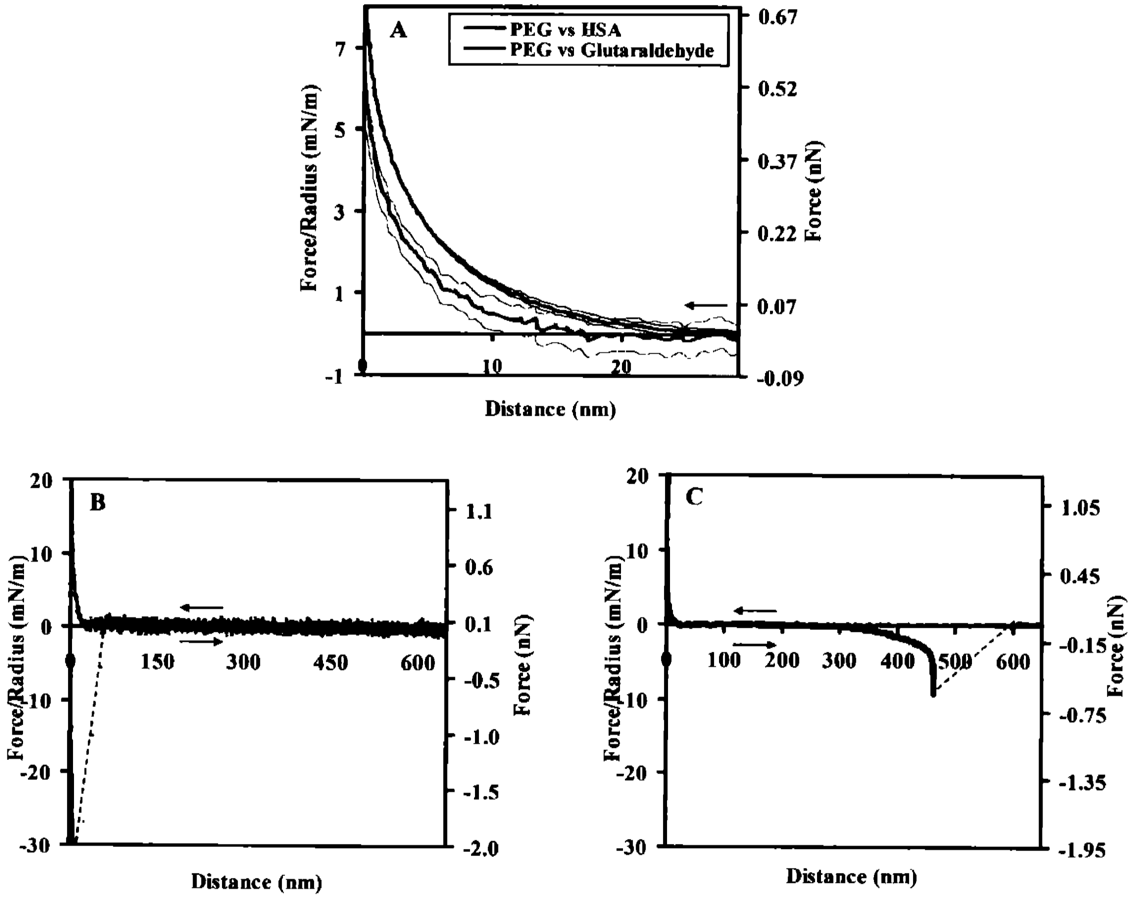

Figure 3.4 Comparison of HRFS data using both glutaraldehyde- and HSA-grafted probe tips on a PEO-grafted surface. Approach data is compared directly in (**A**), and retract data is compared side by side for (**B**) the glutaraldehyde-modified probe tip and (**C**) the HSA-grafted probe tip.

iv. HRFS in the Denaturant Urea. Urea is a well-known protein denaturant, and even small concentrations can have a marked effect on a protein's tertiary and quaternary structures. HRFS experiments were carried using an HSA-modified probe tip in both PBS (IS = 0.01M, pH = 7.4) and in 1M Urea (dissolved in the same PBS solution), on a COO^--terminated SAM. The HSA was allowed 24 hours to equilibrate in the urea solution after being tested in pure PBS, before further experimentation was performed. The force curves obtained under each condition were markedly different. While in pure PBS, HSA experienced no surface adhesion on retract, and its protein extension profiles exhibited a structured form resembling curves often seen for structured polymers such as PEO (Section 1.2.4), in the presence of 1M Urea, surface adhesion became prevalent and protein extension curves took on a shape indicative of a freely jointed chain, which has been found to model randomly oriented polymers quite well. Typical force curves from each experiment are shown below in Figure 3.5. These results support the hypothesis that HSA is in its native conformation under the experimental conditions employed throughout the majority of this project.

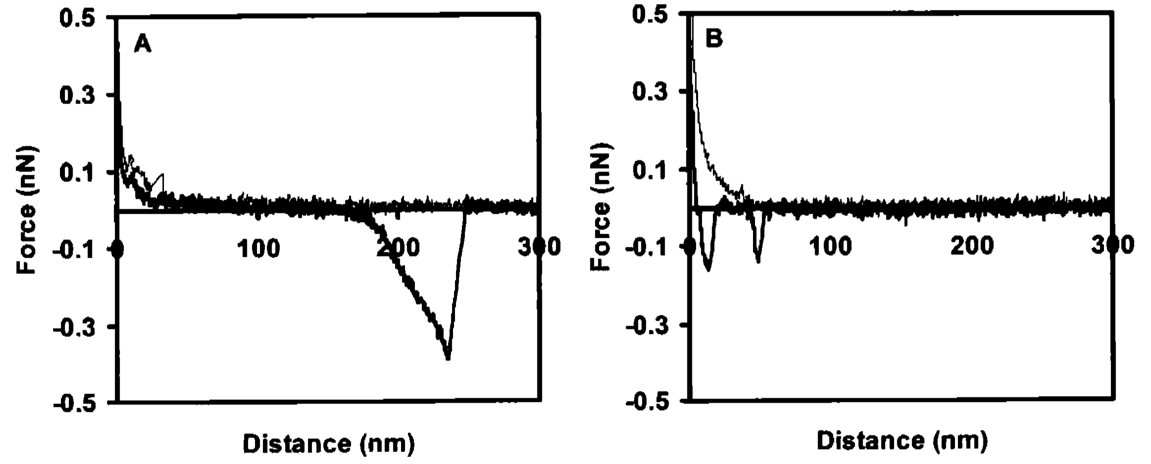

Figure 3.5 Typical force curves between an HSA-grafted probe tip and a COO^--terminated SAM in (**A**) PBS, and (**B**) 1M Urea in PBS.

3.2.3 Measurement of Probe Tip Radii

The radii of the chemically modified probe tips were determined for each individual cantilever by scanning electron microscopy (SEM) (JEOL 6320FV Field-Emission High-resolution SEM, operating voltage = 5 kV, working distance = 8mm, magnification = 100,000x) (Figure 3.6) where R_{TIP} was determined by drawing two intersecting straight lines tangential to the sides of the probe tip and then drawing a circle tangential to both of them. R_{TIP} for the COO^- terminated SAM probe tip was found to be ~ 63 nm. R_{TIP} for the HSA probe tip used on the COO^- terminated SAM surface was found to be ~ 150 nm. R_{TIP} for the HSA probe tip used on the CH_3 terminated SAM and Au surfaces was found to be ~ 65 nm.

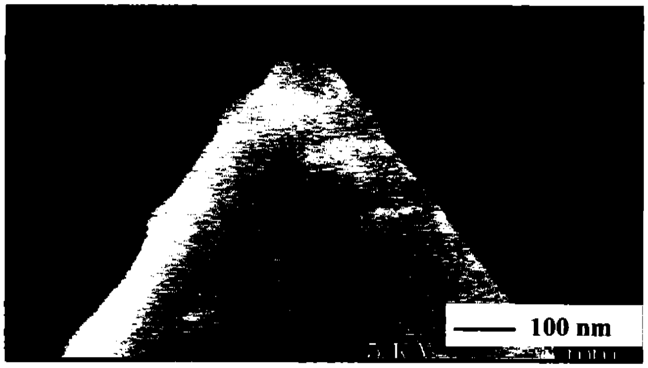

Figure 3.6 SEM image of an HSA-modified Si_3N_4 probe tip. Operating voltage = 5kV; working distance = 8mm.

3.2.4 Estimating the Interaction Area between a Probe Tip and a Planar Surface.

The experimental geometry and schematic of relevant parameters is given in Figure 3.7. As the probe tip begins to penetrate the interaction distance range (i.e. the distance at which forces just begin to be detected between the probe tip and the surface), the surface interaction area will increase from 0 to a maximum value at D = 0.

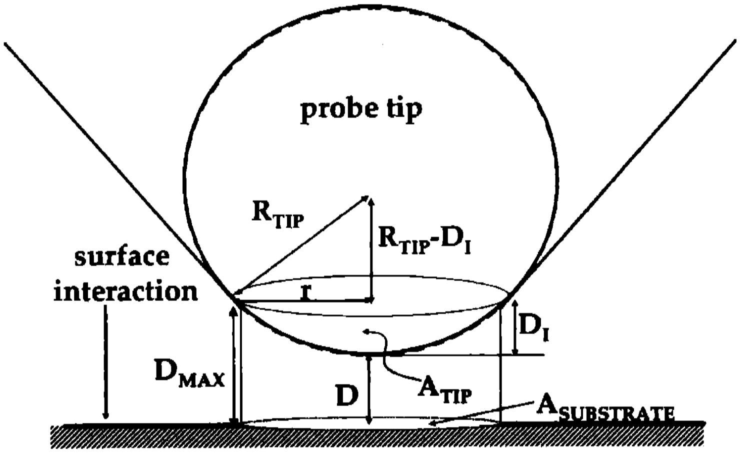

Figure 3.7 The geometry and relevant parameters for defining the surface interaction area between an HSA-grafted probe tip and an underlying surface.

The geometrical parameters are defined as follows: D is the separation distance between probe tip and planar surface, A_{TIP} is the effective interaction surface area on the probe tip at D, D_I is the distance the probe tip has moved into interaction range (i.e. $D_I = D_{MAX}-D$ where D_{MAX} is the maximum tip-sample separation distance range of interaction), and R_{TIP} is the probe tip radius. Using Pythagoreum's theorum, r can be calculated from R_{TIP} and D_I :

$$r=\sqrt{R_{TIP}{}^2-[R_{TIP}-D_I]^2} \qquad \textbf{Equation 3.1}$$

The interaction area on the tip is the surface area of a portion of a sphere which is defined as following:

$$A_{TIP} = \pi R_{TIP} D_I \qquad \textbf{Equation 3.2}$$

The interaction area on the substrate, $A_{SUBSTRATE}$, is the projection of the interacting piece of tip, A_{TIP}, onto a plane. Therefore, it is just the area of the cross-section of the sphere at D_I:

$$A_{SUBSTRATE} = \pi r^2 = \pi\left(R_{TIP}^2 - [R_{TIP} - D_I]^2\right) \qquad \textbf{Equation 3.3}$$

The relevant areas for the force profiles on approach are the surface interaction area of the probe tip and substrate. The maximum probe tip and substrate surface interaction areas at D=0, A_{TIP}, and $A_{SUBSTRATE}$, respectively, were approximated as shown in above for each probe tip-substrate combination from R_{TIP} and the maximum separation distance of interaction measured by HRFS on approach, D_{MAX}, and was found to range between ~3,000-16,000 nm^2. From these values, the maximum number of proteins, assuming a dense monolayer, in A_{TIP} (at D=0) was calculated assuming either a triangular or ellipsoidal shape (lying flat) and found to range ~60-600 proteins. For a maximum applied force of F_{MAX}=3nN at D=0, the maximum force per protein was calculated and found to be < 8.6 pN for CH_3-terminated SAM, < 19 pN for COO^- terminated SAM, and < 44 pN for Au, much less than the expected force needed for mechanical denaturation[95]. Hence, it is expected that steric deformations of the protein on approach within the surface interaction area have a negligible contribution to the interaction force profile. Since the area per SAM molecule on the substrate is 0.216 nm^2, the number of SAM molecules in $A_{SUBSTRATE}$ was 56,000 for the CH_3-terminated SAM and 60,000 for the COO^--terminated SAM. These values are summarized in Table 3.2.

SUBSTRATES→	**CH_3 SAM**	**COO^- SAM**	**Au**
D_{MAX} (nm)	80	15	15
R_{TIP} (nm)	65	150	65
HSA A_{TIP} (nm^2) at D=0	16,000	7,100	3,100
$A_{TRIANGLE}$ (HSA)(nm^2)	28	28	28
$A_{ELLIPSE}$ (HSA)(nm^2)	45	45	45
$A_{SUBSTRATE}$ (nm^2) at D=0	12,000	13,000	5,500
# Proteins in A_{TIP} (assuming a triangularly shaped protein)	580	260	110
# Proteins in A_{TIP} (assuming an elliptically shaped protein)	350	160	68
$A_{SAM\ molecule}$ (nm^2)	0.216	0.216	0.216
# SAM molecules in $A_{SUBSTRATE}$	56,000	60,000	-
F_{MAX} (nN)	3.0	3.0	3.0
F_{MAX} / Protein (pN) (assuming a triangularly shaped protein)	5.2	12	27
F_{MAX}/ Protein (pN) (assuming an elliptically shaped protein)	8.6	19	44
$A_{contact}$ (nm^2)	5.7	9.6	5.5
# of SAM molecules in $A_{contact}$	26	44	-

Table 3.2 Calculated values for the numbers of molecules and the applied forces in the surface and tip interaction areas.

3.2.5 Estimating the Probe Tip Contact Area

On retract and relevant to adhesion data, in addition to the surface interaction area there is a much smaller **elastic contact area** where the molecules on the probe tip apex and the molecules just under the probe tip apex on the substrate are in intimate contact. Within this small region, the forces are amplified, for example by 1.5 times the externally applied force, F, for Hertzian mechanics.

The contact area, $A_{contact}=\pi a^2$, was calculated from Hertzian elastic mechanics[125] for the substrates displaying no adhesive forces as follows :

$$a=\left(\frac{FR_{TIP}}{K}\right)^{1/3}, \qquad K=\frac{4}{3}\left(\frac{1-\nu_1^2}{E_1}+\frac{1-\nu_2^2}{E_2}\right)^{-1} \qquad \textbf{Equation 3.4}$$

where: a = contact area radius, K=reduced elastic modulus, ν = Poisson's ratio, E = Young's (elastic) modulus, E_1(Au)= 64 GPa, ν_1(Au)=0.44 , $E_2(Si_3N_4)$= 300 GPa, and $\nu_2(Si_3N_4)$=0.24, and was found to be 5.5 nm^2 for the Au surface, and 9.6 nm^2 for the COO$^-$ terminated SAM surface (corresponding to ~44 SAM molecules).

$A_{contact}$ was also calculated from (modified Hertzian) DMT theory[119] for the CH_3-terminated SAM displaying an adhesive jump-to-contact on approach as follows :

$$a=\left(\frac{(F+F_{adhesion})R_{TIP}}{K}\right)^{1/3} \qquad \textbf{Equation 3.5}$$

$A_{contact}$ was found to be 5.7 nm^2, (corresponding to ~26 SAM molecules). $A_{contact} \ll A_{SUBSTRATE}$, A_{TIP}, and $A_{protein}$, i.e. much less than a single protein could fit in the maximum elastic contact area. Both of these theories predict nonhysteretic behavior.

3.3 Results on Approach

3.3.1 Approach of an HSA-Grafted Probe Tip to a COO$^-$-terminated Self Assembled Monolayer.

Control Experiment: COO$^-$ Terminated SAM Probe Tip versus COO$^-$-Terminated SAM Surface. Figure 3.8 displays the average Force/Radius (mN/m) and Force (nN) versus Distance (nm) approach curve (with standard deviations) for a COO$^-$ terminated SAM probe tip versus a COO$^-$ terminated SAM surface in PBS, [110] compared to the Derjaguin-Landau-Verwey-Overbeek (DLVO) theory. [126,127] Under these solution conditions, the carboxylic acid group is ionized and negatively charged (pK$_a$(COO$^-$) = 5.5 ± 0.5). [128] Nonlinear, purely repulsive forces were observed for D < 15 nm reaching a maximum magnitude at D = 0 of Force = 0.6 nN corresponding to a Force/Radius ~ 10 mN/m.

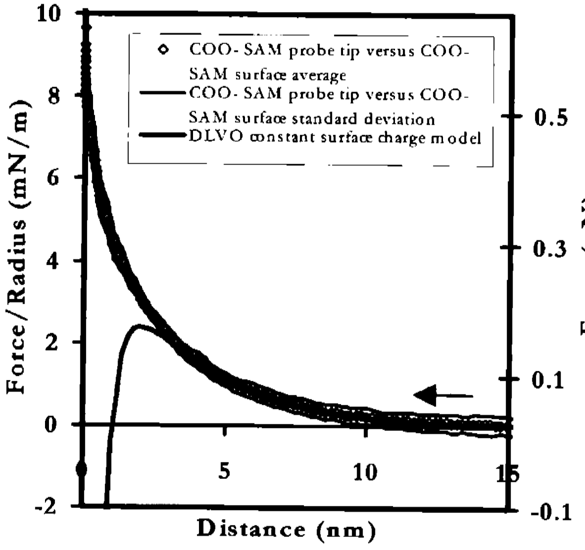

Figure 3.8 Averaged Force (nN) and Force/Radius (mN/m) versus Distance, D (nm) approach curves for COO$^-$-terminated probe tip versus COO$^-$-terminated SAM surface in PBS compared to DLVO electrostatic double layer constant surface charge model. κ^{-1} = 2.96 nm (IS = 0.01 M), A = 6.92x10^{-20} J, and R$_{TIP}$=63 nm were fixed

to their known values, and the charge per unit area was used as the only fitting parameter and found to be $\sigma_{TIP}(COO^-) = \sigma_{PLANE}(COO^-) = -0.018C/m^2$.

Following the DLVO theory, the total interaction force was assumed to be a linear summation of an attractive van der Waals component and a repulsive electrostatic counterion double layer component:

$$F_{TOTAL}(D) = F_{VDW}(D) + F_{ELECTROSTATIC}(D) \qquad \textbf{Equation 3.6}$$

$F_{ELECTROSTATIC}(D)$ was modeled using a constant surface charge approximation based on the numerical solution to the nonlinear Poisson-Boltzmann (PB) equation including divalent ions (Appendix B) in which the substrate is assumed to be a plane of constant charge per unit area (σ_{PLANE}) and the probe tip is modeled as an impermeable hemisphere of radius $R_{HEMISPHERE}$, also with constant charge per unit area, ($\sigma_{TIP} \approx \sigma_{PLANE}$). [129-131] The force was obtained from the electrostatic potential, Φ, using the so-called free energy method[129,132,133] and surface element integration (SEI). [134] In the theoretical datafits, the electrical interaction Debye length, κ^{-1}, was set to its known value for IS = 0.01 M (κ^{-1} = 2.96 nm), $R_{HEMISPHERE}$ was fixed to the known value of R_{TIP} measured by SEM (≈ 63 nm), and $\sigma_{TIP} \approx \sigma_{PLANE}$ was the single fitting parameter.

The nonretarded van der Waals force was also included using the inverse square power law derived using the "Derjaguin approximation" (valid for R ≫ D): [117]

$$F_{VDW}(D) = -\frac{AR}{6D^2} \qquad \textbf{Equation 3.7}$$

where: F_{VDW} is the van der Waals force between a sphere of radius R (assumed to be equal to the probe tip radius, R_{TIP}) and a planar surface separated by a distance D, and A is the nonretarded Hamaker constant which was fixed. The Hamaker constant employed for the van der Waals component of the force for this system ($Si/Cr/Au/HS(CH_2)_{10}CO_2^-$/aqueous electrolyte(IS = 0.01 M, pH = 7.4)/$HS(CH_2)_{10}CO_2^-/Au/Cr/Si_3N_4$) was fixed to $A = 6.92 \times 10^{-20}$

J. This value was chosen based on an average of fits of Equation 3.7 to HRFS experimental results reported by us and others for similar hydrophilic-terminated SAM hemispherical probe tip-planar surface systems including; $A = 5.2 \times 10^{-20}$ J for Si/Cr/Au/$HS(CH_2)_2SO_3^-$ /aqueous electrolyte(IS = 0.1M, pH = 5.6)/$HS(CH_2)_2SO_3^-$/Au/Cr/Si_3N_4, [130] $A = 3.4 \times 10^{-20}$ J for glass/Ti/Au/$C_{16}OH$/HOH/$C_{16}OH$/Au/Ti/Si_3N_4, [135] $A = 10 \times 10^{-20}$ J for mica/Au/$C_{11}OH$/HOH/$C_{11}OH$/Cr/Au/SmCo, [136] $A = 12 \times 10^{-20}$ J for mica/Au/$C_{16}OH$/HOH/$C_{16}OH$/Cr/Au/SmCo, [136] and $A = 4 \times 10^{-20}$ J for Au/Cr/Au/$HS(CH_2)_{10}CO_2^-$/aqueous electrolyte(IS = 0.0001 M, pH = 4-6)/$HS(CH_2)_{10}CO_2^-$ /Au/Cr/Si_3N_4. [137] As described in reference, [135] the calculation of A for our 9-layered systems could be performed using a Lifshitz multilayered model, but due to the lack of the ability to include conductors rigorously in such calculations, we have instead employed an average of experimental values reported on similar systems via HRFS which will give a more accurate estimate of the magnitude, range, and functional form of the attractive van der Waals force.

DLVO theoretical datafits yielded a surface and probe tip charge per unit area, $\sigma_{PLANE}(COO^-) = \sigma_{TIP}(COO^-)$, of -0.018 C/m^2. Allowing more than one free fitting parameter resulted in multiple solutions. The DLVO model fit the experimental data extremely well for $D > 3.4$ nm and increasingly deviated from the data with decreasing separation distance for $D < 3.4$ nm, possibly due to the assumption of uniform permittivity and the approximation of ions as discrete point charges in the electrostatic double layer model, which starts to break down at small distances, in addition to the presence of non-DLVO forces. No jump-to-contact minimum was observed, most likely due to the presence of additional non-DLVO forces, such as possible hydration repulsion at shorter distances. Such phenomena have been observed previously for hydrophilic SAMs and attributed to the additional energy needed to dehydrate surface adsorbed counterions. [130] A more detailed description of the numerical and empirical electrostatic modeling is given in Appendix B.

HSA Probe Tip versus a COO^--Terminated SAM. Figure 3.9 shows the average Force (nN) and Force/Radius (mN/m) versus Distance (nm) approach curve (with standard deviations) for an HSA probe tip versus a COO$^-$ terminated SAM surface in PBS compared

σ_{TIP}(HSA), which was found to be equal to -0.0064 C/m^2. This value represents an average charge per unit area in the planes parallel to the outer exposed atomic van der Waals surface of the protein layer (which was taken to be the plane of constant charge in the model). Surface charge densities obtained in this manner via HRFS have been shown to accurately represent the spatial distribution of charged groups on the exposed protein surface when the protein is oriented uniformly (e.g. in a crystal) when compared to theoretical predictions of the electrostatic potential distribution around the protein surfaces calculated using the Poisson-Boltzmann equation. [139] In our experiment, however, there is no need to believe that the HSA layer on the probe tip is uniformly oriented since the distribution of hydrophobic and hydrophilic sites and the distribution of amine groups through which the covalent attachment takes place is nonuniform (Figure 3.10 (A)). Hence, the measured charge per unit area should reflect an average of the entire HSA surface charge distribution map (Figure 3.10 (B)) and corresponds to a charge per protein of -1.8*e* assuming an elliptical shape and -1.1*e* assuming a triangular shape. The net charge of HSA under the experimental conditions employed here is known to be -15*e*, which takes into account the full amino acid sequence[67] or -19*e* measured experimentally at pH = 7.4 (including bound ions). [72] As expected, these values are greater than that obtained via by HRFS, presumably because many of the charged groups may be unexposed, being located interior to the protein or underneath (facing the probe tip side).

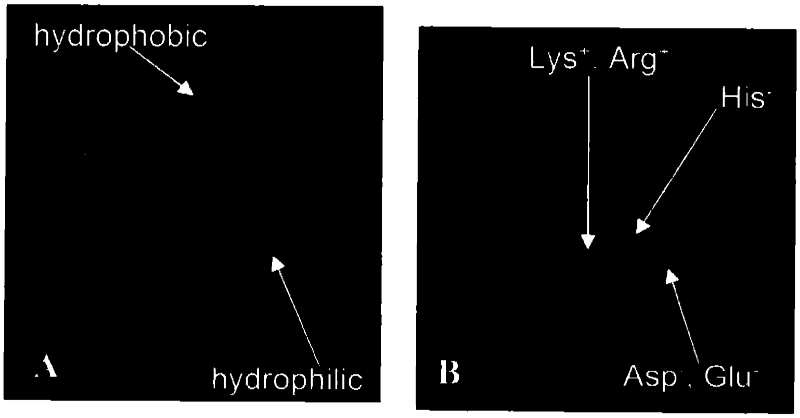

Figure 3.10 Various schematics of crystallized HSA complexed with myristic acid (downloaded from reference[73]; also see reference [74]) (**A**) is a space-filling display showing the locations of hydrophilic

residues (colored blue) and hydrophobic residues (in green). Figure (**B**) is a wire frame backbone display with charged residues using a van der Waals dotted surface. All lysines and arginines (both positively charged at pH 7) are colored blue, aspartic acid and glutamic acid (negatively charged at pH 7) are colored red, and histidine, which is 90% negatively charged at pH = 7, is in cyan.

3.3.2 Approach of an HSA-Grafted Probe Tip to an Unmodified Polygranular Gold Substrate

Figure 3.11 displays an average Force (nN) and Force/Radius (mN/m) versus Distance (nm) approach curve (with standard deviations) for an HSA probe tip versus an Au planar surface in PBS compared to the DLVO constant surface charge model.

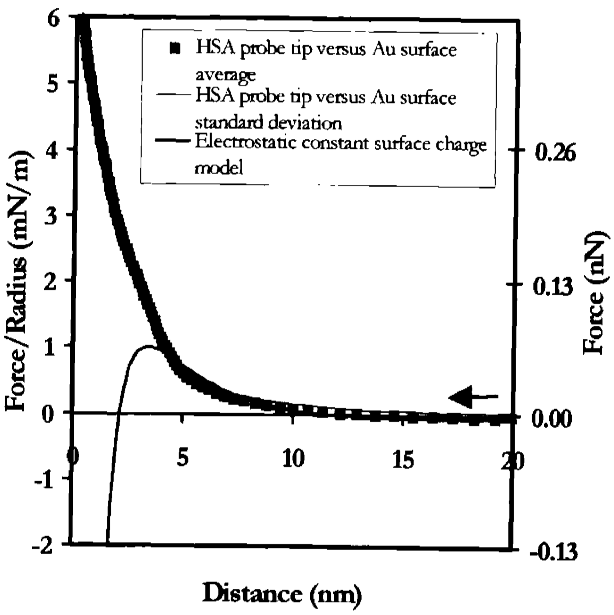

Figure 3.11 Average Force (nN) and Force/Radius (mN/m) versus Distance, D (nm) approach curve for an HSA probe tip on Au surface in PBS with standard deviations. Comparison is made to DLVO theory fixing $\sigma_{TIP}(HSA) = -0.0064$ C/m^2, $\kappa^{-1} = 2.96$ nm (IS = 0.01 M), $R_{TIP} = 65$ nm, and $A = 6.92\times10^{-20}$ J. $\sigma_{PLANE}(Au)$ was the only fitting parameters and found to be 0.014 C/m^2.

Similar to the data shown in Figure 3.8 and Figure 3.9, a nonlinear, purely repulsive force was observed to begin at D < 15 nm, reaching a maximum magnitude at D = 0 of Force = 0.32 nN, corresponding to a Force/Radius ~ 4.9 mN/m with no jump-to-contact. The model parameters for this experiment (Si/Cr/Au/aqueous electrolyte(IS = 0.01 M, pH =

7.4)/HSA/Si_3N_4) that were fixed in the simulation were κ^{-1} = 3 nm for IS = 0.01 M, A = 6.92×10^{-20} J, R_{TIP} = 65 nm, and σ_{TIP}(HSA) = -0.0064 C/m^2 (taken from the DLVO theoretical datafits to the HSA probe tip versus COO^- surface experiment, Figure 3.9). The fit to the theory showed good agreement for D > 4.5 nm with an Au surface charge, σ_{PLANE}(Au) = -0.014 C/m^2, suggesting that the observed repulsive behavior in this range was electrostatic in origin. It is postulated that these forces might arise, in part, from an effective surface charge on the Au substrate due to nonspecific anion adsorption. [140]

3.3.3 Approach of an HSA-Grafted Probe Tip to a CH_3-Terminated Self Assembled Monolayer.

Figure 3.12 displays the average Force (nN) and Force/Radius (mN/m) versus Distance (nm) approach curves for a HSA probe tip versus a CH_3 terminated SAM surface in PBS (blue triangle symbols), as well as the corresponding standard deviations (blue solid lines).

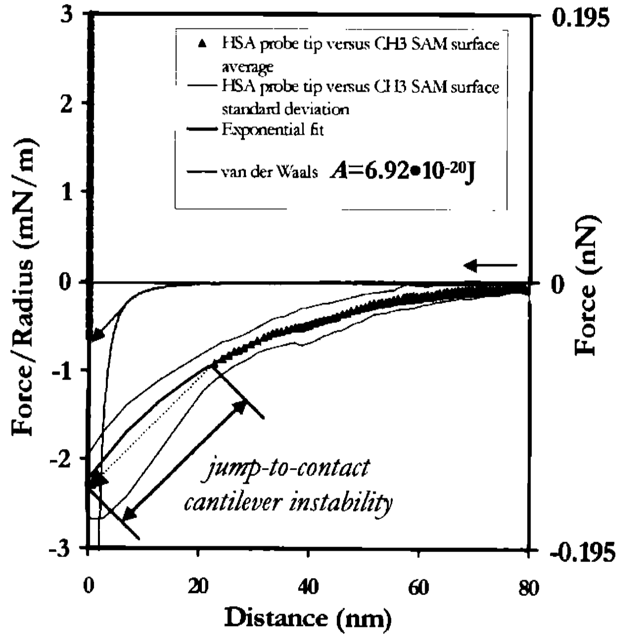

Figure 3.12 Average Force (nN) and Force/Radius (mN/m) versus Distance, D (nm) approach curve for an HSA probe tip on a CH_3–terminated SAM surface in PBS with standard deviations. R_{TIP} = 65nm. Comparison

is made to the van der Waals force (A = 6.92x10^{-20}J) (green line) as well as to an exponential fit (black line). [141]

A purely attractive, nonlinear interaction curve begins at D < 80 nm, with a jump-to-contact at D ~ 20 nm, and a mean attractive minimum of $<F_{\text{minimum}}> = 0.15 \pm 0.02$ nN and $<F_{\text{minimum}}>$/Radius = 2.3 ± 0.3 mN/m (this value is a consequence of the cantilever instability since the slope of the line for D < 20 nm in dF/dD = k_c). This data is consistent with previous observations of long range (~ 10-100 nm), attractive forces between hydrophobic surfaces. [142,143] The known van der Waals interaction for a hydrocarbon SAM terminated with a hydrophilic chemical group on Au (Equation 3.7 with A = 6.92x10^{-20}J) and the theoretical van der Waals jump-to-contact distance :

$$D_{\text{jump-in}} = \left[\frac{A R_{\text{TIP}}}{3k_c} \right]^{1/3}$$ **Equation 3.8**

were calculated to be 5.3 nm, and are shown in Figure 3.12 (green line). Here, we see that the measured force is much larger in magnitude and range than that which is known for a hydrocarbon SAM with a hydrophilic end-group on Au. This long-ranged force is thought to be due to additional attractive interactions between the hydrophobic CH_3 end-groups of the SAM and hydrophobic groups on the HSA that take place in aqueous solution. This data provides a supportive, quantitative explanation for why proteins, even extremely hydrophilic ones such as HSA, are observed to readily adsorb to hydrophobic surfaces. [78,144] The molecular origin of the hydrophobic interaction is controversial and largely unknown, but generally thought to be entropy-driven. [141] Water molecules near a hydrophobic surface cannot form hydrogen bonds with the surface since there are no donor hydrogen atoms or hydrogen bond acceptors and hence the original water structure is disturbed. Rather than having interfacial molecules with partially charged dangling bonds, it is thought that water molecules may reorient themselves into a more ordered structure so as to preserve as many hydrogen bonds as possible. Although this process is not entropically favorable, the associated entropic penalty is less than the corresponding enthalpic penalty for disruption of hydrogen bonds. The strong attraction felt between two hydrophobic surfaces in water is then not only due to the drive to avoid disruption of the surrounding hydrogen bonded network, but also due to the favorability of minimizing the exposed hydrophobic surface area, and thereby minimizing the entropic penalty for rearrangement of the water molecules. The attractive force was empirically fit to Equation 3.9, [141] as shown in Figure 3.12 (black line):

$$F(D) = 4\pi R_{TIP}\gamma_i \exp\left(\frac{D}{\lambda_o}\right)$$ **Equation 3.9**

where γ_i is the surface interfacial energy with water, and λ_o is the characteristic decay length. The interaction force before the jump to contact can be fit well to Equation 3.9 for λ_o= 25.6 nm and $4\pi R_{TIP}\gamma_i = 0.145$ nN, yielding : $\gamma_i = 0.18$ mJ•m^{-2}.

3.4 Results on Retract

3.4.1 General Methodology.

A number of parameters were defined and calculated to characterize the nanoscale adhesion between the HSA probe tip and various surfaces and are summarized in Table 3.3. $F_{adhesion}$ is the maximum attractive force observed on retraction for each distinct adhesion event (which may occur more than once for a single force curve if multiple molecules of varying lengths are tethered between the tip and the substrate), and $\langle F_{adhesion} \rangle$ represents the mean value of $F_{adhesion}$ for one dataset, i.e. corresponding to numerous force versus distance curves for one particular probe tip-sample combination (this notation is used consistently throughout the rest of this document). $\langle D_{adhesion} \rangle$ is the mean distance corresponding to $\langle F_{adhesion} \rangle$. $\langle F_{adhesion}/\text{Radius} \rangle$ is the mean adhesive force normalized by the probe tip radius giving an effective adhesive energy of interaction that can be employed universally for all HRFS data employing a hemispherical probe tip. For data conducted with different probe tips, only $\langle F_{adhesion}/\text{Radius} \rangle$ should be compared, not $F_{adhesion}$, and even then differences may arise due to local variations in probe tip geometry.

For HRFS data exhibiting surface adhesion (as opposed to other long range adhesive mechanisms), $<F_{adhesion}>$ was converted into an average adhesive interaction energy per unit area, $<W_{exp}>$, using adhesion elastic contact mechanics theory which predicts the pull-off force required to separate a hemispherical tip of radius, R_{TIP}, from a planar surface :

$$< W_{exp} >= \frac{< F_{adhesion} >}{\beta \pi R_{TIP}}$$ **Equation 3.10**

where β = 1.4 for the Burnham-Colton-Pollack (BCP) theory, [120] β = 1.5 for the Johnson-Kendall-Roberts (JKR) theory, [121] and β = 2 for the Derjaguin-Muller-Toporov (DMT) theory. [119] BCP and DMT theory account for adhesion via surface forces outside the contact area and within the surface interaction area while JKR theory accounts for adhesive forces only within the contact area. [120] For experiments which undergo energy dissipating processes and mechanical hysteresis (nonequivalence of loading and unloading plots), such as the ones presented in this research study, the experimentally measured adhesion energy per unit area, W_{exp}, is greater than the ideal, reversible thermodynamic work of adhesion, $W_{adhesion}$. [145] Although the timescale of characteristic charge relaxation times is very short, i.e. of order of ns in H_2O at IS = 0.01M, [146,147] the electrostatic double layer interaction may exhibit hysteresis when, for example, charged molecules exhibit structural changes on compression which results in a rearrangement of the spatial distribution of the fixed charge groups and do not relax back during the experimental time scale. Surfaces which exhibit attractive interactions such as van der Waals, hydrophobic interactions, and hydrogen bonding are known to sometimes exhibit hysteresis due to an increase in the number of bonds formed and / or structural rearrangement of the surface molecules during the contact time. [136,148]

Apart from employing these parameters to quantify adhesion, the irreversible adhesive energy lost or dissipated during the loading (approach)-unloading (retract) cycle, U_d (J), which is equal to the total area enclosed by the loading and unloading curve (i.e. amount of hysteresis) was calculated as follows :

$$U_d = \int_{D_{\max(a)}}^{0} F_{\text{approach}}(D)dD - \int_{0}^{D_{\max(r)}} F_{\text{retract}}(D)dD \qquad \textbf{Equation 3.11}$$

where $D_{\max(a)}$ is the maximum distance of the approach interaction and $D_{\max(r)}$ is the maximum distance of the retract interaction. U_d is a measure of the total adhesive energy required to separate the probe tip from the surface, and since the probe tip and surface are much stiffer than the force transducer in these experiments, U_d primarily reflects the dissipative processes taking place at the interface (rather than in the bulk). For force curves which exhibit large surface adhesive forces, the true adhesive interaction profile is hidden within the large regions of cantilever instability and hence, an accurate value for U_d could not be calculated for such data.

3.4.2 Retract of an HSA-Grafted Probe Tip from a COO^--terminated Self Assembled Monolayer.

Figure 3.13 plots typical individual Force (nN) and Force/Radius (mN/m) versus Distance (nm) approach and retract curves for an HSA probe tip versus a COO^-–terminated SAM surface in PBS solution and shows that three distinct mechanisms of interaction were observed, each described in detail following. For the entire dataset, $<F_{adhesion}>(COO^-) = -0.28 \pm -0.38$ nN, $<F_{adhesion}>/R_{TIP}(COO^-) = -1.9 \pm -2.5$ mN/m corresponding to $<D_{adhesion}>(COO^-) = 13.5 \pm 48$ nm.

The various types of force curves observed fell into one of three categories:

1) Completely nonadhesive curves of the type shown in Figure 3.13(A) were observed in 49% of the total HRFS experiments where the HSA probe tip exhibited no attractive forces on retraction away from the SAM surface.

2) Curves of the type shown in Figure 3.13 (B) (plotted on same scale as Figure 3.13 (A)) occurred in 35% of the total HRFS experiments. Here, the probe tip exhibited surface adhesion and separated from the surface suddenly at short distances followed by a region of cantilever instability, where the true adhesive interaction profile was unable to be determined. Hence, U_d was unable to be calculated. For this type of adhesive mechanism, $<F_{adhesion}>(COO^-)$ = -0.73 ± -0.27 nN and $<F_{adhesion}>$/Radius (COO^-) = -4.9 ± -1.8 mN/m corresponding to $<D_{adhesion}>(COO^-)$ = 0.8 ± 4.2 nm. $<W_{exp}>(COO^-)$ was calculated from Equation 3.10 to be -1.1 ± -0.41 mJ/m^2 (BCP), -1.0 ± -0.38 mJ/m^2 (JKR), and -1.0 ± -0.29 mJ/m^2 (DMT), corresponding to -5.3 to -7.5 k_BT per protein (assuming a triangular shape) and -8.7 to -12 k_BT per protein (assuming an elliptical shape).

The contribution to adhesion from the small number of molecules within the elastic contact area versus the larger amount of molecules within the surface interaction area is unknown. A full knowledge of the interaction profile on retract within the cantilever instability region would help clarify this question and could be addressed using stiffer cantilevers with shorter regions of instability (at the cost of lower force resolution). Clearly, the formation and rupture of short range HSA-SAM noncovalent bonds (this mechanism is further verified by subsequent HRFS data), e.g. hydrophobic, van der Waals, H-bonding, is expected to take place mostly within and nearby the elastic contact area, since the surface tethered SAM molecules are too short to access the HSA proteins up the sides of the hemispherical probe tip within the surface interaction area (Figure 3.7). As mentioned in the experimental section, the estimated force per protein at these short distances is much less than the expected force needed for significant structural rearrangements or mechanical denaturation of the proteins. Hence, such short range SAM interactions are probably most prevalent with accessible surface functional groups of the HSA, e.g. with NH_3^+- or OH-functionalized amino acid residues which remain protonated at pH 7.4. Structural rearrangements of the SAM to facilitate attractive interactions, especially the few molecules within the elastic contact area, are likely. Such structural rearrangements could also have a significant effect on the long range attractive forces felt by the surface interaction area. In 11% of force curves exhibiting strong surface adhesion, the region of cantilever instability was followed by protein pulling at longer distances (similar to the curves described in type *3* below).

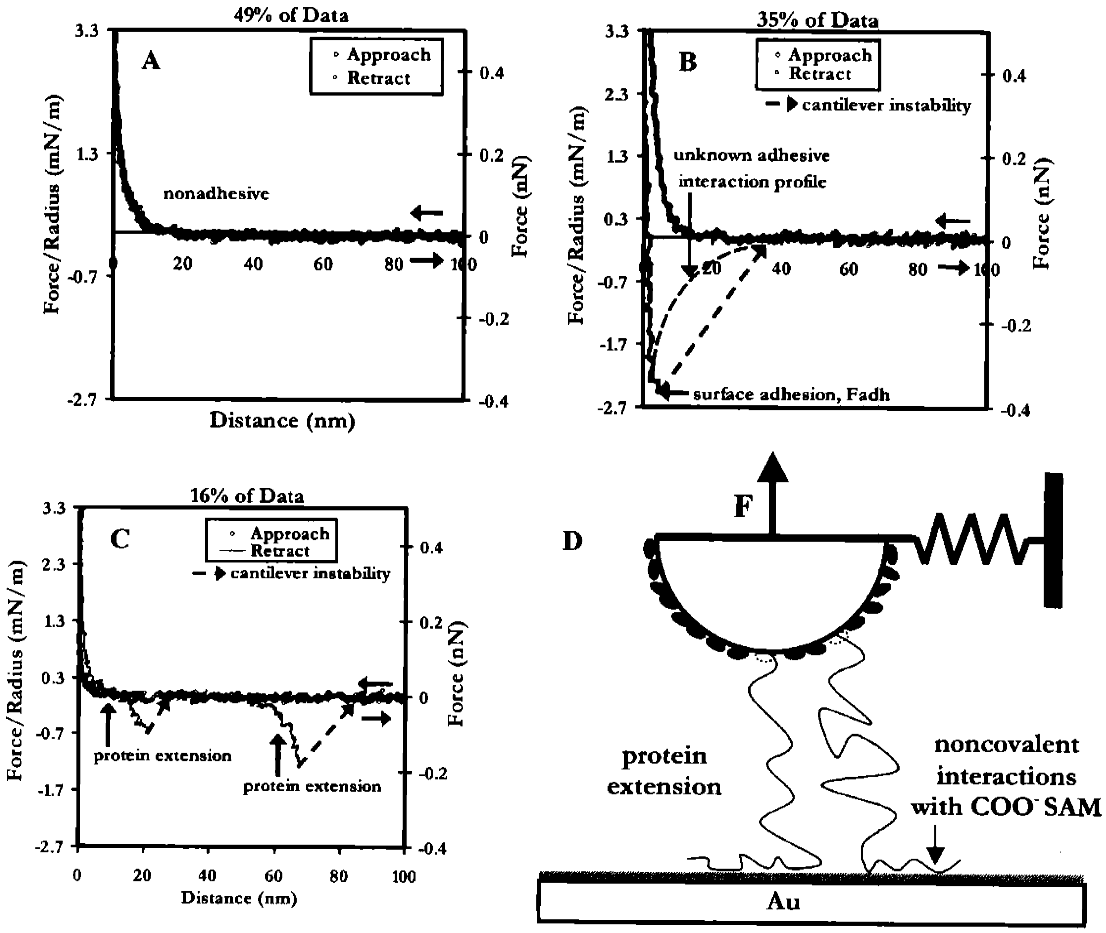

Figure 3.13 Typical individual Force (nN) versus Distance (nm) approach and retraction curves of an HSA probe tip on a COO$^-$-terminated SAM in PBS. (**A**) observed in 49% of total HRFS experiments; (**B**) observed in 35% of total HRFS experiments; (**C**) observed in 16% of total HRFS experiments; (**D**) schematic of proposed adhesive deformation mechanism for the type of force versus distance curve in (C).

3) As shown in Figure 3.13(C) (plotted on the same scale as Figure 3.13 (A) and (B)), in 16% of the total HRFS experiments, at short distances there was no surface adhesion, but rather a few long range, nonlinear, attractive peaks were observed where chain segments of the HSA molecules were adsorbed and tethered firmly enough to the SAM surface to allow stretching of the protein molecules between the probe tip and the surface, presumably inducing mechanical denaturation of the HSA. These nonlinear attractive peaks represent the molecular elasticity of a few HSA molecules tethered in parallel between the probe tip and surface (Figure 3.13 (D)). HSA unfolding can take place at larges distances on retract (extension) because there are a smaller number of proteins tethered to the surface, which increases the force per protein as compared to near the surface, when all proteins within the surface interaction area support the applied load in parallel with each other. The multiple regions of cantilever instability may be attributed to mechanical unfolding of a few HSA molecules or different regions of an individual HSA molecule or detachment of individually tethered molecules from the probe tip. It has also been suggested that such experimental data which exhibits force plateaus may be attributed to chains segment "pull-out" from collapsed globules in a poor solvent (i.e. Rayleigh instabilities). [149] The net attractive force, $F_{retract}$, will have contributions from HSA entropic molecular elasticity and enthalpic unfolding forces (deformation and rupture of noncovalent intramolecular bonds) and noncovalent bond deformation and rupture of the HSA chain segments adsorbed to the SAM surface. Presumably, $F_{retract}$ is dependent on the loading rate due to the fundamental kinetics associated with force-driven bond dissociation pathways. [150] For these types of curves, $<F_{adhesion}>(COO^-) = -0.15 \pm -0.11$ nN or $<F_{adhesion}>$/Radius(COO^-) = -0.98 ± -0.75 mN/m (much less in magnitude compared to previously described surface adhesion mode) corresponding to $<D_{adhesion}>(COO^-) = 82.6 \pm 95.2$ nm (much longer range compared to previously described surface adhesion mode).

3.4.3 Retract of an HSA-Grafted Probe Tip from an Unmodified Polygranular Gold Substrate.

Figure 3.14 plots a typical individual Force (nN) and Force/Radius (mN/m) versus Distance (nm) approach and retract curves for an HSA probe tip versus an Au surface in PBS solution which was observed in 100% of the total HRFS experiments and appears similar in mechanism to that shown in Figure 3.13 (B) (observed in 49% of COO-terminated SAM HRFS experiments).

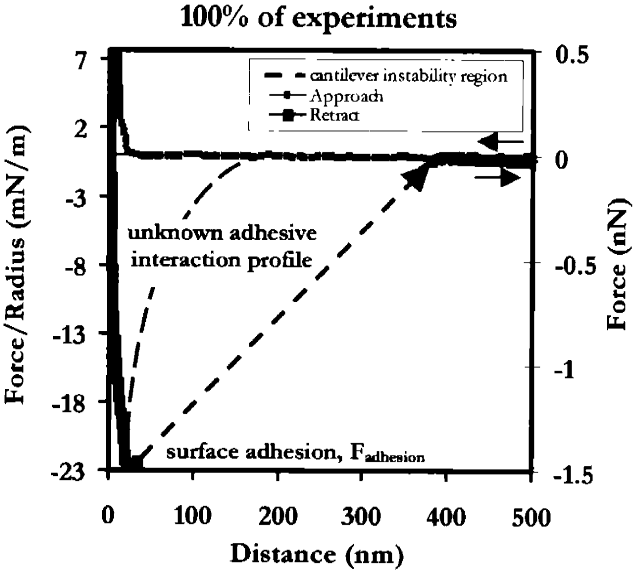

Figure 3.14 Typical individual Force (nN) versus Distance (nm) approach and retraction curve of an HSA probe tip from Au in PBS.

Here, HRFS experiments exhibited large adhesion values, a single pull-off at distances close to the surface that was preceded by a short region in which the force was continuously nonlinear with increasing separation distance. The HSA probe tip exhibited a net attractive force to Au surface at all separation distances. $\langle F_{adhesion}\rangle$(Au) = -1.35 ± -0.19 nN or $\langle F_{adhesion}\rangle$/Radius (Au) = -21 ± -2.9 mN/m corresponding to a distance of $\langle D_{adhesion}\rangle$(Au) = 22.5 ± 6.3 nm. $\langle W_{exp}\rangle$ (Au) was calculated from Equation 3.10 to be -4.7 ± -0.66 mJ/m^2 (BCP), -4.4 ± -0.62 mJ/m^2 (JKR), and -3.3 ± -0.47 mJ/m^2 (DMT), corresponding to -23 to -32 k_BT per protein (assuming a triangular shape) and -37 to -52 k_BT per protein (assuming an elliptical shape. Once again, these curves had large regions of cantilever instability and hence, the true adhesive interaction profile was unable to be determined.

It has been postulated that the free thiol group on HSA amino acid residue Cysteine-34 may react with the gold surface in these experiments. However, this scenario is in fact rather unlikely, as multiple studies done by electron spin resonance[151,152] and X-ray diffraction studies[75] suggest that not only is this residue buried in a hydrophobic pocket ~ 9.5 Å beneath the surface of the protein, but that its local environment effectively lowers its pKa (relative to typical free thiol groups) to ~ 5-8, with values often reported < 5. At physiological pH and in our experiments, therefore, Cys-34 is ionized (i.e. in the form of S^- rather than SH), and incapable of reacting with the gold surface.

3.4.4 Retract of an HSA-Grafted Probe Tip from a CH_3-Terminated Self Assembled Monolayer.

Figure 3.15 plots typical individual Force (nN) and Force/Radius (mN/m) versus Distance (nm) approach and retract curves for an HSA probe tip versus a CH_3–terminated SAM surface in PBS solution and shows two different types of force curves were observed.

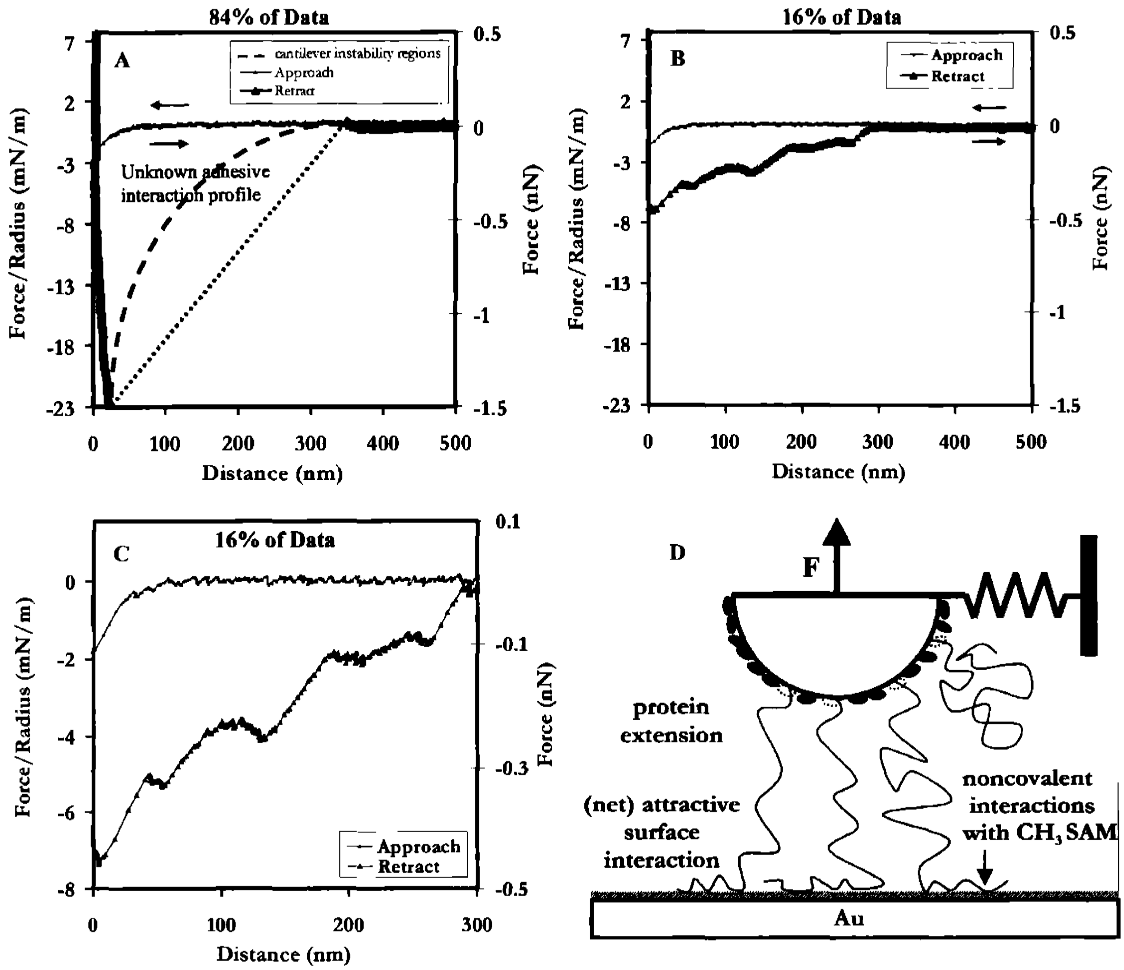

Figure 3.15 Typical individual Force (nN) versus Distance (nm) approach and retraction curves of an HSA probe tip from a CH_3–terminated SAM in PBS. (**A**) observed in 84% of total HRFS experiments; (**B**) observed in 16% of total HRFS experiments; (**C**) expanded axis plot of (B); and (**D**) schematic of proposed adhesive deformation mechanism.

Curves of the type shown in 3.15(A) were observed in 84% of the total HRFS experiments and curves of the type shown in 3.15(B) (plotted on same scale as Figure 3.15 (A)) occurred in 16% of the total HRFS experiments (for clarity, Figure 3.15(C) shows an expanded axis scale of the data given in Figure 3.15 (B)). For both types of force curves, the HSA probe tip exhibited a net attractive force to CH_3 SAM surface at all separation distances. For the entire dataset, $<F_{adhesion}>(CH_3) = -1.70 \pm -0.66$ nN and $<F_{adhesion}>/Radius(CH_3) = -26 \pm -10$ mN/m corresponding to $<D_{adhesion}>(CH_3) = 20.8 \pm 22.5$ nm. $<W_{exp}>(CH_3)$ was calculated to be -6.6 ± -2.0 mJ/m^2 (BCP), -6.2 ± -1.9 mJ/m^2 (JKR), and -4.6 ± -1.4 mJ/m^2 (DMT), corresponding to -31 to -45 k_BT per protein (assuming triangular shape) and -51 to -73 k_BT per protein (assuming elliptical shape). As shown in Figure 3.15(A), in the HRFS data which exhibited the larger adhesion values, the probe tip separated from the surface suddenly at short distances after a region in which the force grew continuously nonlinear with increasing separation distance. These curves had large regions of cantilever instability and hence, the true adhesive interaction profile, the range of the interaction, and whether or not adhesion hysteresis existed (as opposed to mechanical hysteresis of the cantilever) was unable to be determined. As shown in Figure 3.15(B), the force spectroscopy experiments which exhibited smaller adhesion values showed a combination of surface adhesion followed by multiple long range, nonlinear attractive peaks due to mechanical unfolding of a number of HSA molecules or different regions of the HSA molecules (Figure 3.15(D)). More of the force profile is exposed for the HRFS experiments exhibiting smaller adhesive forces (Figure 3.15 (B)), and a reasonably accurate value for U_d was calculated to be $-(7.9 \pm 3.6)x10^{-17}$ J = $-(1.9 \pm 0.9)x10^4$ k_BT. The energy per unit interaction area and per protein were unable to be determined since the interaction area on retract and the number of proteins tethered to the CH_3-terminated surface on retract was unknown. Figure 3.16 (B) compares $<F_{adhesion}/Radius>$ for all three surfaces tested, and indicates statistically significant trends as determined by the "Student's t" (p = 0.05, Section 2.2.6). The probability distribution histograms corresponding to this data are shown in Figure 3.17.

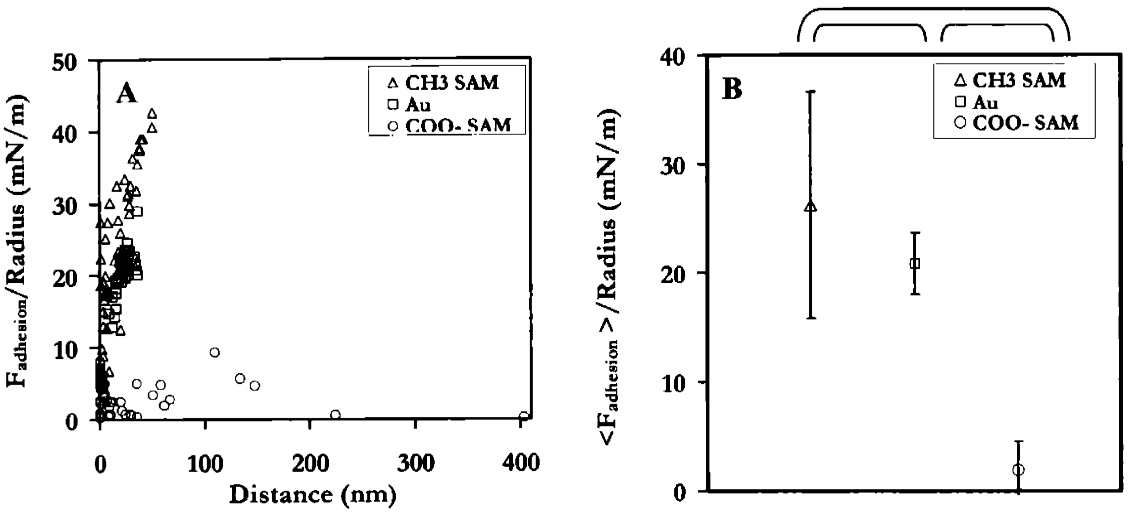

Figure 3.16 (**A**) $F_{adhesion}$/ Radius versus $D_{adhesion}$ for HSA probe tip on retraction from various surfaces, each datapoint corresponds to one HRFS experiment; (**B**) <$F_{adhesion}$/Radius> for HSA probe tip on retraction from various surfaces. Statistically different data points (as determined by the "Student's t", $p = 0.05$, Section 2.2.6) are connected by brackets above.

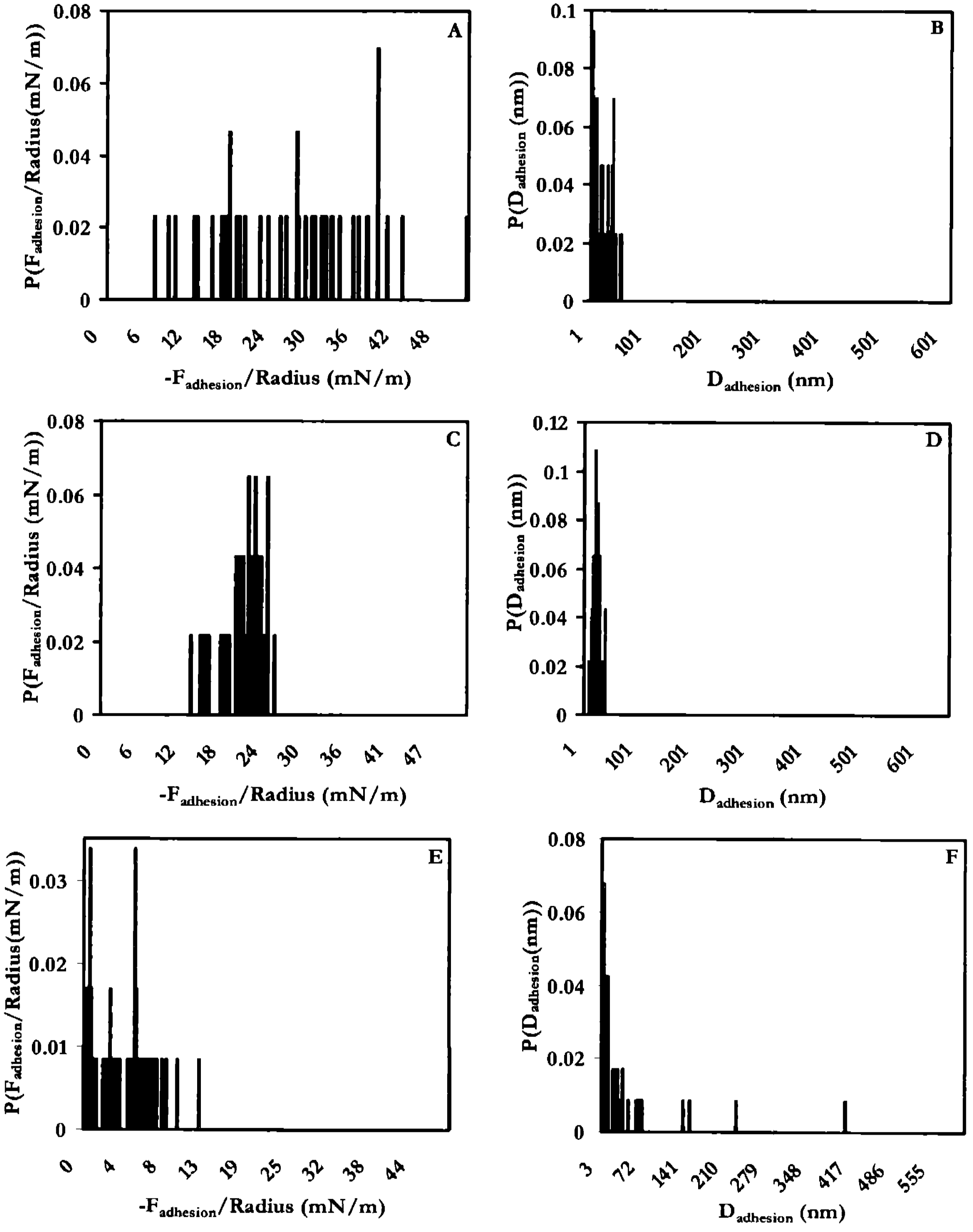

Figure 3.17 Probability distribution histograms corresponding to the experimental data shown in Figure 3.13 for the COO$^-$-terminated SAM: (**A**) and (**B**); Au: (**C**) and (**D**); and the CH$_3$-terminated SAM: (**E**) and (**F**).

SUBSTRATES→	**CH_3 SAM**	**COO^- SAM**	**Au**
$\langle F_{adhesion}\rangle$ (nN)	-1.70 ± -0.66 (total n = 44) -1.88 ± -0.57 (n = 37)* -0.12 ± -0.30 (n = 7)**	-0.28 ± -0.38 (total n=119) -0.73± -0.27 (n=42)† 0.15 ± -0.11 (n=19)†† zero adhesion (n=58)	-1.35 ± -0.19 (n=46)
$\langle D_{adhesion}\rangle$ (nm)	20.8 ± 22.5 (total n = 44) 19.2 ± 16.7 (n = 37)* 4.64 ± 19.36 (n = 7)**	13.5 ± 48.0 (total n = 119) 0.8 ± 4.2 (n=42)† 82.6 ± 95.2 (n=19)†† zero adhesion (n=58)	22.5 ± 6.3 (n=46)
$\langle F_{adhesion}\rangle$/Radius (mN/m)	-26 ± -10 (total n = 44) -29 ± -8.8(n = 37)* -12 ± -2.9 (n = 7)**	-1.9 ± -2.5 (total n = 119) -4.9 ± -1.8 (n = 42)† - 0.98 ± -0.75 (n = 19)†† zero adhesion (n=58)	-21 ±-2.9 (n=46)
BCP: **$\langle W_{exp}\rangle$ (mJ/m^2)** **$\langle W_{exp}\rangle$/protein (k_BT)**	-6.6 ± -2.0* -45 (triangle) -73 (ellipse)	-1.1 ± -0.41† -7.5 (triangle) -12 (ellipse)	-4.7±-0.66 -32 (triangle) -52 (ellipse)
JKR : **$\langle W_{exp}\rangle$ (mJ/m^2)** **$\langle W_{exp}\rangle$/protein (k_BT)**	-6.1 ± -1.9* -41 (triangle) -68 (ellipse)	-1.0 ± -0.38† -6.8 (triangle) -11 (ellipse)	-4.4 ± -0.62 -30 (triangle) -49 (ellipse)
DMT : **$\langle W_{exp}\rangle$ (mJ/m^2)** **$\langle W_{exp}\rangle$/protein (k_BT)**	-4.6±-1.4* -31 (triangle) -51 (ellipse)	-1.0 ± -0.29† -5.3 (triangle) -8.7 (ellipse)	-3.3 ± -0.47 -22 (triangle) -37 (ellipse)
$\langle U_d\rangle$ (J)	-(7.90 ± 3.6)x10^{-17}	-	-
$\langle U_d\rangle$ (k_BT)	-(1.93 ± 0.88)x10^{4}	-	-

n = number of force versus distance curves used in calculation

total = all data including zero adhesion data (if applicable)

CH_3 SAM: *surface adhesion without identifiable protein extension; **identifiable protein extension, 16% of data

COO^- SAM : †surface adhesion only, 35% of data; ††protein extension, no surface adhesion, 16% of data

Table 3.3 Average experimental forces and distances of adhesion for an HSA-grafted probe tip on Au and alkanethiol SAMs.

3.5 Discussion

3.5.1 HRFS Experimental Data on Approach.

The experimental data on approach was averaged over many experiments and presented always with standard deviations and normalized by the probe tip radius, giving a representative effective energy of interaction. Calculations of the compressive force per protein on approach within in the maximum surface interaction area were much less than the expected force needed for HSA denaturation, and hence, it is expected that steric deformations of the protein on approach have a negligible contribution to the interaction force profile. The approach interaction of the HSA probe tip on the COO^- terminated SAM and Au substrates was found to be purely repulsive for $D < 15$ nm, nonlinear with decreasing separation distance, and consistent with electrostatic double layer and hydration repulsion theories. A comparison of HRFS experimental data to DLVO theoretical predictions yielded a surface charge per protein of -1.1*e* to -1.8*e*, depending on the assumed shape of the protein. As expected, these values are less than the known HSA net charge of -19*e*, presumably because many of the charged groups may be unexposed, being located interior to the protein or underneath (facing the probe tip side).

The approach interaction of the HSA probe tip on the CH_3 terminated SAM substrate was found to be purely attractive, long range ($D < 80$ nm), nonlinear with decreasing separation distance, and much greater in magnitude and range than that known for van der Waals interactions between hydrocarbon SAMs terminated with hydrophilic chemical groups on Au. This effect is most likely due to interactions between the hydrophobic CH_3 end-groups of the SAM and hydrophobic groups on the HSA that take place in aqueous solution. The observation of such a strong and long-ranged attractive force is interesting when one considers that the HSA is complexed with fatty acids which fill up its hydrophobic channels, and the surface of HSA is predominantly hydrophilic. This data provides a supportive, quantitative explanation for why proteins, e.g. even extremely hydrophilic ones such as HSA, are observed to readily adsorb to hydrophobic surfaces. [78,144]

3.5.2 HRFS Experimental Data on Retract.

A number of general parameters were defined to characterize the nanoscale adhesion between the HSA probe tip and various surfaces, i.e. $<F_{adhesion}>$, $<F_{adhesion}/Radius>$, $<D_{adhesion}>$,$<W_{exp}>$, and $<U_d>$, and the validity of each parameter was discussed with regards to the geometry of the HRFS experiment and the type of experimental data obtained. $<F_{adhesion}/Radius>$ is a parameter that can be employed universally for all HRFS data employing a hemispherical probe tip. $<W_{exp}>$ was calculated via the JKR, DMT, and BCP elastic contact mechanical theories, and can only be employed when the retraction force profile exhibited short range surface adhesion. $<U_d>$ was calculated only in the absence of excessive regions of cantilever instability (typical for weak cantilevers) which prevent knowledge of the true adhesive interaction profile (in the future, stiffer cantilevers with shorter instability ranges will be employed to determine more of the adhesive interaction profile). The adhesion is expected to have contributions from interfacial energy dissipative processes occurring in both the surface interaction area and the elastic contact area, where the forces are amplified over a much smaller length scale (i.e. < 1 HSA protein and a few SAM molecules are expected to fit within $A_{contact}$).

Large surface adhesive energies (< -29 mN/m, -22 to -73 k_BT/protein) were observed for the HSA probe tip on both the CH_3-terminated SAM and Au surfaces while smaller surface adhesive energies were observed for the COO^- terminated SAM surface (< -4.9 mN/m, -5.3 to -12 k_BT/protein). The COO^--terminated SAM exhibited three distinct types of interaction mechanisms; including 49% pure repulsion (nonadhesion), 35% surface adhesion (12% of which also exhibited protein extension subsequent to surface adhesion), and 16% protein extension. For the surfaces which exhibited adhesion, it was shown that short range adhesive contacts between the HSA chain segments and these surfaces give rise to energy dissipating mechanisms, such as HSA entropic molecular elasticity and enthalpic unfolding forces (deformation and rupture of noncovalent intramolecular bonds) and noncovalent bond rupture of the HSA chain segments adsorbed to the surface. $<F_{adhesion}/Radius>$ for the HSA versus CH_3 SAM surface is approximately one order of magnitude less than that typically observed for a interactions between purely hydrophobic surfaces, i.e. a CH_3 terminated SAM probe tip versus a CH_3 terminated SAM surface. [110] Even though the HSA versus Au and COO^--terminated SAM interaction is purely repulsive on approach, significant adhesion is frequently observed on retraction due to interfacial energy dissipating processes that take place during contact. Hence, generally for HRFS adhesion experiments, there is no clear correlation between approaching and retracting profiles without a knowledge of the details of the energy dissipating processes taking place at the molecular level. In fact, the adhesion hysteresis present is a unique signature of those processes and can be employed, in many cases, to characterize them quantitatively.

3.5.3 Consequences for HSA Adsorption.

It is interesting to note that the systolic blood pressure is typically 120 mm Hg = 16 kPa and corresponds to very short separation distances in the HRFS experiments; D = 5.6 nm on approach for the Au substrate (i.e. by calculating the stress = F/A_{TIP} from Equation 3.2), D = 4.6 nm on approach for the COO^- terminated SAM, and D=0 nm for the CH_3 terminated SAM (since it only has a purely attractive force). Hence, it is expected that this physiological degree of compression would allow for a high probability of energy dissipating and adhesive mechanisms to occur.

HSA adsorption to SAMs has been observed and studied using total internal refelection fluorescence, neutron reflectivity, and atomic force microscopy (AFM) imaging. [144,153-157] These studies shed light on the conformational changes that take place upon irreversible adsorption, where the area occupied by the protein molecule increases ("spreading"), thus achieving closer contact with the surface until, in many cases, a highly aggregated and entangled, tightly bound network of polypeptide chains results. [158] This process is a balance between the time-dependent formation of noncovalent HSA-surface interactions and structural rearrangement entropic and enthalpic penalties for protein expansion and denaturation. Even though the extensional modes of protein deformation induced in the HRFS experiments on retraction will be different from surface spreading deformations, HRFS can detect and probe the short range adhesive HSA-surface contacts that are ultimately responsible for both processes, for example by looking at the effect of surface "dwell time," or time delay in contact between approach and retract cycles, on the adhesive forces. In the above cited papers, the adsorption process has been shown to be sensitive to the SAM packing density and HSA fatty acid binding, suggesting the importance of SAM chain flexibility and "specific" hydrophobic interactions, i.e. SAM alkyl chain penetration into the fatty acid binding sites. Analogous HRFS studies, in addition to the use of "antihydrophobic" agents, such as isopropanol, were able to quantify these effects on the intermolecular interactions directly, and are reported in Chapter 5.

3.6 Conclusions

The main findings of this study were as follows:

1) The strength and range of the nanoscale interaction of an HSA-modified probe tip was highly sensitive to the type of alkanethiol SAM terminal functional group.

2) Although the approach curves for the HSA probe tip versus the COO^--terminated SAM and Au surface were purely repulsive on approach due to electrostatic double layer and possibly hydration forces, interfacial energy dissipating mechanisms at the nanoscale lead to adhesion hysteresis on retract. Hence, the experimentally measured adhesive energy per unit area, $<W_{exp}>$ is expected to be much greater than the thermodynamic work of adhesion, $<W_{adhesion}>$.

3) Upon compression, the hydrophilic, alkanethiol COO^--terminated SAM exhibited minimal adhesion to the HSA-modified probe tip (-4.9 mN/m, -5.3 to -12 k_BT/protein) while the hydrophobic CH_3-terminated, alkanethiol SAM and Au exhibited significant adhesion hysteresis (more than an order of magnitude greater, -21 to -29 mN/m, -22 to -73 k_BT/protein).

4) Multiple modes of interaction or adhesive mechanisms were observed within a single dataset for the COO^- terminated SAM.

5) The possible mechanisms involved in HSA adhesion include: a) formation and rupture of short range HSA-SAM noncovalents bonds, b) structural rearrangements of the SAM molecules leading to surface force hysteresis, and c) entropic and enthalpic penalties for extensional protein denaturation on retract.

Chapter 4

NANOSCALE INTERMOLECULAR INTERACTIONS BETWEEN HUMAN SERUM ALBUMIN AND LOW GRAFTING DENSITY SURFACES OF POLY(ETHYLENE OXIDE)

4.1 Introduction

Approaches for improving the hemocompatibility of blood-contacting biomedical devices include the use of polymeric coatings in the form of physisorbed layers or end-grafted brushes, [109,159,160] self-assembling monolayers, [19,161,162] surface fixation of anticoagulants such as heparin, prostaglandin derivatives, [163] thrombolytic enzymes, [164] endothelial cell surface glycoproteins such as thrombomodulin, [165] polymers which exhibit the controlled release of nitric oxide (a potential platelet antiaggregating and vasodilating agent), [166] or endothelial cell seeding, [167] sometimes in conjunction with blood preclotting or precoating with extracellular matrix components such as fibronectin, laminin, albumin, collagen, gelatin, and RGD-containing peptides. [168]

Poly(ethylene oxide) (PEO), poly(oxyethylene) (POE), or poly(ethylene glycol) (PEG), -$[CH_2\text{-}CH_2\text{-}O]_n$- is a synthetic polymer that is typically thought of as biologically inert and used extensively to provide a protective coating to improve the protein resistance of biomaterial surfaces. However, a variety of different experimental techniques have shown that proteins do indeed adsorb to PEO given enough time and certain disadvantageous conditions (e.g. high forces, dilute polymer solutions, long incubation times, etc.) [11,25-36] Despite extensive efforts and debates in the literature, the detailed molecular mechanisms of the interaction of PEO with proteins is still largely unknown. A brief summary of the numerous suggested nonspecific attractive and repulsive constituent contributions to the net protein-PEO intermolecular interaction potential as a function of separation distance, U(D), was given in Section 1.2.1.

This chapter focuses on investigations of the molecular origins of PEO hemocompatibility using HRFS. Human serum albumin (HSA), the most abundant blood plasma protein and typically the first to adsorb to the surfaces of implanted biomaterials, [24] was covalently grafted to a silicon nitride probe tip of radius, $R_{TIP} \sim 65$ nm, at the end of a soft, microfabricated cantilever force transducer. Relatively long mono(thiol)-terminated PEO chains ($M_n \approx 50{,}000$ g/mol, Flory Radius, $R_F \sim 8.7$ nm in aqueous solution, $L_{contour} = 393$ nm) were covalently end-grafted to gold surfaces at low density, i.e. in the mushroom regime ($s > 2R_{F,}$ where s is the distance between end-grafting sites and in our experiments was $\sim$ 62 nm), yielding an areal chain packing of $\sigma_{.} = 0.00026$ chains/nm^2). In the mushroom regime, the theoretical height of the polymer chain is = R_F. The net nanoscale force versus separation distance between this HSA modified probe tip and the PEO-modified surface was measured directly on approach and retract in aqueous buffer solution using HRFS as shown in Figure 4.1. The probe tips used in this study have a small maximum interaction area at a D = 0 tip-surface separation distance of 6100 nm^2 = 0.0061 μm^2 on the tip which corresponds to ~ 220 HSA proteins (assuming a triangular shape[73-75]) or ~134 HSA proteins (assuming an ellipsoidal shape lying flat[56,70,71]) for a close packed monolayer, as compared to the crossed cylinder geometry of a similar technique, the surface force apparatus (SFA), which has an interaction area of ~ 100 μm^2 corresponding to

>2.2 x 10^6 HSA molecules. [27,169] For the substrate, a maximum interaction area of 9,500 $nm^2 = 0.0095\ \mu m^2$ corresponding to ~ 2.5 PEO chains under the probe tip. [170] The soft microfabricated cantilever used as the force transducer in our nanomechanical apparatus, the Molecular Force Probe® (MFP), [116] produces a lower limit of force detection ± 5 pN in fluids, as compared to ± 1 nN of the SFA. [169] Both of these features enable many interesting observations to be made, including the measurement of HSA adhesive binding to individual PEO macromolecules. The approach data was analyzed through a comparison with molecular level theoretical models for the individual constituent components of the total net force, including van der Waals, electrostatic, and steric, and the retract data was analyzed statistically employing single molecule elasticity theories. Our long term objective is to develop the rigorous experimental and theoretical approaches needed to assess macromolecular biocompatibility at the nanoscale and to use this information as a guideline for the design of improved synthetic macromolecular systems for biomedical applications. It should be noted that this study also has a broader significance in the context of presenting new methodologies for macromolecular nanoscale adhesion, and in other areas such as colloid stabilization, marine biofouling, and selective deposition of polyelectrolytes.

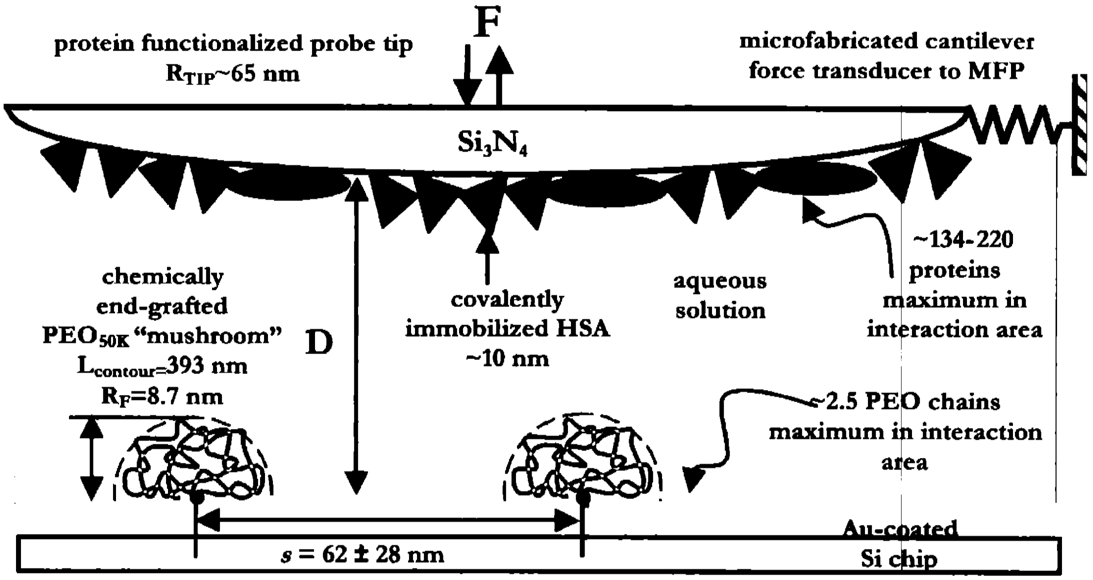

Figure 4.1 HRFS experimental setup for HSA probe tip versus PEO mushrooms in PBS.

4.2 Experimental Procedures

4.2.1 HRFS Experiments.

All HRFS experiments were conducted using the Molecular Force Probe® (Asylum Research, Santa Barbara, CA) to measure force, F (nN), versus tip-sample separation distance, D (nm) (henceforth referred to and labeled on graphs as "Distance") on "approach" (i.e. probe tip advancing towards surface) and "retract" (i.e. probe tip moving away from surface). A full description of this instrument, its limits of force and displacement detection in fluids, procedures for spring constant calibration and conversion of raw data, details of measurement errors, and description of typical force versus distance curves including the mechanical instabilities of the cantilever, are given in Section 2.2.1, and in Appendix A.1., as well in our previous works. [110,130,170]

It should be noted that, similar to many cantilever-based instruments such as the atomic force microscope (AFM), the MFP does not have an absolute measurement of the probe tip-surface separation distance, and the probe tips employed can have highly variable geometry. Figure 4.2 is a schematic of all of the distances in the HSA probe tip versus PEO surface HRFS experiments.

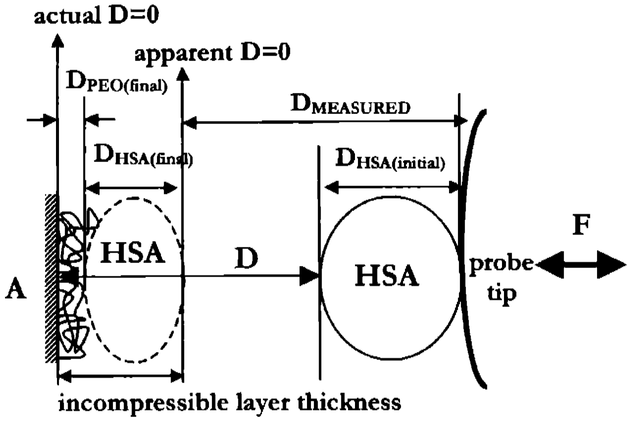

Figure 4.2 Visual explanation of the measured separation distances in an HSA probe tip versus PEO force spectroscopy experiment.

The distance of relevance, D, is the separation distance between the gold substrate or the real D = 0 point and the surface of the HSA on the probe tip which equals the height of PEO chain under compression when in contact, D_{PEO}. D can be defined as follows:

$$D = D_{MEASURED} - D_{HSA(initial)} + D_{PEO(final)} + D_{HSA(final)} \qquad \textbf{Equation 4.1}$$

where $D_{MEASURED}$ is the measured distance from the "apparent" D = 0 to the probe tip, $D_{HSA(initial)}$ is the height of HSA protein at a given separation distance, $D_{HSA(final)}$ is the incompressible height of HSA protein, and $D_{PEO(final)}$ is the incompressible height of PEO chain. The "apparent" D = 0 is set as the point where the two respective surfaces have reached their limits of compressibility. This vertical region of apparent infinite slope in the high-force, constant compliance regime is due to the fact that the spring constant of the cantilever is much less than the stiffness of the substrate. For high-density polymer brushes, it has been shown that the height of the incompressible polymer layer, $D_{PEO(final)}$, can be significant. [171,172] However, for low density PEO mushrooms in the molecular weight range employed here, $D_{PEO(final)}$ is expected to be negligible. In addition, significant distortions (denaturation) of protein structures are expected to take place under ~nN of force. [95] The maximum force per protein on approach, F_{MAX}, at D=0 was 1.6 pN assuming a triangular shape and 8.6 pN assuming a ellipsoidal shape lying flat, much less than the expected force needed for HSA denaturation. Hence, it is expected that steric deformations of the protein have negligible contribution to the interaction force profile, i.e. $D_{HSA(initial)} = D_{HSA(final)}$. If this is the case, then the last three terms of Equation 4.1 may be neglected and $D \approx D_{MEASURED}$.

As mentioned in the introduction, the probe tip maximum surface interaction area at a D = 0 was calculated as described in Chapter 3, and found to be 6100 nm^2 corresponding to ~ 220 HSA proteins (assuming a triangular shape[73-75] and ~ 134 HSA proteins (assuming an ellipsoidal shape lying flat[67,70,71]) for a close packed monolayer. Then, the maximum force per protein on approach, F_{MAX}, at D=0 was 14 pN assuming a triangular shape and 23 pN assuming a ellipsoidal shape lying flat, much less than the expected force needed for HSA denaturation. Hence, it is expected that steric deformations of the protein have negligible contribution to the interaction force profile. All experiments were conducted in phosphate buffer saline (PBS) solution (pH = 7.4, IS = 0.01M) under the same experimental conditions described in Chapter 3. As mentioned in the introduction, it is known that the K^+ and Na^+ cations in PBS do not form complexes with PEO in aqueous salt solution, and hence, the chain can be assumed to be effectively neutral.

4.2.2 Control Experiments: HSA Probe Tip on a Gold Substrate.

The same exact HSA modified probe tip which was used in Chapter 3 was used for all experiments presented in this chapter, on the same day of experimentation. In Chapter 3, the nanoscale intermolecular forces between a 65 nm radius probe tip covalently grafted with HSA and a polycrystalline gold substrate in PBS (IS=0.01M, pH7.4) were reported, the results of which are also employed in this chapter. Preparation and characterization of the

HSA probe tip and gold substrates, as well as detailed description of the analysis of the experimental results was given in the previous chapter. To summarize the relevant results for the readers' convenience, it was found that the HSA probe tip exhibited a purely repulsive, nonlinear force on approach to the Au substrate which, based on DLVO theoretical models, [126,127] is believed to be predominantly electrostatic in nature. It was determined that the HSA probe tip possessed an net negative charge of $-0.0064 C/m^2$ within an interaction area of $3100\ nm^2$ and that the Au substrate possessed a net negative charge of $-0.014\ C/m^2$ (possibly due to adsorbed anions). On retraction, the HSA and Au interaction became attractive, and average forces and distances of adhesion at the point of tip-sample separation were $<F_{adhesion}> = 1.35 \pm 0.19$ nN, $<F_{adhesion}>/R_{TIP} = 21 \pm 2.9$ nN (where R_{TIP} is the radius of curvature of the probe tip), and $<D_{adhesion}> = 22.5 \pm 6.3$ nm (n = 46 datapoints).

4.2.3 End-Grafting and Characterization of Poly(ethylene oxide) to Gold Substrates.

Linear PEO50K-SH, custom synthesized by Polymersource, Inc. (lot #P2415-EOSH), was covalently end-grafted to polygranular Au, and characterized by atomic force microscopy as described in Section 2.2.4. For the substrate, a maximum interaction area of $9{,}500\ nm^2$ was calculated as described in Chapter 3, corresponding to ~ 2.5 PEO chains under the probe tip.

4.3 Results on Approach

Figure 4.3 displays the average Force/Radius (mN/m) versus Distance, D (nm) approach curves for an HSA probe tip versus PEO end-grafted on Au (denoted "PEO-Au" and graphically represented by black diamond symbols) compared to Au (represented by red squares) and CH_3-terminated and COO^--terminated alkanethiol SAM surfaces (represented by blue triangles and green circles, respectively) in PBS solution, as well as the corresponding standard deviations. Nonlinear, purely repulsive forces were observed to begin at $D < 30$ nm, reaching a maximum magnitude at $D = 0$ of Force/Radius ~ 6.6 mN/m, with no attractive jump-to-contact.

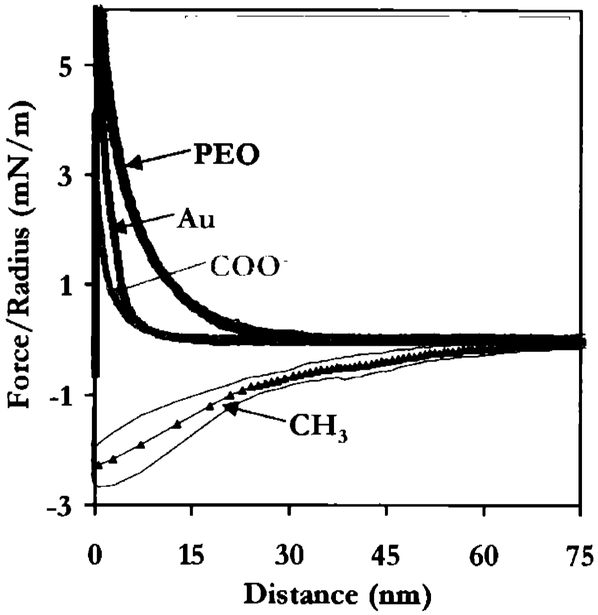

Figure 4.3 Average Force (nN) and Force/Radius (mN/m) versus Distance, D (nm) approach curves for an HSA probe tip on Au-PEO$_{50K}$ (black diamonds), bare gold (red squares), a CH$_3$–terminated SAM (blue triangles), and a COO$^-$–terminated SAM (green circles), surfaces in PBS solution (I = 0.01M, pH = 7.4), as well as standard deviations.

Figures 4.4 (A) and (B) show two individual approach and retract curve pairs for the HSA probe tip versus PEO-Au substrate showing nonhysteretic (observed in 20% of the force curves taken) and minimally hysteretic (observed in 54% of the force curves taken) behavior on retract, respectively, indicating minimal interaction of the PEO chain with the underlying Au substrate.

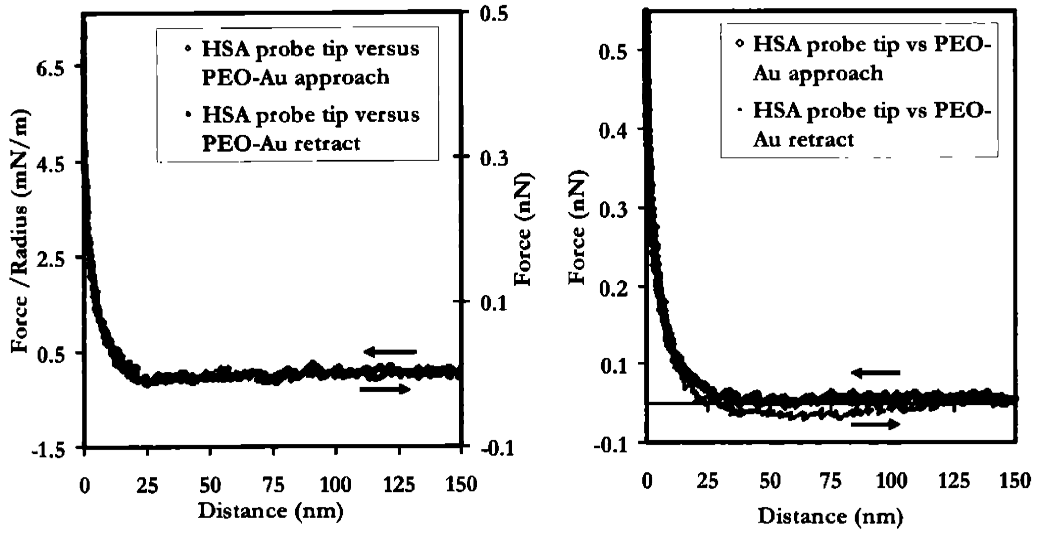

Figure 4.4 Individual HSA versus PEO force curves showing (**A**) nonhysteretic and (**B**) slightly hysteretic repulsion between the approach (i.e. loading, open diamonds) and retract (i.e. unloading, closed diamonds) curves.

As a first order approximation, additivity is assumed so that this measured net interaction is a linear superposition of the HSA probe tip interaction with the underlying Au substrate plus that of the PEO chain(s):

$$F(D)_{HSA/PEO-AU} = F(D)_{HSA/AU} + F(D)_{HSA/PEO} \qquad \textbf{Equation 4.2}$$

To isolate the HSA versus PEO interaction, 94% of the magnitude of HSA versus Au curve (Figure 4.3, red square symbols) (i.e. the average percentage of the PEO-grafted substrate that is not covered by PEO) was subtracted from the HSA versus PEO-Au (Figure 4.3, black diamond symbols) yielding the curve shown in Figure 4.5 (black diamond symbols). Here, we see that the HSA versus PEO force curve also shows a nonlinear, purely repulsive force beginning at $D < 30$ nm but also exhibits a local maximum (force barrier) at $D = 3.6$ nm corresponding to 2.1 mN/m and 0.14 nN, after which the force decreases with decreasing separation distance to 1.5 mN/m and 0.09 nN at $D = 0$ (i.e. the constant compliance regime). Interestingly, the range of this force is significantly greater than $<R_F>$. As mentioned in the introduction, the net HSA versus PEO interaction on approach may have multiple components including electrostatic counterion double layer, steric, van der Waals, hydration, and hydrodynamic lubrication forces. Figure 4.5 compares this experimental data for the HSA probe tip versus PEO chain(s) to a variety of theoretical curves showing the magnitudes, range, and form of these possible force constituents. Each one of these theoretical curves was calculated based on known parameters and will be described in detail following. It is instructive to note that the presence of a local maximum, or force barrier, at D ~ 4 nm when the Au interaction is subtracted from the PEO curve, was observed to occur using an unmodified Si_3N_4 probe tip as well, indicating that this phenomenon is not directly related to HSA-PEO intermolecular interactions, but rather an intimate property of the polymer under compression.

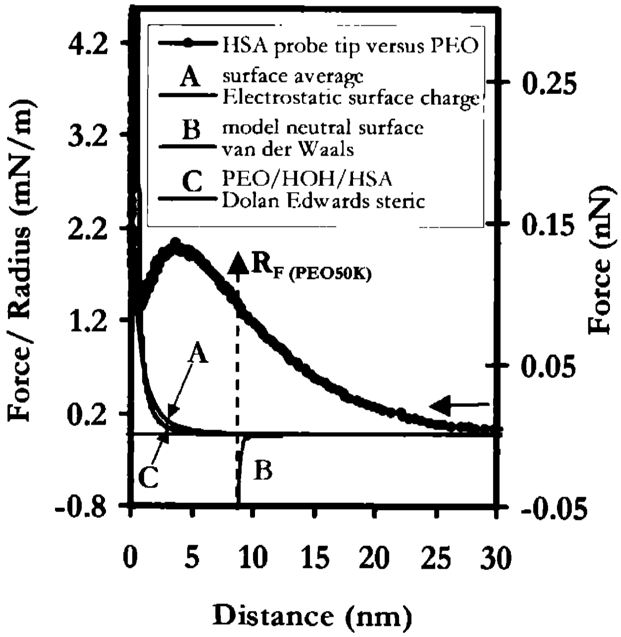

Figure 4.5 Averaged Force (nN) and Force/Radius (mN/m) versus Distance, D (nm) of an HSA probe tip on approach to a PEO_{50K} substrate in PBS solution, for which 94% of the averaged approach curve of HSA vs bare Au surface has been subtracted so that the curve represents only HSA-PEO interactions. The experimental data is compared to (**A**) a constant surface charge model[130] between an impermeable, hemispherical HSA-grafted probe tip of radius 65 nm and constant surface charge $\sigma_{TIP} = -0.018$ C/m^2, and a neutral, flat PEO surface in which $A = 6.92 \times 10^{-20}$ (red line); (**B**) the van der Waals attractive force between a PEO mushroom and an HSA-grafted probe tip in an aqueous medium (green line); and (**C**) the Dolan-Edwards model for steric repulsion at short distances[54] between an incompressible probe tip of radius 65nm and a PEO mushroom of $R_g = 8.7$ nm, $L_{contour} = 393$ nm, segment length a = 0.19 nm, and a mean area per PEO molecule of $\sigma = 3844$ nm^2 (purple line).

4.3.1 Electrostatic Counterion Double Layer Forces.

The electrostatic component of the force was modeled using a constant surface charge approximation based on the numerical solution to the nonlinear Poisson-Boltzmann (PB) equation including divalent ions[129-131] in which the PEO substrate is assumed to have neutral charge (σ_{PLANE}(PEO) = 0 C/m^2) and the HSA probe tip is modeled as an impermeable hemisphere of radius $R_{HEMISPHERE}$, also with constant charge per unit area, (σ_{TIP}(HSA) = -0.0064 C/m^2 determined from previous experiments (see Section 3.3.1). The force was obtained from the electrostatic potential, Φ, using the so-called free energy method[129,132,133] and surface element integration (SEI). [134] In the theoretical datafits, the electrical interaction Debye length, κ^{-1}, was set to its known value for IS = 0.01 M (κ^{-1} = 2.96 nm), $R_{HEMISPHERE}$ was fixed to the known value of R_{TIP} measured by SEM ($\approx$ 65 nm), and there were no fitting parameters. Figure 4.5(A) (red line) shows a relatively small, purely repulsive force is predicted even though the surface charge per unit area of the substrate has been set to zero since the tip and substrates are large compared to the Debye length and they are impermeable to ions. [118]

4.3.2 van der Waals Interactions.

The van der Waals interaction between the hydrated PEO mushroom layer on the surface and the HSA layer on the probe tip was calculated using the inverse square power law, derived using the "Derjaguin approximation" (which is valid for D << R): [117]

$$F_{VDW}(D) = -\frac{A R}{6D^2} \qquad \textbf{Equation 4.3}$$

where F_{VDW} is the van der Waals force between a sphere of radius R (assumed to be equal to the probe tip radius, R_{TIP}) and a planar surface separated by a distance D, and A is the nonretarded Hamaker constant, which was fixed. F_{VDW}(D) is plotted in Figure 4.5 (B) (green line). An approximate expression for the non-retarded Hamaker constant, A_{132}, between two macroscopic media 1 (hydrated PEO mushroom layer) and 2 (HSA layer) interacting across medium 3 (HOH) is given by the Lifshitz continuum theory[141] which, for bare surfaces, are known to correlate with experimentally measured van der Waals adhesion energies at separation distances of 0.5 nm: [173]

$$A_{132} \approx \frac{3k_BT}{4}\frac{(\varepsilon_1-\varepsilon_3)}{(\varepsilon_1+\varepsilon_3)}\frac{(\varepsilon_1-\varepsilon_2)}{(\varepsilon_1+\varepsilon_2)}+\frac{3h\nu_e}{8\sqrt{2}}*\frac{(\eta_1^2-\eta_3^2)(\eta_2^2-\eta_3^2)}{(\eta_1^2+\eta_3^2)^{1/2}(\eta_2^2+\eta_3^2)^{1/2}\left[(\eta_1^2+\eta_3^2)^{1/2}+(\eta_2^2+\eta_3^2)^{1/2}\right]}$$

Equation 4.4

where ε is the dielectric constant, η is the refractive index, h is Planck's constant = $6.626\text{x}10^{-34}$ J·s, and ν_e is the electronic absorption frequency in the UV = $3\text{x}10^{15}\text{s}^{-1}$. [141] The dielectric constant and refractive index of the uncompressed, hydrated polymer mushroom layer was calculated using: [18]

$$\begin{aligned}\eta_1 &= \phi_{\mathrm{PEO}}\eta_{\mathrm{PEO}} + \phi_{\mathrm{HOH}}\eta_{\mathrm{HOH}}\\ \varepsilon_1 &= \phi_{\mathrm{PEO}}\varepsilon_{\mathrm{PEO}} + \phi_{\mathrm{HOH}}\varepsilon_{\mathrm{HOH}}\\ \phi_{\mathrm{PEO}} &+ \phi_{\mathrm{HOH}} = 1\end{aligned}$$

Equation 4.5

where $\phi_{PEO} = 3.5$, $\phi_{HOH} = 80$, $\eta_{PEO} = 1.45$, and $\eta_{HOH} = 1.33$. The average volume fractions of PEO and HOH were calculated from the PEO chain grafting density, Γ = 0.00026 chains/nm^2, and the density of PEO in the solid state, $\rho_{PEO} = 1.2$ g/cm^3, yielding, $\phi_{PEO} = 0.00199$. η_1 was calculated to be 1.33 and ε_1 to be 79.85 from Equation 4.7, both dominated by water due to the low chain grafting density. For the HSA layer on the probe tip, η_2 was taken to be 1.47[174] and ε_2 to be 2.5. [175] Using these values, A_{132} was calculated to be $1.26\text{x}10^{-22}$ J and the outer van der Waals plane was assumed to be equal to R_F. As shown in Figure 4.5 (B) (green line), a relatively weak attractive force is predicted which would lead to a jump-to-contact at the top of the polymer mushroom layer. It should be noted PEO is predicted to have the lowest van der Waals interaction when compared to other common water-soluble synthetic polymers. [17] This result is qualitative at best due to the assumptions of constant dielectric constant throughout the PEO and HSA layers, a constant PEO segment density profile which exhibits a sharp cutoff at the equilibrium mushroom height, and underlying substrate surface roughness, all of which result in an overestimation of the van der Waals force. [27] Such an attractive jump-to-contact has been observed previously for high-grafting density poly(L-glutamic acid) brushes measured via the SFA, [176]but was most likely too small to be observed here experimentally. It should be noted that a finite attraction is theoretically predicted at contact (rather than the infinite attraction for uniform dielectric layers described by the Lifshitz theory), because the dielectric properties of the diffuse outer layers of the polymer layer at the surface decay to those of water at the outer edge. [177]

4.3.3 Steric Interactions.

Figure 4.5 (C) (purple line) shows the Dolan-Edwards theory for the repulsive interaction between a rigid, planar surface and a dilute layer of end-grafted, noninteracting mushrooms on an opposing planar surface. [54] This theory is based on the configurational entropy loss of ideal random flight (flexible) polymer chains, and the force in a good solvent can be solved analytically and converted to the appropriate geometry for these experiments via the Derjaguin approximation (valid for $D \ll R_{TIP}$):

$$F = 2\pi R_{TIP} \Gamma k_B T \left[\frac{\pi^2 \langle R_F \rangle^2}{6D^2} + \ln D \left(\frac{3}{8\pi \langle R_F \rangle^2} \right)^{1/2} \right], D < 1.73 \langle R_F \rangle \quad \textbf{Equation 4.6}$$

This theory takes excluded volume interactions into account indirectly through $\langle R_F \rangle$.

4.3.4 Hydration or Structural Forces.

A very short range (< 4 nm) monotonic, exponentially repulsive force has been observed experimentally between a variety of different smooth, hydrophilic, charged surfaces in electrolyte solutions of intermediate and high ionic strength. [141] The origin of this force has been quite controversial and is generally attributed to the displacement of hydrated, adsorbed surface counterions and is due to the energy needed to dehydrate the bound counterions, which retain some of their water of hydration on binding. Presumably, this force is highly sensitive to and will decrease with increasing surface roughness. As mentioned in the introduction, HSA is known to have a 0.55 nm thick monolayer of closely associated water molecules on its surface, with most (98%) oriented with their H atoms pointed towards the protein surface. The next layer of water is about 30% oriented creating a "fuzzy" hydrated interphase in aqueous solution. [67]

4.4 Results on Retract

4.4.1 General Description of Force Curves.

Figure 4.6 plots typical individual Force (nN) and Force/Radius (mN/m) versus Distance, D (nm), approach and retract curves for an HSA probe tip versus a PEO-Au surface in PBS solution. Retraction of the probe tip away from the surface almost always yielded a nonhysteretic interaction profile for D < 30 nm, indicating minimal interaction of the PEO chain with the underlying Au substrate and near-complete elimination of short-range surface adhesion (1% of the data exhibited surface adhesion). Curves similar to Figure 4.6 (A) were observed in 20% of the force spectroscopy experiments, while those similar to Figure 4.6(B) were observed in 24% of the force spectroscopy experiments, those shown in (C) were observed in 2% of the force spectroscopy experiments, and those in (D) were observed in 54% of the force spectroscopy experiments (a total of n = 318 force curves were taken). Figure 4.6(B) shows an individual, long-ranged attractive peak in which the magnitude of the force increases nonlinearly with distance. This peak is attributed to the stretching of an individual PEO chain that had become strongly physically adsorbed to the HSA probe tip on approach and bridges the substrate and tip. At high enough extensions, the elastic restoring force of the chain becomes equal to and just exceeds the desorption force tethering the chain segments to the tip and the tethered chain segments detach from the probe tip. Upon detachment, the cantilever exhibits a mechanical instability and is returned back to its undeflected position corresponding to zero force. The mechanical instability of the cantilever hides an unknown desorption interaction profile between the adsorbed PEO chain segments and the HSA proteins. The detachment or desorption force represents the adhesive binding interaction between an individual PEO chain and the HSA probe tip. As is shown in Figure 4.6(C), a small number of the experiments performed exhibited 2 attractive peaks, corresponding to two strongly adsorbed PEO chains. As shown in Figure 4.6(D), 54% of the total HRFS experiments exhibited a weak, long-range adhesion with a gradual detachment back to the zero force baseline rather than a distinct desorption event and cantilever instability. It is suspected that these curves represent an individual polymer bridging chain that is only weakly adsorbed to the probe tip and undergoes a small amount of extension as the tip retracts.

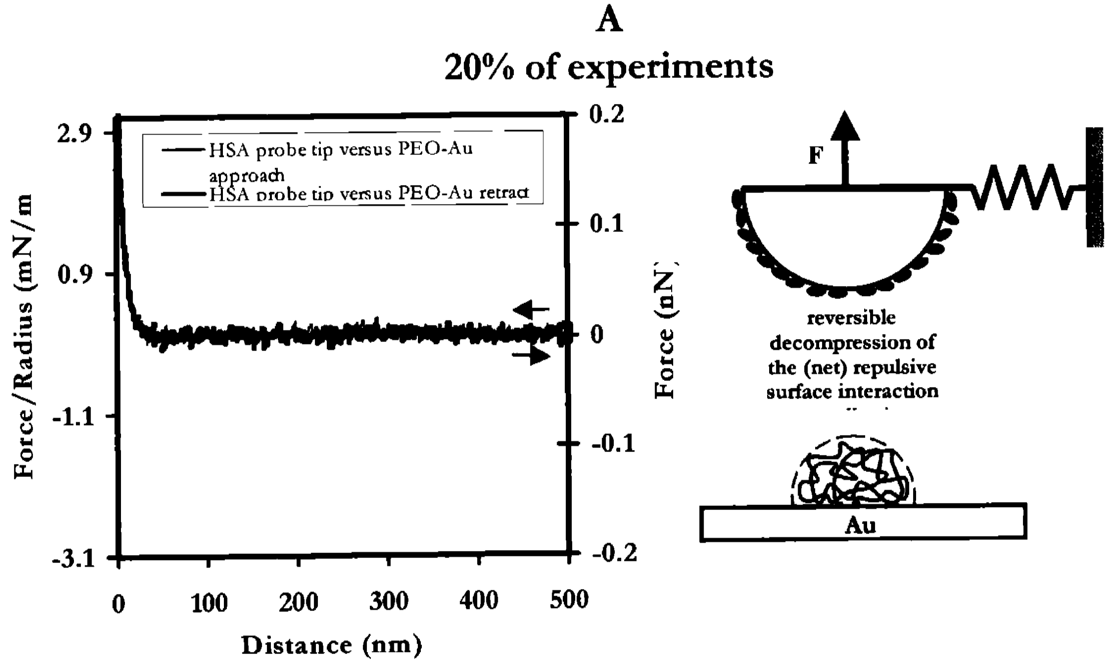

A

20% of experiments

B

24% of experiments

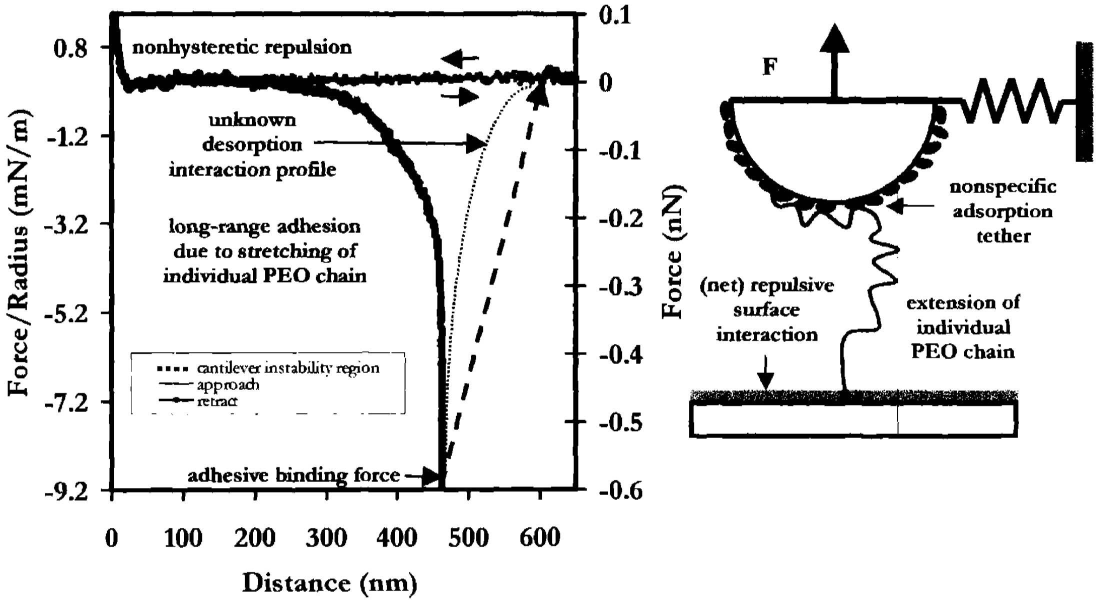

C

2% of experiments

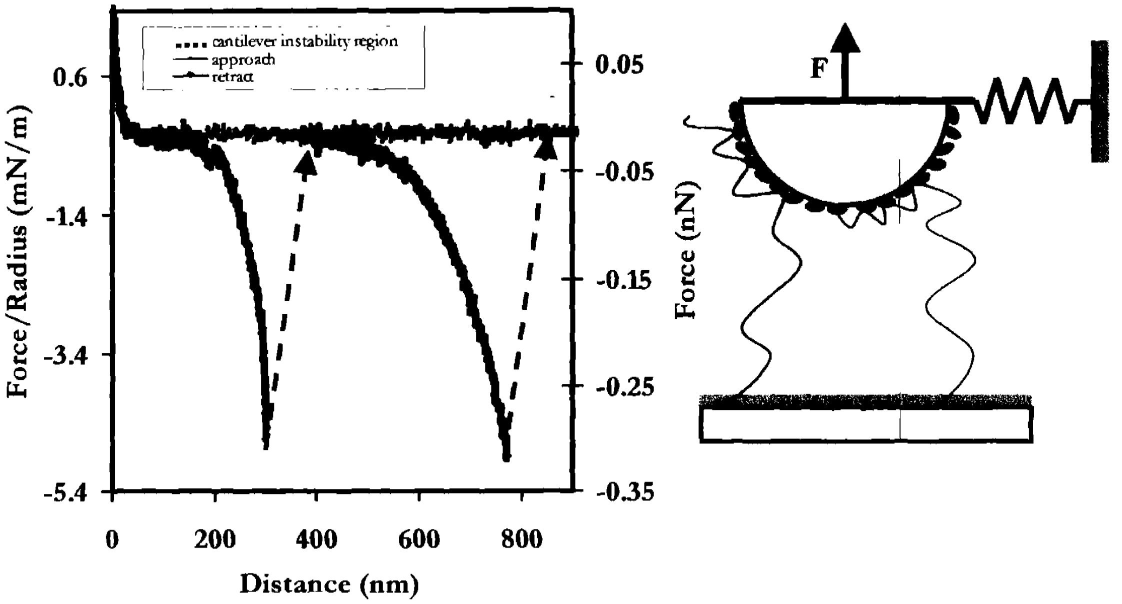

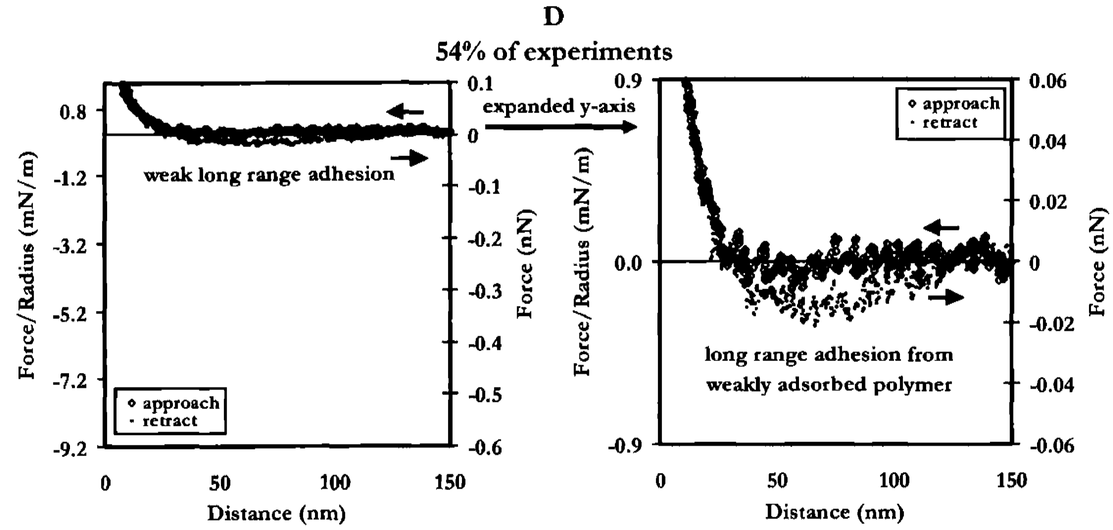

Figure 4.6 Typical individual Force (nN) (linear scale) versus Distance (nm) retraction curves of an HSA probe tip from a PEO_{50K}-grafted polygranular gold substrate in phosphate buffer solution (I = 0.01 M, pH = 7.4), and their relative frequencies of occurrence.

4.4.2 Comparison to Single Molecule Elasticity Theories.

Figure 4.7 (A) overlays multiple retraction curves from numerous force spectroscopy experiments and Figure 4.7 (B) normalizes the x-axis of these multiple experiments by the contour length of the bridging chain macromolecules in order to create a master curve which represents the molecular elasticity of the bridging chain macromolecule. [178]

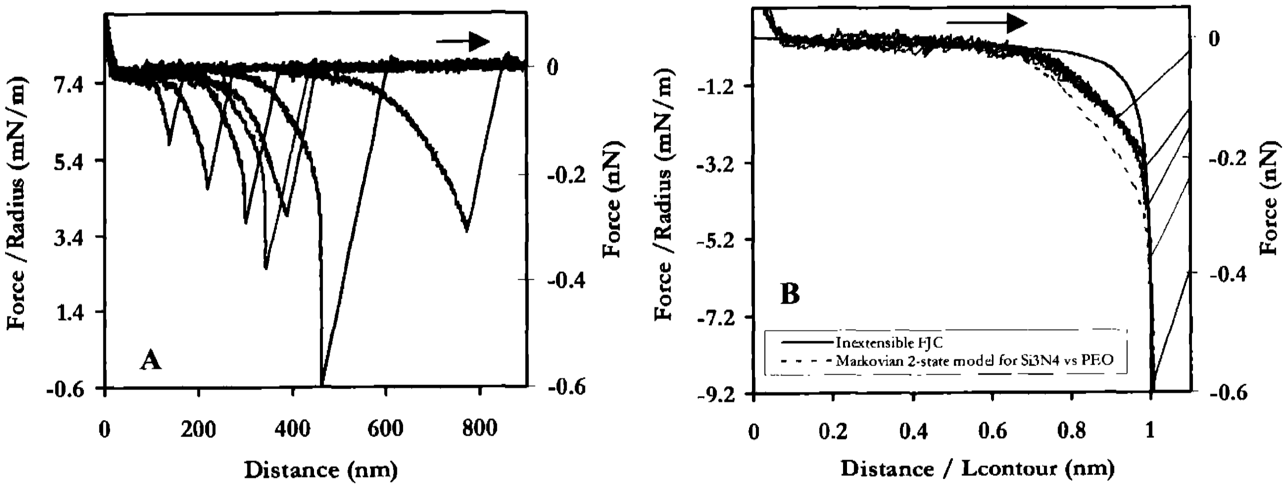

Figure 4.7 (**A**) Individual retraction curves of an HSA probe tip from a PEO_{50K}-grafted polygranular gold substrate, showing extension of individual polymer chains. The curves have been overlaid to demonstrate the distribution in $D_{adhesion}$. (**B**) The overlaid curves in a. have been normalized by $L_{contour} = 393nm$ to yield a master curve which represents the molecular elasticity of the bridging chain macromolecule. The master curve is compared with the inextensible freely jointed chain model[79] (solid red line), known to represent extension of randomly coiled macromolecules in good solvents (or otherwise ordered macromolecules such as PEO, in bad solvents), and the Markovian two-level model[43] (dashed red line), reported to represent the extension of somewhat ordered macromolecules such as PEO, in good solvents. Parameters were as follows: $\Delta G = 3 \pm 0.3$ k_BT, $L_{planar} = 0.358$ nm, $L_{helical} = 0.28 \pm 0.005$ nm, $a \sim L_{Kuhn} = 0.7$ nm, $k_s = 150N/m$.

This master curve was compared to the extensible freely-jointed chain model[84] (Figure 4.7 (B), solid red line) which is known to describe the single molecule extensional behavior of PEO in a nonpolar solvent (e.g. hexadecane) stretched by a bare Si_3N_4 probe tip (Equation 1.2): [43]

$$D(F) = L_T \coth\left(\frac{Fa}{k_BT} - \frac{k_BT}{Fa}\right)$$

where $L_T = L_{contour} + n_{FJC}F/k_s$ is the total contour length of the bridging chain which takes into account extensibility of the statistical segments, k_s = 150 N/m is the statistical segment elasticity, n_{FJC} is the number of statistical segments, a is the statistical segment length which was fixed to its known value of $\approx$ 0.7 nm, T is the absolute temperature, and k_B is Boltzmann's constant. This data was also plotted against a Markovian two-level thermodynamic model (Figure 4.7 (B), red dashed line), [94] using the parameters which are known to describe well the behavior of PEO in PBS solution with a bare Si_3N_4 probe tip. [43] This model takes in account both entropic and enthalpic contributions to elastic deformation, and it has been suggested that the additional force required to extend PEO in aqueous solution (relative to nonpolar solvents) is due to the presence of a fully reversible, strain-induced conformational transition from the water-bound, contracted trans-trans-gauche (ttg) state to the more extended trans-trans-trans (ttt) state (Equation 1.3):

$$D(F) = n_{Mar} \cdot \left(\frac{l_u}{e^{-\Delta G/k_BT}+1} + \frac{l_f}{e^{+\Delta G/k_BT}+1}\right) \cdot \left[\coth\left(\frac{F \cdot a}{k_B \cdot T}\right) - \frac{k_B \cdot T}{F \cdot a}\right] + n_{Mar} \cdot \frac{F}{k_S}$$

where l_f is the length of the contracted polymer subunit (for ttg, l_f = 0.278 nm), l_u is the length of the extended polymer subunit (for ttt, l_u = 0.358 nm), n_{Mar} is the number of extended segments (ttt), $\Delta G = 3 \pm 0.3\ k_BT$ is the Gibbs free energy difference between the ttg and ttt conformations, a = 0.7 nm is the statistical segment length, and k_S = 150 N/m is the segment elasticity. [43] The experimental data corresponding to these theoretical models, previously reported by Oesterhelt, et al., [43] was also reproduced in our laboratory (see Chapter 2). Surprisingly, it is noted that in the experiments performed here with an HSA probe tip, the magnitude of the restoring force is shifted to lower values in the intermediate strain regime (relative to that performed with a bare Si_3N_4 probe tip) and can possibly be attributed to either distortion of the local water structure around the PEO in the vicinity of the probe tip, or a restriction of the hydrogen bonding capability of PEO due to the competitive water bonding of the approaching HSA molecules.

4.4.3 HSA-PEO Adhesion.

The adhesive or binding force between the HSA probe tip and a PEO chain corresponding to curves of the type shown in Figure 4.6 (B)-(D) (79% of the total dataset) was found to be $\langle F_{adhesion}\rangle = 0.06 \pm 0.1$nN or $\langle F_{adhesion}\rangle/R_{TIP} = 0.9 \pm 1.6$ mN/m, corresponding to a distance of $\langle D_{adhesion}\rangle = 131.9 \pm 120.1$ nm. For data which exhibited weak adhesion (Figure 4.6(D)), $F_{adhesion}$ was recorded as the maximum adhesive force observed on retraction, and $D_{adhesion}$ was recorded as the distance corresponding to $F_{adhesion}$. This dataset clearly demonstrates the formation of attractive contacts between the HSA and PEO, presumably dominated by hydrogen bonds between protonated basic groups of the HSA and the -O- groups of the PEO, as well as van der Waals and hydrophobic interactions. Since $F_{adhesion}$ was found to always be less than the predicted force necessary to cleave the weakest covalent bond (i.e., the Au-S bond; $F_{cleavage} \approx$ 2-3 nN[178]), it is assured that the PEO chain always detaches from the probe tip after each force spectroscopy experiment. For these experiments, the adhesion energy per unit area, $\langle W_{exp}\rangle$, was not calculated from the $\langle F_{adhesion}\rangle$ value using contact mechanical theories[119-121] because the hemispherical geometry does not hold for a single macromolecule desorbing from a hemispherical probe tip. The energy dissipated during the loading-unloading cycle, U_d, was determined by the molecular elasticity of the bridging chain segment and the desorption or detachment of the PEO chain segments from the HSA probe tip. The molecular elasticity contribution can be obtained via integration of Equation 1.3, and will be a function of the bridging chain segment detachment or desorption force, $F_{adhesion}$, and the corresponding detachment distance, $D_{adhesion}$. $<U_d>$(molecular elasticity) was calculated to be 1.2×10^{-18} J = 296 k_BT.

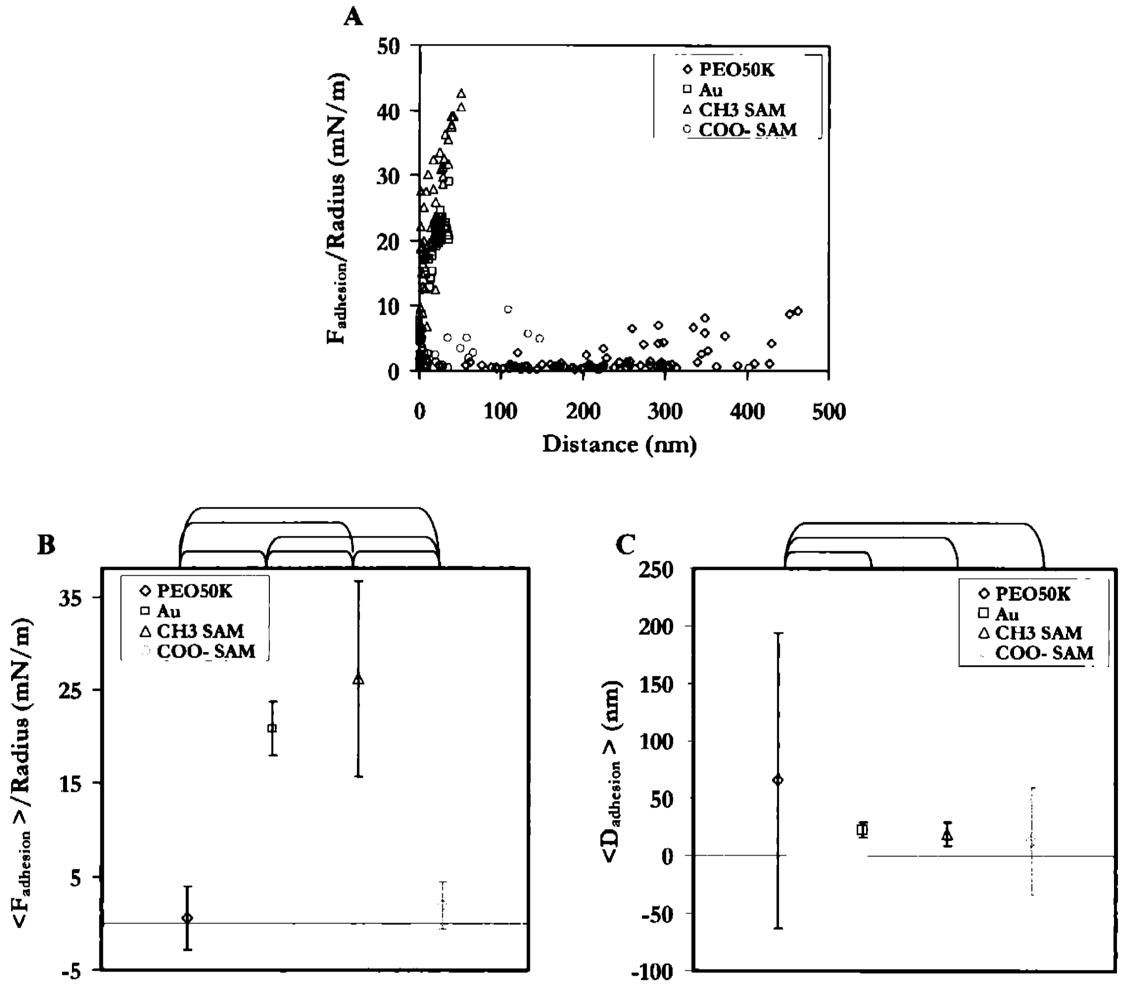

Figure 4.8 (**A**) Experimentally observed adhesion forces and distances taken from the minima in attractive peaks from individual Force (nN) (linear scale) versus Distance (nm) retraction curves; (**B**) Average forces of adhesion; and (**C**) Average distances of adhesion; of an HSA probe tip on bare gold (red squares), a CH_3–terminated hydrocarbon SAM (blue triangles), a COO^-–terminated hydrocarbon SAM (green circles), and PEO_{50K} (black diamonds). b and c also include corresponding standard deviations. Statistically different data points (as determined by the "Student's t", Section 2.2.6) are connected by brackets above.

4.4.4 Statistical Analysis of Adhesion Forces and Distances.

Figure 4.8 (A) plots the values of $F_{adhesion}/R_{TIP}$ (mN/m) versus $D_{adhesion}$ (nm) for individual HRFS experiments on retraction for the HSA probe tip versus the PEO-Au surfaces in PBS for the entire dataset, including nonadhesion values (black diamond symbols), compared to unmodified Au (red square symbols), as well as CH_3- and COO^--terminated SAM substrates (blue triangle and green circle symbols, respectively) (re: Chapter 3). Figures 4.8 (B) and (C) plot the mean and standard deviation values $<F_{adhesion}>/R_{TIP}$ (mN/m) and $<D_{adhesion}>$ (nm), and Figure 4.9 gives the probability distribution histograms corresponding to the data for PEO shown in Figure 4.8 (A). For the entire dataset, $<F_{adhesion}> = 0.05 \pm 0.09$ nN or $<F_{adhesion}>/R_{TIP} = 0.73 \pm 1.5$ mN/m, corresponding to a distance of $<D_{adhesion}> = 104.7 \pm 119.5$ nm which is ~97% less than that observed for the CH_3-terminated SAM and Au surfaces, and ~62% less than that for the COO^--terminated SAM surface data, reported in the previous chapter. As discussed in the text previously, short-range surface adhesion is completely eliminated at all locations on the PEO-Au surface. The broad distribution and large standard deviation of $<D_{adhesion}>$ on the Au-PEO surface reflect the nonspecificity of the PEO chain segment physisorption to the HSA probe tip, which causes the PEO chain to adsorb various amounts of chain segments to the probe tip, as well as the polydispersity of the polymer chains. Hence, as the adhesion mechanism varies from short-range surface adhesion to chain tethering and long-range chain extension, a drop in the adhesive force is observed, as well as a broadening of the adhesion distance distribution (Figure 4.9).

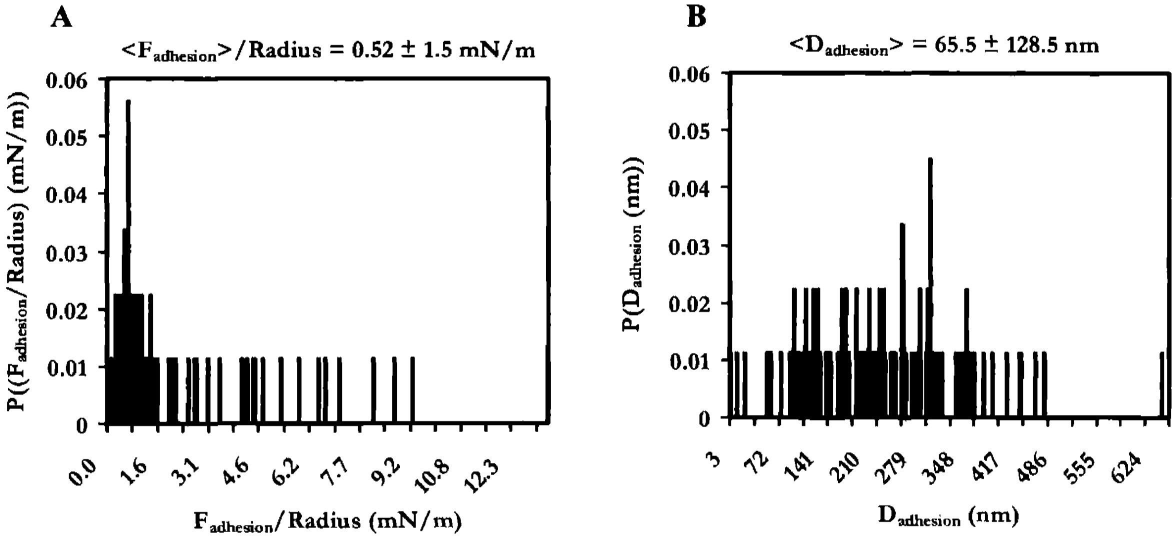

Figure 4.9 Probability distribution histograms corresponding to the experimentally observed adhesion forces (**A**) and distances (**B**) shown in Figure 4.8(A).

Figure 4.10(A) compares the frequencies of observed adhesion events (i.e. the percentage of the total number of force curves for which either surface adhesion or chain tethering and extension was observed) for HSA versus PEO-Au (black diamonds) with that of Au (red squares), as well as those of the CH_3- and COO^--terminated SAM substrates (blue triangles and green circles, respectively). It is clear that HSA exhibits significantly less adhesion events on the hydrophilic surfaces of PEO and the COO--terminated SAM than on the other two substrates, and the least affinity for adhesion is observed on the PEO-grafted substrate.

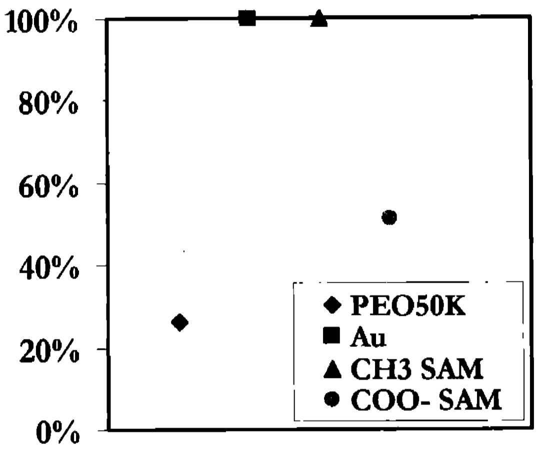

Figure 4.10 Percentage of the total number of force curves in a given data set which exhibited either surface adhesion or chain extension, for an HSA probe tip on bare gold (red squares), a CH_3–terminated hydrocarbon SAM (blue triangles), a COO^-–terminated hydrocarbon SAM (green circles), and PEO_{50K} (black diamonds).

4.5 Discussion

Prior work related to this study reported in the literature includes the measurement of forces between surfaces bearing adsorbed PEO layers using the SFA[179-185] and the AFM, [186]electrostatically anchored PEO brushes using the AFM[187] and the SFA, [29]and weakly overlapping, end-grafted low molecular weight (2K) PEG brushes using the AFM. [143] A few force spectroscopy studies have been reported involving HSA with the AFM[123,188,189] and the SFA. [76,190] The only reports, to our knowledge, on the direct measurement of protein-PEO interactions include studies between streptavidin and electrostatically anchored lipid bilayers displaying lower molecular weight PEG (1.2K-5K) chains in both the mushroom and brush regimes using the SFA. [27,169] In this study, a combined theoretical and experimental approach was employed to study the molecular origins of PEO hemocompatibility and yielded significant information on this technologically important higher molecular weight regime using a well-characterized, chemically end-grafted system. Two critical components of this work were a detailed comparison of the experimental results to: 1) HRFS experiments on Au (the "background" substrate for the PEO), and 2) quantitative predictions of various theories calculated based on known parameters.

Experimental Data on Approach. It was found that the HSA versus PEO interaction (Figure 4.3) exhibits a rather broad, nonhysteretic, nonlinear, purely repulsive net force beginning at $D < 30$ nm. The relatively low standard deviation indicates that this interaction was fairly uniform both at different locations on the sample surface and for repeated HRFS experiments at a single sample location. It is clear from this data that under these conditions and at long distances, the repulsive force constituents outweigh any attractive hydrophobic and van der Waals interactions. A comparison to the predicted theoretical force constituents including the electrostatic double layer repulsion (based on the Poisson-Boltzmann theory), steric repulsion (based on the Dolan-Edwards theory for configurational entropy), and attractive van der Waals forces (based on Lifshitz theory), is enlightening. Although it is reasonable to assume that steric forces may be present at separation distances equal to a few multiples of $<R_F>$ since the chain will statistically explore more extended configurations beyond $<R_F>$, the magnitude of the experimentally measured force is severely underestimated by any of the individual theoretical predictions or a linear summation thereof. This additional repulsive force is most likely one of the key factors in understanding the protein resistant properties of PEO. As discussed in Section 4.2.1, it is worthwhile to note, based on our AFM imaging studies of PEO and previous studies on end-grafted polymer systems, [110] that for such low density PEO mushrooms in this molecular weight range, the incompressible layer thickness of the PEO, $D_{PEO(final)}$, and hence, the offset of the $D = 0$ position, is expected to be negligible because the polymer chain compression is not highly restricted by excluded volume of neighboring chains. Even if this was not the case, the data would be shifted by $D_{PEO(final)}$ along the distance (x)-axis to the right, thus increasing the range of the interaction, and hence, this general conclusion would still be valid, and in fact, even more pronounced. The contribution of compressional deformation of the HSA (e.g. from conformational transitions, mechanical denaturation, etc.) on the probe tip to this net force has been ruled out via control experiments with both Si_3N_4 and glutaraldehyde probe tips on similar end-grafted PEO_{50K} mushroom surfaces (Figures 2.2, 2.4, and 3.4), which show a similar range and magnitude of the net repulsive force on approach, as well as by estimations of the compressive force per protein which are much less than the expected forces needed for significant distortions of the protein structure (Section 4.2.1).

Feldman, et al. [143] have reported ionic strength dependent, long-range ($D < 50$ nm), nonlinear repulsive forces on a short methoxy-oligo(ethylene glycol) (OEG) -terminated SAM on Au using the AFM (which has no steric interactions since these are solely associated with long polymer chains), and interpreted this force as originating from electrostatic double layer repulsion due to an effective surface charge imparted by a polarizable dipole layer on the surface. Additional resistance of a stable, long-range oriented water interphase layer templated by the ordered structure of the OEG-SAM on Au is also possible. Even though HSA is known to have a 0.55 nm thick monolayer of closely associated water molecules on its surface, [67] and additional translationally restricted interfacial water layers may exist, this latter mechanism seems unlikely in the PEO_{50K} system studied here, given the long range of the interaction observed, and the high macromolecular flexibility and mobility of the PEO chain. One possible explanation for this additional repulsive force, which is also supported by single molecule extensional experiments discussed in the following section, is enthalpic disruption of the compacted, water-bound ttg helical supramolecular structure of the PEO chain under compression to the extended ttt state; that is, the polymer chain extends in the x/y plane of the sample perpendicular to the direction of the applied compressive force (z). As mentioned previously, an interesting local maximum followed by a drop in the net repulsive force with decreasing separation distance was observed at $D < 4$ nm when the protein is pushed into close contact with the PEO. The source of this local maximum may be one or a combination of the following: 1) Penetration of the probe tip at apex through the polymer layer so that it may form attractive interactions (e.g. van der Waals) with the underlying Au surface; 2) additional attractive interactions, such as hydrogen bonding between the HSA and PEO; 3) rearrangement of hydration layers; and 4) polymer conformational transitions such as escape transitions. [15]

Experimental Data on Retract. Near-complete elimination of surface adhesion was observed on the PEO-grafted surface, relative to the Au and CH_3 surfaces, as evidenced by the nonhysteretic nature of the net repulsive force for $D < 30$ nm. It is interesting that this result is obtained, considering the very low grafting density and intermediate molecular weight range of the PEO. In 78% of the total HRFS experiments, a number of the PEO chain segments become physically adsorbed to the HSA probe tip on approach; this physisorption is strong enough to act as a tether and enable extension of individual PEO chains between the surface and probe tip on retract, resulting in a long range, nonlinear, adhesive interaction between the probe tip and surface. Extensive discussion of single molecule force spectroscopy (SMFS) data analysis and comparison with theory (e.g. freely-jointed chain, worm-like-chain, Markovian two-state model, etc.) has been published previously by us and others[43,178] and will not be repeated here. It is instructive, though, to consider the relevant time scales of various processes involved in particular for these experiments, which are summarized in Table 4.1. The intrinsic relaxation of a single polymer chain in dilute solution using the classic Rouse approximation of a solvent "draining" freely-jointed chain[191] can be described by a characteristic time, τ_{ROUSE}, determined by diffusion of segments over the scale of the chain length $L_{contour}$, giving:

$$\tau_{ROUSE} \approx \frac{\eta_{HOH} L_{contour}^{2} a}{k_B T} \approx 2.7 \bullet 10^{-5} \text{ s } (PEO_{50K}) \qquad \textbf{Equation 4.7}$$

where : η_{HOH} is the viscosity of the solvent (HOH) and $\eta_{HOH} / k_B T = 2.45 \times 10^{-10}$ s·nm^{-3}. The characteristic time for single polymer chain using the "non-free draining" Zimm approximation, τ_{ZIMM}, is given by: [192]

$$\tau_{ZIMM} \approx \frac{\eta_{HOH} R_F^{3}}{k_B T} \approx 1.6 \bullet 10^{-7} \text{s } (PEO_{50K}) \qquad \textbf{Equation 4.8}$$

which includes hydrodynamic effects of trapped solvent inside the coil. It has been postulated that as a polymer chain is extended it goes from a non-free draining to a free draining state because of an increase in the friction coefficient of the polymer chain.

[193,194] For either case (free draining or non-free draining), since the rate of thermal randomization ($1/\tau_{ROUSE} = 3.7x10^4\ s^{-1}$ or $1/\tau_{ZIMM} = 6.3x10^6\ s^{-1}$) is much faster than the experimental polymer extension rate ($\approx 1\ s^{-1}$), the polymer configurations are sufficiently randomized by thermal excitations and the polymer extension may thus be treated as quasielastic. [195]

Symbol	Definition	Numerical Value (s)	REF.
$\mathbf{t_{HOH}}$	time between successive Brownian collisions of a water molecule with its neighbors	10^{-12} s	-
$\mathbf{t_{amino(HSA)}}$	time scale for reorientation of amino acid side chains in HSA	10^{-10}-10^{-11} s	[196]
$\boldsymbol{\tau_{R(HSA)}}$	time scale for rotation of HSA	10^{-8}-10^{-9} s	[67]
$\boldsymbol{\tau_{ZIMM}}$ **(PEO_{50K})**	Zimm time (PEO_{50K})	10^{-7} s	[192]
$\boldsymbol{\tau_{ROUSE}}$ **(PEO_{50K})**	Rouse time (PEO_{50K})	10^{-5} s	[123]
$\mathbf{t_c}$	time scale for thermal oscillations of cantilever = inverse resonant frequency (ω') in water	10^{-3} s	measured
$\mathbf{t_{L(HSA)}}$	time scale for ligand binding to HSA	10^{-2} s	[67]
$\mathbf{t_{exp}}$	total experimental time	10^{0} s	set

Table 4.1 Time scales of molecular movement, binding, and bond rotations relevant to the experiments performed herein.

As discovered previously, [43] additional force is needed in the extension of individual PEO molecules in aqueous solution (compared to nonpolar solvents) presumably due to enthalpic disruption of the compacted, water-bound ttg helical supramolecular structure as the polymer is extended to the ttt configuration. Surprisingly, it is noted that in the experiments performed here with an HSA probe tip, the magnitude of the restoring force is shifted to slightly lower values in the intermediate strain regime (relative to that performed with an unmodified Si_3N_4 probe tip) and can possibly be attributed to distortion of the local water structure around the PEO in the vicinity of the probe tip.

The HSA versus PEO HRFS experiments discussed above clearly demonstrate that, given enough compressive force and time, short range attractive interactions between the PEO chain segments and the HSA protein surface are formed where the binding force per PEO chain is $<F_{adhesion}>= 0.06 \pm 0.1$ nN and $<F_{adhesion}>/R_{TIP} = 0.9 \pm 1.6$ mN/m. The number of proteins involved in this adhesion is unknown, but should be less than or equal to the total number of proteins (~134-220) present in the maximum interaction area at D = 0. The attractive PEO-HSA binding leads to energy dissipation as the bridging polymer chain stretches and detaches from the probe tip, and the magnitude of this energy dissipation is determined by the area under the molecular elasticity profile of the bridging polymer chain, as well as the binding strength. The presence of attractive interactions and the magnitude of the adhesion energies between HSA and PEO are consistent with the reports on adhesion between streptavidin and electrostatically anchored lipid bilayers reported previously. [27,169] This interaction may have contributions from hydrogen bonds between protonated basic groups of the HSA and the -O- groups of the PEO, and van der Waals and hydrophobic forces. To deconvolute the constituent contributions to the total net attractive HSA versus PEO binding force, further studies employing "antihydrophobic" agents in the solution, such as 2-propanol, which are substances that increase the water solubility of nonpolar molecules by acting as a bridge between the polar water and nonpolar solute, but do not affect H-bonding strength between solvated molecules, [110,197] are reported in Chapter 5. Another experiment to be discussed in Chapter 5 is the use of lipid-free HSA, which has exposed hydrophobic channels, to study the effect of lipid complexation on the adhesive binding force.

4.6 Conclusions

The net nanoscale force versus separation distance between an HSA modified probe tip and a surface of neutral, chemically end-grafted PEO_{50K} mushrooms was measured directly on approach (loading) and retract (unloading) in aqueous buffer solution (IS = 0.01M, pH = 7.4) using the technique of HRFS. On approach, a fairly broad, nonhysteretic, nonlinear, purely repulsive net force is observed to begin at $D < 30$ nm. The magnitude of this force, even under such low grafting density conditions, is much larger than that predicted by either electrostatic or steric (configurational entropy) theories, and is one of the key factors in understanding the protein resistant properties of PEO. One possible source for this "additional" force, which is also supported by single molecule extensional experiments, is enthalpic disruption of the compacted, water-bound ttg segments and helical supramolecular structure of the PEO chain under compression to the extended ttt state as the chain extends in the x/y plane of the sample perpendicular to the direction of the applied compressive force (*z*). A local maximum followed by an interesting drop in the net repulsive force with decreasing separation distance is observed at $D < 4$ nm. During approach of the HSA probe tip on the PEO surface, a number of PEO chain segments become physically adsorbed to the HSA probe tip, enough so that they are strong enough to act as a "tether" and enable extension of individual PEO chains between the surface and probe tip on retract, resulting in a long range, nonlinear, adhesive interaction between the probe tip and surface. This clearly demonstrates that, given enough compressive force and time, short range attractive interactions between the PEO chain segments and the HSA protein surface may form, where the binding force per PEO chain is $\langle F_{adhesion} \rangle / R_{TIP} = 0.9 \pm 1.6$ mN/m. This interaction may have contributions from hydrogen bonds between protonated basic groups of the HSA and the -O- groups of the PEO, and from van der Waals and hydrophobic forces.

Chapter 5

IDENTIFYING AND QUANTIFYING CONTRIBUTIONS FROM CONSTITUENT INTERMOLECULAR FORCES TO THE TOTAL INTERACTION POTENTIAL BETWEEN HUMAN SERUM ALBUMIN AND POLY(ETHYLENE OXIDE) BY VARYING SOLUTION CONDITIONS

5.1 Introduction

5.1.1 Principal Foci of Investigation

Chapter 4 presented our results from measurements of the total interaction potential between HSA and PEO in PBS (IS = 0.01 M, pH = 7.4), and compared U(D) to various theoretical and numerical models, as well as to control substrates of unmodified Au and self-assembled monolayers of hydrophobic CH_3-terminated and hydrophilic COO^--terminated alkanethiols. We observed that PEO, even at such a low surface grafting density, was capable of imparting a strong, long-ranged repulsive force to HSA, the range and magnitude of which was far greater than even a superposition of all of our numerical and theoretical models combined. The yet unanswered (though widely speculated on) question of the molecular origins of the ability of PEO to resist protein adsorption, led us to continue, and intensify, our investigations. In this Chapter, we report the manipulation of various solvent conditions such as increasing ionic strength, adding of small amounts of the antihydrophobic agent isopropanol to PBS, and conducting experiments under organic solvent conditions, in order to deconvolute U(D) in terms of the role of the aqueous environment in HSA-PEO interactions, as well as the roles of specific constituent forces such as electrostatics, hydrophobic forces, and steric interactions. In isolating and directly quantifying each of these forces, we have essentially taken the next step beyond theoretical modeling in an attempt to more thoroughly understand the fundamental molecular origins of hemocompatibility.

As was first discussed in Chapter 3, In aqueous solution at pH = 7.4 (i.e. the pH of human blood), HSA possesses a net charge of -19*e*. [72]Bound to the cantilever probe tip in the native folded conformation, however, many of the charge groups are either hidden on the side of the protein attached to the probe tip, or buried within the quaternary structure, thus lowering its overall effective charge in our experiments. Through numerical modeling, we determined[170] that the effective charge of an HSA molecule bound to a Si_3N_4 probe tip via a linker group is 1.1-1.8*e*, assuming that the proteins form a monolayer on the probe surface, and depending on whether the protein is assumed to be either ellipsoidal[56,70,71] or triangular. [73-75] Although PEO is believed to be neutral due to its inability in aqueous solution to complex the cations present in our buffer (Na^+ and K^+), [46-49] it is possible for an electrostatic double layer to form between the approaching charged HSA proteins and the surface-bound PEO mushrooms, due to the local ionic osmotic pressure and Maxwell electric stress. [50] Thus, it was of interest to us to explore the possibility of a significant electrostatic repulsive contribution to U(D). Increasing the ionic strength of the solution (by the addition of Na^+Cl^-) introduces more counterions for electrostatic charge *shielding*, thus lowering the effective charge of the two surfaces and thereby diminishing the electrostatic repulsion between them. In this way we sought to obtain an estimate of the contributions from electrostatics to U(D). It is wise to note, however, that NaCl is known to have a "salting out" effect on PEO (i.e. the effect of promoting the association of hydrocarbons and thereby decreasing their solubility in aqueous solution), and thus may be suspected to have an effect on the radius of gyration and steric repulsion due to configurational entropy as well.

The addition of as little as 0.5% (v/v) isopropanol has been shown to be effective in completely shielding hydrophobic interactions between polyamines and oligo(ethylene oxide). [110] The mechanism of this effect, illustrated in Figure 5.1, is attributed to the amphilic nature of isopropanol and its ability to facilitate solvation of hydrophobic moieties in aqueous environments. Although we have found that 100% isopropanol is a poor solvent for both PEO and HSA at room temperature,[198] we have observed no adverse effects on the solvation or conformation of either the protein or polymer in the low concentrations of the mixed solvent conditions employed here, in which the total concentration of isopropanol in PBS (v/v) does not exceed 5%. Thus, by comparing experiments performed in unadulterated PBS and those conducted under mixed solvent conditions, the hydrophobic force per protein may be estimated quite simply as the difference between the U_d values, divided by the number of proteins in the interaction area.

In short, in this study we have sought to isolate the individual constituent forces contributing to the total interaction potential, U(D), by the manipulation of solvent conditions. Our overall goal is to develop a more fundamental understanding of the molecular origins of hemocompatibility, and to utilize this knowledge in the design of novel biomaterial surfaces coatings with superior protein resistance.

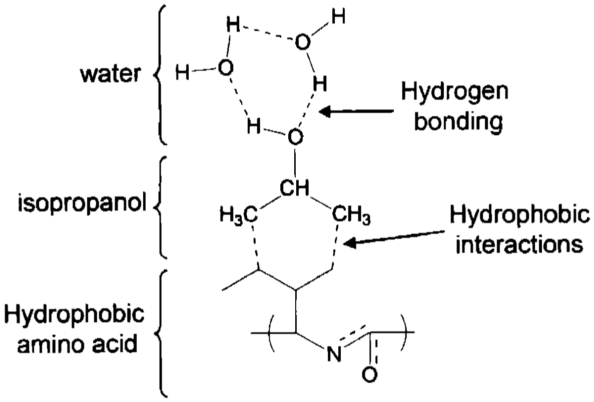

Figure 5.1 Illustration of the "antihydrophobic" mechanism of isopropanol in water.

5.1.2 Data Treatment, Analysis, and Presentation

The intermolecular forces exerted on a protein by a nearby biomaterial surface vary in type and magnitude as a function of the distance of the protein from the biomaterial surface, and in cases in which the protein is already *in contact* with the surface, such forces may also vary as a function of the time that the protein *remains* in contact if energy dissipating mechanisms are active, as well as the relative numbers of proteins and polymers present in the interaction area (Table 5.2), which are a function of the tip radius. In terms of HRFS experiments, this means that the approach and retraction curves may not necessarily correlate, and results from experiment to experiment may vary slightly in range and magnitude if the radii are not similar. For these reasons, we examine the approach and retract portions of our data separately, and then consider the total accumulation of our observations in formulating our final conclusions. Data presented in this chapter was analyzed in an analogous fashion to the methods described in Section 2.3, including the application of the Q-test and the "Student's t" test to identify statistically significant trends. It is also important to note that since our surfaces are only sparsely grafted with PEO and effectively 94% of the interaction area contains bare Au, control experiments were run for both forms of HSA on unmodified polygranular Au at each of the solvent conditions reported, and then 94% of $U_{Au,\ total}(D)$ under each of the conditions was subtracted from $U_{PEO,\ total}(D)$ under the same conditions, in order to isolate the contributions to U(D) from the

HSA/PEO intermolecular interactions (this data treatment is identical to that performed on the approach data in Chapter 4). All approach curves are reported in this way. In terms of the data on retract, the points of maximum adhesion from force curves on three different sample sites on each sample, under each experimental condition, were analyzed in a systematic statistical manner. First, each of the data sets was subjected individually to a "Q test" using a 95% confidence level[104] in order to remove statistical "outliers" from the data pool, after which each of the data sets was compared to each of the others within a given set of experiments with the same probe tip using the "Student's t", in order to determine if the data sets were statistically different from one another. [66] For example, the $<F_{adhesion}>$ values for the HSA-PEO experiment at IS = 0.01 M were compared to the $<F_{adhesion}>$ values for the HSA-PEO experiment with the same tip at each of IS = 0.15 M and IS = 1.0M, as well as the $<F_{adhesion}>$ values for the HSA-Au experiment with the same tip at IS = 0.01 M. A similar procedure was likewise performed for $<D_{adhesion}>$ and the frequencies of adhesion on Au and PEO-Au, and at each ionic strength. Again, a 95% confidence level (also often referred to as $p = 0.05$) was set as our minimum criterion for "statistically different".

Finally, the standard deviations for the adhesion frequency data were calculated by comparing average frequencies at different sample sites for each of the experimental conditions.

In general, four different types of force curves were observed among the various experiments conducted. As shown in Figure 5.2, these types are: 1) a reversible, nonhysteretic, purely repulsive approach-retract cycle (Figure 5.2(A)), a repulsive approach curve followed by an adhesive event of convex curvature occurring at very short distances, which is referred to here to as "surface adhesion" Figure 5.2(B); a repulsive approach curve followed by a relatively nonhysteric retract at short distances that later transitions to a strong adhesive event of concave curvature at long distances, which is referred to here as "protein/polymer extension" Figure 5.2(C); and a curve that shows characteristics of *both* surface adhesion and protein/polymer extension Figure 5.2(D).

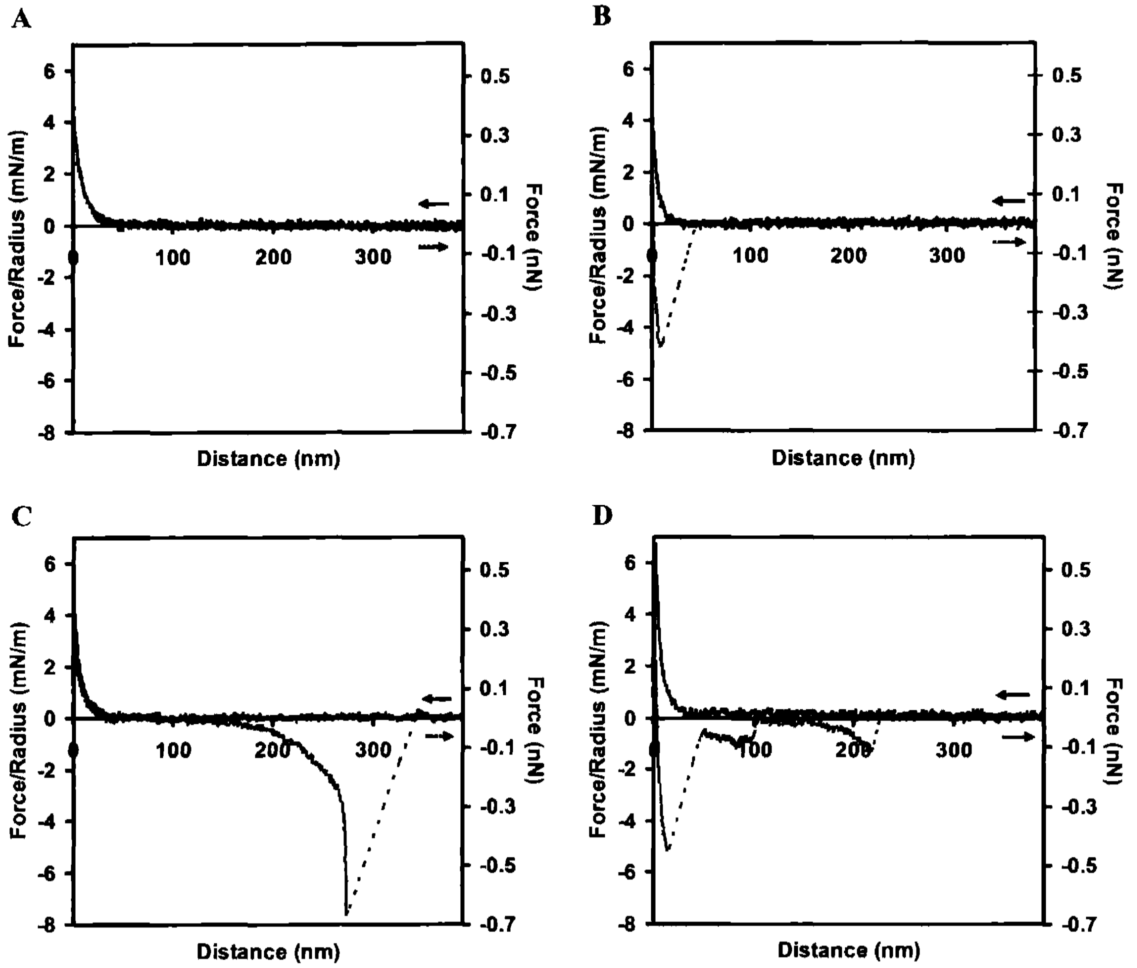

Figure 5.2 Examples of the types of force curves observed between HSA and PEO-Au: (**A**): nonhysteretic, purely repulsive approach-retract cycle; (**B**): short-ranged surface adhesion on retract; (**C**): protein/polymer extension on retract; and (**D**): both short-ranged surface adhesion and long-ranged polymer/protein extension on retract. Approach curves are shown solid lines (——), whereas retract curves are depicted by dotted lines (- - - -).

5.2 Experimental Procedures

5.2.1 Preparation of Salt and Isopropanol Solutions

PBS solutions were made using sodium phosphate buffer tablets (*Sigma* lot #59H03371) which contain 8 g/L NaCl, 0.2 g/L $K^+H_2PO_4^-$, 1.15 g/L $2Na^+{\cdot}HPO_4^{2-}$, and 0.2 g/L KCl. An ionic strength of 0.15 M is automatically obtained by dissolving 1 tablet in 200 mL DI H_2O.

Solutions with an ionic strength of 0.01M were prepared by dilution of a 16.66 mL aliquot from the IS = 0.15 M stock solution to 250 mL, using DI H_2O. Dilution did not have any effect on the efficacy of the buffer (i.e. the pH of the diluted buffer solutions remained stable). Solutions with an ionic strength of 1.0 M were prepared by addition of 1.242g (0.0212mol) NaCl (Mallinckrodt, product #7581) to 25mL of IS = 0.15M PBS. The same PBS stock solution was used for preparation of all solutions for the ionic strength experiment. All water used for solutions, rinsing, and storage was first deionized (18 MΩ·cm resistivity, Purelab Plus UV/UF, US Filter, Lowell, MA), then filtered through Millipore syringe filters (pore size = 0.22μm) prior to use. Isopropanol was purchased from Mallinckrodt (product # H604), and added to aliquots from a PBS stock solution (IS = 0.01 M) to prepare the 0.5% and 5% (v/v) mixed solvent solutions. The same PBS stock solution was used for all isopropanol experiments.

5.2.2 Probe Tip and Au Surface Modification

Au wafers were purchased from Asylum Research (model #Gold200C) in the form of a 20 nm thick layer of polygranular gold on unpatterned glass microscope slides. Linear PEO_{50K}-SH, M_n = 48,320 g/mol, M_w = 51,700 g/mol, PDI = 1.07 (as determined by GPC in tetrahydrofuran using monodisperse poly(ethylene glycol) standards) was custom synthesized by *Polymersource, Inc.* (lot #P2415-EOSH). Calculation of the Flory radius (or radius of gyration) and the extended contour length in aqueous solution was presented previously[199] and found to be R_F = 8.7 nm and $L_{contour}$ = 393 nm, respectively. PEO_{50K}-SH was chemisorbed to 1 cm^2 gold wafers as described in Section 4.2.3.

HSA was covalently attached to Si_3N_4 cantilever probe tips using the method described by Vansteenkiste, et al., [123] and reported here in Section 3.2.2.

5.2.3 HRFS Experiments

All HRFS experiments were conducted using the Molecular Force Probe® (Asylum Research, Santa Barbara, CA) to measure force, F (nN), versus tip-sample separation distance, D (nm) (henceforth referred to and labeled on graphs as "Distance") on "approach" (i.e. probe tip advancing towards surface) and "retract" (i.e. probe tip moving away from surface). A full description of this instrument, its limits of force and displacement detection in fluids, procedures for spring constant calibration and conversion of raw data, details of measurement errors, and description of typical force versus distance curves including the mechanical instabilities of the cantilever, are given in Section 2.2.1, and in Appendix A.1., as well in our previous works. [110,130,170]

Two separate probe tips were employed for the experiments reported here; one probe tip was used in all experiments involving isopropanol, while another probe tip was used for all ionic strength experiments. The radii of the chemically modified probe tips were determined for each individual cantilever by scanning electron microscopy (SEM) (JEOL 6320FV Field-Emission High-resolution SEM, operating voltage = 1 kV, magnitude = 200,000x) where R_{TIP} was determined by drawing two intersecting straight lines tangential to the sides of the probe tip and then drawing a circle tangential to both of them. R_{TIP} for the fatty acid-bound HSA probe tip was found to be ~ 45 nm. R_{TIP} for the fatty acid-free HSA probe tip was found to be ~ 75 nm.

The maximum surface interaction areas on the probe tip and on the substrate at a D = 0 were calculated as previously (Section 3.2.4) for each of the probe tips, and are reported along with the number of HSA and PEO molecules within these interaction areas and the maximum compressive force per protein, in Table 5.2. As discussed in Section 4.2.1, it is expected that steric deformations of the protein have negligible contribution to the interaction force profile. All experiments were conducted at room temperature (23°C), at a scan rate of 1 μm/s, using a pulling distance of 1 μm and a data collection rate of 5,000 points per second. On changing solutions during the course of the experiments reported here, the probe tips and substrates were allowed to soak in next solution to be tested for a full 24 hours before testing was performed, in order to allow the molecular conformations and bound ions to equilibrate. The force versus distance curves on approach from at least three different sites on the sample surface were averaged (minimum of 20 curves per site) and the standard deviations were calculated and reported. Upon retraction, the full force versus distance curves were not averaged because of the large adhesion force and distance distributions inherent in the nonspecific adhesion events, which would smooth out many characteristic features of the curve. Rather, statistical analysis of the maximum forces and distances of adhesion under each of the experimental conditions was performed. The normalized Force/Radius (mN/m) values are reported along with the unnormalized Force (nN) on a double y-axis for all experimental data presented.

Parameter / Experiment →	Varying % (v/v) Isopropanol in PBS	Varying Ionic Strength
R_{tip} (nm)	45	88
A_{tip} (nm^2)	5,700	11,000
# HSA molecules (ellipsoidal) in A_{tip}	120	240
# HSA molecules (triangular) in A_{tip}	200	400
Maximum applied force (nN)	3	3
Maximum applied force per HSA molecule (ellipsoidal) (nN)	0.025	0.013
Maximum applied force per HSA molecule (triangular) (nN)	0.015	0.0075
$A_{substrate}$ (nm^2)	6,300	17,000
# Polymers in $A_{substrate}$	1.6	4.4

Table 5.1 Force and areal experimental parameters.

5.3 Variations in Ionic Strength

5.3.1 Ionic Strength Results on Approach

Similar to our results on the HSA-PEO system (Chapter 4), on approach of the HSA-grafted probe tip to PEO, we observed a long-ranged, nonlinear repulsion beginning at D < 50 nm that continuously increased nonlinearly until reaching a local maximum at D < 4 nm, at which point the curves exhibit a short region of negative slope (in which the net intermolecular interaction is attractive) until the tip comes in to contact with the surface at D = 0, indicated by an upward transition to infinite positive slope which corresponds to the linear elastic bending of the compliant cantilever on the (relatively) nondeformable underlying Au surface. **Error! Reference source not found.** overlays the average approach curves under each of the solvent conditions. The curves are derived from averaging ~20 force curves from each of at least three different sites on each sample. In order to exclude those force curves in which polymer molecules may not have been in the interaction area, only force curves which also showed some form of polymer extension on retract were counted in the averaging data sets. The figure indicates that an increase in the ionic strength from 0.01 M to 0.15 M does not appear to affect the repulsive force on approach until D < 7 nm, at which point the repulsion at IS = 0.15 M exceeds that at 0.01 M dramatically. A further increase in the ionic strength intensifies this effect, extending the range of increased repulsion as far as D < 25 nm. The magnitude and distance at which the local maximum at D < 4 nm is reached is also markedly affected by the change in ionic strength: at IS = 0.01 M, the local maximum occurs at D = 2.9 nm and Force/Radius = 1.2 mN/m; at IS = 0.15 M the local maximum is shifted to D = 0.9 nm and Force/Radius = 2.6 mN/m; a final increase in the ionic strength to IS = 1.0 M further shifts the peak to D = 0.6 nm and Force/Radius = 2.8 nm. In effect, the range of the repulsion is continuously increased with the ionic strength. These results are rather counterintuitive in terms of electrostatic interactions, and indeed in terms of steric interactions as well. As was discussed in the introduction, an increase in the ionic strength of the solution results in a larger number of available counterions for charge shielding, and is thus expected to reduce the overall electrostatic repulsion between two like-charged surfaces. Furthermore, as NaCl has a "salting out" effect on PEO, the addition of NaCl to the system would be expected to partially collapse the PEO coil, thus reducing the magnitude of the repulsion imparted by configurational entropy. Clearly, neither of these predicted effects was observed in this experiment. It is interesting to note that this result has been repeated by us many times, [198] both with protein-bound and umodified Si_3N_4 probe tips, suggesting that PEO, rather than HSA, is responsible for the observed phenomenon. Possible sources of this additional repulsive force may be a change in the PEO coil conformation in the presence of high concentrations of NaCl, and/or a shift in the structure and density of the interstitial water layer between the PEO coils and the approach probe tip.

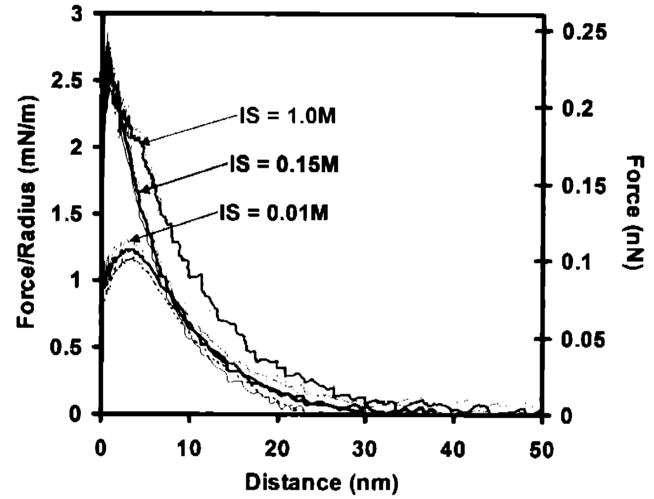

Figure 5.3 Averaged approach Force (nN) and Force/Radius (mN/m) versus Distance (nm) curves for HSA vs PEO-Au in PBS, as a function of solution ionic strength.

5.3.2 Ionic Strength Results on Retract

Figure 5.4 gives the data points of maximum adhesion for HSA on PEO at each ionic strength. Perhaps the most prominent and interesting feature of this data is the recurrence of certain distance ranges of chain extension, with the first occurring from D ~ 0-90 nm, the second stretching from D ~ 100-190 nm, and the third spanning from D ~ 200-275 nm. This phenomenon is most pronounced at IS = 0.01 M It is speculated that these modes of extension may be directly related to the unfolding of specific HSA domains. It is well known that certain "modular" proteins, with the giant muscle protein *titin* being perhaps the most studied, [85,86,89,90,95,200-202] unfold domain-by-domain during simple force spectroscopy experiments. The unfolding is likened to a string of springs in series, with the weakest one unfolding first, and the strongest one unfolding last; such force curves on retract tend to exhibit a "sawtooth" profile. What is interesting about the modes of extension observed in our experiments is that they are clearly grouped into subsets by distance, with the force of extension increasing nonlinearly with distance in each subset, and the overall shape of the force curve is very much like the sawtooth profiles reported for titin, e.g. HSA is comprised of three homologous domains, [203] each of which contains approximately equal numbers of amino acids[204] and a contour length roughly ~ 75 nm (assuming an amino acid contour length of 0.38 nm and a total protein contour length of 216 nm (Section 1.2.2)). Given that PEO is also present and capable of stretching with the HSA, it is quite likely that each of these modes, which span from 0-88nm, 100-192nm, and 198-273nm, corresponds to each of the primary domains of the protein's quaternary structure. Furthermore, it is logical that the force necessary to extend these domains to distances approaching their individual contour lengths will increase with distance, and in direct correlation with the degree of nonspecific intramolecular bonding, the locations of the protein-polymer binding sites, and the magnitudes of the various energetic barriers to bond rotation. This motif is observed at the higher ionic strengths as well, though as the ionic strength is increased, unfolding of the second and third domains becomes less common, possibly because the salt ions are effectively dehydrating the protein in their competition for H_2O complexation, and thereby decreasing its solubility and affinity for amino acid-solvent interactions relative to amino acid-amino acid interactions. A similar effect may also be at play between the PEO and H_2O molecules. Finally, which domain is extended is likely dominated by which orientation the approaching proteins are predominantly in as the probe tip comes into contact with the polymer surface. This factor is unknown to us and assumed to be random given our procedure for covalent attachment of the HSA to the probe tip.

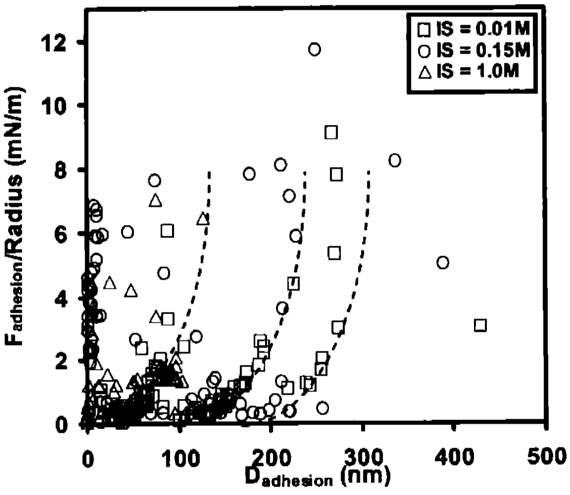

Figure 5.4 Experimental data points of the Distances (nm) and Forces/Radius (mN/m) of adhesion for HSA vs PEO at IS = 0.01M (□), IS = 0.15M (○), and IS = 1.0M (Δ). Dotted curves have been drawn to guide the eye.

The probability histograms of the forces and distances of adhesion are given in Figure 5.5. $<D_{adhesion}>$ decreases from 57.4 ± 91.3 nm at IS = 0.01 M to 28.2 ± 65.1 nm at IS = 0.15 M and 27.3 ± 39.3 nm at IS = 1.0 M, and $<F_{adhesion}>$/Radius increases from 0.62 ± 1.3 mN/m at IS = 0.01 M to 0.93 ± 2.0 mN/m at IS = 0.15 M and 0.99 ± 1.4 mN/m at IS = 1.0 M. None of the data on retract yielded a statistically significant trend as a function of ionic strength.

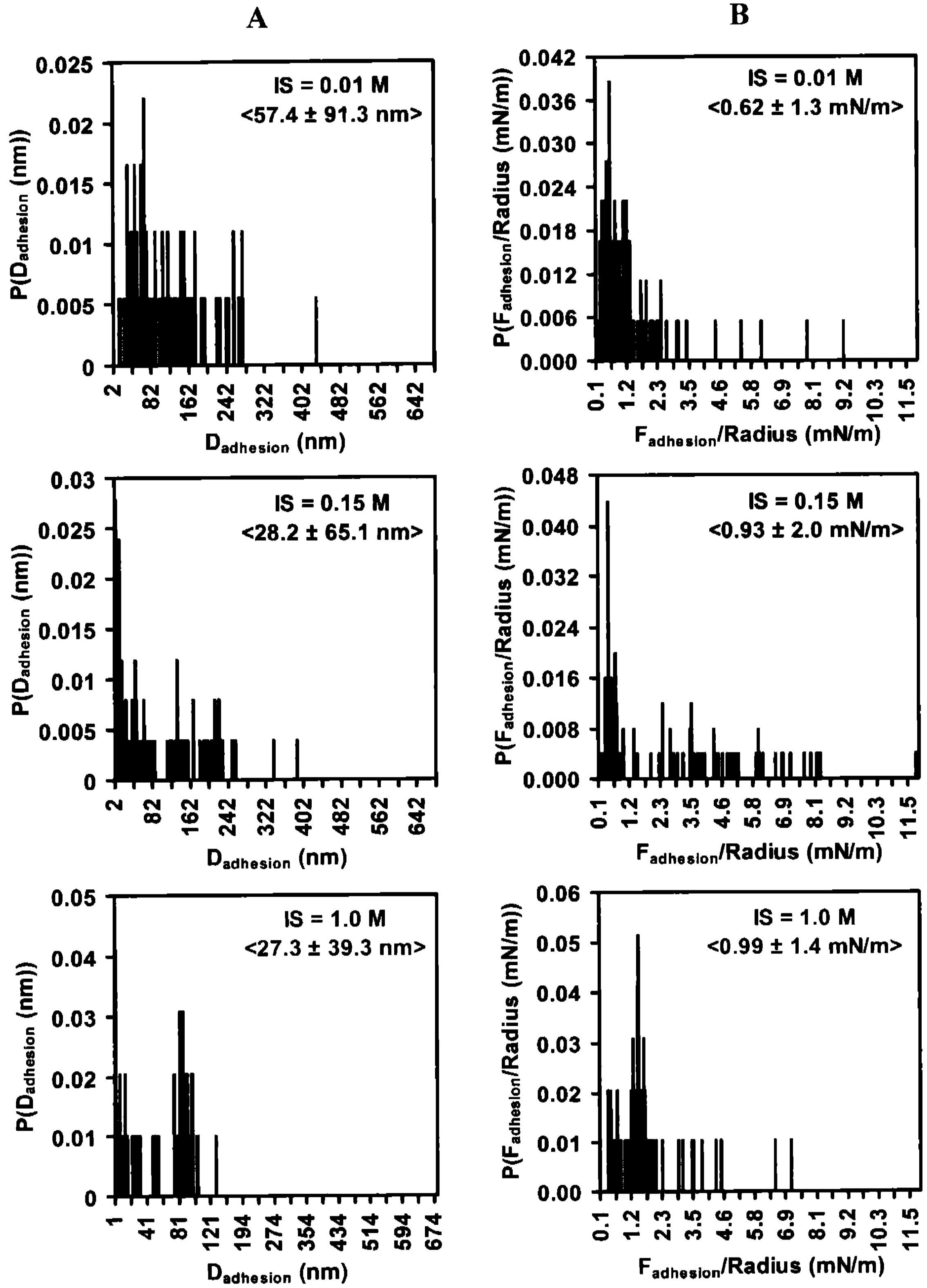
A
B
IS = 0.01 M
<57.4 ± 91.3 nm>
P(D_adhesion (nm))
D_adhesion (nm)
0 0.005 0.01 0.015 0.02 0.025
2 82 162 242 322 402 482 562 642
IS = 0.01 M
<0.62 ± 1.3 mN/m>
P(F_adhesion/Radius (mN/m))
F_adhesion/Radius (mN/m)
0.000 0.006 0.012 0.018 0.024 0.030 0.036 0.042
0.1 1.2 2.3 3.5 4.6 5.8 6.9 8.1 9.2 10.3 11.5
IS = 0.15 M
<28.2 ± 65.1 nm>
0 0.005 0.01 0.015 0.02 0.025 0.03
IS = 0.15 M
<0.93 ± 2.0 mN/m>
0.000 0.008 0.016 0.024 0.032 0.040 0.048
IS = 1.0 M
<27.3 ± 39.3 nm>
0 0.01 0.02 0.03 0.04 0.05
1 41 81 121 194 274 354 434 514 594 674
IS = 1.0 M
<0.99 ± 1.4 mN/m>
0.00 0.01 0.02 0.03 0.04 0.05 0.06

Figure 5.5 Probability distributions for the experimental data points of the (**A**) Distances (nm) and (**B**) Forces/Radius (mN/m) of adhesion for HSA vs PEO at IS = 0.01M (blue), IS = 0.15M (black), and IS = 1.0M (pink).

5.4 Addition of the Antihydrophobic Agent Isopropanol

5.4.1 Isopropanol Results on Approach

Figure 5.6 overlays the average approach curves for HSA vs PEO in IS = 0.01M PBS, 0.5% and 5.0% (v/v) isopropanol in PBS, and in 100% isopropanol. The curves are derived from averaging ~20 force curves from each of at least three different sites on each sample. In order to exclude those force curves in which polymer molecules may not have been in the interaction area, only force curves which also showed some form of polymer extension on retract were counted in the averaging data sets. HSA vs Au data has been subtracted from the HSA vs PEO-Au data to yield the curves shown below.

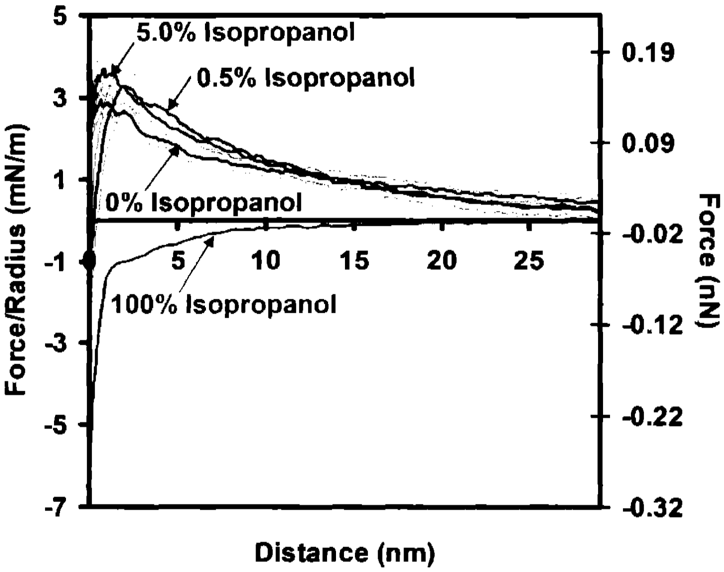

Figure 5.6 Averaged approach Force and Force/Radius versus Distance curves for lipid-bound HSA vs PEO as a function of v/v % isopropanol content in PBS.

As before, on approach of the HSA-grafted probe tip to PEO, a long-ranged, nonlinear repulsion was observed beginning at $D < 50$ nm for 0-5.0% (v/v) isopropanol in 0.01M PBS; the repulsion increases until reaching a local maximum at $D < 4$ nm, at which point a short region of negative slope (in which the net intermolecular interaction is attractive) is observed, until the tip comes in to contact with the surface at $D = 0$. In this case, the force magnitude of the local maximum at $D < 4$ nm is affected by the addition of just 0.5% (v/v) of isopropanol to PBS, while the distance is not: at 0% (v/v) isopropanol (i.e. pure PBS), the local maximum occurs at Force/R_{TIP} = 3.0 mN/m and $D = 0.6$ nm; at 0.5% (v/v) isopropanol, the local maximum is shifted to Force/ R_{TIP} = 3.3 mN/m at $D = 2.0$ nm; a final increase in the concentration of isopropanol in PBS to 5.0% further shifts the peak to Force/ R_{TIP} = 3.7 nm, at $D = 0.8$ nm. In effect, at $D < 10$ nm the magnitude of the repulsion is continuously increased as the concentration of isopropanol increases. A possible reason for this may be an increased affinity and competition for the aqueous solvent molecules, due to the enhanced solvation of the HSA imparted by isopropanol, which results in a hydrophilic-hydrophilic intersurface repulsion between the HSA and PEO. Clearly there exists a significant hydrophobic component to the total U(D) which has been revealed by the addition of isopropanol. At the local maxima of the approach curves, i.e. at $D \sim 1$ nm, this component comprises approximately 20% of the total intermolecular interaction potential. Furthermore, by integrating and subtracting the 0% Force versus Distance curve from the 0.5% Force versus Distance curve, and then dividing this work energy by the number of proteins in the probe tip interaction area (Table 5.2), we determined the hydrophobic energy to be 11 k_BT per protein (assuming a triangular protein shape), or 18 k_BT per protein (assuming an ellipsoidal shape).

In 100% isopropanol (i.e. in a purely organic solvent), the situation is markedly different from that in aqueous solution: rather than a long-ranged repulsion, the protein and polymer exhibit a long-range attraction, beginning at $D < 20$ nm. As isopropanol is a poor solvent for both HSA and PEO at room temperature and atmospheric pressure, the macromolecules have likely collapsed on their respective surfaces, and configurational entropy has been significantly reduced. It is interesting to note that such a net attractive force was not observed in 100% isopropanol on the Au control substrate, suggesting that its origin likely stems from a "solvophobic" force from the PEO. Since the HSA and PEO hydration layers and counterions have been eliminated, but they are still capable of hydrogen bonding with each other, the only intermolecular forces that remain between HSA and PEO are van der Waals interactions, and so-called solvophobic forces. Solvophobic forces may be interpreted in much the same way as hydrophobic forces, and may be similarly modeled. Figure 5.7(A) shows the HSA vs PEO approach curve in 100% isopropanol, fitted to the models for van der Waals[117] (Equation 3.7, where the Hamaker constant was used as a fitting parameter and was found to be A = 1.5x10^{-21} J) and hydrophobic interactions[141] (Equation 3.9, where the characteristic decay length λ_0 and the surface interfacial energy γ_i were used as fitting parameters and found to be λ_0 = 5 nm, and γ_i = 0.12 mJ/m^2). If we assume a linear summation of these two models in U(D)$_{total}$, the combined force fits the experimental data remarkably well, as shown in Figure 5.7(B).

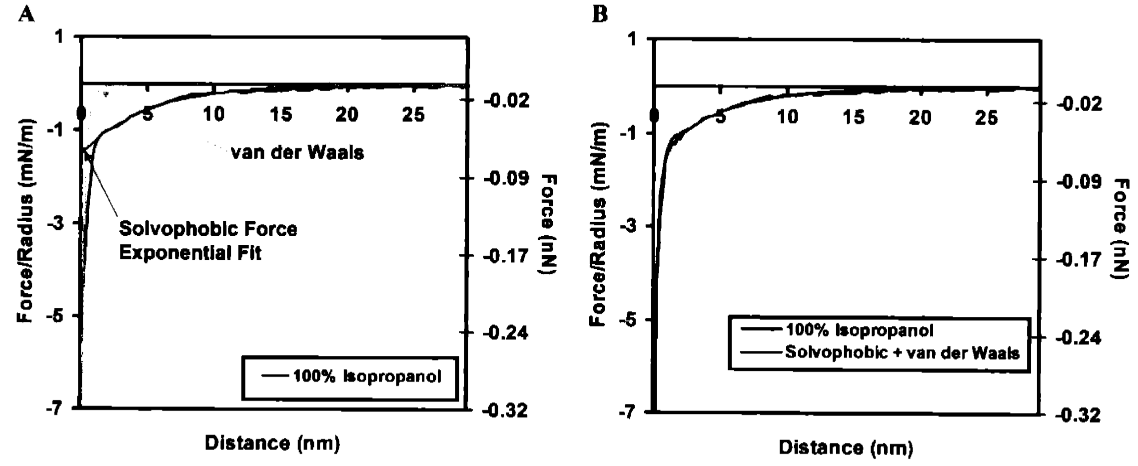

Figure 5.7 Average approach curve of HAS vs PEO in 100% Isopropanol, compared to theoretical models: (**A**) is a comparison to van der Waals[117] and solvophobic interaction[141] models; (**B**) is a comparison to a linear summation of the models shown in (A).

5.4.2 Isopropanol Results on Retract

Figure 5.8 gives the data points of maximum adhesion for HSA on PEO-Au under each concentration of isopropanol. It is clear from first glance that in the presence of mixed solvent conditions, the typical adhesion event shifted from occurring at long distances and low forces, to short distances and large forces. Similar to the results observed in the ionic strength experiments, there appears to be three distinct modes of pulling in the distances ranges 0-60 nm, 0-115 nm, 100-160 nm, and 245-315 nm, though only in 100% isopropanol is the mode of longest extension observed, most likely because the denatured tertiary structure of the HSA easily unfolds in the organic solvent, as the strong intramolecular hydrophobic interactions within the protein have been eliminated.

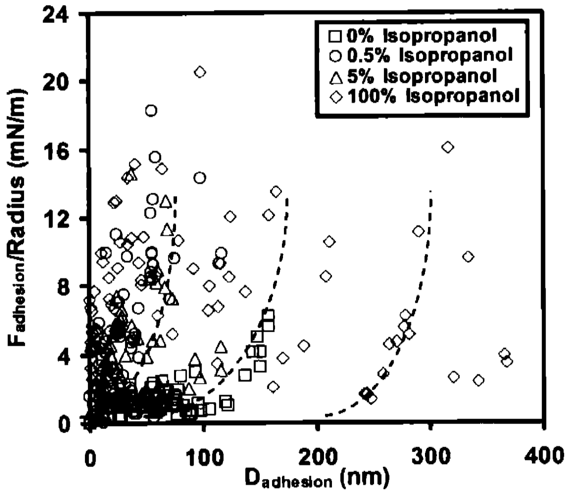

Figure 5.8 Experimental data points of the Distances (nm) and Forces/Radius (mN/m) of adhesion for HSA vs PEO at 0% (□), 0.5% (○), 5.0% (Δ), and 100% (◇) isopropanol (v/v) in PBS. Dotted lines have been drawn to guide the eye.

Figure 5.9 gives the probability distributions of the distances (A) and forces (B) of adhesion for each of the isopropanol solvent conditions. As was done with the retraction data for the experiments varying ionic strength, the adhesion data was treated with the *Q* test and the Student's t in order to analyze the statistical significance of the averages as a function of isopropanol concentration in PBS. Although trends were observed in the HSA vs PEO-Au dataset, the data was not statistically different from that observed in the HSA vs Au data, and thus no conclusions can be made as to the effect of isopropanol on the adhesive interactions between HSA and PEO on retract.

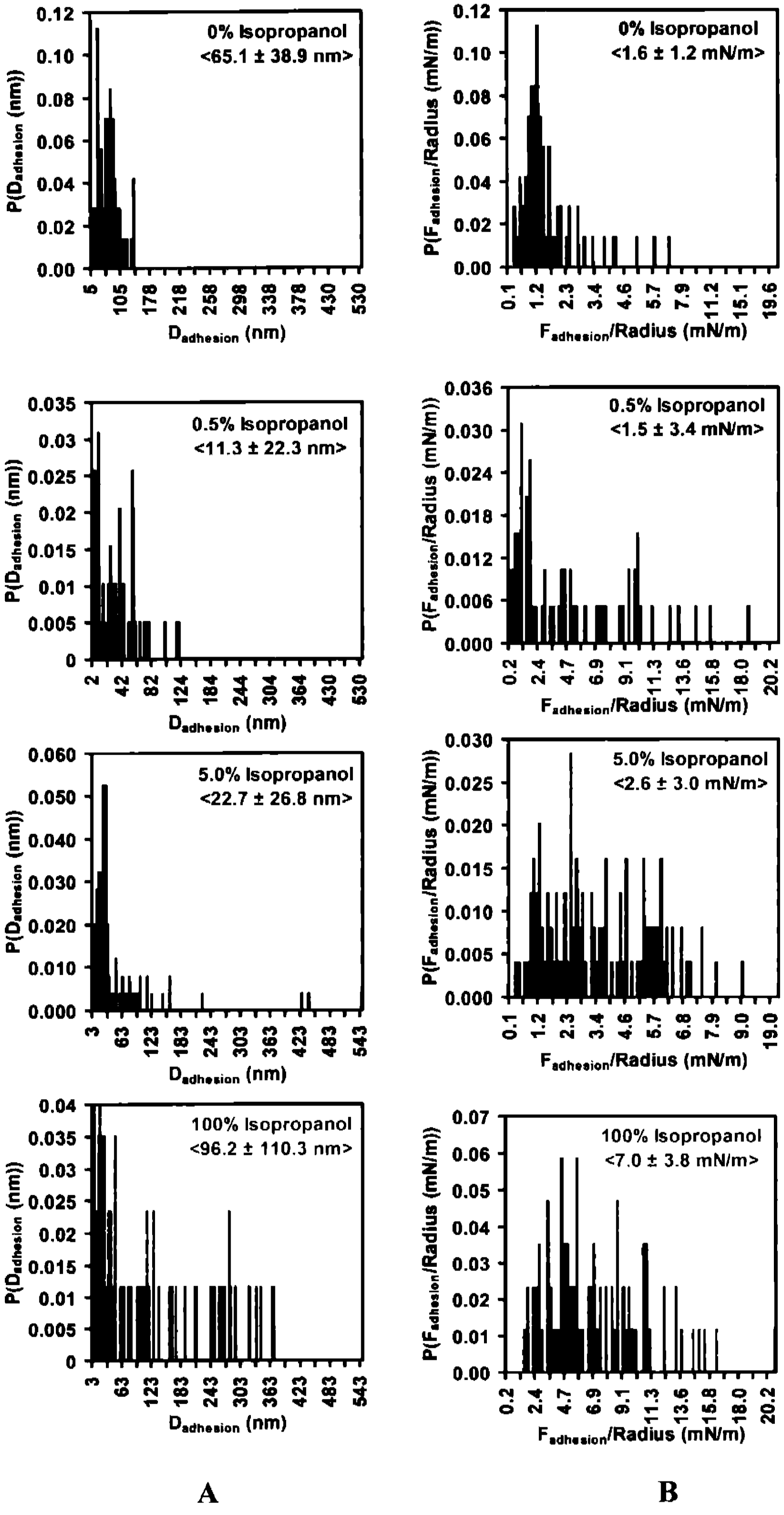
0% Isopropanol
<65.1 ± 38.9 nm>
P(D_adhesion (nm))
D_adhesion (nm)
0.12
0.10
0.08
0.06
0.04
0.02
0.00
5
105
178
218
258
298
338
378
430
530
0% Isopropanol
<1.6 ± 1.2 mN/m>
P(F_adhesion/Radius (mN/m))
F_adhesion/Radius (mN/m)
0.1
1.2
2.3
3.4
4.6
5.7
7.9
11.2
15.1
19.6
0.5% Isopropanol
<11.3 ± 22.3 nm>
0.035
0.03
0.025
0.02
0.015
0.01
0.005
0
2
42
82
124
184
244
304
364
430
530
0.5% Isopropanol
<1.5 ± 3.4 mN/m>
0.036
0.030
0.024
0.018
0.012
0.006
0.000
0.2
2.4
4.7
6.9
9.1
11.3
13.6
15.8
18.0
20.2
5.0% Isopropanol
<22.7 ± 26.8 nm>
0.060
0.050
0.040
0.030
0.020
0.010
0.000
3
63
123
183
243
303
363
423
483
543
5.0% Isopropanol
<2.6 ± 3.0 mN/m>
0.030
0.025
0.020
0.015
0.010
0.005
0.000
0.1
1.2
2.3
3.4
4.6
5.7
6.8
7.9
9.0
19.0
100% Isopropanol
<96.2 ± 110.3 nm>
0.04
0.035
0.03
0.025
0.02
0.015
0.01
0.005
0
3
63
123
183
243
303
363
423
483
543
100% Isopropanol
<7.0 ± 3.8 mN/m>
0.07
0.06
0.05
0.04
0.03
0.02
0.01
0.00
0.2
2.4
4.7
6.9
9.1
11.3
13.6
15.8
18.0
20.2
A
B

Figure 5.9 Probability distributions for the experimental data points of the (**A**) Distances (nm) and (**B**) Forces/Radius (mN/m) of adhesion for HSA vs PEO at 0% (blue), 0.5% (purple), 5.0% (red), and 100% (green) isopropanol (v/v) in PBS.

5.5 Role of HSA-Bound Lipids

Having quantified the hydrophobic component to the long-ranged intermolecular interactions between HSA and PEO, the question then arose as to how the fatty acids that naturally bind into the hydrophobic pockets of HSA in a ~2:1 (lipid:protein) ratio in the human blood stream[67] affect the hydrophobic component of U(D). To address is problem, we obtained lipid-free HSA (Sigma #A-3782) and attached it to a cantilever probe tip in the same way as previously described for lipid bound HSA (Section 3.2.2). We then repeated the isopropanol experiments described in section 5.4, using the lipid-free tip. The exact same isopropanol solutions and the same substrates were used in this study, and the experiments were performed at the same time as the isopropanol experiments with the lipid-bound probe tip, to minimize the number of experimental variables. The efficacy of the probe tip functionalization procedure was verified by fluorescence, AFM, and contact angle measurements, as was done previously for the lipid-bound HSA-grafted probe tip. The advancing contact angle of the lipid-free surface with DI water was found to be 47° ± 1°, as compared with 40.1° ± 1° for the lipid-bound HSA surface, indicating that the lipid-free HSA is slightly more hydrophobic than the lipid-bound, presumably because of exposure of the hydrophobic channels of the protein in the absence of lipids. The areal parameters for the probe tip used in this study are given in Table 5.2.

Parameter	Lipid-Free HSA vs PEO
R_{tip} (nm)	75
A_{tip} (nm^2)	9,400
# HSA molecules (ellipsoidal) in A_{tip}	210
# HSA molecules (triangular) in A_{tip}	340
Maximum applied force (nN)	3
Maximum applied force per HSA molecule (ellipsoidal) (nN)	0.014
Maximum applied force per HSA molecule (triangular) (nN)	0.010
$A_{substrate}$ (nm^2)	14,000
# Polymers in $A_{substrate}$	3.6

Table 5.2 Areal parameters for the lipid-free HSA-grafted probe tip.

5.5.1 Lipid-Free Isopropanol Results on Approach

On approach of the lipid-free HSA-grafted probe tip to PEO, a long-ranged, nonlinear repulsion was observed beginning at D = 40 nm under all solvent conditions; however, the rate of increase of repulsion, and the maximum repulsive energy that is ultimately obtained, are dramatically reduced upon the addition of 0.5% isopropanol to PBS. No further reduction in repulsion is observed upon the further addition of isopropanol to a total concentration of 5% – i.e. the approach curves under both of the mixed solvent conditions overlay extremely well. These results, depicted in Figure 5.10, are rather counterintuitive; addition of isopropanol is expected to make the surface of the protein more hydrophilic overall as the hydrophobic moieties are solubilized, but quite the opposite is observed experimentally. What is clear from these results is that lipids play a key role in the hydrophobic interactions of HSA, and by calculating the area between the pure PBS and mixed solvent average approach curves and dividing by the total number of proteins in the interaction area, we may quantify this role directly. We determined the hydrophobic interaction energy per protein to be -0.97 k_BT/protein (assuming a triangular protein shape), or -1.6 k_BT/protein (assuming an elliptical shape lying flat) for the lipid-free probe tip, 12-20 k_BT less than that observed on the lipid-bound probe tip. These results suggest that lipid-binding actually results in a decrease in the overall hydrophobicity of HSA. Direct comparison of the lipid-bound and lipid-free probe tips on a Force/Radius vs Distance graph was not found to be meaningful in light of the deviations in the experimental data from tip to tip, presumably due to differences in probe tip geometry, or fine details of the surface chemistry. Finally, no difference was detectable in 100% isopropanol between the approach curves with lipid-bound and lipid-free HSA-grafted probe tips.

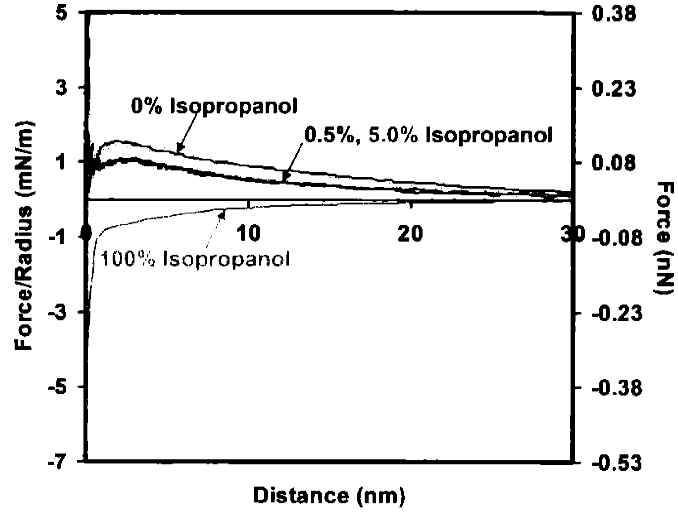

Figure 5.10 Average approach curves for HSA vs PEO (94% of HSA-Au interaction subtracted) as a function of % (v/v) isopropanol in 0.01M PBS: 0% (blue), 0.5% (purple), 5.0% (pink), and 100% (green).

5.5.2 Lipid-Free Isopropanol Results on Retract

The data points of maximum adhesion under each of the solvent conditions are plotted in Figure 5.11. It appears from this graph that in the presence of isopropanol, the force curves shift from exhibiting long-range pulling under low force to exhibiting short-range pulling under high force. However, a careful statistical analysis of this data (along with data from parallel experiments conducted on Au with the same probe tip) as described previously reveals that any observed changes in $\langle F_{adhesion} \rangle$ and $\langle D_{adhesion} \rangle$ were not a direct result of a change in HSA-PEO interactions. The only parameter from the retract data that showed a statistically significant trend was the frequencies of protein and/or polymer extension (pulling), illustrated in Figure 5.12. It is clear from the plot that the addition of isopropanol results in a dramatic reduction in the frequency of chain extension, from 98% in PBS, to 13-24% under mixed solvent conditions. In 100% isopropanol, however, chain extension once again becomes the dominant mechanism of adhesion, as both the protein and polymer have "denatured" from their conformations in PBS.

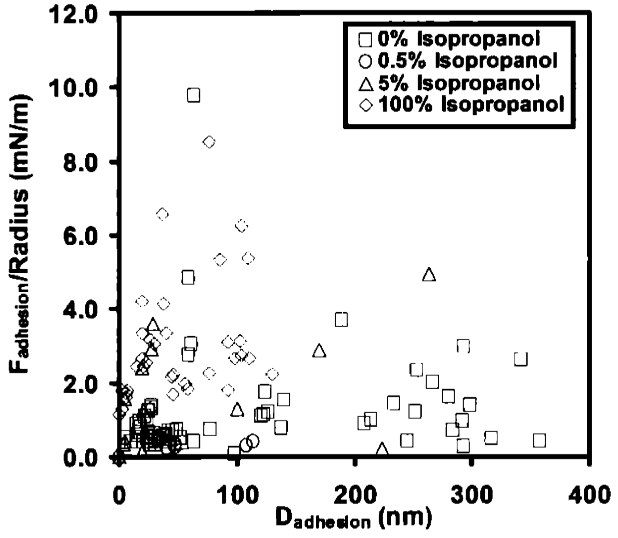

Figure 5.11 Experimental data points of the Distances (nm) and Forces/Radius (mN/m) of adhesion for HSA vs PEO at 0% (□), 0.5% (○), 5.0% (Δ), and 100% (◊) isopropanol (v/v) in 0.01M PBS. Dotted lines have been drawn to guide the eye.

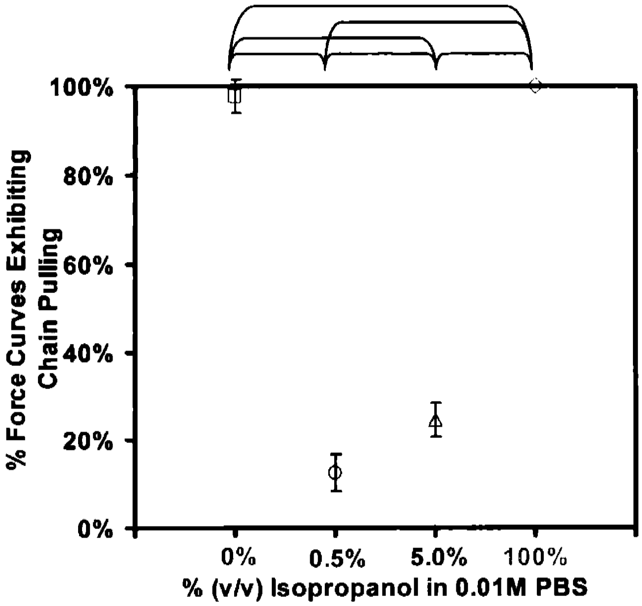

Figure 5.12 Average frequencies of protein or polymer extension, along with standard deviations, for HSA vs PEO at 0% (□), 0.5% (○), 5.0% (Δ), and 100% (◇) isopropanol (v/v) in 0.01M PBS.

5.6 Conclusions

The net nanoscale interaction potential as a function of distance, U(D), was measured between a probe tip covalently bound with human serum albumin (HSA) and poly(ethylene oxide) (PEO) under a variety of solution conditions, including variations in ionic strength, addition of small amounts of the antihydrophobic agent isopropanol to a PBS stock solution, and in a 100% organic solvent. The role of bound lipids in HSA hydrophobic interactions was also investigated by studying the effect of isopropanol on the U(D) between lipid-free HSA and PEO.

An increase in the ionic strength from IS = 0.01 M to IS = 1.0 M resulted in an increase in the range and magnitude of the repulsive force observed on approach at $D < 10$ nm. This interference dominates over any electrostatic or steric interactions from configurational entropy that may be contributing to U(D). This effect was also observed in previous experiments[198] between PEO and an unmodified Si_3N_4 probe tip (Chapter 2), suggesting that it is primarily attributable to the PEO rather than HSA. It is suspected that the addition of salt to the system may be affecting the conformation of the PEO coils, and/or the structure and density of the water molecules residing between the PEO and the approaching probe tip. No statistically significant effects on $<F_{adhesion}>$ or $<D_{adhesion}>$ were observed on retract.

Addition of isopropanol to a PBS stock solution in MFP experiments resulted in an increase in the magnitude of U(D) on approach, likely due to the mutual hydrophilic-hydrophilic repulsive force between the protein tip and the polymer surface. The approach data suggest the presence of a quantifiable hydrophobic component to U(D), which was determined to comprise 20% of the total intermolecular interaction potential at ~1nm, the local miximum of the approach curves. If the difference in the total area between the approach curves with and without isopropanol is calculated, and the resultant energy divided by the number of proteins in the interaction area, it is found that the hydrophobic component is ~ 11-18 k_BT/protein. The addition of isopropanol did not have any significant effect on the retraction data, as determined by a rigorous series of statistical analyses.

In 100% isopropanol, i.e. under pure organic solvent conditions, the approach curve exhibited a somewhat long-ranged ($D < 25$ nm) net attractive force, presumably due to a solvophobic effect imparted by the precipitation of PEO and HSA. The approach curve was found to fit a function comprised solely of models of the solvophobic and van der Waals forces rather well. Once in contact, the HSA, which is completely denatured in the isopropanol, binds nonspecifically to the polymer-grafted surface, and extends readily to long distances under relatively low adhesive force. It is clear from these results that the presence of water is absolutely essential to the protein-resistant properties of PEO.

Addition of isopropanol to MFP experiments using a probe tip bound with lipid-free HSA resulted in a decrease in the magnitude of U(D) on approach, a rather counterintuitive result considering that, in the absence of fatty acids, the hydrophobic pockets of the protein should be exposed, and the effective hydrophobic force thereby magnified. The addition of isopropanol should then result in an even more pronounced increase in the repulsive force on approach than that which was observed with the lipid-bound probe tip. In fact, the change in repulsive force from the addition of 0.5% isopropanol to 0.01M PBS, -0.97 to -1.58 k_BT/protein, was 10-20 k_BT less per protein with the lipid-free tip than with the lipid-bound probe tip. On retract, a dramatic decrease in the frequency of protein and/or polymer extension was observed on the addition of isopropanol. In 100% isopropanol, the system behaved in a similar solvophobic manner as observed with the lipid-bound tip, and chain extension again became the dominant mechanism for the denatured molecules.

Overall, the above results suggest that while hydrogen bonding is crucial to the binding of HSA to PEO, hydrophobic interactions are also clearly important, and novel devices aiming to exhibit enhanced protein resistance should possess a hydrophobic component less than 20%. Furthermore, the protein resistant properties of PEO are enhanced in high ionic strength environments, and hence are likely to be most successful in such situations. Depending on the application of the desired biomaterial, one may choose to seek a surface coating with a PEO-like response to the ionic strength, or a material with a more traditional electrostatic response in which the intermolecular repulsion is increased in low ionic strength environments.

Finally, an interesting feature of our retract data is the presence of various "modes" of protein/polymer extension, which we attribute to extension of specific domains of the HSA macromolecule. There appears to be three distinct distance ranges in which adhesion and extension occurs: D ~ 0-90 nm, D ~ 100-190 nm, and D ~ 200-275 nm, which individually are rather consistent with the average contour length of each of the three domains of HSA, $L_{contour,domain}$ ~ 75 nm. Which domain is extended on a given retract cycle is likely dominated by the specific orientation that the majority of the proteins are in as the probe tip comes into contact with the surface, which is assumed to be random.

Now empowered by a thorough understanding of HSA-PEO intermolecular interactions, we are prepared to use our studies as a foundation on which to test novel materials for relative hemocompatibility. In the following chapter, we attempt to identify a series of candidates with potentially superior protein resistant properties, and test them via HRFS against PEO and SAMs of tri(ethylene glycol).

Chapter 6

NANOSCALE INTERMOLECULAR INTERACTIONS BETWEEN HUMAN SERUM ALBUMIN AND MONOLAYERS OF OLIGOMANNOSE-9 DERIVATIVES

6.1 Introduction

For some time now, researchers have been exploring the viability of saccharide derivatives as biomaterial candidates, many of which are found in abundance on the surfaces of blood components such as cells, bacteria, and viruses, which are, necessarily, naturally hemocompatible. For example, the hydrogel-like polysaccharide layer that coats all living cells, known as the "glycocalyx" (shown in Figure 6.1), serves to maintain hydration, prevent cellular aggregation, and protect against nonspecific protein adhesion to cellular surfaces. [205] Heparin is a sulfonated, negatively charged polysaccharide that imparts a unique anticoagulant effect and has been shown to increase the rate of thrombin-antithrombin interactions 1000-fold. [4] Hyaluronan, or hyaluronic acid is a very hydrophilic and lubricious polysaccharide used in a variety of medical applications, [206] including arthritis treatment, [207] as a viscoelastic in ophthalmic surgery, [208] and for adhesion prevention following abdominal surgery. [209] The major advantage of hyaluronan is that its structure is identical in all animals and all tissues, and therefore is inherently biocompatible. [206] Mucins, as well as being a highly glycosylated protein component of the glycocalyx, are responsible for masking the surfaces of the epithelium, which is extremely hydrophobic and thus prone to cellular and protein adhesion. Interestingly, mucin has been found to possess surfactant qualities on par with poly(ethylene oxide)-containing block copolymers. [210] Most of the polysaccharides just mentioned are charged, however, and therefore have the potential to incite attractive electrostatic interactions with blood proteins, which are amphoteric. Other potentially viable alternatives not explored here include polysaccharides such as guar gum (galactomannan), polymers or copolymers of cellulose or its more water-soluble derivative hydroxyethylcellulose, [211] or starch (a copolymer of amylose and amylopectin). On bacterial cell surfaces, the type and orientation of the constituent molecules, which also tend to be heavily glycosylated, play a key role in determining the virulence of a great many pathogens by mediating adhesion, permeability, ligand-receptor interactions, inihibition of phagocytosis, and environmental adaptation. [212] Oligosaccharides are found on blood-contacting surfaces throughout the human body, and are thus an interesting candidate to test Mother Nature's wisdom against Herself.

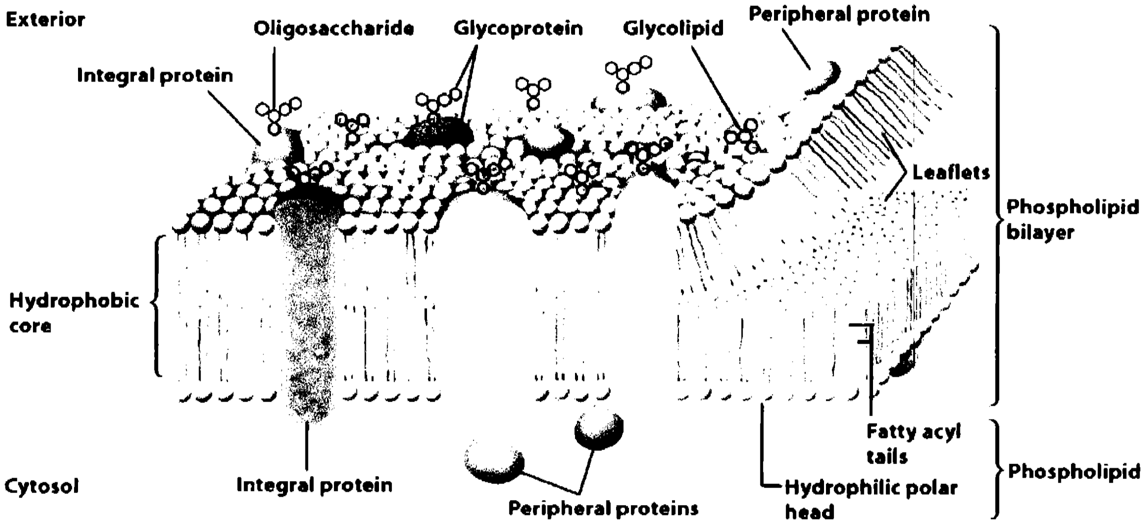

Figure 6.1 Schematic of the glycocalyx. [205]

In this chapter, we chose to examine a family of derivatives of the sugar **Oligomannose-9** (or "Man-9"), shown in Figure 6.2.

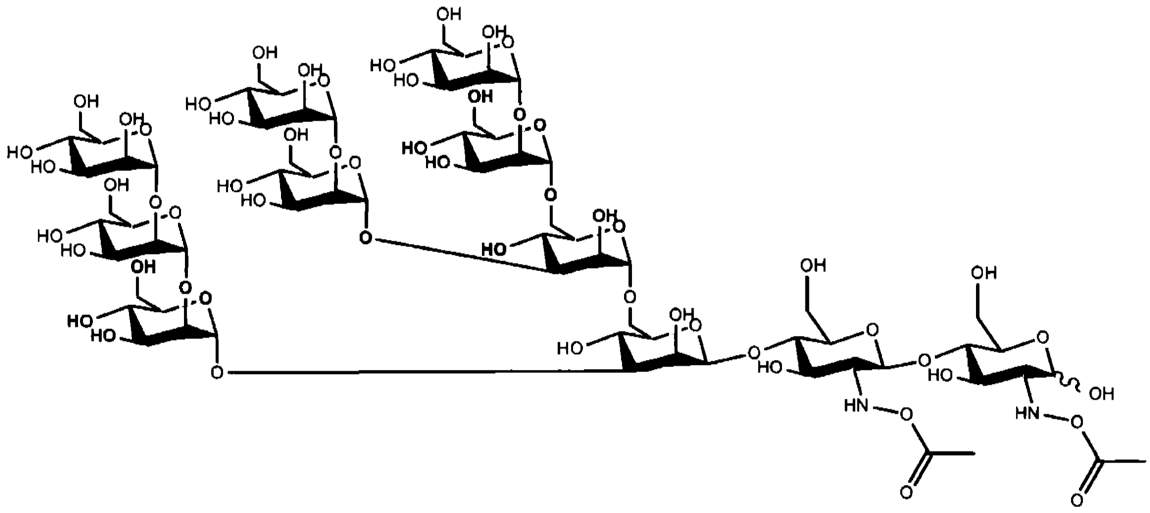

Figure 6.2 Structure of Oligomannose-9.

Four derivatives of Man-9 were custom synthesized by Ratner, et al, [213] and specifically functionalized with tails of thiol-terminated tri(ethylene glycol) (EG_3-SH) which enables direct linkage of the sugars to a gold surface. The structures, ranging from a mannose monomer to a branched nonamer, are shown in Figure 6.3.

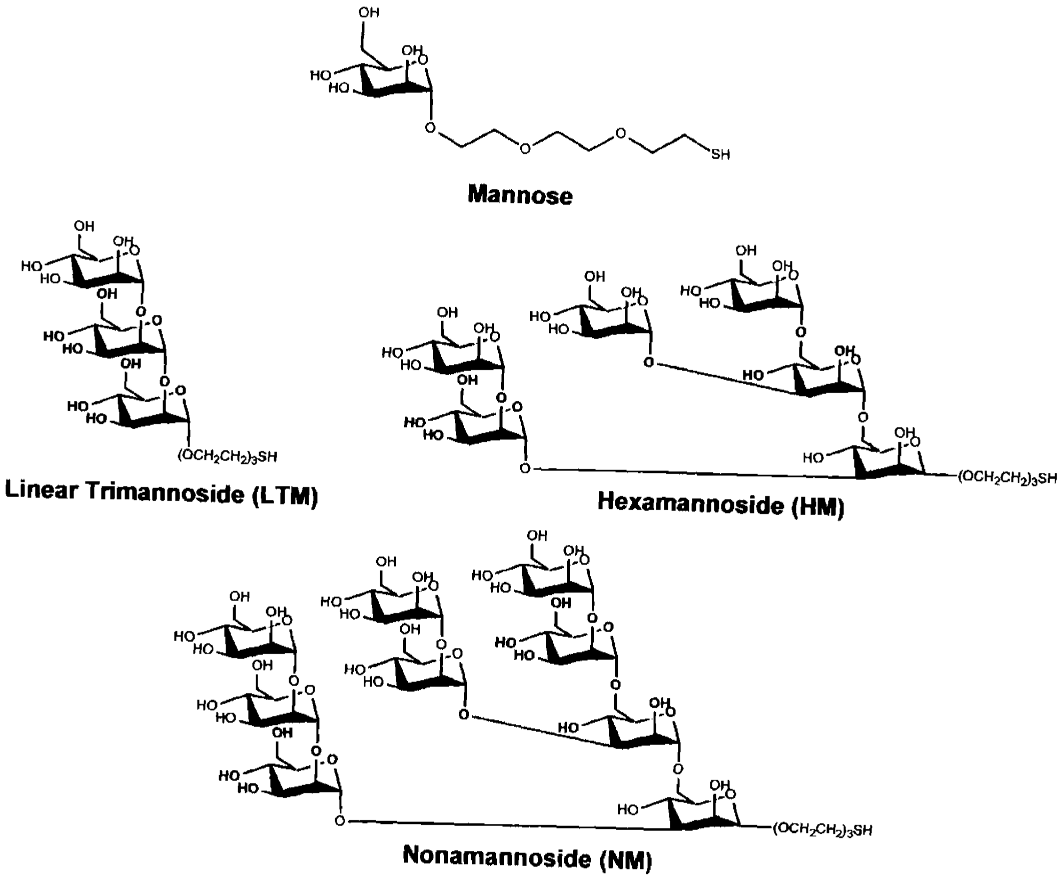

Mannose

Linear Trimannoside (LTM)

Hexamannoside (HM)

Nonamannoside (NM)

Figure 6.3 Chemical structures of Oligomannose-9 derivatives custom synthesized by Ratner, et al. [213]

Unconjugated ring structures like the ones used in this study sample a large variety of conformations in solution, and thus possess some degree of conformational entropy. They are also neutral, thereby evading electrostatic interactions with charged species such as proteins. Furthermore, they possess a large number of hydroxyl groups which are capable of engaging in hydrogen bonding both inter- and intramolecularly. Finally, sugars are naturally occurring in nature and in vivo, and are extremely inexpensive. For all of these reasons, they were particularly attractive candidates for a study investigating novel biomaterial surface coatings for improved hemocompatibility.

As our studies to date have developed a thorough understanding of the nonspecific intermolecular interactions of human serum albumin, we chose to use this system in qualitatively assessing the relative protein resistance of these materials as compared to both single molecules of poly(ethylene oxide) (in order to compare directly to our previous experiments) and tri(ethylene glycol), which has been shown[214] to effectively resist protein adsorption with greater efficacy than other common self-assembled monolayers.

6.2 Materials and Methods

6.2.1 Preparation and Characterization of Oligosaccharide Substrates

Each of the Man-9 derivatives shown in Figure 6.3, as well as an unmodified EG_3-SH, were prepared into 1mM solutions in PBS (IS = 0.01M, pH = 7.4). To these solutions, a 1:1 molar ratio of tris(carboxyethyl)phosphine hydrochloride (TCEP•HCl, *Sigma* product #C-4706), a chemical commonly employed to break disulphide bonds that naturally form over time in solutions of thiol-functionalized compounds, was added, and the solutions were stirred for 1 hour (the reaction scheme for this process is shown in Figure 6.4). The oligosaccharide/TCEP solutions were then added dropwise until completely covering the surfaces of substrates (each ~1 cm^2) of polygranular gold on glass (*Asylum Research, Santa Barbara, CA*), which were cleaned before use by thorough rinsing with 100% ethanol and drying with a steady stream on N_2 (g). The total volume of solution deposited on each substrate depended on the exact dimensions of the substrates, but in all cases was 0.2-0.5 mL. The substrates were then enclosed in small, airtight containers to prevent excessive evaporation, and allowed to react for 48 hours. After this time, the substrates were removed and rinsed with copious amounts of PBS, followed by ethanol, to remove all unreacted compounds from the surface. Finally, the substrates were rinsed with deionized (DI) water and stored in DI water in airtight containers until being tested by HRFS.

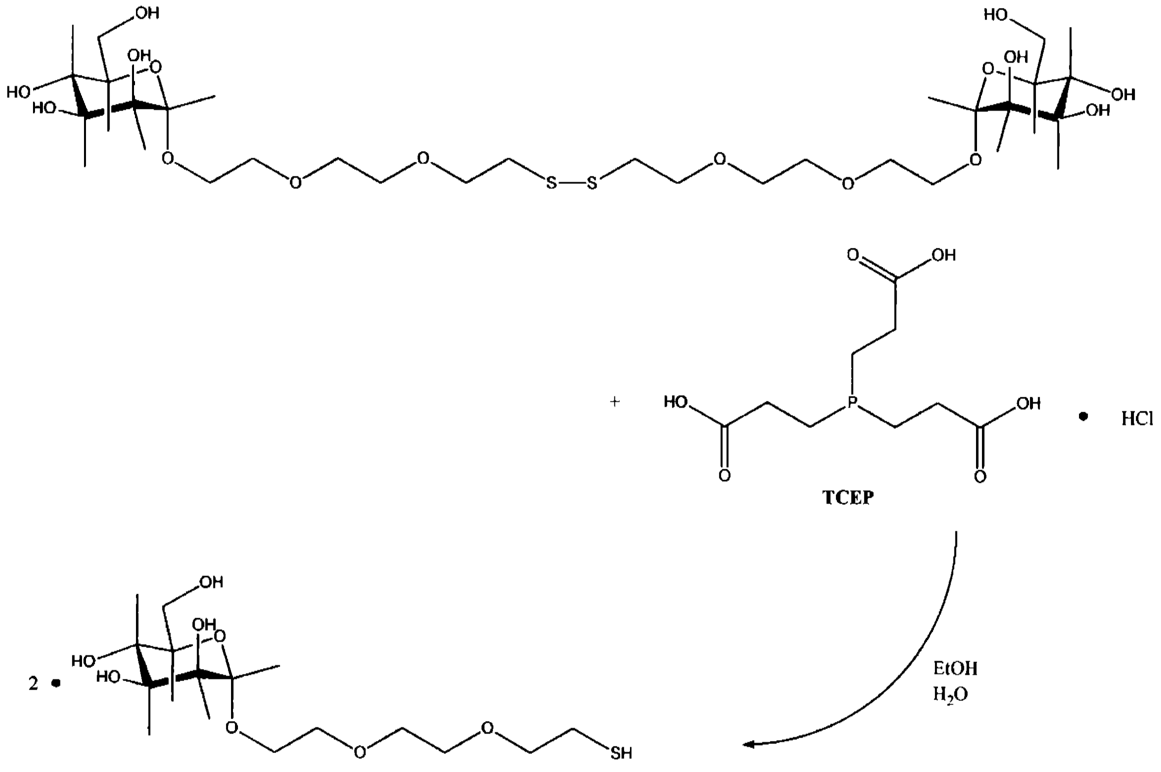

Figure 6.4 Chemical scheme for the breakage of disulphide bonds by reaction with TCEP.

The polygranular gold substrates employed in this study were imaged by atomic force microscopy using a Digital Instruments Multimode 3a AFM, as was done for all gold substrates employed in previous chapters. The grain dimensions were found to be approximately 0.57 ± 0.2 nm in height, and 110 ± 53 nm in diameter.

Several methods were attempted to characterize the oligosaccharide monolayers, including glancing-angle X-ray diffraction (GAXRD), ellipsometry, and atomic force microscopy. In all cases, the roughness of the substrate and the limited availability of the oligosaccharides, which precluded the preparation of additional substrates, inhibited the collection of any meaningful quantitative data from these methods. Substantive data was able to be collected, however, through contact angle measurements and X-Ray Photoelectron Spectroscopy (XPS), the results of which are detailed below It should be noted, however that these two methods provide only a macroscale picture of the packing density and homogeneity of the monolayer.

Data obtained from contact angle measurements with DI H_2O indicated macroscopically homogenous coverage (on the order of mm^2) of the oligosaccharides, and markedly greater hydrophilicity than both PEO and EG_3. The contact angle values on each of the substrates are given in Table 6.1, and were collected by taking several measurements at different sites on each sample, in order to obtain an average and a standard deviation. Receding angles were not obtainable on the oligosaccharide surfaces, as the substrates were completely wetted as the water droplet was receded ($\theta_R < 10°$).

Substrate →	**Au**	**PEO**	**EG_3**	**Mannose**	**LTM**	**HM**	**NM**
Advancing angle, θ_A	95° ± 3°	60° ± 1°	34° ± 2°	12° ± 3°	13° ± 1°	9° ± 2°	14° ± 2°
Receding angle, θ_R	70° ± 6°	22° ± 1°	27° ± 1°	n/a	n/a	n/a	n/a

Table 6.1 Advancing and receding contact angle measurements with DI H_2O on oligosaccharide substrates, compared to EG_3, PEO, and unmodified Au.

Together with GAXRD, FTIR, and ellipsometry, XPS is a commonly employed method to study monolayer packing, [115] although as mentioned previously, it is capable of only macroscale analysis due to the large area of the X-ray beam and the statistical nature of the technique. It can be quite tricky to obtain a decent signal from the sulfur groups that attach alkanethiols to gold, as the signal-to-noise ratios are often quite low. We were successful in obtaining a relatively strong signal compared to previously reported studies, [215] and thus were able to utilize XPS in a first-order approximation of the determination of the packing densities of our oligosaccharide monolayers. XPS measurements were taken using a Kratos Analytical Axis Ultra, equipped with an Al-Kα monochromatic X-Ray source, operating at a power of 150W and a path energy of 80eV. [216] Data was collected at angles of 0°, 35°, and 70° relative the surface normal, on a COO^--terminated alkanethiol SAM, the EG_3 SAM, as well as each of the oligomannose-9 derivative monolayers. All substrates had been prepared by the same method, using pieces cleaved from the same gold wafer (covering of a 20 nm-thick polygranular gold-on-glass 1 cm^2 substrate with 0.2-0.5mL of a 1mM solution, for 48 hours, followed by rinsing with DI H_2O (or ethanol, in the case of the COO^--terminated alkanethiol) and PBS (IS = 0.01 M)), and were the identical substrates to those used in all experiments reported in this Chapter. Following a similar method reported by Whitesides, [215] and later by Fritz and Spencer, [217] the S/Au energy ratios obtained from the XPS measurements were then used to calculate the monolayer packing densities for each of the substrates. In order interpret the results in a meaningful manner, it was first necessary to assume a crystal structure and orientation for the polygranular gold substrate, and then to determine from the inelastic mean free path the number of atomic layers to consider in our calculations. Au tends to crystallize in a cubic close-packed (ccp) structure, illustrated in Figure 6.5: [218]

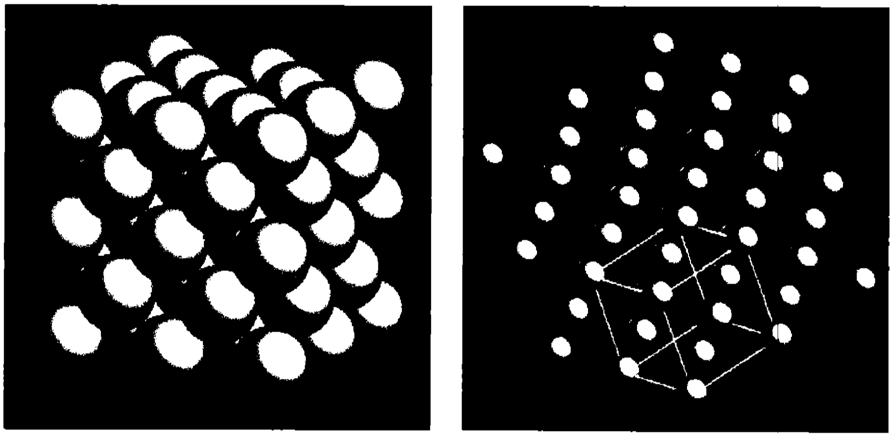

Figure 6.5 The cubic close-packed (ccp) structure of Au (adapted from reference [218]).

It was assumed that the lowest energy plane (i.e. the most close-packed plane), the (111) plane, was the top-most exposed surface of the gold substrates used in this study. Given an atomic spacing of 0.2884 nm, [218] on a 1 cm^2 gold substrate there exists approximately $1.20x10^{15}$ Au atoms per atomic layer, with each individual layer being 0.2884 nm thick.

Since the layers are intermeshed, the thickness of two layers of Au may be calculated from simple geometry to be 0.3796 nm, and likewise three layers occupy a depth of 0.65 nm. Assuming the typical inelastic mean free path normal to the (111) plane (0°) to be 0.503 nm for a path energy of 80 eV, [219]we can calculate, again from basic geometry, the depths of the gold surface that was penetrated at beam angles of 35° and 70° to be 0.412 nm and 0.172 nm, respectively. From the Au-Au atomic spacing, we may then conclude that at 0°, we are penetrating three layers of atoms, at 35° we are only penetrating two layers, and at 70° the depth is further reduced to one layer. We may then incorporate these calculations into the experimentally obtained atomic signal ratios from XPS as follows:

$$\frac{\#\,\mathrm{S\ atoms}}{\mathrm{cm}^2} = \frac{\mathrm{total\ S\ signal}}{\mathrm{total\ Au\ signal}} \bullet \frac{\#\,\mathrm{Au\ atoms}}{\mathrm{cm}^2}$$

Since there is only one sulfur atoms per alkanethiol, EG_3, or oligosaccharide molecule, this calculation yields a direct determination of the surface packing density. The experimentally determined packing density obtained by this method for the COO^--terminated alkanethiol SAM using a beam angle of 0° was 1.73 molecules/nm^2. A similar value of 1.73 molecules/nm^2 was obtained at 35°, and a slightly higher value of 1.9 molecules/nm^2 was observed and at 70°. It is instructive to compare these values to experimentally determined values for a COO^--terminated SAM, which report nominal values of 4.62 molecules/nm^2, and a molecular tilt of 34° relative to the surface normal. [115] It is encouraging to note that our experimentally determined values are reproducibly less than an order of magnitude of the nominal values. It is felt by some that this nominal packing density represents an upper limit of experimentally obtainable SAM densities on gold, [215] and hence the experimentally determined values at 70° may in fact be an overestimation of the packing density. Furthermore, while the results at 0° are neither expected to underestimate nor overestimate the packing density, since our experimental beam angle of 35° is oriented along the theoretical plane of the SAM molecular backbones, [115] these calculated values may represent the most accurate results obtained from XPS on the COO^- SAM substrate. Extremely similar values were obtained for all of the SAM substrates studied, with no apparent trend with molecular size. We may therefore assume that all of the SAMs obtained on average the same packing density, which we determined to be 1.87 ± 0.27 molecules/nm^2 at a scan angle of 35°. It should be noted, however, that these results do not give an indication of the micro- or even nanoscopic homogeneity of the SAM packing.

6.2.2 HRFS Experiments

All HRFS experiments were conducted using the Molecular Force Probe® (Asylum Research, Santa Barbara, CA) to measure force, F (nN), versus tip-sample separation distance, D (nm) (henceforth referred to and labeled on graphs as "Distance") on "approach" (i.e. probe tip advancing towards surface) and "retract" (i.e. probe tip moving away from surface). A full description of this instrument, its limits of force and displacement detection in fluids, procedures for spring constant calibration and conversion of raw data, details of measurement errors, and description of typical force versus distance curves including the mechanical instabilities of the cantilever, are given in Section 2.2.1, and in Appendix A.1., as well in our previous works. [110,130,170]

Experiments were performed in PBS (IS = 0.01M, pH = 7.4), using a 220μm long V-shaped Si_3N_4 cantilever of $k_c \sim 0.03$ N/m (Thermomicroscopes, Inc.), which had been covalently modified with human serum albumin as described previously in Section 3.2.2. All experiments were conducted using the same probe tip, and at least 24 hours was allotted between substrates in order to allow the HSA sufficient time to regain its most stable native configuration. Parallel experiments on a PEO-grafted substrate (prepared as described previously in Section 4.2.3) and unmodified Au were also conducted with the same probe tip, in order to draw a direct comparison between these trials and the experiments previously performed on PEO.

Unfortunately, no data on the hexamannose (HM) substrate could be obtained, as the probe tip was irrevocable damaged before this experiment could be performed.

6.3 Results on Approach

Averaged approach curves are overlayed and shown in Figure 6.5.

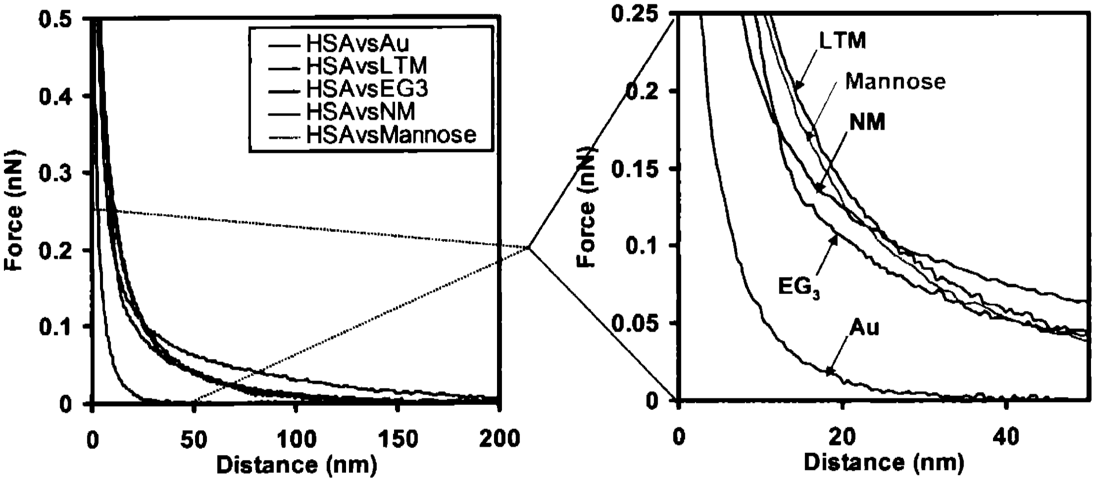

Figure 6.6 Averaged approach curves of a HSA-grafted probe tip to oligosaccharide monolayers. Comparison is made to a monolayer of EG_3, as well as an unmodified gold substrate. The figure on the right is a magnified version of the figure on the left. Standard deviations have been omitted for clarity.

At D > 20nm, the nonamannoside (NM) substrate exhibits by far the greatest repulsion to HSA. At D < 20nm, however, it lags behind EG_3, mannose, and LTM, which overlap rather closely. All substrates are much more repulsive than Au, indicating complete or near-complete shielding of HSA-Au interactions. These results suggest that while the monomer and the trimer are at least as good as EG_3 in imparting long range repulsion to a surface, the nonamer (NM), perhaps in part due to its size, greater configurational entropy, and broader possibilities for hydrogen bonding, excels at preventing long-range attraction of proteins to the surface when compared to its monomeric and trimeric counterparts.

In contrast to the macroscale analytical techniques used to characterize the SAMs in this study, the standard deviations of the averaged approach data, which were quite small and comparable to previous experiments between HSA and PEO, indicate rather homogenous surface coverage of the oligosaccharides on the Au surface. Together with the XPS data, which suggest overall similar packing densities of the various SAMs, we may directly compare the experimental data on the various surfaces with some confidence.

6.4 Results on Retract

On retract, while the oligomannose substrates appeared to bind with the same frequency as EG_3 and PEO, they bound with considerably lesser force, as shown in Figure 6.6.

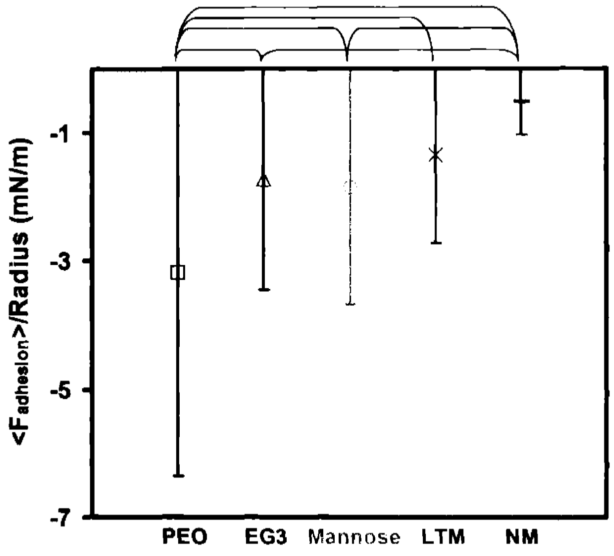

Figure 6.7 Averages of Force/Radius of protein extension on oligomannose monolayers, along with standard deviations, compared to averages obtained on EG_3 and PEO. Statistically different data points are connect by brackets above.

The average binding force on Mannose is $F_{adhesion}/R_{TIP}$ = -1.84 ± -0.81 mN/m, nearly half that observed on PEO, which had an $F_{adhesion}/R_{TIP}$ = -3.18 ± -2.55 mN/m. While values on the EG_3 substrate were comparable to Mannose, the adhesion strength drops again slightly to $F_{adhesion}/R_{TIP}$ = -1.36 ± -1.06 mN/m when the oligosaccharide size is increased to the trimer, and then dramatically in half again on the nonamer, to $F_{adhesion}/R_{TIP}$ = -0.52 ± -0.37 mN/m.

6.5 Conclusions

The intention of this study was to select a series of molecules commonly found on the peripheries of components of the blood in living systems, which are naturally and necessarily hemocompatible, and to test them via HRFS against polymers and oligomers of ethylene oxide, a system in which we have developed a solid understanding, and which is perhaps the most protein-resistant material currently in use in biomaterial surface coatings. The family of molecules selected were derivatives of the oligosaccharide oligomannose-9, in a variety of sizes and architectures. The results suggest that higher oligosaccharides, which clearly exhibit a greater long range repulsion on approach to, and a lower binding force on retract from, an HSA-grafted probe tip (as compared to PEO and EG_3), have the potential to outperform poly- and oligo(ethylene oxide) in their ability to resist the adhesion of blood plasma proteins. The ability to evade protein adsorption, the first step in the biological thrombic and inflammatory responses, is considered key in the design of novel materials for bio- and hemocompatible blood-contacting biomedical applications. Furthermore, the large availability and low-cost of oligosaccharide derivatives makes them particularly attractive alternatives for commercial-scale applications.

Chapter 7

USING HRFS TO STUDY THE BINDING OF HIV TO THERAPEUTIC DRUGS: NANOSCALE INTERMOLECULAR INTERACTIONS BETWEEN CYANOVIRIN-N AND MONOLAYERS OF OLIGOMANNOSE-9 DERIVATIVES

7.1 Introduction

As was mentioned in the previous chapter, oligosaccharides are found in abundance on various surfaces in contact with the blood stream, such as cells, bacteria, and viruses. Oligomannose-9 is present on myriad biological surfaces, perhaps the most notable of which is the viral envelope of the human immunodeficiency virus (HIV). The viral envelope of HIV is highly glycosylated, and those glycoproteins known to be most involved in the infection process, gp120 and gp41, possess up to 50% carbohydrate content by weight. [220] Of the 24 N-linked oligosaccharides on the carbohydrate moiety of gp120, nearly half are believed to be either *high-mannose* (HM) or *hybrid-type* (HT). [221] The HM oligosaccharides are believed to be essential in defending gp120 from proteolytic attack or barrage by the host immune system. [222] In addition, and currently of great interest to researchers battling HIV, the mechanism by which HIV enters host cells is mediated by interactions between the HM moieties of glycoprotein ligands gp120 and gp41 on the viral envelope and the protein receptors CD4, CCP5, and CXCR4 on the cell surfaces. HIV therapeutic drugs work by binding to the virus ligands, thus inhibiting their ability to interact with the host cell surface and ultimately preventing infection (or the spread of infection). [223] Cyanovirin-N ("CV-N", shown in Figure 7.1), a protein found in the blue-green algae cyanobacterium *Nostoc ellipsosporum*, [213,224] has been found to bind with higher affinity to gp120 than all other HIV therapeutics currently in use. [223] In addition, CV-N is nontoxic, structurally stable, [224,226] and to date even prolonged exposure to CV-N has resulted in no HIV variants resistant to CV-N binding. [224,227] Furthermore, CV-N has been found to neutralize a wide variety of HIV-1, HIV-2, and simian immunodeficiency virus (SIV) strains. [228] The protein binds irreversibly to gp120 via the high-mannose (HM) moieties, crosslinking specific oligosaccharide arms and making it impossible for the glycoprotein to achieve the necessary conformations for binding to host cell receptors. [223]

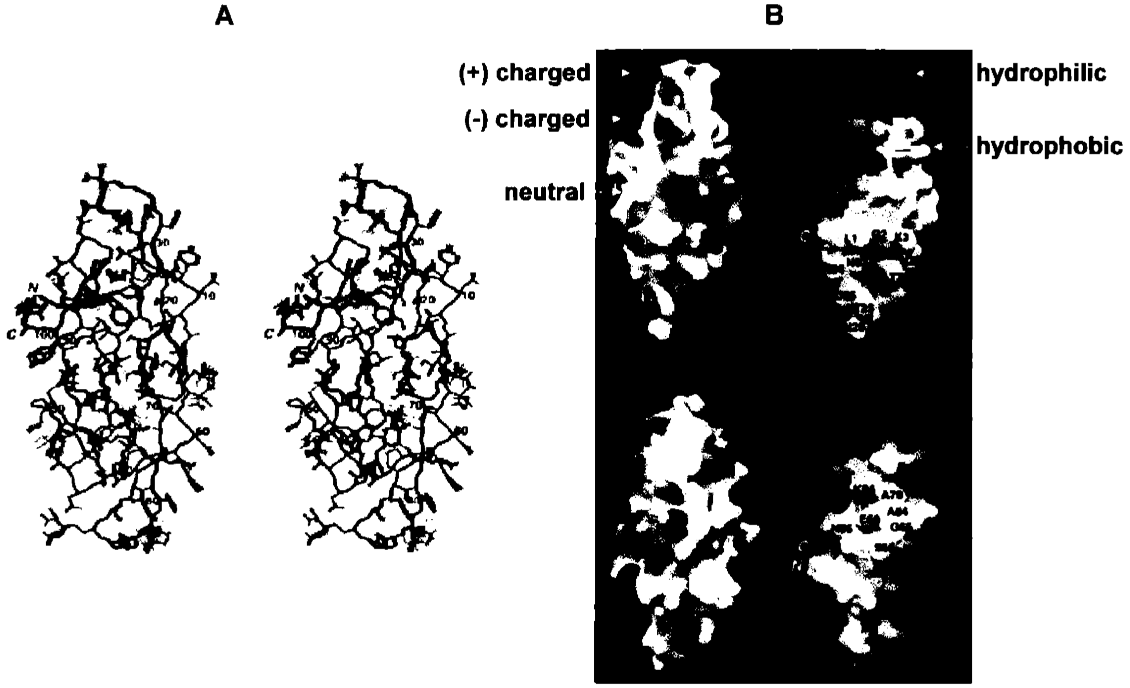

Figure 7.1 **(A)** Two views of the three-dimensional structure of *cyanovirin-N*, a protein found to block HIV interactions with host cells. The backbone is shown in red, the disulphide bridges are shown in green, and all other side chains are in blue. **(B)** Front and side views of surface maps of cyanovirin-N with respect electrostatic potential (left), and hydrophobic residue clustering (right). In the electrostatic models, red regions are negatively charged and the blue regions are positively charged. White regions are neutral. In the hydrophobic models, the regions of highest hydrophobicity are colored yellow, the regions of lowest hydrophobicity are colored purple, and white regions are intermediate. (Images adapted from Bewley, et al., ref [229])

Our experimental setup provided a unique opportunity to study the intermolecular interactions between the HIV oligosaccharide and the therapeutic drug Cyanovirin-N, the results of which are reported in this chapter, and were made possible through a collaboration with the National Cancer Insitute (Frederick, MD). It should be noted, however, that unlike typical ligand-receptor binding experiments, the random nature of our chemical attachment procedure for the CV-N inevitably results in randomness in the conformation the protein is in when it contacts the substrate. Having hundreds of proteins on the probe tip, however, may enable binding measurements despite these circumstances.

7.2 Materials and Methods

Oligosaccharide substrates were identical to those prepared as described previously in Section 6.2.1.

All HRFS experiments were conducted using the Molecular Force Probe® (Asylum Research, Santa Barbara, CA) to measure force, F (nN), versus tip-sample separation distance, D (nm) (henceforth referred to and labeled on graphs as "Distance") on "approach" (i.e. probe tip advancing towards surface) and "retract" (i.e. probe tip moving away from surface). A full description of this instrument, its limits of force and displacement detection in fluids, procedures for spring constant calibration and conversion of raw data, details of measurement errors, and description of typical force versus distance curves including the mechanical instabilities of the cantilever, are given in Section 2.2.1, and in Appendix A.1., as well in our previous works. [110,130,170]

Experiments were performed in PBS (IS = 0.01M, pH = 7.4), using a 220μm long V-shaped Si_3N_4 cantilever of $k_c \sim 0.03$ N/m (Thermomicroscopes, Inc.), which had been covalently modified with Cyanovirin-N by the exact method described in Section 3.2.2 for HSA. Cyanovirin-N was obtained via a research collaboration between the Ortiz Polymer Mechanics Laboratory (M.I.T.) and the Natural Products Chemistry Group (of the Molecular Targets Discovery Program) at the National Cancer Institute in Frederick, MD. Attachment of the CV-N to the probe tip was verified both by AFM and by fluorescent tagging and imaging with Oregon Green, as was done previously for the HSA probe tips, and reported in Section 3.2.2. Resuts were remarkably similar, and hence will not be repeated here.

All experiments were conducted using the same probe tip, and at least 24 hours was allotted between substrates in order to allow the CV-N sufficient time to regain its most stable native configuration. Parallel experiments on an EG_3-grafted substrate (prepared as described previously in Section 4.2.3) were also conducted with the same probe tip, as a "control".

7.3 Results on Approach

On approach, the HM, Mannose, and EG_3 substrates elicited a similar long-ranged repulsive profile (with repulsion beginning at D ~ 100nm) in response to the CV-N grafted probe tip. Unusually, LTM exhibited a much stronger repulsion on approach than did the others, with a force beginning at D ~ 150 nm from the surface. This result, though unexpected and not entirely understood, was reproduced experimentally several times. Nonamannoside exhibited significantly less repulsion at $D < 25$nm. The averaged force curves on approach are shown in Figure 7.2.

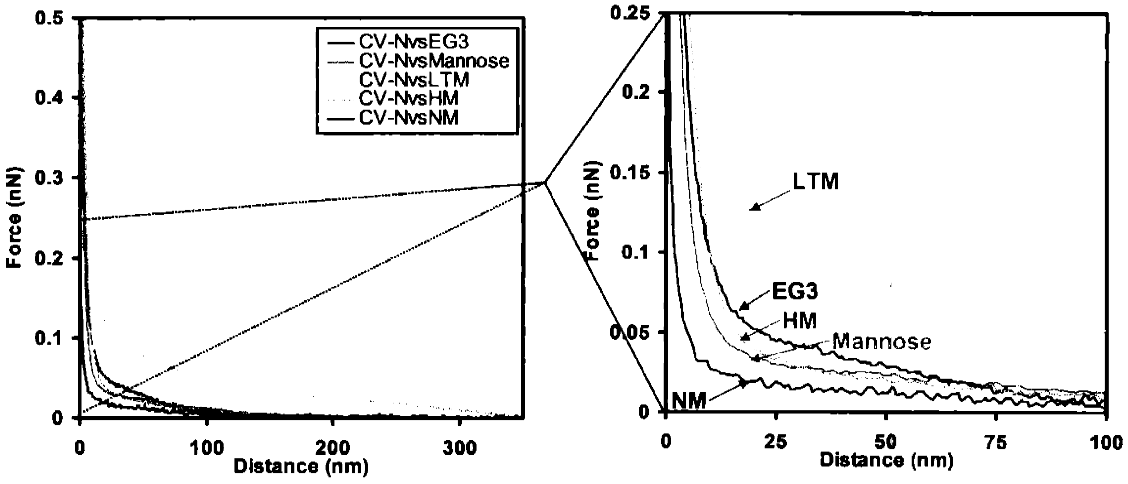

Figure 7.2 Averaged approach curves of a HSA-grafted probe tip to oligosaccharide monolayers. Comparison is made to a monolayer of EG_3, as well as an unmodified gold substrate. The figure on the right is a magnified version of the figure on the left. Standard deviations have been omitted for clarity.

7.4 Results on Retract

On retract, the various substrates had markedly different adhesion force profiles. While EG_3 and Mannose consistently averaged higher adhesion forces and longer distances of extension than the other substrates, the higher oligomannose structures exhibited statistically lower adhesion forces and frequencies of adhesion, and shorter distances of extension, than their monomeric counterpart. The frequencies of adhesion events on each of the substrates are shown in Figure 7.3.

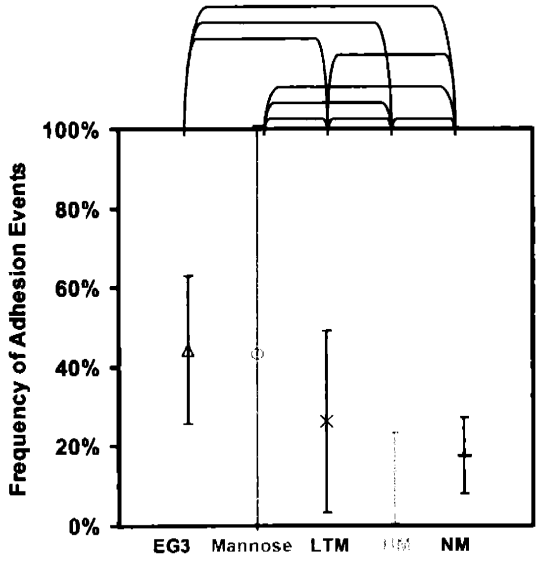

Figure 7.3 Frequencies of adhesion of a CV-N grafted probe tip on various Oligomannose-9 derivative monolayers. Data on an EG_3 SAM is shown as a control. Statistically different data points are connected by brackets above.

Table 7.1 gives the average forces and distances of adhesion on each of the substrates. These values take into account all data points included in the statistical analyses, including points of zero-adhesion, surface adhesion, and protein extension.

Substrate →	**EG_3**	**Mannose**	**LTM**	**HM**	**NM**
	(n = 61)	**(n = 65)**	**(n=126)**	**(n=133)**	**(n=125)**
$<D_{adhesion}>$ (nm)	14.39 ± 16.89	3.47 ± 7.87	0.22 ± 1.55	4.46 ± 15.23	4.28 ± 11.70
$<F_{adhesion}>$/Radius (mN)/m	-0.58 ± -0.79	-0.55 ± -0.78	-0.01 ± -0.13	-0.29 ± -0.87	-0.19 ± -0.49
Frequency of Adhesion (%)	44.26 ± 18.63	43.08 ± 57.14	26.19 ±22.89	12.03 ± 11.40	17.6 ± 14.17

Table 7.1 Average forces, distances, and frequencies of adhesion for a Cyanovirin-N –grafted probe tip on various monolayers of Oligomannose-9 derivatives. "n" is the number of data point in the statistical data set.

These results are puzzling, as they do not correlate well with experiments conducted by Shenoy, et al., [230] in which they measured the binding between CV-N and these materials via calorimetry and nuclear magnetic resonance in solution. The findings from the Shenoy study concluded that the binding affinity was in the order: NM > HM > LTM > Mannose, quite the opposite of our results obtained via HRFS. The discrepancy in the results may be due to the fact that, in the Shenoy study, the molecules were all free in solution and able to bind in a very specific manner, while in our study, both ligand and receptor were bound to their respective surfaces, and the random binding of the CV-N to the probe tip does not ensure that it will be in the correct conformation to bind to mannose on tip-surface contact. It is therefore likely that the adhesion forces measured in our study reflected nonspecific CV-N – Oligomannose binding, rather than a specific ligand-receptor interaction.

7.5 Conclusions

The experiments reported in this chapter, in which the binding affinity of the HIV therapeutic drug Cyanovirin-N to various oligosaccharide moieties involved in the binding of HIV to host cells, was studied by HRFS, demonstrates the possibilities of this technique for studying a large variety of chemical and biochemical interactions, but also reveals its limitations. If future studies are performed with a similar intention as the study conducted here, it is suggested that care be taken to ensure specific binding of the ligand protein such that its conformation will reproducibly be in the desired form.

Chapter 8

CONCLUSIONS AND SUGGESTIONS FOR FUTURE WORK

8.1 Single Molecule Force Spectroscopy of PEO with a Si_3N_4 Probe Tip

We successfully optimized our experimental protocol for attachment of single molecules of PEO to Au, and found that incubation of a piranha solution-cleaned Au substrate in 2mL of a 1mM solution of PEO_{50K} for 45 minutes, followed by thorough rinsing with DI H_2O, was sufficient to end-graft PEO chains such that the distance between grafting sites, s, is > $2R_F$ (so the polymers are in the isolated, "mushroom" conformation on the surface), and yet close enough together that HRFS may be done with ease. We tested the efficacy of our system, by repeating previously reported results by Oesterhelt, et al, [43]that demonstrate the strain-induced conformational transition when a water-solvated PEO molecule is extended in an HRFS experiment, and the freely jointed chain force curve extension profile of PEO in the poor solvent hexadecane. On exploring the sensitivity of our system to ionic strength, we observed an unusual increase in the repulsion on approach, and a decrease in the frequencies and forces of adhesion on retract, as the concentration of NaCl was increased in a standard PBS solution. The origin of this effect is not yet fully understood, but does discourage the hypothesis that the long-range repulsion between Si_3N_4 and PEO is due to electrostatic parameters. Possible explanations may include changes in the conformation and dimensions of the PEO coil in the presence of high ionic strength, and/or an effect on the structure and density of the interstitial water layer between the PEO mushrooms and the approaching probe tip. Steric effects, on the other hand, were observed to play an important role in the repulsion on approach to PEO; we were able to demonstrate this by investigating the "salting out" effect of PEO in the presence of K_2SO_4, from which we observed a marked reduction in the repulsive force on approach as the concentration of K_2SO_4 in PBS was increased. Finally, we found that the piezo velocity (scan rate) and tip compliance have negligible effects on both the shape of force curves and the forces and distances of repulsive forces on approach and adhesive forces on retract. Although scan rate can play an important role in larger scale systems in which hydrodynamic effects are nontrivial, our nanosized cantilever probe tips would require a scan rate many times greater than the upper limits achievable by the MFP, in order to exhibit significant sensitivity to the scan rate.

8.2 Nanoscale Intermolecular Interactions between HSA and Alkanethiol Self-Assembled Monolayers

Overall, the strength and range of the nanoscale interaction of an HSA-modified probe tip was highly sensitive to the type of alkanethiol SAM terminal functional group. Furthermore, the intermolecular forces exhibited on approach did not necessarily predict the often adhesive forces that were observed on retract as a result of time-dependent attractive interactions that developed while the tip and substrate were in contact. For example, although the approach curves for the HSA probe tip versus the COO^--terminated SAM and Au surface were purely repulsive on approach due to electrostatic double layer and possibly hydration forces, interfacial energy dissipating mechanisms at the nanoscale lead to adhesion hysteresis on retract. Hence, the experimentally measured adhesive energy per unit area, $<W_{exp}>$ is expected to be much greater than the thermodynamic work of adhesion,

$<W_{adhesion}>$. Upon compression, the hydrophilic, alkanethiol COO^--terminated SAM exhibited minimal adhesion to the HSA-modified probe tip (-4.9 mN/m, -5.3 to -12 k_BT/protein) while the hydrophobic CH_3-terminated, alkanethiol SAM and Au exhibited significant adhesion hysteresis (more than an order of magnitude greater, -21 to -29 mN/m, -22 to -73 k_BT/protein). On retract, multiple modes of interaction or adhesive mechanisms were observed within a single dataset for the COO^- terminated SAM.

The possible mechanisms involved in HSA adhesion include: a) formation and rupture of short range HSA-SAM noncovalents bonds, b) structural rearrangements of the SAM molecules leading to surface force hysteresis, and c) entropic and enthalpic penalties for extensional protein denaturation on retract.

8.3 Nanoscale Intermolecular Interactions between HSA and Low Grafting Density Surfaces of PEO

The net nanoscale force versus separation distance between an HSA modified probe tip and a surface of neutral, chemically end-grafted PEO_{50K} mushrooms was measured directly on approach (loading) and retract (unloading) in aqueous buffer solution (IS = 0.01M, pH = 7.4). On approach, a fairly broad, nonhysteretic, nonlinear, purely repulsive net force is observed to begin at $D < 30$ nm. The magnitude of this force, even under such low grafting density conditions, is much larger than that predicted by either electrostatic or steric (configurational entropy) theories, and is one of the key factors in understanding the protein resistant properties of PEO. One possible source for this "additional" force, which is also supported by single molecule extensional experiments, is enthalpic disruption of the compacted, water-bound ttg segments and helical supramolecular structure of the PEO chain under compression to the extended ttt state as the chain extends in the x/y plane of the sample perpendicular to the direction of the applied compressive force (z). A local maximum followed by an interesting drop in the net repulsive force with decreasing separation distance is observed at $D < 4$ nm. During approach of the HSA probe tip on the PEO surface, a number of PEO chain segments become physically adsorbed to the HSA probe tip, enough so that they are strong enough to act as a "tether" and enable extension of individual PEO chains between the surface and probe tip on retract, resulting in a long range, nonlinear, adhesive interaction between the probe tip and surface. This clearly demonstrates that, given enough compressive force and time, short range attractive interactions between the PEO chain segments and the HSA protein surface may form, where the binding force per PEO chain is $<F_{adhesion}>/R_{TIP} = 0.9 \pm 1.6$ mN/m. This interaction may have contributions from hydrogen bonds between protonated basic groups of the HSA and the -O- groups of the PEO, and from van der Waals and hydrophobic forces.

8.4 Deconvoluting the Total Intermolecular Interaction Potential through manipulation of Solvent Conditions

The net nanoscale interaction potential as a function of distance, U(D), was measured between a probe tip covalently bound with human serum albumin (HSA) and poly(ethylene oxide) (PEO) under a variety of solution conditions, including variations in ionic strength, addition of small amounts of the antihydrophobic agent isopropanol to a PBS stock solution, and in a 100% organic solvent. The role of bound lipids in HSA hydrophobic interactions was also investigated by studying the effect of isopropanol on the U(D) between lipid-free HSA and PEO.

An increase in the ionic strength from IS = 0.01 M to IS = 1.0 M resulted in an increase in the range and magnitude of the repulsive force observed on approach at $D < 10$ nm. On retract, an increase in the $<F_{adhesion}>$ and a decrease in $<D_{adhesion}>$ was observed. Overall, it is clear that conditions of increased ionic strength interfere with the intermolecular binding between HSA and PEO, inhibiting their ability to tether and extend on retraction. This interference dominates over any electrostatic or steric interactions from configurational entropy that may be present in U(D). This effect was also observed in previous experiments[198] between PEO and an unmodified Si_3N_4 probe tip, suggesting that it is primarily attributable to the PEO rather than the HSA.

Addition of isopropanol to a PBS stock solution in MFP experiments resulted in an increase in the magnitude of U(D) on approach, likely due to the mutual hydrophilic-hydrophilic repulsive force between the protein tip and the polymer surface. The approach data suggest the presence of a quantifiable hydrophobic component to U(D), which we determined to be approximately 20% of the total intermolecular interaction potential at the local maxima on approach ($D \sim 1$ nm), which amounts to ~ 11-18 k_BT/protein. The addition of isopropanol did not have any significant effect on the retraction data, as determined by a rigorous series of statistical analyses.

In 100% isopropanol, i.e. under pure organic solvent conditions, the approach curve exhibited a long-ranged ($D < 25$ nm) net attractive force, presumably due to a solvophobic effect imparted by the precipitation of PEO and HSA. The approach curve was found to fit a function comprised solely of models of the solvophobic and van der Waals forces rather well. Once in contact, the HSA, which is completely denatured in the isopropanol, binds nonspecifically to the polymer-grafted surface, and extends readily to long distances under relatively low adhesive force. It is clear from these results that the presence of water is absolutely essential to the protein-resistant properties of PEO.

Addition of isopropanol to MFP experiments using a probe tip bound with lipid-free HSA resulted in a decrease in the magnitude of U(D) on approach, a rather counterintuitive result considering that, in the absence of fatty acids, the hydrophobic pockets of the protein should be exposed, and the effective hydrophobic force thereby magnified. The addition of isopropanol should then result in an even more pronounced increase in the repulsive force on approach than that which was observed with the lipid-bound probe tip. In fact, the change in repulsive force from the addition of 0.5% isopropanol to 0.01M PBS, -0.97 to -1.58 k_BT/protein, was 10-20 k_BT less with the lipid-free tip than with the lipid-bound probe tip. On retract, a dramatic decrease in the frequency of protein and/or polymer extension was observed on the addition of isopropanol. In 100% isopropanol, the system behaved in a similar solvophobic manner as observed with the lipid-bound tip, and chain extension again became the dominant mechanism for the denatured molecules.

Overall, the above results suggest that while hydrogen bonding is crucial to the binding of HSA to PEO, hydrophobic interactions are also clearly important, and novel devices aiming to exhibit enhanced protein resistance should possess a hydrophobic component less than 20%. Furthermore, the protein resistant properties of PEO are enhanced in high ionic strength environments, and hence are likely to be most successful in such situations. Depending on the application of the desired biomaterial, one may choose to seek a surface coating with a PEO-like response to the ionic strength, or a material with a more traditional electrostatic response in which the intermolecular repulsion is increased in low ionic strength environments.

Lastly, an interesting feature of our retract data is the presence of various "modes" of protein/polymer extension, which we attribute to extension of specific domains of the HSA macromolecule. There appears to be three distinct distance ranges in which adhesion and extension occurs: D ~ 0-90 nm, D ~ 100-190 nm, and D ~ 200-275 nm, which individually are rather consistent with the average contour length of each of the three domains of HSA, $L_{contour,domain} \sim 75$ nm. Which domain is extended on a given retract cycle is likely dominated by the specific orientation that the majority of the proteins are in as the probe tip comes into contact with the surface, which is assumed to be random.

8.5 Testing the Hypothesis: Intermolecular Interactions between HSA and Oligomannose Monolayers

Oligosaccharides are found on blood-contacting surfaces throughout the human body, and are thus an interesting candidate to test Mother Nature's wisdom against Herself. To this end, we selected a series of derivatives of the oligosaccharide Oligomannose-9 (Man-9), and tested them via HRFS with an HSA-grafted probe tip, and compared the results with parallel experiments conducted with the same probe tip on polymers and oligomers of ethylene oxide, perhaps the most protein-resistant material currently in use for biomaterial surface coatings, and a system in which we have developed a solid understanding. The results suggest that higher oligosaccharides, which clearly exhibit a greater long range repulsion on approach to, and a lower binding force on retract from, an HSA-grafted probe tip (as compared to PEO and EG_3), have the potential to outperform poly- and oligo(ethylene oxide) in their ability to resist the adhesion of blood plasma proteins. The ability to evade protein adsorption, the first step in the biological thrombic and inflammatory responses, is considered key in the design of novel materials for bio- and hemocompatible blood-contacting biomedical applications. Furthermore, the large availability and low-cost of oligosaccharide derivatives makes them particularly attractive alternatives for commercial-scale applications.

8.6 Extending the Technique to Other Applications: Intermolecular Interactions between the HIV Therapeutic Drug Cyanovirin-N and Oligomannose Monolayers

Our studies of the binding affinity of the HIV therapeutic drug Cyanovirin-N to various oligosaccharide moieties involved in the binding of HIV to host cells, demonstrated the possibilities of our technique for studying a large variety of chemical and biochemical interactions. The results also clearly revealed some limitations of the current experimental setup, as our results correlated poorly with previously reported binding affinity studies. We suspect that the discrepancy in the results may be due to the fact that, in the previous study, the molecules were all free in solution and able to bind in a very specific manner, while in our study, both ligand and receptor were bound to their respective surfaces, and the random binding of the CV-N to the probe tip does not ensure that it will be in the correct conformation to bind to mannose on tip-surface contact. It is therefore likely that the adhesion forces measured in our study reflected nonspecific CV-N – Oligomannose binding, rather than a specific ligand-receptor interaction.

8.7 Suggestions for Future Work

This work has laid the groundwork for a barrage of future studies in the development of novel biomaterial surface coatings. The technique of HRFS has proven to be extremely useful and cost-effective at investigating the molecular details of protein-biomaterial surface interactions, and at qualitatively evaluating the potential of a novel material to outperform its predecessors in resisting protein adsorption. This application may prove to be exceptionally useful in the design of biomaterials with enhanced thromboresistant or anti-inflammatory properties.

I believe that it would be worthwhile to conduct a thorough search of inexpensive, commercially available materials that meet the suggested criteria for designing a hemocompatible surface as outlined in this thesis, and to conduct a series of in-depth biocompatibility studies on them as potentially commercially viable product. As a first step, HRFS would be a powerful tool to pre-screen candidates before conducting more time-consuming study. Although HSA is an excellent model protein for a fundamental study such as that presented here, it may be more relevant to materials designed to prevent thrombosis if other proteins such as fibrinogen or immunoglobulin, which are more proactive in the thrombic and inflammatory processes, were utilized instead. The simple chemistry employed here to graft the proteins to the cantilever probe tip would likely be useful as well in attaching as variety of proteins to Si_3N_4, as the success of our CV-N attachment procedures indicated. One modification I might suggest to the current protocol is to seek an amino*propyl*-siloxane compound for modifying the Si_3N_4 rather than an aminobutyl-, as these materials are less expensive and more readily available.

Once HRFS experiments have established a potential candidate, I recommend embarking on a series of practical biocompatibility tests, such as surface plasmon resonance (SPR, to correlate with HRFS experiments) and blood flow loop testing, as well as various other forms of *in vitro* protocols. If these experiments prove to be successful, I would highly recommend beginning to experiment with actual biomaterial surface modification using the new materials, and preclinical testing in animal studies. The ideal application for materials stemming from these particular studies is clearly vascular in nature, and could emcompass a wide variety of devices such as coronary stents, vascular grafts and catheters, and heart defibrillators. I have full confidence that this technique has great potential to make headway in the biomaterials market of the future.

In terms of extending HRFS to use in other biochemical studies, researchers are already conducting experiments involving the use of hundreds of cantilevers at a time to serve as chemical sensor nanoarrays. Clearly the potential exists for huge strides to be made in applying AFM technologies to yet unimaginable innovations.

Appendix A

Note: The following are excerpts from "Molecular Mechanics of Cartilage: Quantification of GAG Electrostatic Interactions Via High-Resolution Force Spectroscopy", Doctoral Thesis, Department of Mechanical Engineering, Massachusetts Institute of Technology, 2003, by Dr. Joonil Seog, and have been reprinted here with explicit permission by the author.

A.1 The Molecular Force Probe: Instrumentation and Data Conversion

Instrumentation. HRFS experiments were conducted using a new cantilever-based, piconewton-sensitive instrument; the *Molecular Force Probe* (MFP) (Asylum Research, Santa Barbara, CA) to measure force, F (nN), versus tip-sample separation distance, D (nm). (**Figure A.1**) Modeled on AFM technology, the MFP employs a micro-machined soft, flexible cantilever with a sharp tip as a force transducer that deflects in response to the small forces between the cantilever tip and a sample surface. A near-IR laser beam is focused on the backside of the end of the cantilever and directed with a mirror into a split position-sensitive photodiode (PSPD). Depending on the interaction between the tip and the sample, the cantilever bends upward (repulsion) or downward (attraction), which changes the path of the laser. The laser path is recorded by photodiode and converted to force vs tip-sample separation distance.

The MFP has an open fluid cell design with an optical (video) microscope located in the base, making it easy to perform an experiment at various aqueous environments and ideal to work on polymeric and biological samples. An adjustable laser focus, novel optic lever geometry, and a low coherence light source optimize response and minimize interference reflections from reflective samples. A piezoelectric translator (10 μm range) located on a flexure plate in the head incrementally moves the tip towards the sample in the z-direction perpendicular to sample plane ("approach") and away from the sample ("retract") at a constant rate. An LVDT (Linearly Variable Differential Transformer) position sensor (<3Å noise in 0.1-1 kHz bandwidth, 15 μm extensional capability, 0.02% linearity), also located on the flexure plate in the head, quantifies the distance the z-piezo moves the cantilever directly, thus eliminating error due to piezo hysteresis and other nonlinearities, and also reducing or eliminating the effects of thermal drift over long time scales.

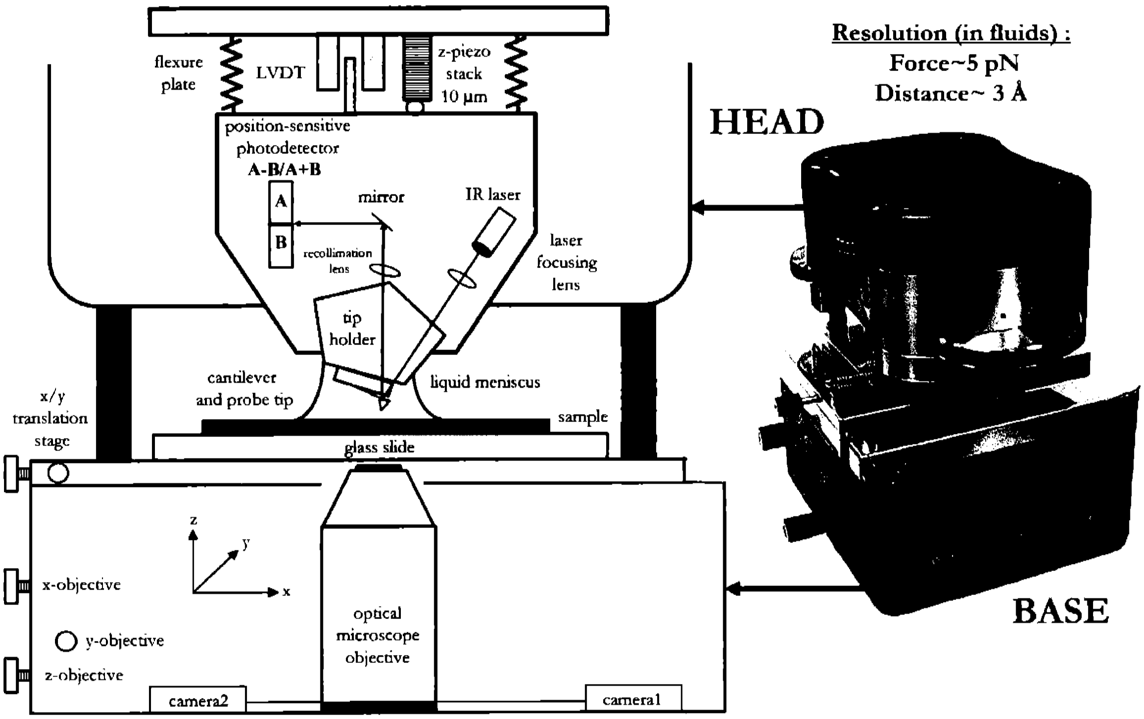

Figure A 1 Schematic diagram of Molecular Force Probe (MFP).

Conversion of Raw Data and Measurement Errors. Igor Pro software routines (Wavemetrics) were used for conversion of photodiode sensor output voltage (V) into force, F(nN), and LVDT output (nm) into tip-sample separation distance, D (nm). The vertical sensor outputs (V) (i.e., the difference of the top minus bottom quadrants of the PSPD normalized by the total PSPD output, s(V)=(T-B)/(T+B)), were converted into cantilever deflection, δ (nm). This was implemented assuming that the change in z-piezo position dz measured by the LVDT (equal to the change in position of the base of the probe tip) is equivalent to the change in cantilever deflection, dδ (nm), in the repulsive, contact regime of constant compliance:

$$\delta\,(\text{nm}) = s\,(\text{V}) \bullet \text{IOLS}\,(\text{nm/V}) \qquad \textbf{Equation A.1}$$

where the IOLS is the "inverse optical lever sensitivity" (nm/V) and is equal to the inverse slope of sensor versus LVDT output curve in the constant compliance regime. The force was then calculated by using Hooke's law for a linear elastic spring:

$$F\,(\text{nN}) = k_c\,(\text{N/m}) \bullet \delta\,(\text{nm}) \qquad \textbf{Equation A.2}$$

where F (nN) is the interaction force and k_c is the cantilever spring constant (N/m). k_c was determined for each individual cantilever according to a nondestructive method described in the literature. [231]The usual convention of positive (+) for repulsive forces and negative (-) for attractive forces was employed. The zero force baseline was taken from data obtained when the cantilever was undeflected far away from the surface (~1000 nm). The error in force measurements is due to calculation of the IOLS (± 5%), the spring constant calibration

(± 20%), and nonlinearities of the photodetector associated with the finite size of the laser spot (± 2%). Using a *Thermomicroscopes* V-shaped probe tip of nominal tip radius ~20-50, length = 320μm, and nominal spring constant k=0.01N/m, the MFP is able to achieve a thermally limited force detection of ~5 pN in aqueous solution in a 1 kHz Bandwidth. [232]

The LVDT signal output (volts) was converted into z-piezo distance, z (nm), by calibration at Asylum Research, Inc. via interferometry. The LVDT was found to have a sensitivity of 1.47 μm/V. z (nm) was converted into the tip-sample separation distance, D (nm), by correcting for the cantilever displacement due to the surface interaction force:

$$D\ (\text{nm}) = z\ (\text{nm}) - \delta\ (\text{nm}) \qquad \textbf{Equation A.3}$$

where δ is calculated from Equation A.2. The vertical region of apparent infinite slope in the high-force, constant compliance regime was set to D=0, which is due to the fact that the spring constant of the cantilever is much less than the stiffness of the substrate.

Appendix B

Note: The following are excerpts from "Molecular Mechanics of Cartilage: Quantification of GAG Electrostatic Interactions Via High-Resolution Force Spectroscopy", Doctoral Thesis, Department of Mechanical Engineering, Massachusetts Institute of Technology, 2003, by Dr. Joonil Seog, and have been reprinted here with explicit permission by the author.

B.1 Theoretical Models for Electrostatic Forces: Diffuse Electrical Double Layer Theory

The Poisson-Boltzmann (PB) equation gives an expression for the electrical potential, Φ (V), between two charged surfaces in an electrolyte solution which, for a mono-monovalent electrolyte has the form: [233,234]

$$\nabla^2\Phi = \frac{2FC_0}{\varepsilon_w}\sinh\left(\frac{F\Phi}{RT}\right) \qquad \textbf{Equation B.1 1}$$

where F is the Faraday Constant (=96,500 Coulombs/mole), C_o the bulk concentration of ions (moles/m^3), ε_w the dielectric permittivity of water (=6.9*10^{-10} Coulombs/Nm^2), R the Universal Gas Constant (=8.314 J/mole·K), and T the absolute temperature=298 K. To uniquely determine the potential, two boundary conditions on either the potential or its derivative (the electric field) are required. Unfortunately, the PB equation is nonlinear and therefore is difficult to solve analytically except for simple geometries. The force, F, per unit area acting in the z-direction on the charged surface or, more generally, at any position $z=z_0$ between the charged surfaces is the sum of two terms: the osmotic pressure due to the ion concentration gradients and the Maxwell electric field stress due to the force of the electric field action on ionic: [233,234]

$$\frac{\mathrm{F}}{\mathrm{Area}} = \left(2RTC_0(\cosh(\frac{F\Phi}{RT}) - 1) + \frac{\varepsilon_w}{2}(\nabla\Phi)^2 \right)\Bigg|_{z=z_0}$$ **Equation B.1 2**

B.1.1 Constant Surface Charge Density Model: Analytical Solution[118,131,141,235]

This model represents the tip as a smooth hemisphere with constant surface charge per unit area, σ_1 (Coulombs/m^2), and the substrate as a flat plane with constant surface charge per unit area, σ_2. An analytical solution of the linearized PB equation is often used in the literature and can be obtained by first linearizing Equation B.1_1 for small enough $F\Phi/RT$ to obtain:

$$\nabla^2\Phi \approx \frac{2F^2C_0}{\varepsilon_w RT}\Phi = \kappa^2\Phi$$ **Equation B.1 3**

where κ^{-1} is the electrical Debye length that can be calculated independently from the ionic strength using:

$$\kappa^{-1} = \sqrt{\frac{\varepsilon_w RT}{2z^2F^2C_{io}}}$$ **Equation B.1 4**

where the ion valence z = 1 for our experiments. The PB equation has been solved for two infinite parallel planes of charge, [118] and the result integrated to obtain the force between a hemisphere and plane. [235] For two infinite planes of charge with the specified surface charges σ_1 and σ_2, the boundary conditions at these surfaces are: $\frac{\partial\Phi}{\partial z} = \frac{\sigma_1}{\varepsilon_w}$ and $\frac{\partial\Phi}{\partial z} = -\frac{\sigma_2}{\varepsilon_w}$.

As $z \to \infty$, the potential and the electric field approach zero. The force per unit area between two infinite flat planes of charge having densities σ_1 and σ_2 and separated by a distance D reduces to: [118]

$$\frac{F_{FLAT}}{Area} = \frac{\sigma_1^2 + 2\sigma_1\sigma_2\cosh(\kappa D) + \sigma_2^2}{2\varepsilon_w \sinh^2(\kappa D)}$$ **Equation B.1 5**

The force on a hemispherical tip of radius $R_{HEMISPHERE}$ is obtained by integrating the force between flat surfaces over appropriately sized concentric cylinders. If the surface charge on the tip and the substrate are of the same order and κD is small, then the σ^2 terms can be neglected and the sinh can be linearized, thus yielding:

$$F_{HEMISPHERE} \approx \frac{4\pi\sigma_1\sigma_2 R_{HEMISPHERE}}{\varepsilon_w \kappa} e^{-\kappa D}$$ **Equation B.1 6**

This approximation is only valid when |Φ| is much smaller than the "thermal voltage" $\frac{RT}{F} \approx 25.7\mathrm{mV}$. When |Φ| >> 25.7mV, the linearized model will overestimate the force. As we are using a constant charge boundary condition, the magnitude of the potential on the surface will increase as the tip approaches the surface. Therefore, when using a constant charge boundary condition, the linearized PB equation may not be accurate for small separations.

B.1.2. Constant Surface Charge Model: Numerical Solution

We used a Newton method on finite differences[236] to solve the full nonlinear PB equation subject to one boundary condition at each surface. The force between two infinite charged planes was first obtained and then numerically integrated to give the force between a hemispherical tip and planar substrate. Since the problem is one dimensional, the potential in space can be represented as a one-dimensional matrix or vector in which each entry is the potential at evenly spaced points along the *z*-direction. The derivatives in the *z*-direction can be written as differences between neighboring points. The PB equation for each discrete entry plus the boundary conditions give a set of N nonlinear equations, where N is the number of discretizations, all satisfied if the potential at each point is correct. If a close enough initial guess for the value of the potential at all points is given, then that guess can be refined using a Taylor series expansion. This is repeated until the change in potential at each step is smaller than an error threshold. This algorithm is known as a Newton method for solving multidimensional systems. The potential is then converted to a force by taking a bounding box with one surface at point *i* between the two charged planes (where the derivative of the potential is zero; i.e. the electrical field is zero) and the other surface at infinity (where the potential and electric fields are zero). The force on the enclosed surface is then:

$$\frac{\mathrm{F}}{\mathrm{Area}} = \left(2RTC_0 \cosh(\frac{F\Phi[\mathrm{i}]}{RT}) - 1 \right) \qquad \textbf{Equation B.1 7}$$

The hemispherical tip geometry is approximated by using the calculated force between the flat surfaces and summing up the force on appropriately sized concentric cylinders. In effect, this method, sometimes known as Surface Element Integration (SEI), [134] is the numerical version of the integral for the linearized hemisphere tip solution above. SEI will give the exact interaction if the stress (force per unit area) is normal to the surfaces. This requirement is met if there are constant potential boundary conditions. [134] However, when the boundary conditions are constant charge, the electric field will not be directed normal to the surface (the surfaces are no longer equipotential) and the stress will not act normal to the surfaces of the tip and substrate. SEI will then underestimate the total force since it does not take the tangential components of the stress into account. Therefore, SEI can only be used to estimate the force between constant charge hemisphere tip and substrate when the radius of the tip is bigger than the Debye length, since the tangential components of the stress will then be small. This method still has advantages over the standard Derjaguin approximation, [141] in which the force between a hemisphere and plane separated by distance D is approximated by calculating the force per unit area between two infinite planes separated by D and then multiplying by $2\pi R_{\mathrm{HEMISPHERE}}$. This is only valid when $R_{\mathrm{HEMISPHERE}}$ is very large and D is very small. The SEI approximation is valid for any value of D as long as $R_{\mathrm{HEMISPHERE}}$ is larger than the Debye length. In addition, SEI can be used for many geometries and not just hemispheres, while the Derjaguin approximation is only valid for convex tip geometries. The above numerical method was implemented in C and run in Matlab (MathWorks Inc., Natick). Space was discretized to 800 increments (i.e. N= 800); the program ran until the solution converged sufficiently. [236]

REFERENCES

[1] *Wikipedia Home Page*. http://www.wikipedia.org/wiki/ (accessed October 2004).

[2] *FDA Device Classes*. U.S. Food and Drug Administration: http://www.fda.gov/cdrh/devadvice/3132.html (accessed October 2003).

[3] Inc., B. *Biogroove Hip System*. 2003. http://www.biomet.com/hips/primary_biogroove.cfm (accessed April 23 2003).

[4] Lum, L., Wainscott, S., Tamhidi, L., Ramey, N., Peace, C., Rivera, M. and Hormel, J. *Nonthrombogenic Treatments and Strategies*. http://www.jhu.edu/~matsci/teaching/510.420/presentation%2042902.doc (accessed September 24 2002).

[5] Spector, M., Ph.D. Joints: Prosthetic Replacement and Regeneration (Bone, Cartilage, Meniscus, Ligament, and Tendon); Boston, MA.

[6] Yannas, I. V., Lee, E., Orgill, D. P., Skrabut, E. M. and Murphy, G. F. Synthesis and characterization of a model extracellular matrix that induces partial regeneration of asult mammalian skin; Natl. Acad. Sci., USA, 1989; Vol. 86.

[7] Chang, A., Yannas, I. A., Perutz, S., Loree, H., Sethi, R. R., Krarup, C., Norregaard, T. V., Zervas, N. T. and Silver, J. In Electrophysiological Study of Recovery of Peripheral Nerves Regenerated by a Collagen-Glycosaminoglycan Polymer Matrix, C. G. Gebelein and R. L. Dunn, Eds.; Plenum Press: New York, 1990.

[8] Barenburg, S. A. *MRS Bull.* **1991**, *16*, 26.

[9] Hubbell, J. A. and Langer, R. *Chem. Eng. News* **1995**, 42-54.

[10] Peppas, N. A. and Langer, R. *Science* **1994**, *263*, 1715.

[11] Halperin, A. and Leckband, D. *C. R. Acad. Sci. Paris: Polymers at Interfaces* **2000**, *Series IV*, 1171-1178.

[12] Anderson, J. M. and Kottke-Merchant, K. *CRC Critical Reviews Biocompatibility* **1985**, *1*, 111-204.

[13] Lane, D. A. and Bowry, S. K. *Nephrel. Dial. Transplant* **1993**, *9*, 18-28.

[14] Halperin, A. *Langmuir* **1999**, *15*, 2525-2533.

[15] Fredrickson, G. H. and Pincus, P. *Langmuir* **1991**, *7*, 786.

[16] Hermans, J. *J. Chem. Phys.* **1982**, *77*, 2193-2203.

[17] Jeon, S. I., Lee, J. H., Andrade, J. D. and DeGennes, P. G. *J. Colloid Interface Sci.* **1991**, *142*, 149-158.

[18] Jeon, S. I. and Andrade, J. D. *J. Colloid Interface Sci.* **1991**, *142*, 159-166.

[19] Ostuni, E., Chapman, R. G., Liang, M. N., Meluleni, G., Pier, G. I., D. E. and Whitesides, G. M. *Langmuir* **2001**, *17*, 6336-6343.

[20] International Organization for Standardization, *ISO 10993-4.*

[21] Europea Standard, *EN 30993.*

[22] American Society for Testing and Materials, *ASTM F-756.*

[23] British Standard, *BS 5736.*

[24] Vroman, L. and Adams, A. L. In Why Plasma Proteins Interact at Interfaces, J. L. Brash and T. A. Horbett, Eds.; Washington, D. C., 1987.

[25] Abbott, N. L., Blankschtein, D. and Hatton, T. A. *Macromolecules* **1992**, *25*, 3932-3941.

[26] Azegami, S., Tsuboi, A., Izumi, T., Hirata, M., Dubin, P. L., Wang, B. and E., K. *Langmuir* **1999**, *15*, 940-947.

[27] Sheth, S. R. and Leckband, D. Measurements of attractive forces between proteins and end-grafted poly(ethylene glycol) chains; Natl. Acad. Sci., USA, 1997; Vol. 94.

[28] Leckband, D., Sheth, S. and Halperin, A. *J. Biomater. Sci. Polymer Edn.* **1999**, *10*, 1125-1147.

[29] Efremova, N. V., Bondurant, B., O'Brien, D. F. and Leckband, D. E. *Biochemistry* **2000**, *39*, 3441-3451.

[30] Xua, Z. and Marchant, R. E. *Biomaterials* **2000**, *21*, 1075-1083.

[31] Currie, E. P. K., Van Der Gucht, J., Borisov, O. V. and Stuart, M. A. C. *Pure Appl. Chem.* **1999**, *71*, 1227.

[32] Harris, J. M. *Poly(ethylene glycol) Chemistry: Biotechnical and Biomedical Applications*; Plenum: New York, 1992.

[33] Efremova, N. V., Huang, Y., Peppas, N. A., Leckband, D. E. and 2002 18, -. *Langmuir* **2002**, *18*, 836-845.

[34] Cleland, J. L., Builder, S. E., Swartz, J. R., Winkler, M., Chang, J. Y. and Wang, D. I. C. *Bio/Technology* **1992**, *10*, 1013-1019.

[35] Furness, E., Ross, A., Davis, T. P. and King, G. C. *Biomaterials* **1998**, *19*, 1361-1369.

[36] Topchieva, I. N., Efremova, N. V., Khvorov, N. V., Magretova, N. V. and 1995, 380-388. *Bioconjugate Chemistry* **1995**, *6*, 380-388.

[37] Brandrup, J. and Immergut, E. H. In Polymer Handbook, 3rd; Eds.; Wiley: New York, 1989.

[38] Tasaki, K. *J. Am. Chem. Soc.* **1996**, *118*, 8459-8469.

[39] Begum, R. and Matsuura, H. *J. Chem. Soc. Faraday Trans.* **1997**, *93*, 3839.

[40] Matsura, H. and Miyazawa, T. *Bull. Chem. Soc. Japan* **1968**, *41*, 1798.

[41] Koenig, J. I. and Angood, A. C. *J. Polymer Sci.* **1970**, *8*, 1787-1796.

[42] Lui, K. J. and Parsons, J. L. *Macromolecules* **1969**, *2*, 529.

[43] Oesterhelt, F., Rief, M. and Gaub, H. E. *New J. Physics* **1999**, *1*, 6.1-6.11.

[44] Maron, S. H. and Filisko, F. E. *J. Macro. Sci.* **1972**, *hys. B6*, 79.

[45] Tadokoro, H. *Structure of Crystalline Polymers*, Malabar: Kriege, 1990.

[46] Armstrong, J. K., Leharne, S. A., B. H. Stuart, B. H., Snowden, M. J. and Chowdhry, B. Z. *Langmuir* **2001**, *17*, 4482-4485.

[47] Scott, H. *J. Coll. Interf. Sci.* **1973**, *43*.

[48] Irvine, D. J., Mayes, A. M., Satija, S. K., Barker, S. J., Sofia-Allgor, S. J. and Griffith, L. G. *J. Biomed. Mat. Res.* **1998**, *40*, 498-509.

[49] Schick, M. J. and 17. *J. Coll. Sci.* **1962**, *17*, 801-813.

[50] Sanfeld, A. *Thermodynamics of Charged and Polarized Layers*, Wiley-interscience publication: Bath (UK), 1968; Vol. 10.

[51] Jimenez, J. and Rajagopolan, R. *Langmuir* **1998**, *14*, 2598-2601.

[52] Szleifer, I. *Biophys. J.* **1997**, *72*, 595-612.

[53] Guffond, M. C., Williams, D. R. M. and Sevick, E. M. *Langmuir* **1997**, *13*, 5691-5696.

[54] Dolan, A. and Edwards, F. *Proc. R. Soc. London* **1974**, *337*, 509-516.

[55] Wade, L. G., Jr. *Organic Chemistry*, 3rd; Prentice Hall: Upper Saddle River, New Jersey, 1995.

[56] Peters, T. *Adv. Protein Chem.* **1985**, *37*, 161.

[57] Wu, S. *Polymer Interfaces and Stability*, Marcel Dekker, Inc.: New York, 1982.

[58] Israelachvili, J. and Adams, G. E. *J. Chem. Soc. Faraday Trans. 1* **1978**, *74*, 975-1001.

[59] Kretschmann, E. and Rather, H. *Z. Naturforsch.* **1968**, *Teil A 241*, 2135-2136.

[60] Mahn, W. K. *Colloids Surf. A* **1997**, *128*, 145-154.

[61] Ahrens, H., Baekmark, T. R., Merkel, R., Schmitt, J., Graf, K., Raiteri, R. and Helm, C. A. *Chem. Phys. Chem.* **2000**, *1*, 101.

[62] Cao, B. and Kim, M. W. *Faraday Disc.* **1994**, *98*, 245.

[63] Kim, M. *Colloids Surf.A.* **1997**, *128*, 145.

[64] Blombaek, B. and Hanson, L. *Plasma Proteins*, John Wiley & Sons: 1979.

[65] Dayhoff, M. O. *Atlas of Protein Sequence and Structure*, National Biomedical Foundation: Washington DC, 1972.

[66] Harris, D. C. *Quantitative Chemical Analysis*, 4th; W. H. Freeman and Company: New York, 1995.

[67] Peters, T. *All About Albumin: Biochemistry, Genetics, and Medical Applications*, Academic Press: 1992.

[68] Longsworth, L. G. and Jacobsen, C. F. *J. Phys. Colloid. Chem.* **1949**, *53*, 126.

[69] Gianazza, E., Firgerio, A., Astrua-Testori, S. and Righetti, P. G., 310. *Electrophoresis* **1984**, *5*, 310.

[70] Haynes, C. A. and Norde, W. *Colloids. Surf. B. : Biointerfaces* **1994**, *2*, 517.

[71] Soderquist, M. E. and Walton, A. G. *J. Colloid. Interf. Sci.* **1980**, *75*, 386.

[72] Tanford, C., 72, 441. *J. Am. Chem. Soc.* **1950**, *72*, 441.

[73] Curry, S., Mandelkow, H., Brick, P. and Franks, N. *Brookhaven Protein Databank.* http://www.rcsb.org/pdb.

[74] Curry, S., Mandelkow, H., Brick, P. and Franks, N. *Nat. Struct. Bio.* **1998**, *5*, 827.

[75] Carter, D. C. and Ho, J. X. *Adv. Protein Chem.* **1994**, *45*, 153-204.

[76] Blomberg, E., Claesson, P. M. and Tilton, R. D. *J. Colloid Interf. Sci.* **1994**, *166*, 427.

[77] Kragh-Hansen, U. *Pharmacological Review* **1981**, *33*, 17.

[78] Ladam, G., Gergely, C., Senger, B., Decher, G., Voegel, J.-C., Schaaf, P. and Cuisinier, F. J. G. *Biomacromolecules* **2000**, *1*, 674.

[79] Kuhn, W. *Kolloid Z.* **1934**, *68*, 2.

[80] Kratky, O. and Porod, G. *Chim. Pas-Bas* **1949**, *68*, 1106.

[81] Fixman, M. and Kovac, J. *J. Chem. Phys.* **1973**, *58*, 1564.

[82] Flory, P. J. *Statistical Mechanics of Chain Molecules*, Hanser: Munich, 1988.

[83] Flory, P. J. *Principles of Polymer Chemistry*, Cornell University Press: Ithaca, New York, 1953.

[84] Marko, J. F. and Siggia, E. D. *Macromolecules* **1995**, *28*, 8759.

[85] Tskhovrebova, L., Trinik, J., Sleep, J. A. and Simmons, R. M. *Nature* **1997**, *387*, 308-312.

[86] Erickson, H. P. *Science* **1997**, *276*, 1090-1092.

[87] Carrion-Vasquez, M., Marszalek, P. E., Oberhauser, A. F. and Fernandez, J. M. *PNAS (Biophys.)* **1999**, *96*, 11288-11292.

[88] Oberhauser, A. F., Marszalek, P. E., Erickson, H. P. and Fernandez, J. M. *Nature* **1998**, *393*, 181.

[89] Fernandez, J. M., Gautel, M., Rief, M. and Gaub, H. E. In *Single Molecule Force Spectroscopy with Individual Proteins*, G. Tsoucaris, Ed.; Kluwer Academic Publishers: The Netherlands, 1999.

[90] Fernandez, J. M. *Fernandez Homepage : Research Highlights*. Columbia University: http://www.columbia.edu/cu/biology/faculty/fernandez/ (accessed October 2003).

[91] Li, H., Rief, M., Oesterhelt, F. and Gaub, H. E. *Adv. Mater.* **1998**, *4*, 316-319.

[92] Li, H., Rief, M., Oesterhelt, F. and Gaub, H. E. *Appl. Phys.* **1999**, *68*, 407-410.

[93] Li, H., Rief, M., Oesterhelt, F., Gaub, H. E., Zhang, X. and Shen. *Chem. Phys. Lett.* **1999**, *305*.

[94] Rief, M., Fernandez, J. M. and Gaub, H. E. *Phys. Rev. Lett.* **1998**, *81*, 4764-4767.

[95] Rief, M., Gautel, M., Oesterhelt, F., Fernandez, J. M. and Gaub, H. E. *Science* **1997**, *276*, 1109-1112.

[96] Rief, M., Pascual, J., Saraste, M. and Gaub, H. E. *J. Mol. Biol.* **1999**, *286*, 553-561.

[97] Rief, M., Claussen-Schaumann, H. and Gaub, H. E. *Nature Struct. Bio.* **1999**, *6*, 346.

[98] Marszalek, P. E., Pang, Y.-P., Li, H., Yazal, J. E., Oberhauser, A. F. and Fernandez, J. M. *PNAS (Biophys.)* **1999**, *96*, 7894-7898.

[99] Luzinov, I., Julthongpiput, D., Liebmann-Vinson, A., Cregger, T., Foster, M. D. and Tsukruk, V. V. *Langmuir* **2000**, *16*, 504-516.

[100] Rief, M., Oesterhelt, F., Heymann, B. and Gaub, H. E. *Science* **1997**, *275*, 1295-1297.

[101] Grandbois, M., Beyer, M., Rief, M., Claussen-Schaumann, H. and Gaub, H. E. *Science* **1999**, *283*.

[102] Ludwig, M., Rief, M., Schmidt, L., Li, H., Oesterhelt, F., Gautel, M. and Gaub, H. E. *Appl. Phys. A.* **1999**, *68*, 173-176.

[103] Gaub, H. E. and Fernandez, J. M. *Naturwissenschaften* **1998**, *71*, 11-18.

[104] Rorabacher, D. L. *Anal. Chem.* **1991**, *63*, 139-146.

[105] Yoshimura, Y. *J. Phys. Soc. Japan* **2000**, *69*, 1084-1092.

[106] Teschke, O. and de Souza, E. F. *Langmuir* **2003**, *accepted for publication.*

[107] Parker, J. L. and Claesson, P. M. *J. Phys. Chem.* **1994**, *98*, 8468-8480.

[108] Carambassis, A., Jonker, L. C., Attard, P. and Rutland, M. W. *Phys. Rev. Lett.* **1998**, *80*, 5357-5360.

[109] Leckband, D. *Annu. Rev. Biophys. Biomol. Struct.* **2000**, *29*, 1-26.

[110] Jiang, X.-P., Ortiz, C. and Hammond, P. *Langmuir* **2002**, *18*, 1131-1143.

[111] Von Smoluchowski, M. *Z. Phys. Chem.* **1917**, *92*, 129-168.

[112] Kramers, H. A. *Physica* **1940**, *7*, 284.

[113] Hammes, G. G. *Principles of Chemical Kinetics*, Academic Press: New York, 1978.

[114] Van Oss, C. J. *Journal of Molecular Recognition* **1997**, *10*, 203-216.

[115] Schreiber, F. *Prog. Surf. Sci.* **2000**, *65*, 151-256.

[116] Asylum Research, I. S. B., CA, USA). *Asylum Research, Inc. homepage*. http://www.AsylumResearch.com/frame/index.html.

[117] Derjaguin, B. V. *Kolloid Z.* **1934**, *69*, 155-164.

[118] Parsegian, V. A. and D., G. *Biophys. J.* **1972**, *12*, 1192-1204.

[119] Derjaguin, B. V., Muller, V. M. and Toporov, Y. P. *J. Coll. Interf. Sci.* **1975**, *53*, 314-326.

[120] Burnham, N. A. and Colton, R. J. In D. A. Bonnel, Eds.; VCH Publishers: New York, 1993.

[121] Johnson, K. L., Kendall, K. and Roberts, A. D. *Proc. R. Soc. London* **1971**, *A324*, 301-313.

[122] Vinckier, A., Heyvaert, I., D'Hoore, A., McKittrick, T., C., V. H., Engelborghs, Y. and Hellemans, I. *Ultramicroscopy* **1995**, *57*, 337.

[123] Vansteenkiste, S. O., Corneillie, S. I., Schacht, E. H., Chen, X., Davies, M. C., Moens, M. and Van Vaeck, L. *Langmuir* **2000**, *16*, 3330.

[124] Ruiter, T. Personal communication with M. A. Rixman; Cambridge, MA, 2002.

[125] Hertz, H. *Hertz's Miscillaneous Papers*, MacMillan: London, 1896.

[126] Verwey, E. and Overbeek, W. J. T. *Theory of Stability of Lyophobic Colloids*, Elsevier: Amsterdam, The Netherlands, 1948.

[127] Derjaguin, B. V. and Landau, L. D. *Acta Physiochim. URSS* **1941**, *14*, 633.

[128] Vezenov, D. V., Noy, A., Rozsnyai, L. F. and Lieber, C. M. *J. Am. Chem. Soc.* **1997**, *119*, 2006-2015.

[129] Dean, D., Seog, J., Ortiz, C. and Grodzinsky, A. *Langmuir* **2003**,

[130] Seog, J., Dean, D., Grodzinsky, A., Plaas, A., Wong-Palms, S. and Ortiz, C. *Macromolecules* **2002**, *35*, 5601-5615.

[131] Ninham, M. and Parsegian, A. *J. Theor. Biol.* **1971**, *31*, 405-428.

[132] Sharp, K. A. and Honig, B. *J. Phys. Chem. B.* **1990**, *94*, 7684-7692.

[133] Jin, M. and Grodzinsky, A. J. *Macromolecules* **2001**, *34*, 8330-8339.

[134] Bhattacharjee, S. and Elimelech, M. J. *Colloid Interface Sci.* **1997**, *193*, 273-285.

[135] Ederth, T., Claesson, P. and Liedberg, C. *Langmuir* **1998**, *14*, 4782.

[136] Ashby, P. D., Chen, L. and Lieber, C. M. *J. Am. Chem. Soc.* **2000**, *122*, 9467.

[137] Kane, V. and Mulvaney, P. *Langmuir* **1998**, *14*, 3303-3311.

[138] The Hamaker constant for the HSA versus COO^- system may be somewhat lower than that for COO^- versus COO^- due to the presence of the thicker low dielectric protein layer on the probe tip, which would result in a slight overestimation of the fit HSA probe tip charge per unit area.

[139] Sivasankar, S., Subramaniam, S., Leckband, D. Proc. Natl. Acad. Sci. USA, 1998; Vol. 95.

[140] Biggs, S., Mulvaney, P., Zukoski, C. F. and Grieser, F. *J. Am. Chem. Soc.* **1994**, *116*, 9150-9157.

[141] Israelachvili, J. N. and Adams, G. E. *Intermolecular and Surface Forces*; Academic Press: 1992.

[142] Christenson, H. K., Claesson, P. M., Berg, J. and Herder, P. C. *J. Phys. Chem.* **1989**, *93*, 1472.

[143] Feldman, K., Haehner, G., Spenser, N. D., Harder, P. and Grunze, M. *J. Am. Chem. Soc.* **1999**, *121*, 10134-10141.

[144] Petrash, S., Liebmann-Vinson, A., Foster, M. D., Lander, L. M. and Brittain, W. J. *Biotech. Prog.* **1997**, *13*, 635-639.

[145] Ghatak, A., Vorvolakos, K., She, H., Malotky, D. L. and M.K., C. *J. Phys. Chem. B.* **2000**, *104*, 4018.

[146] Haus, H. A. and Melcher, J. R. *Electromagnetic Fields and Energy*, Prentice-Hall: Englewood Cliffs, NJ, 1989.

[147] Weiss, T. F. *Cellular Biophysics*, MIT Press: Cambridge, MA, 1995; Vol. 1.

[148] Joyce, S. A., Thomas, R. N., Houston, J. E., Michalske, T. A. and Crooks, R. M. *Phys. Rev. Lett.* **1992**, *68*, 2790.

[149] Haupt, B. J., Senden, T. J., Sevick, E. M. and 2002 18. *Langmuir* **2002**, *18*, 2174-2182.

[150] Merkel, R., Nassoy, P., Leung, A., Ritchie, K. and Evans, E. *Nature* **1999**, *397*, 50.

[151] Cornell, C. N., Chang, R. and Kaplan, L. J. *Arch. Biochem. Biophys.* **1981**, *209*, 1-6.

[152] Graceffa, P. *Arch. Biochem. Biophys.* **1983**, *225*, 802-808.

[153] Petrash, S., Cregger, T., Zhao, B., Pokidysheva, E., Foster, M. D., Brittaini, W. J., Sevastianov, V. and Majkrzak , C. F. *Langmuir* **2001**, *17*, 7645-7651.

[154] Petrash, S., Sheller, B., Dando, W. and Foster, M. D. *Langmuir* **1997**, *13*, 1881.

[155] Sheller, N. D., Petrash, S. and Foster, M. D. *Langmuir* **1998**, *14*, 4535.

[156] Choi, E. J. and Foster, M. D. *Langmuir* **2002**, *18*, 557.

[157] Liebman-Vinson, A., Lander, L. M., Foster, M. D., Brittain, M. J., Vogler, E. A., Majkrzak , C. F. and Satija, S. *Langmuir* **1996**, *12*, 2256.

[158] Yang, A., Galloway, J. A. and Yu, H. *Langmuir* **1999**, *15*, 8405-8411.

[159] Lee, J. H., Lee, H. B. and Andrade, J. D. *Prog. Polym. Sci.* **1995**, *20*, 1043-1079.

[160] Israelachvili, J. The different faces of poly(ethylene glycol); Natl. Acad. Sci., USA, 1997; Vol. 94.

[161] Ostuni, E., Holmlin, R. E., Takayama, S. and Whitesides, G. M. *Langmuir* **2001**, *17*, 5605-5620.

[162] Holmlin, R. E., Chen, X., Chapman, R. G., Takayama, S. and Whitesides, G. M. *Langmuir* **2001**, *17*, 2841-2850.

[163] Akashi, M., Takeda, S., Miyazaki, T., Yashima, E. and Miyauchi, N. *J. Bioact. Compat. Polym.* **1989**, *4*, 4.

[164] Oshiro, T. and Kosaki, F. *Artific. Organs* **1980**, *4*, 58.

[165] Li, J.-M., Singh, M. J., Nelson, P. R., Hendricks, G. M., Itani, M., Rohrer, M. J. and Cutler, B. S. *J. Surg. Res.* **2002**, *105*, 200-208.

[166] Mowery, K. A., Schoenfischa, M. H., Saavedrab, J. E., Keeferc, L. K. and Meyerhoff, M. E. *Biomaterials* **2000**, *21*, 9-21.

[167] Pasic, M., MullerGlauser, W., L., v., Odermatt, B., Lachat, M. and Turina, M. *J. Cardio-Thorac. Surg.* **1996**, *10*, 372-379.

[168] Maroisa, Y., Chakféa, N., Guidoina, R., Roya, R., Maroisa, M., Kinga, M. W. and DouvilleaY. *Biomaterials* **1996**, *17*, 3-14.

[169] Efremova, N. V., Sheth, S. and Leckband, D. *Langmuir* **2001**, *17*, 7628-7636.

[170] Rixman, M. A., Dean, D., Macias, C. E. and Ortiz, C. *Langmuir* **2003**, *19* (15), 6202-6218.

[171] Yamamoto, S., Ejaz, M., Tsujii, Y. and Fukuda, T. *Macromolecules* **2000**, *33*, 5608-5612.

[172] Yamamoto, S., Ejaz, M., Tsujii, Y., Matsumoto, M. and Fukuda, T. *Macromolecules* **2000**, *33*, 5602-5607.

[173] Langbein, D. *Theory of van der Waals Attraction*, Springer-Verlag: Berlin, 1974; Vol. 72.

[174] Brynda, E., Houska, M., Wikerstal, A., Pientka, Z., Dyr, J. E. and Bradenburg, A. *Langmuir* **2000**, *16*, 4352-4357.

[175] Grymonpré, K., Staggemeir, B., Dubin, P. L. and Mattison, K. W. *Biomacromolecules* **2001**, *2*, 422.

[176] Abe, T., Higashi, N., Niwa, M., Kurihara, K. and Langmuir 1999, 7725-7731. *Langmuir* **1999**, *15*, 7725-7731.

[177] Bevin, M. A. and Prieve, D. C. *Langmuir* **2000**, *16*, 9274-9281.

[178] Ortiz, C. and Hadziiouannou, G. *Macromolecules* **1999**, *32*, 780-787.

[179] Israelachvili, J. N., Tandon, R. K. and White, L. R. *J. Coll. Interf. Sci.* **1980**, *78*, 430-443.

[180] Klein, J. and Luckham, P. *Nature* **1982**, *300*, 429-431.

[181] Klein, J. and Luckham, P. *Nature* **1984**, *308*, 836-837.

[182] Klein, J. and Luckham, P. *Macromolecules* **1984**, *17*, 1041-1048.

[183] Kuhl, T., Guo, Y., Alderfer, J. L., Berman, A. D., Leckband, D., Israelachvili, J. N. and Hui, S. W. *Langmuir* **1996**, *12*, 3003-3014.

[184] Kuhl, T. L., Berman, A. D., Hui, S. W. and Israelachvili, J. N. *Macromolecules* **1998**, *31*, 8250-8257.

[185] Hui, S. W., Kuhl, T. L., Guo, Y. Q. and Israelachvili, J. N. *Colloids and Surf. B. Biointerfaces* **1999**, *14*, 213-222.

[186] Braithwaite, G. J. C., Howe, A. and Luckham, P. F. *Langmuir* **1996**, *12*, 4224-4237.

[187] Butt, H. J., Kappl, M., Mueller, H. and Raiteri, R. *Langmuir* **1999**, *15*, 2559-3565.

[188] Kidoaki, S. and Matsuda, T. *Langmuir* **1999**, *15*, 7639.

[189] Kidoaki, S., Nakayama, Y. and Takehisa, M. *Langmuir* **2001**, *17*, 1080-1087.

[190] Claesson, P. M., Blomberg, E., Froberg, J. C., Nylander, T. and Arnebrant, T. *Adv. Coll. Interf. Sci.* **1995**, *57*, 161-227.

[191] Doi, M. and Edwards, S. F. *The Theory of Polymer Dynamics*, Clarendon Press: Oxford, 1986.

[192] Zimm, B. H. *J. Chem. Phys.* **1956**, *24*, 269.

[193] deGennes, P. G. *J. Chem. Phys.* **1974**, *60*, 5030.

[194] Pincus, P. *Macromolecules* **1990**, *9*, 386.

[195] Ritchie, K. and Evans, E. *Biophys. J.* **1999**, *76*, 2439-2447.

[196] Gurd, F. R. N. and Rothgeb, T. M. *Adv. Protein Chem.* **1979**, *33*, 74-165.

[197]Craighead, H. G., Turner, S. W., Davis, R. C., James, C., Perez, A. M., St. John, P. M., S., I. M., Kam, L. S. W., Turner, J. N. and Banker, G. *Biomed Microdevices* **1998**, *1*, 49-64.

[198] Rixman, M. A. 2002-2003. *Unpublished experiments.*

[199] Rixman, M. A., Dean, D. and Ortiz, C. *Langmuir* **2003**, *19*, 9357-9372.

[200] Kellermayer, M. S. Z. and Granzier, H. L. *Biochem. Biophys. Res. Commun.* **1996**, *221*, 491-497.

[201] Kellermayer, M. S. Z., Smith, S. B., Granzier, H. L. and Bustamante, C. *Science* **1997**, *276*, 1112-1116.

[202] Marszalek, P. E., Lu, H., Li, H., Carrion-Vasquez, M., Oberhauser, A. F., Schulten, K. and Fernandez, J. M. *Nature* **1999**, *402*, 100.

[203] *Human Serum Albumin.*
http://bssv01.lancs.ac.uk/StuWork/BIOS316/Bios31698/HumanSerumAlbumin/Bios316.html
(accessed June 21 2000).

[204] Ostolovskii, E. M., Botsyanksii, A. D., Borisenko, S. N. and Tolkacheva, N. V. *Biopolarimetry i Kletka* **1990**, *6*, 59-64.

[205] Homepage, B. R. G. *Biomaterial and Interfacial Design*. 2002. http://www.cchem.berkeley.edu/~crbgrp/research5.htm (accessed April 13 2002).

[206] Hoekstra, D. In *Hyaluronan as a Versatile Biomaterial for Surface Treatment of Medical Devices*; Biocoat, Inc.

[207] Adams, M. E. In *Viscosupplementation as articular therapy.*

[208] Denliger, J. L. In Hyaluronan and its derviatives as viscoelastics in medicine, T. C. Laurent, Eds.; Portland Press: London, 1998; Vol. 72.

[209] Larsen, N. E. Management of adhesion formation and soft tissue augmentation with viscoelastics: hyaluronan derivatives. In *The Chemistry, Biology, and Medical Applications of Hyaluranan and its Derivatives.*

[210] Lei, S. *Trends in Glycoscience and Glycotechnology* **2000**, *12*, 229-239.

[211] Vincent, J. F. V. *Sugars and Fillers*; Princeton University Press: Princeton, NJ, 1990.

[212] Todar, K. *Bacterial Structure in Relationship to Pathogenicity*. 2002. http://www.bact.wisc.edu/bact330/LectureBSRP (accessed April 13 2002).

[213] Ratner, D. M., Plante, O. J. and Seeberger, P. H. *Eur. J. Org. Chem.* **2002**, *5*, 826-833.

[214] Prime, K. L. and Whitesides, G. M. *J. Am. Chem. Soc.* **1993**, *115*,

[215] Bain, C. D., Biebuyck, H. A. and Whitesides, G. M. *Langmuir* **1989**, *5*, 723-727.

[216] This work, conducted in October of 2003, made use of MRSEC Shared Facilities supported by the National Science Foundation under Award Number DMR-0213282.

[217] Fritz, M. C., Haehner, G. and Spencer, N. D. *Langmuir* **1996**, *12*, 6074-6082.

[218] *Gold Crystal Structure*. WebElements: http://www.webelements.com/webelements/elements/print/Au/xtal.html (accessed October 2003).

[219] Tanuma, Powell and Penn. *NIST Electron Inelastic-Mean Free-Path Database 71.*

[220] Geyer, H., Holschbach, C., Hunsmann, G. and Scheider, J. *J. Biol. Chem* **1988**, *263*, 11760-11767.

[221] Leonard, C. K., Spellman, M. W., Riddle, L., Harris, R. J., Thomas, J. N. and Gregory, T. J. *J. Biol. Chem* **1990**, *265*, 10373-10382.

[222] Losman, B., Bolmstedt, A. J., Schonnig, K., Bjorndal, A., Westin, C., Fenyo, E. M. and Olofsson, S. *AIDS Res. Hum. Retrovir.* **2001**, *17*, 1067-1076.

[223] Shenoy, S. R., Barrientos, L. G., Ratner, D. M., O'Keefe, B. R., Seeberger, P. H., Gronenborn, A. M. and Boyd, M. R. *NMR and Calorimetric Titration Studies ofthe Anti-HIV Protein Cyanovirin-N with Branched Oligomannosides: Characterixation of Multi-Site and Multivalent Binding*; Cambridge, MA, 2002.

[224] Bolmstedt, A. J., O'Keefe, B. R., Shenoy, S. R., McMahon, J. B. and Boyd, M. R. *Mol. Pharmacol.* **2001**, *59*, 949-954.

[226] Esser, M. T., Mori, T., Mondor, I., Sattentau, Q. J., Dey, B., Berger, E. A., Boyd, M. R. and Lifson, J. D. *J. Virol.* **1999**, *73*, 4360-4371.

[227] McMahon, J. B. and Boyd, M. R. *Unpublished experiments.*

[228] Boyd, M. R., Gustafson, K. R., McMahon, J. B., Shoemaker, R. H., O'Keefe, B. R., Mori, T., Gulakowski, R. J., Wu, L., Rivera, M. I., Laurencot, C. M. and al., e. *Antimicrob. Agents Chemother.* **1997**, *41*, 1521-1530.

[229] Bewley, C. A., Gustafson, K. R., Boyd, M. R., Covell, D. G., Bax, A., Clore, G. M. and Gronenborn, A. M. *Nat. Struct. Biol.* **1998**, *5*, 571-578.

[230] Shenoy, S. R., Barrientos, L. G., Ratner, D. M., O'Keefe, B. R., Seeberger, P. H., Gronenborn, A. M. and Boyd, M. R. *Chem. & Biol.* **2002**, *9*, 1109-1118.

[231] Hutter, J. L. and Bechhoefer, J. *J. Rev. Sci. Instr.* **1993**, *64*, 1868.

[232] Sarid, D. In *Scanning Force Microscopy,* Oxford University Press.

[233] Sanfeld, A. *Thermodynamics of Charged and Polarized Layers*, Wiley-interscience publication: Bath (UK), 1968; Vol. 10.

[234] Devereux, O. F. and de Bruyn, P. L. *Interaction of Plane-Parallel Double Layers*, M. I. T. Press: Cambridge, MA, 1963.

[235] Butt, H. J. *Biophysical Journal* **1991**, *60*, 777-785.

[236] Forsythe, G. E. and Wasow, W. R. *Finite Difference Methods for Partial Differential Equations*, John Wiley & Sons, Inc.: New York, 1960.